BRNO UNIVERSITY OF TECHNOLOGY
VYSOKÉ UČENÍ TECHNICKÉ V BRNĚ

FACULTY OF MECHANICAL ENGINEERING
FAKULTA STROJNÍHO INŽENÝRSTVÍ

INSTITUTE OF MATERIALS SCIENCE AND ENGINEERING
ÚSTAV MATERIÁLOVÝCH VĚD A INŽENÝRSTVÍ

METAL MATRIX COMPOSITES PREPARED BY POWDER METALLURGY ROUTE
METAL MATRIX COMPOSITES PREPARED BY POWDER METALLURGY ROUTE

DOCTORAL THESIS
DIZERTAČNÍ PRÁCE

AUTHOR — Larissa Moravčíková de Almeida Gouvêa
AUTOR PRÁCE

SUPERVISOR — prof. Ing. Ivo Dlouhý, CSc.
ŠKOLITEL

BRNO 2021

Abstract

The development of new materials for applications in extreme environments is currently of a great importance in modern engineering technologies. Hence, the industries' requirement for enhanced structural performance of materials is constantly increasing.

In the light of that, this study aims to evaluate promising compositions of high-entropy alloys for critical applications produced by powder metallurgy through a combination of mechanical alloying and solid state sintering. For comparative purposes, the selected compositions were produced by melting routes in liquid state as well, such as vacuum induction melting and subsequent casting or vacuum arc-melting.

The powder metallurgy route enables a consequential development of metal matrix composites (MMC) via the manufacturing of oxide dispersed strengthened HEAs. This is possible due to inherent in-situ reactions during the process. In case of melting route fabrication, metallic materials with great differences in structures and related properties are manufactured, compared to those produced by powder routes. The produced MMCs and their melted counterparts are thoroughly studied.

A comprehensive evaluation of the influence of the different processing methods, especially on the materials' microstructural features and their mechanical properties is undertaken, including the effect of heat treatments on the phase transformations and stability of the materials.

Keywords: High Entropy Alloys; Complex Concentrated Alloys; Powder Metallurgy; Composites; Microstructure; Mechanical properties; Mechanical Alloying; Phase Transformations.

Abstrakt

Vývoj nových materiálů pro součásti v moderních technologiích vystavené extrémním podmínkám má v současné době rostoucí význam. Děje se tak v důsledku neustále se zvyšujících požadavků průmyslových odvětví na lepší konstrukční vlastnosti nosných materiálů.

Ve světle těchto faktů si tato studie klade za cíl posoudit nové složení slitin s vysokou entropií, které se vyznačují vysokým aplikačním potenciálem pro kritické aplikace. Slitiny jsou připravovány práškovou metalurgií, t.j. kombinací mechanického legování a slinování v pevné fázi. Pro účely srovnávaní vlastností jsou vybrané kompozice vyrobeny také tradičními metalurgickými metodami v roztaveném stavu, jako je vakuové indukční tavení a následné lití nebo vakuové obloukové tavení.

Prášková metalurgie umožňuje postupný vývoj kompozitů s kovovou matricí (MMC) prostřednictvím přípravy oxidicky zpevněných HEA slitin. To je možné díky inherentním in-situ reakcím během procesu výroby. Když se naopak zvolí výrobní postup z taveniny, připravený kovový materiál vykazuje velké rozdíly v mikrostrukturách a souvisejících vlastnostech, v porovnání se stejným materiálem vyrobeným práškovou cestou (PM). Vyrobené práškové a tavené materiály jsou detailně charakterizovány s ohledem na komplexní vyhodnocení vlivu různých metod zpracování. Práce se zejména orientuje na mikrostrukturní charakteristiky materiálů a jejich mechanické vlastnosti, včetně vlivu tepelného zpracování na fázové transformaci a mikrostrukturní stabilitu připravených materiálů.

Klíčová slova: Vysoko-entropické slitiny; Komplexní koncentrované slitiny; Prášková metalurgie; Kompozity; Mikrostruktura; Mechanické vlastnosti; Mechanické legování; Fázové transformace.

Bibliographic citation:

MORAVČÍKOVÁ DE ALMEIDA GOUVÊA, Larissa. Metal Matrix Composites Prepared by Powder Metallurgy Route. Brno, 2021. Doctoral Thesis. Brno University of Technology, Faculty of Mechanical Engineering, Institute of Materials Science and Engineering. 163 pages. Supervisor of the doctoral thesis prof. Ing. Ivo Dlouhý, CSc.

Bibliografická citace:

MORAVČÍKOVÁ DE ALMEIDA GOUVÊA, Larissa. Metal Matrix Composites Prepared by Powder Metallurgy Route. Brno, 2021. Dizertační práce. Vysoké učení technické v Brně, Fakulta strojního Inženýrství, Ústav materiálových věd a inženýrství. 163 s. Školitel dizertační práce prof. Ing. Ivo Dlouhý, CSc.

Acknowledgements

I would like to express my sincere gratitude to prof. Ivo Dlouhý for all his valuable advices, support and guidance along this entire study.

Furthermore, I would like to thank doc. Vít Jan for his advices as my supervisor specialist. I would also like to thank Dr. Igor Moravčík for the countless hours of discussion during my Ph.D. program; Mgr. Jan Čupera, Dr. Zdeněk Špotz, Dr. Josef Zapletal, Dr. Martin Zelený, Dr. Dina Kičmerová, Dr. Petr Minárik, Dr. Jozef Veselý, Dr. Jan Čížek, Ing. Ondřej Adam, Dr. Petra Krajňáková, Dr. Lukáš Řehořek, Dr. Roman Štěpánek, Dr. Petr Havlík, Ing. Ondřej Fikar, Ing. Jakub Judas and all the UMVI team for all the help, assistance, shared ideas and knowledge with the experimental and theoretical parts of this Ph.D. program, also for the fun and incredible moments during my Ph.D. journey.

Additionally, I would like to specially thank prof. Gerhard Dehm and Dr. Christian Liebscher for supervising my studies during the research stay in Max-Planck-Institut für Eisenforschung. Dr. Benjamin Breitbach is further acknowledged for the XRD experiments during this stay.

Additionally, Zuzana Kovacova, Michael Kitzmantel, Erich Neubauer from RHP-Technology GmbH, Austria; Dr. Václav Pouchlý and Dr. Hua Tan from CEITEC, Brno; doc. Antonín Záděra and Dr. Milan Omasta from FME – BUT; are gratefully acknowledged.

This work has been funded by the research project no. 19-22016S of Czech Science Foundation and by the projects no. FSI-S-20-6313 and FSI-S-17-4711 of Brno University of Technology. The support of the JCMM organization in the Internationalization program for non-EU citizens is gratefully acknowledged. The Free Mover mobility program is further acknowledged for supporting the research internship in Max-Planck-Institut für Eisenforschung in Düsseldorf, Germany.

Most importantly, I would like to specially thank my mother Lucia Maria for everything, for being the most supportive person during my entire life and for always being by my side, for her unconditional love – all that I accomplished in my life was thanks to her support. Also, I would like to thank my both fathers José Carlos and Gaspar, my sister Raíssa and my husband Igor for everything – the love, care and for being my pillar in all moments of my life – I couldn't have reached this far without you all. Also, to my family and friends for all words of encouragement and for being so supportive and understanding during this long journey.

Declaration

I hereby confirm that I am the sole author of the written work here enclosed and that I have compiled it in my own words. The work was made under the supervision of prof. Ing. Ivo Dlouhý, CSc.

Brno, …… ……...……..

Ing. Larissa Moravčíková de Almeida Gouvêa

Table of contents

1 Introduction

Modern engineering technologies require an ever-increasing structural integrity and performance, driving the research into the development of materials that are lighter, stronger, tougher and multifunctional. When it comes to high temperature purposes, there is an even greater challenge: the performance characteristics are limited by the operating conditions which can be withstood by the materials used.

The main characteristics of a high temperature material should be: ability to tolerate loading at working temperatures close to its melting point (≥0.6 T_m); resistance to mechanical degradation over extended periods of time, i.e. low rates of creep; microstructural stability at high temperatures; oxidation and fatigue resistance; as well as maintenance of properties such as high yield stress, ultimate tensile strength and fracture toughness over long exposure times. When significant resistance to loading under static, fatigue and creep conditions is required, the superalloys, specially nickel-base ones [1–3], have arisen, so far, as the fittest material for most of the high-temperature applications (e.g. jet engines, turbines for electricity generation, combustors, etc.) due to their unique features. In spite of that, their properties are also limited by their high-temperature strength – possessing a melting point of 1455 °C - an absolute limit for their temperature capability (in reality, their operating temperature is usually below 1200 °C due to some detrimental effects within the microstructure, such as presence of low melting phases, cracking and fast growth rate of Al_2O_3 and Cr_2O_3 [4], for instance). Therefore, new developments in superalloy metallurgy are required for the next generation of ultra-efficient high temperature materials.

Other metallic materials, such as the conventional refractory Nb and Mo alloys, have been considered and examined as potential alternatives for high-temperature applications, not only to their obvious higher melting points, but as well as their high-temperature strength and creep resistance, which are their key properties. Simultaneously, however, poor low-temperature ductility, very poor oxidation resistance at elevated temperatures and their high-density [5] limit the range of applications of many refractory alloys.

A prospective strategy for development of high-temperature resistant alloys could be exploring the high-entropy alloys (HEAs) approach, also known as multi-principal element alloys (MPEAs) or complex-concentrated alloys (CCAs). HEAs comprise at least five elements with near equiatomic compositions without a prominent base element, distinguishing them from the conventional alloying tactic, which typically involves a single-base element with addition of small proportions of other constituents [6–8]. They possess distinctive properties resulting from the novelty of their design concept, including – but not limited to - high softening resistance at elevated temperatures and slow diffusion kinetics [9], as well as an improved oxidation resistance has been presented by some of them [10], a simultaneous combination of high-strength and high-ductility [11], exceptional fracture resistance and damage-tolerance even at cryogenic temperatures [12,13], among other interesting features that will be further discussed in more detail within the next chapters.

By a careful selection of appropriate elements in near equiatomic ratio, for instance, refractory metals from groups IV, V and VI, one could produce refractory high-entropy alloys (RHEAs) to be tailored in a manner to further enhance these unique advantages for high-temperature applications.

Additionally, one could produce superalloy-like microstructures utilizing the HEAs approach, the so-called high-entropy superalloys, resembling the microstructures exhibited by many nickel base superalloys - composed of a disordered FCC matrix with atomically coherent precipitates with an ordered FCC (L_{12}) crystal structure. Several Al-containing HEAs have been reported to have these superalloy-like microstructures, presenting both the conventional γ(fcc) + γ'(ordered L_{12} precipitates) [14,15] as well as a BCC nanoscale precipitates within a coherent B2 matrix (or vice-versa) [16,17].

HEAs are generally fabricated by casting. Nonetheless, the route is subject to processing problems which may be detrimental for the final material. Since the alloys comprise multiple elements, they may suffer from selective evaporation of elements with intrinsic low-melting temperatures or segregation of elements with high-melting points during the melting [18–20].

Alternatively, powder metallurgy (PM) has been proven to be a reliable and low-cost method capable of relatively easy and efficient production of a varied scope of advanced materials, including high-entropy alloys [21–24]. Compared to casting, PM requires lower temperatures for its processing, since it can be realized through solid state sintering. Additionally, PM can be explored as a route for production of metal matrix composites, for example by fabrication of oxide dispersed strengthened (ODS) materials.

In this light, this study is focused on comparing some promising compositions of high-entropy alloys for high-temperature applications produced by both powder metallurgy and casting routes by using pure feedstock metallic elements. When the PM route is chosen, a consequential production of metal matrix composites (MMC) via the manufacturing of oxide dispersed strengthened HEA matrices is developed due to inherent in-situ reactions during the process. The produced MMCs are thoroughly studied and a comprehensive evaluation of the influence of the two processing methods specially on the materials' microstructural features and, consequently, on their mechanical properties are assessed.

The high-entropy alloys' concept opens room for innumerous possibilities within the compositional space, where unique properties could be achieved. Consequently, profound studies into the topic are necessary in order to achieve a basic understanding, since properties such as mechanical response, creep, oxidation resistance and fatigue of HEAs are in need to be carefully studied to see the viability of this alternative approach.

2 State of the art: high-entropy alloys

2.1 General background

The exploration of materials and their improvement have been always a significant concern for the civilization. Inhabitants of the Stone age discovered natural materials to be used for their own benefit, such as stone, wood, leather, gold, copper and silver as pure metals.

Alloying was an unintentional discovery, in which the very first kind of alloy was accidentally done by mixing copper ores with arsenic ones. The mixing of copper with tin brought the Bronze Age [25] and all the consecutive ages were named due to the importance of the principle of alloying to the humankind – in order: Bronze, Iron and Steel.

Adding small proportions of alloying elements were proven to offer superior performance by altering of the properties of materials. For instance, steels are made by adding small amounts of alloying elements to Iron. By adding chromium, a higher corrosion resistance and hardenability can be guaranteed; nickel may provide strength, toughness and corrosion resistance; manganese can improve ductility and hardenability; niobium can stabilize carbon, thus forming carbides for high-temperature steels [26,27] and so on.

Over millennia, the conventional concept of alloying small proportions of elements to a base material remained unchanged. Recently, however, two independent scientific groups – Cantor et al. [28] and Yeh et al. [6] - proposed a novel strategy to investigate the missing vast compositional space that was not explored up to 2004: the multi-element base alloying approach, also known as high-entropy alloys (HEAs).

By definition, HEAs are alloys which contain multiple principal elements, at least five or more, each having atomic percentage between 5 % and 35 %; if required, minor additions (≤ 5%) are also a possibility, therefore increasing the number of HEAs significantly. The original principle behind a HEAs concept is that supposedly achieving maximized configurational entropy using multi-component elements in near-equiatomic ratios could stabilize single solid-solution phases, instead of intermetallic compounds. As properly pointed out in [29], this claim is, however, counterintuitive, as the greater the number of elements in one alloy, the higher is the probability to form intermetallics. Therefore, most recently, other names were adopted, such as complex concentrated alloys (CCAs).

Theoretically, unique properties were claimed to present in HEAs, named as the four core effects [30] which will be briefly described in the next sections. Some of these effects, though, are questionable and were never proved to exist for the whole compositional range of possibilities.

It is valid to mention that the concept might have a predecessor from the eighteen century. The multi-element alloying approach with equimass composition with five up to seven elements was considered by Franz Karl Archard's group. However, his results showed that the properties were not attractive [31,32] and, even since, it has never been further explored during more than a two-century gap.

The new design concept came to the scientific community as a breakthrough for the restriction of a prevalent base element, opening numerous possibilities for exploration of new compositions and attracting significant attention.

The properties of conventional alloys are relatively well known and they are indicated as the yellow regions in Fig. 1. For these alloys, the number of possible element combinations is restricted. However, there is a lack of knowledge on the other regions of the compositional space. Lately, the scientific community is putting effort on fulfilling the other regions which are depicted in the same figure as red and green regions.

This information imbalance becomes more pronounced as the number of components increases. For higher-order systems, knowledge about alloys is precarious [29,33].

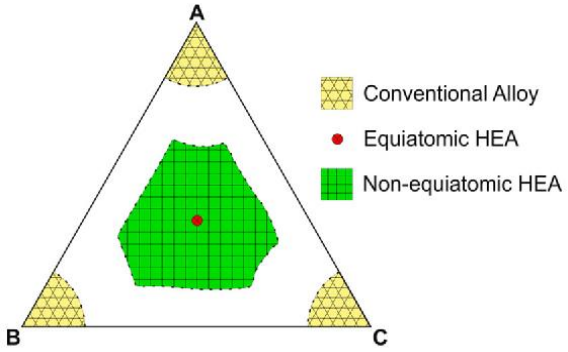

Fig. 1. Schematic ternary diagram showing the numerous possibilities of alloying in the range of the compositional space [34].

Recent studies focused on HEAs represent a great importance on fulfilling the lack of information in the compositional space range of high-order phase diagrams. Investigating the underlying properties of these concentrated solid solutions, whether possessing intermetallics or not, are a fundamental key for potentially considering the application of this new class of alloys in the industry in the future.

2.2 Definitions and thermodynamic criteria

The exploration of High-Entropy alloys motivated the scientific community to broaden their field of investigation outside the HEAs standard constituents. Now HEAs have many branches and could be classified by a range of categories, assessed by Miracle et al. [35,36]:

- Transition metal based HEAs, based on transition elements, e.g. Co, Ni, Cr, Fe, etc.
- Refractory HEAs. Most frequently used elements: Cr, Ti, V, Nb, Mo, Hf, Ta, Zr, W [20].
- Low-density HEAs. The main elements are: Li, Be, Mg, Al, Si, Sc, Ti, Zn, and Sn [37].
- Ceramic HEAs:
    - Oxides [38].
    - Metal diborides [39].
    - Perovskite-base structures [40].
- Other types of HEAs:
    - Lanthanide HEAs - comprising elements from the group 4f of the periodic table: Dy, Gd, Lu, Tb and Tm. The element Y is also frequently used [41,42].

- Brasses and bronzes, and precious metals (Ag, Au, Co, Cr, Cu, Ni, Pd, Pt, Rh and Ru for catalysis applications) [43,44].

2.2.1 Four "core effects"

High-entropy alloys were initially assumed to be governed by four main attributes which made them unique; the so-called "four core effects", namely High Entropy Effect, Lattice Distortion Effect, Sluggish Diffusion and Cocktail Effect [8,30,45]. These effects were established according to the initially available data in the literature in the beginning of the exploration of HEAs. However, up to date, after a thorough analysis of these alloys, it is clear that these effects cannot be considered as a rule, since the vast majority of these alloys do not follow the phenomena described by the claimed four effects – nor all of the hypotheses were proven. Herein, the effects will be described, and the contradictions raised since their first establishment will be supported by theoretical and practical evidences, as follows:

2.2.1.1.1 High entropy effect

It was initially believed that as the number of elements in an alloy increased, the entropic contribution to the total free energy would overcome the enthalpic contribution, thus, stabilizing solid solutions at the expenses of intermetallic compounds being suppressed [6,30]. The rationale is the following:

Based on the Boltzmann's equation, one can calculate the ideal configurational entropy per mole of a system of a random n-component solid solution, in which the i^{th} component has a mole fraction X_i [46]:

$$\Delta S_{config} = -k_b ln w = -R \sum_{i=1}^{n} X_i ln X_i \quad (1)$$

Here k_b is Boltzmann's constant, w is the number of ways in which the available energy can be mixed or shared among the particles in the system, R is the gas constant, 8.134 J/K/mol. The configurational entropy is related to distribution and the arrangement of the constituent particles in a system, i.e. in what manner they can be randomly arranged in a single lattice with the absence of any chemical affinity amongst the elements [47].

During the formation of a n-component in its liquid state or regular solid solution state with equimolar fractions, its configurational entropy is given by [6]:

$$\Delta S_{config} = -R\left(\frac{1}{n} ln \frac{1}{n} + \frac{1}{n} ln \frac{1}{n} + \cdots + \frac{1}{n} ln \frac{1}{n}\right) = -R ln \frac{1}{n} = R ln(n) \quad (2)$$

As a result, the maximum configurational entropy in equimolar alloy systems increases with increasing the number of elements.

When an equiatomic alloy system has more than five elements, its configurational entropy $\Delta S_{config} > 1.5\mathrm{R}$ [30].

Phase stability is a competition among entropy, enthalpy and other terms, such as strain energy and applied temperature. The thermodynamics of solid solution formation can be described by the fundamental equation of Gibbs free energy [47], as it is stated:

$$\Delta G_{mix} = \Delta H_{mix} - T\Delta S_{mix} \quad (3)$$

Here G_{mix} is the Gibbs free energy, H_{mix} is the enthalpy of mixing, S_{mix} is the entropy of mixing and T is the absolute temperature. At high temperatures, the term $T\Delta S_{mix}$ becomes significantly larger, thus a higher number of elements in equiatomic ratio is contributing for a potential decrease of free energy of mixing due to the highest values of entropy obtained. Since the equilibrium in the solid state is obtained at the lowest possible free energy of mixing, the phase stability is obtained at the lowest values of G_{mix}, i.e. when all elemental components are present within solid-solution phases. This is the rationale for the high-entropy effect.

One or more intermetallic phases can be also formed depending on the alloying elements. The thermodynamics of intermetallic phases formation in a two-element alloy from pure elements X and Y is described by the same Gibbs free energy equation, as follows:

$$\Delta G_{IM} = \Delta H_{IM} - T\Delta S_{IM} \quad (4)$$

Here ΔG_{IM}, ΔH_{IM} and ΔS_{IM} are the equivalent Gibbs free energy, enthalpy and entropy for intermetallic formation of a XY compound. So there is a competition between the formation of solid solution and intermetallic phases [29], while the complexity increases substantially by the addition of more elements, as more intermetallic compounds might form.

As George et al. well explained [29], in an ideal scenario which only solid solution would form, there could be even clustering of dissimilar atoms when the ΔH_{mix} would be positive, or else, there could be an ordering effect on the lattice when ΔH_{mix} is negative.

It is worth mentioning that the total molar entropy (S_{total}) of a system has several contributions: atomic configurations give an ideal component via the Boltzmann equation described above for both solid solution and intermetallics; configurational – resulting from short-range ordering or differences in atomic sizes; vibrational, magnetic dipole and electronic randomness, so the entropy change of mixing for equimolar alloys is even higher than calculated [48].

$$S_{total} = S_{ideal} + S_{config} + S_{vib} + S_{elec} + S_{mag} \quad (5)$$

The relative contributions of ideal and excess entropies to the total entropy could be modified by, for instance, the previously mentioned competition between solid solution (SS) and intermetallic (IM) phases. The difference in total molar entropy between these two [36] is:

$$\Delta S^{ss-IM} = \left(S^{SS,ideal} - S^{IM,ideal}\right) + \left(S^{SS,conf} - S^{IM,conf}\right) + \left(S^{SS,vib} - S^{IM,vib}\right) + (S^{SS,elec} - S^{IM,elec}) + (S^{SS,mag} - S^{IM,mag}) \quad (6)$$

The configurational entropy was believed to be dominant over the other three. However, the other effects in the total mixing entropy might play an important role in the phase selection. The excess vibrational contribution due to mixing at high temperatures could be calculated from Debye [49]. The negative contribution of excess vibrational entropy to overall mixing entropy might happen and attractive interactions between unlike atomic pairs could enhance this contribution. It is known that the vibrational entropy in alloys also plays an important role in the thermodynamics of substitutional solid solutions [50,51]. Particularly in HEAs, this vibrational effect should be carefully considered, due to their own nature of possessing so different atoms and therefore diverse inharmonic vibration.

The calculated lattice variations in binary alloys can even reach values of 0.2 R, in the same order of the configurational entropy contribution [52].

For solid solution alloys, there is even another indication that the contribution of the configurational entropy cannot be solely taken into consideration on the entropy of mixing calculation, as thermodynamic activities frequently diverge from Raoult's law [52], meaning that the mixing entropy is much higher than only the configurational one.

In most examples seen in the literature for HEAs, ΔS_{mix} is calculated only as configurational entropy [46], ignoring the contribution of the other fractions, which can greatly contribute for the phase stability and other properties in HEAs.

With the theories stated, after a careful literature review on the work of HEAs, one can easily find contradictions to the hypothesis reasoned by J.-W. Yeh [6]. His group considered that ΔH_{mix} = 0 for homogeneously disordered solid solution and the competing intermetallic compound would be perfect ordered, meaning that ΔS_{IM}=0, which is simply not the case in nearly all scenarios. The assumption of stabilizing solid-solution phases over intermetallics for these alloys is insufficient to counteract the driving forces that favor the formation of secondary phases. Most of the published papers about high-entropy alloys reveals multi-phase microstructures, often containing intermetallics.

That said, E.P George, D. Raabe and R.O. Ritchie [29] properly pointed out to the fact that there are four possible competing reactions of mixing three (or more) elements in equiatomic composition, as shown in Fig. 2.

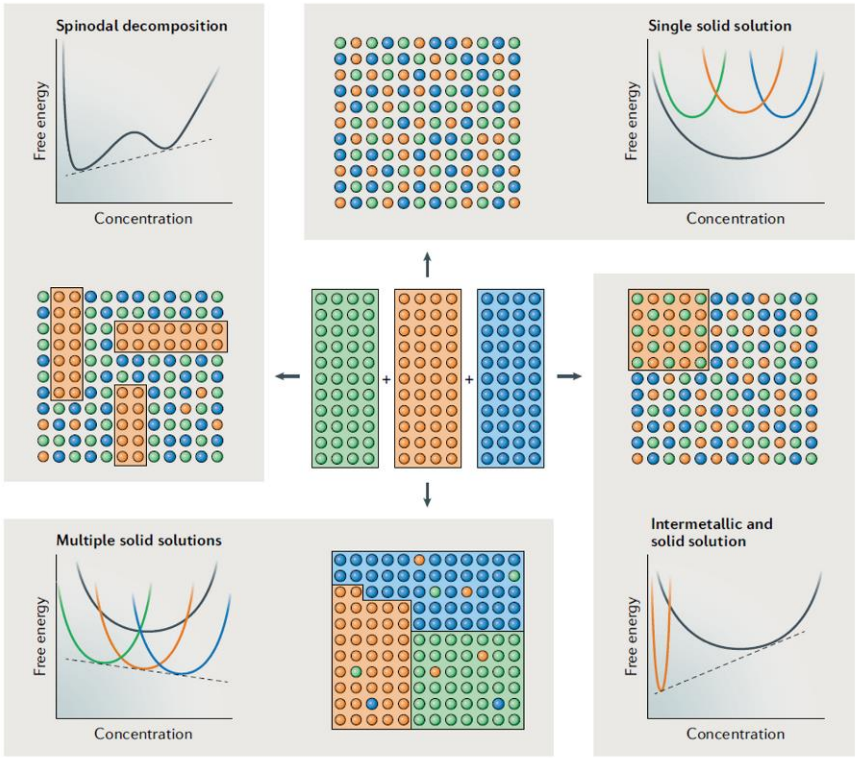

Fig. 2. Possible mixing reactions for three alloying elements mixed in equiatomic ratio [29].

The possibilities are a single solid solution, as initially expected; spinodal decomposition; intermetallic and solid solution; multiple solid solutions. Consequently, the result could be much more complex than simply predicting it according to the configurational mixing entropy. On this light, Wang et al. [52] calculated the contribution of the excess entropy calculated from the excess heat capacity and reasoned that the vibrational entropy, which is dependent on the atomic configuration and possesses a temperature dependent behaviour, is such that can greatly influence the phase stability of HEAs, proving that the configurational entropy contribution is not enough to predict phase formation.

Additionally, Miracle and Senkov [36] contradicted the mentioned initial hypothesis with coherent reasoning. First of all, they pointed out that an alloy has not only a single value of configurational entropy, as it is temperature dependent – which reinforces the results of Wang et al. The temperature effect can be minimum (minor variations in short-range atomic ordering) but it also can be great, i.e. chemical partitioning between parent and product phases at a first-order phase transformation. Therefore, the excess entropy can be a major contributor to the total entropy in HEAs, especially considering the atomic size differences and random atom positions (Fig. 3).

They evidenced also that simple ordered phases, such as L_{12} or B2 phases, possess a similar configurational entropy term once existent in HEAs for disordered solid solutions. As the ordered phases contain two sublattices, both the configurational entropy and the enthalpy terms of one of these ordered phases would raise together with that of the disordered parent phase, for instance simple FCC for L_{12}; BCC for B2 structures.

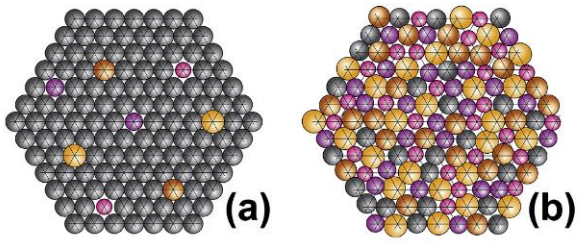

Fig. 3. The effect of atom size variations on their sites in (a) a dilute solution, where solute atoms are constrained to lattice positions by surrounding solvent atoms and (b) HEAs, where there is no principal element and their positions diverge from mean lattice sites. The changeability in atom sites in (b) leads to an excess configurational entropy [36].

Therefore, the phase selection will depend on the small differences between enthalpy and entropy, as in conventional alloys.

The catchy “high-entropy alloy” name remained due to the efforts of Yeh and colleagues [6], despite entropy not being the cause for the structures and properties of these alloys.

The conception that a single solid-solution phase would have better properties than a multi-phase structure is rather premature. Intermetallic compounds could confer an incredible set of properties to the material and these properties can be tailored according to the final purpose. For example, for high-temperature purposes, it has been exhaustively shown that intermetallics are the reason for great and unique properties of superalloys [1].

The HEAs concept may open room for a vast number of possibilities and different range of properties, therefore one should not limit them to applications where single-phase alloys would be better suited, just for the sake of its own initial misguided definition.

2.2.1.1.2 Lattice distortion effect – solid-solution strengthening

The lattice distortion effect was initially based on the hypothesis that unique properties are a consequence of the local atomic structure of HEAs. The mixing of atoms with dissimilar atomic radii in near-equiatomic ratio may increase lattice distortion by deviating the atoms from the ideal lattice sites, resulting in an intrinsic elastic residual stress field which fluctuates from one atom to another [33,43].

Consequently, an energy barrier against dislocation movement will be locally generated, providing solid solution strengthening and sluggish diffusion of atoms. Therefore, the mechanical properties of HEAs could be tailored by this effect. On the other hand, for diluted solid-solutions, the difference in lattice distortion may be minimum, so the periodic Peierls-Nabarro energy barriers for dislocation motion are not much influenced [54]. One could see this effect in the schematics of Fig. 4. It is clear that HEAs exhibit distortions in lattice and more expressive fluctuations in Peierls-Nabarro energy.

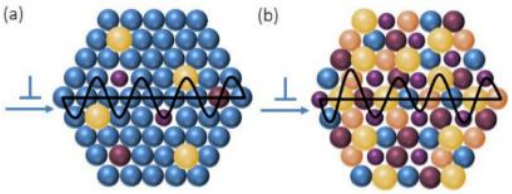

Fig. 4. Scheme of dislocation motion overcoming periodic Peierls-Nabarro energy barrier field in (a) a dilute solid-solution; (b) HEAs [54].

Yeh et al. [55] examined a set of AlCoCrCuFeNiSi HEA alloys by x-ray diffraction (XRD) by adding different elements to Cu (Fig. 5).

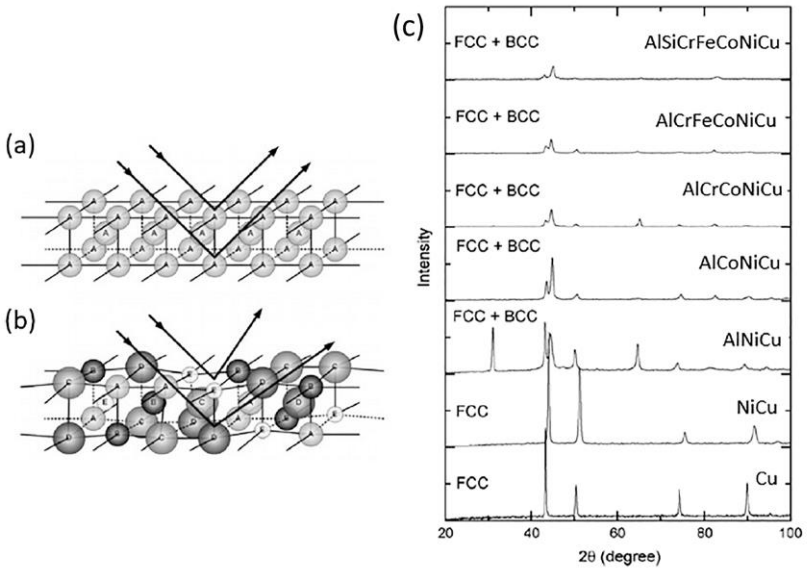

Fig. 5. Effect of lattice-distortion on XRD intensities of AlCoCrCuFeNiSi alloys: a) ideal crystal structure of pure metals – typical beam incidence and no scattering. b) HEAs with dissimilar atomic radii – a severe scattering is observed. c) Peak intensities are reduced with addition of other elements [55].

The results show that there is a significant suppression in the XRD intensities with the addition of more elements in equiatomic ratio to Cu, meaning that more severe x-ray scattering stems from more severe lattice distortions.

The lattice distortion effect was never fully understood and may be true for many cases, where HEAs exhibited improved strengths over traditional alloys. However, one could easily find controversial examples in literature as well. Lattice strain measurements performed by high energy neutron diffraction indicated that, for CrMnFeCoNi HEA, the lattice distortion was only slightly larger than of conventional Ni-base alloys [56]. Not limited to this, one can see that the ternary equiatomic CoCrNi [57,58] is stronger than the quinary equiatomic CoCrNiMnFe (or its variants) [59], even though both exhibit a single phase FCC microstructure at room temperature. These facts [60] show that the veracity of the lattice distortion effect may be questionable for all HEAs.

2.2.1.1.3 Phase prediction

The phase prediction of HEAs was initially believed to be closely related to the lattice distortion effect. To describe such atomic size differences in HEAs, Zhang et al. [46] suggested a model, the δ parameter:

$$\delta = \sqrt{\sum_{i=1}^{n} c_i (1 - r_i / \sum_{j=1}^{n} c_j r_j)^2}\ , \tag{7}$$

in which c_i is the atomic fraction of element *i*, r_i stands for the atomic radius of element *i* and *n* is the total number of constituent elements. Initially, the δ parameter was generally accepted as one of the empirical parameters to predict HEAs phase formation, due to the initially satisfactory correlation between these two [46,61].

However, as the high-entropy alloys were gaining popularity, later some scientific studies contradicted this generally accepted δ parameter, as it has been proved to fail for a precise assessment of local lattice distortions [53,62]. According to these published papers, the δ parameter leads to an overestimation of the real lattice distortion of refractory HEAs, whereas underestimate those in HEAs comprising 3d valence electrons. Nonetheless, according to He and Yang [53], as for ranking different HEAs, the parameter represents a well-fit to the expected phase formation (Fig. 6).

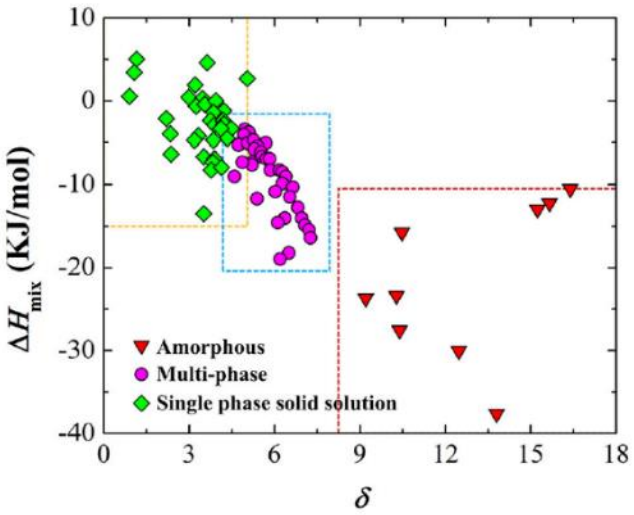

Fig. 6. The atomic size difference parameter (δ) vs. the mixing enthalpy for a set of HEAs [53].

Other criteria such as electronegativities, valence electron concentration (VEC) and mixing enthalpies have been considered by the scientific community as an attempt to describe the phase stability of HEAs [61,63,64]. However, many of these ignore the competing compounds formation enthalpies, limiting their real application in predicting the phase formation [29,36,60]. As an example, it was proposed by Guo et al. [65] that one can distinguish BCC and FCC phases in HEAs depending on an empiric VEC value within a range of alloys of a specific group, utilizing the average VEC as such:

$$VEC = \sum c_i VEC \tag{8}$$

When VEC ≥ 8.0, one could assume the formation of solely FCC phase; otherwise, when 6.87 ≤ VEC < 8.0, a combination of BCC and FCC phase should form; once VEC < 6.87, only BCC would form. As Miracle and Senkov [36] properly pointed out, the phase prediction is very general and works for families of alloys such as $Al_xCoCrCuFeNi$ and $Al_xCoCrFeNi_2$. However, when one adds more elements to them, specially Mn, the empirical VEC prediction of phase formation may no longer be precise for HEAs [65].

Despite the phase prediction of BCC and FCC in HEAs through an empirical VEC value being uncertain, the values of VEC are importantly explored in similar matters. For example, according to ab-initio calculations, bearing in mind VEC values may be a way of ductilizing BCC refractory alloys [9,66], which will be explained further in the “Toughening Mechanisms” section of this thesis.

The parameter δ is indeed possibly the only one that could be considered useful for a series of HEAs, with some exceptions already mentioned above. This parameter may permit the identification of suitable compositional subspaces where single-phase HEAs might exist by also considering the enthalpies of competing intermetallic compounds.

2.2.1.1.4 Sluggish diffusion effect

It was generally believed that, along with the other effects, the dissimilar atomic sizes in the same alloy would cause a slower diffusion as compared to conventional alloys, hindering many solid-state phase transformations. There is evidence that this hypothesis could be true [64], as Tsai et al. proposed on their paper that CoCrNiFeMn possesses a higher diffusion coefficient than conventional austenitic steels and pure metals. However, Miracle and Senkov [36] counteracted this fact by saying that after normalizing the activation energies by the melting temperature, the diffusion coefficients appear to be lower. Thus, they proposed that the sluggish diffusion would be explained by the variability of diffusion data present in literature.

With that said, this hypothesis is still up to debate as an accurate measurement of diffusion coefficients is challenging and there is not enough data available up to date to confirm this theory.

2.2.1.1.5 Cocktail effect

This effect was first proposed by S. Ranganathan [67], where he suggested that HEA mixtures may generate a result greater than the sum of the individual parts, leading to unexpected and synergistic properties. No rigorous scientific bases were given to confirm the claim. Paraphrasing Miracle and Senkov [36]: "(…) it is not an hypothesis and requires no proof. It is a colorful and evocative statement of the often surprising and unpredictable nature of unknown materials."

2.2.2 Relevance of the HEAs in the scientific community

Even though the so-called "four core effects" may not be completely relevant on a broader spectrum, HEAs indeed have very interesting combination of properties that drives the research into the stimulation of new alloys design concept and creation of novel property-driven strategies.

These phase/property strategies may be useful for a series of given applications where there is a lack of development of new materials. For instance, the exploration of new refractory alloys would be of a great significance, as most of the research regarding them took place at latest on 1980's. The reasoning for this is that there is a great challenge on dealing with these kinds of materials, as most of them have no room-temperature ductility and exhibit poor corrosion resistance. Alternatively, Ni-base superalloys serve as a good substitute for many applications where exceptionally high temperatures are not needed. However, for extreme environments, the development of new alloys is required and necessary, such as in aerospace applications.

2.3 Microstructures and properties

Up to date, the most studied HEAs are divided in two groups: HEAs with face-centered cubic (FCC) microstructures and HEAs with body-centered cubic (BCC) ones. Among HEAs, there are successful cases of significantly superior properties when compared to conventional alloys. Some of these will be described herein, with emphasis in these two different groups.

2.3.1 HEAs with face-centered cubic microstructures

One of the most popular HEAs is CrMnFeCoNi in its single-phase FCC solid-solution published by B. Gludovatz et al [13] in *Science*. The alloy was first discovered by Cantor et al. [28] and it became so popular that now this alloy and its variants are named as the author, i.e. Cantor alloys. The alloy exhibited exceptional damage tolerance with tensile strengths above 1 GPa and fracture toughness values exceeding 200 MPa·$m^{1/2}$, even under cryogenic conditions. This HEA was produced by casting (arc-melting technique) followed by cold forging and cross rolling at room temperature.

In the same fashion, the medium entropy CoCrNi alloy was eventually found to have excellent damage tolerance under cryogenic temperatures as well [12], even superior to the CrMnFeCoNi, with strength above 1.3 GPa, failure strains up to 90 % and K_{JC} values of 275 MPa·$m^{1/2}$. The results are exhibited in Fig. 7.

CoCrFeMnNi and CrFeCoNi [11,59,68], CoCrNi [12,69], VCoNi [70] and other alloys have shown to possess an excellent combination of strength and ductility.

In the case of CoCrNi [71], for instance, this combination of unique properties is attributed to the lower stacking- fault energy compared with the CoCrFeMnNi. Additionally, it exhibits a higher yield strength in comparison to the latter. These both effects enable the alloy to reach the twinning stress more easily, resulting in severe nano-twinning, even at room temperature, thus improving both strength and ductility of the material.

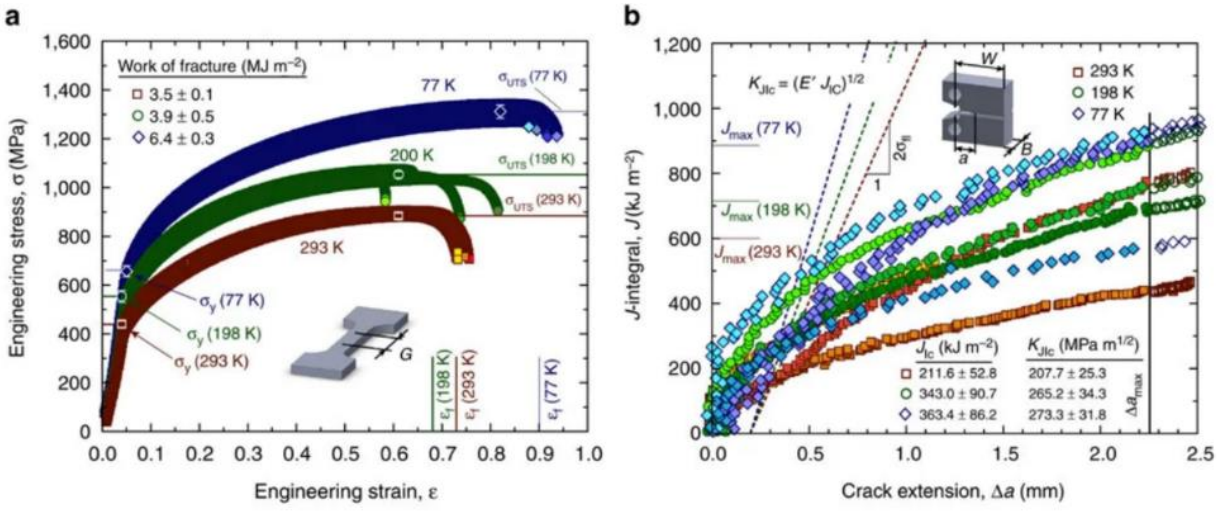

Fig. 7. Mechanical properties of the CoCrNi MEA. a) Yield strength σy, ultimate tensile strength σuts and ductility (strain to failure, εf) all increase with decreasing temperature. b) Fracture toughness measurements show increasing results for 77 K, 200 K and 293 K. An increasing fracture resistance is shown in terms of the J integral as a function of crack extension Δ_a (R curve behavior). Adapted from [12].

The stacking fault energy (SFE) of FCC alloys initiates several plastic deformation modes, such as dislocation slip, mechanical twinning and phase transformations (e.g. phase-transformation-induced plasticity (TRIP)). As a result, work hardening ability is greatly influenced by these effects. With that said, one could easily tune the mechanical properties of these alloys [34,72,73]

Normally, for FCC alloys, the governing deformation mechanism can be associated SFE values: ~15 mJ/m^2 < SFE < 50 mJ/m^2 for twinning, SFE < 15-18 mJ/m^2 for phase transformation, and 50 mJ/m^2 < SFE for dislocation slip-based plasticity [74].

The presence of nano-twinning has been shown to improve the mechanical properties of HEAs significantly. As an example, for $Cr_{10}Mn_{10}Fe_{60}Co_{10}Ni_1$, named as NT-HEA (nano-twinning dominated HEA; FG and CG stands for fine and coarse grains) shows enhanced properties [75] when compared to traditional steels as shown in Fig. 8.

Additionally, phase-transformation-induced plasticity (TRIP) dual-phase HEAs with low SFE can also show improved properties which are attributed to the bidirectional transformation of FCC and HCP, providing work hardening capacity while keeping the ductility levels.

As a successful example, a dual-phase TRIP HEA $Fe_{50}Mn_{30}Co_{10}Cr_{10}$ is exhibited in Fig. 9 (red engineering stress-strain curves) and shows improved strength and ductility when compared to pure FCC HEAs (black curves) at a comparable grain size. The TRIP is evident during tensile deformation, as martensitic transition from FCC to HCP at room temperature is shown once deformation is increased gradually.

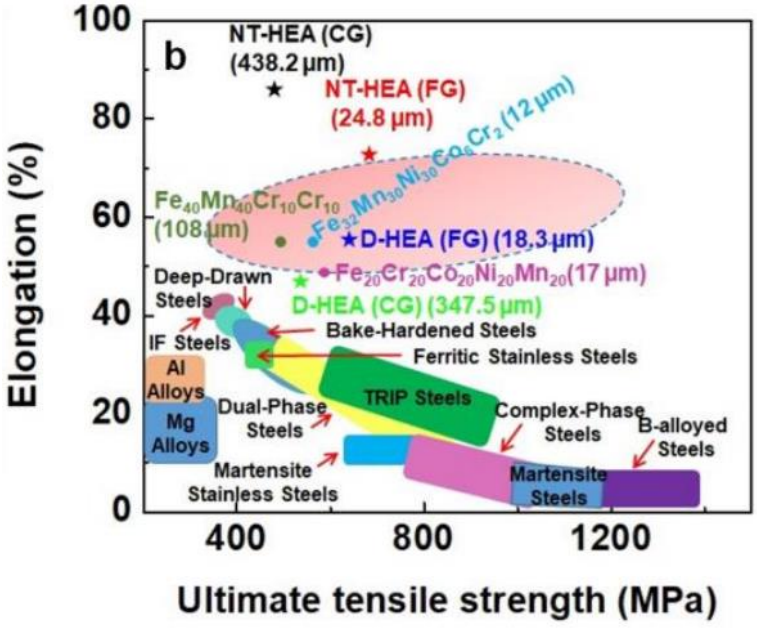

Fig. 8. Mechanical behaviour of HEAs compared to conventional alloys. NT stands for nano-twinning dominated HEA. Adapted from [75].

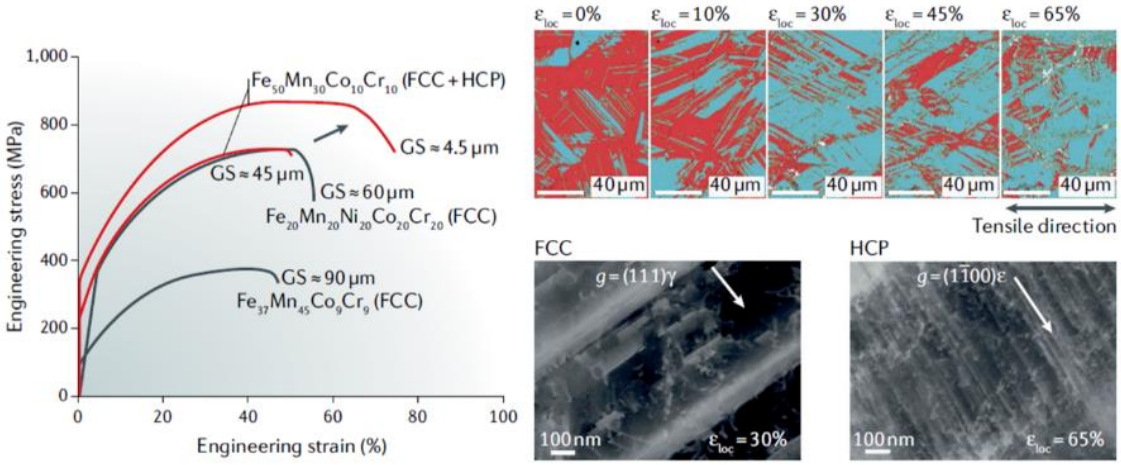

Fig. 9. Mechanical properties and microstructures of TRIP dual-phase $Fe_{50}Mn_{30}Co_{10}Cr_{10}$ HEA. Engineering stress-strain curves for TRIP HEA with different grain sizes (GS) are marked in red; for comparison, the black curves are related to FCC HEAs with no TRIP effect. The phase maps are shown according to the local strain levels (red is the FCC and blue is HCP). Martensitic transition from FCC to HCP at RT during tensile deformation is shown. Electron Channeling Contrast images exhibits the diffraction vector g. Adapted from [29,76].

Fig. 10 shows mechanical properties from room to high temperatures for a series of 3d transition metal HEAs in comparison to commercially available engineering alloys, such as INCONEL 600, INCOLOR 800, Stainless Steel 316.

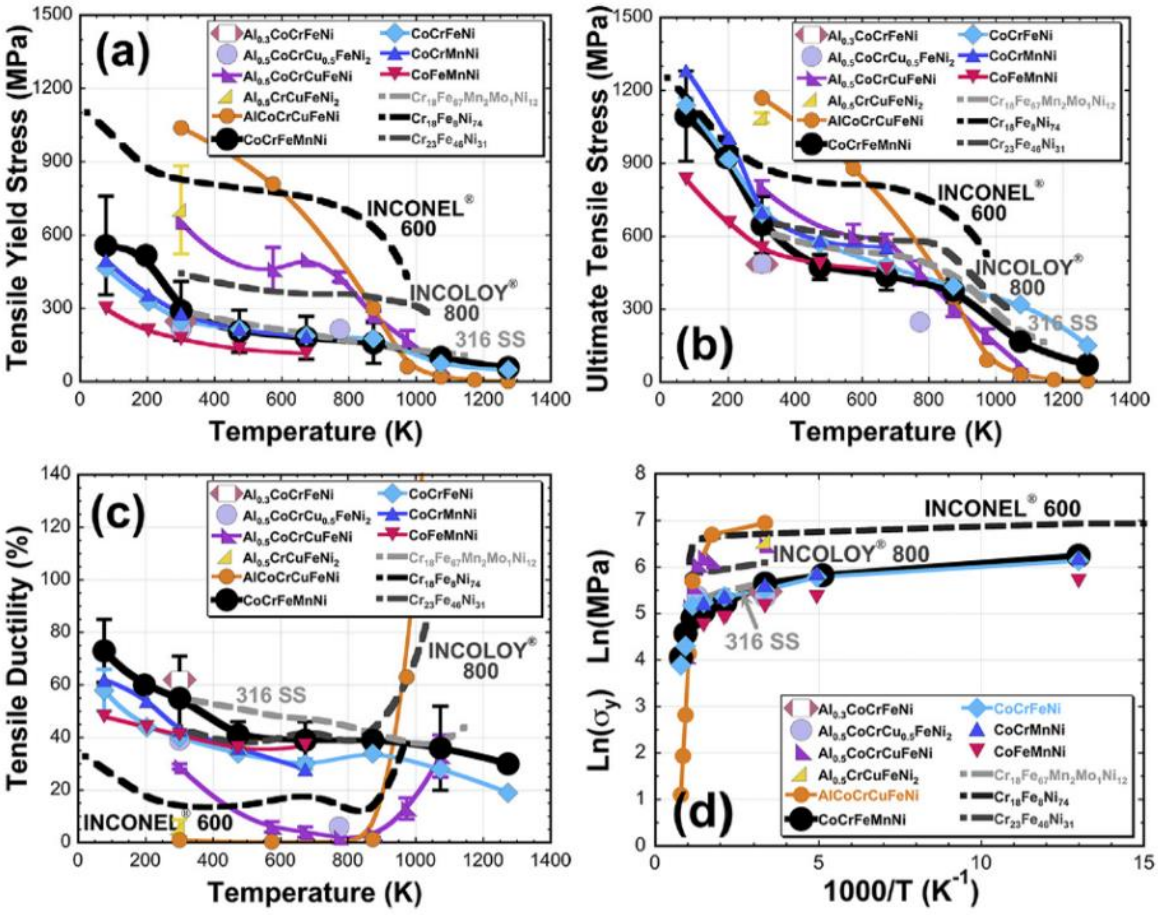

Fig. 10. Tensile data of 3d transition metal HEAs: (a) yield strength, σ_y. (b) Ultimate strength, σ_{uts}. (c) Tensile ductility, ε vs. temperature. (d) Plot of $ln(\sigma_y)$ vs. 1000/T to show the thermally activated nature of yield [36].

These HEAs exhibit mostly FCC microstructures with addition of secondary phases, such L_{12} and B_2. After annealing, BCC phase might form in certain alloys, such as in AlCoCuCrFeNi. As one can perceive, the mechanical performance of this series of HEAs, at times, have similar response as the conventional alloys even at high temperatures of exposure.

It is worth noticing that Al addition importantly affects the mechanical properties of the alloys, as it is believed to be a strong BCC [77] and intermetallic former, specially of L_{12} and B2 [54,78]. At low levels of Al content, such as in $Al_{0.3}$CoCrFeNi, the yield strength and room temperature ductility are similar to those of Cantor alloy, however presenting lower ultimate strength values and ductility at higher temperatures. At higher Al contents, such as in AlCoCrCuFeNi [79], the alloy presents a brittle-to-ductile transition and becomes superplastic [80,81] in higher temperatures of exposure.

2.3.2 HEAs with body-centered cubic microstructures

In the range of BCC HEAs, there are several compositions owing interesting mechanical properties. As this study is focused on refractory high-entropy alloys (RHEAs), promising compositions within this group will be shown herein.

Several RHEA systems were developed up to date, and they have typically shown dominance of BCC phase - as these alloys are based on refractory metals of subgroups V and VI, which have BCC crystal lattices and high mutual solubility, and metals of subgroup IV (Ti, Zr, and Hf), which are also BCC at high temperatures (at room temperature, they go through HCP transformation). Some of the develop RHEAs also contain Al (FCC crystal structure), but they usually possess a BCC structure as well, as Al is a BCC stabilizing element for Ti, Zr and Hf and it also has high solubility in refractory metals [82]. Besides the dominance of BCC, they could contain other phases, such as B2, Laves (usually associated with the presence of Cr due to its smaller atomic radius compared to other refractory elements [83]), and others.

Some of them possess better specific strengths from room temperature up to their melting points than conventional superalloys, as shown in Fig. 11.

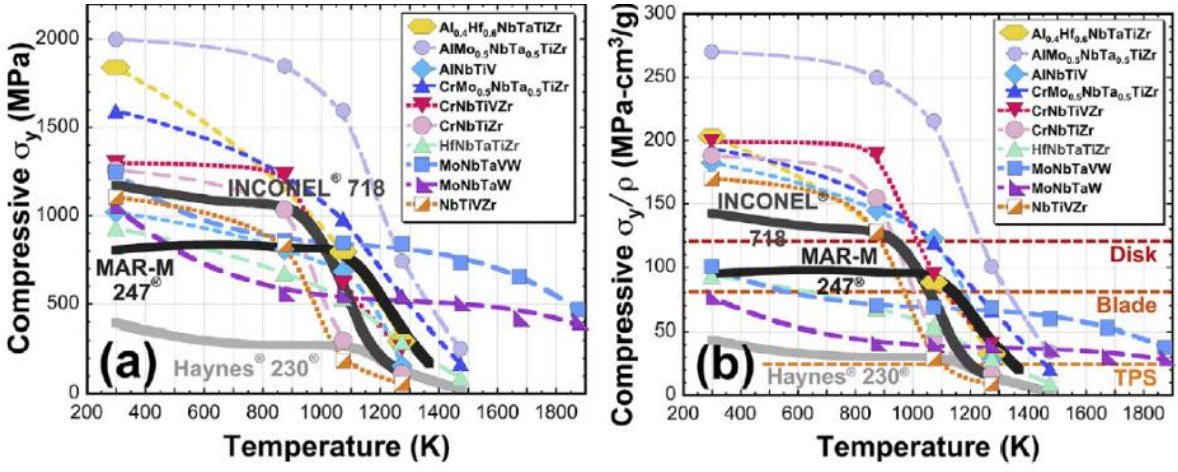

Fig. 11. Compressive strength in terms of temperature of some refractory HEAs compared to commercially available superalloys. a) Compressive strength vs T. b) Specific strength vs T. The horizontal lines denote the minimum requirements for aerospace applications. Adapted from [36].

As currently there is a strong need for materials that withstand higher temperatures than conventional superalloys, the RHEAs approach appears to be a potential alternative for high-temperature applications. Since they possess higher melting temperatures, the maximum operating temperatures may be increased. Additionally, they own a remarkably high strength at room and high temperatures [17,20,84].

However, investigation and further research on the improvement of this HEAs group are necessary, since up to date, superalloys are the best option for these specific applications as they fulfill requirements such as ductility, fracture toughness, creep and fatigue strength and oxidation resistance; but limited by their relatively low melting temperatures when compared to refractory alloys.

The first RHEAs were reported quite recently in 2010 [20]. The first two RHEAs, NbMoTaW and NbMoTaVW, showed weak temperature dependence of yield strength in the temperature range from 600 °C to 1600 °C, with yield strength above 400 MPa at 1600 °C [84,85]. Unfortunately, these two alloys exhibited high-density (>12 g/cm^3) and further developments aimed at reducing it while keeping superior high-temperature properties. 3d transition HEAs have shown incredible properties as well, some of them ressembling superalloys, however they are also limited by their lower melting temperatures when compared to refractories. Since then, they are being subject of intense studies.

Most of the reported RHEAs lack in ductility at room temperatures, with some exceptions [9,86,87]. For instance, the $Hf_xMoNbTaTiZr$ alloys, with $x \leq 0.75$, have shown to possess exceptional room-temperature ductility and undergo a compression strain of 50 % without fracturing. However, when x = 1, the compressive strain decreases to only 12 % [9]. Other outstanding ductile alloys at room temperature are $Hf_{0.5}Nb_{0.5}Ta_{0.5}Ti_{1.5}Zr$ [9] and HfNbTiZr [88], possessing tensile elongations of 18.8 % and 14.9 %, respectively. When Ta is added to the latter, the tensile elongation decreases to 6-9 % [87].

Sheikh et al. [9], in 2016, proposed that the ductility of RHEAs comprising elements from groups IV, V and VI of the periodic table can be predicted following the electron theory. They claimed that for VEC ≤ 4.4, RHEAs should be ductile. As for VEC ≥ 4.6, RHEAs should be brittle. With a threshould VEC of below about 4.5, one could theoretically achieve intrinsic ductility, as seen in Fig. 12. However, the predictions were based only on a set of nine RHEAs and the theory is assumed to be too general to be applied to all RHEAs possibilities containing elements from the mentioned groups. It is important to note that when one adds elements outside the mentioned groups ranges (e.g. Al), this theory becomes invalid.

That said, the behavior of these ductile RHEAs at high temperatures may be problematic, as they possess large grain sizes in cast states, thus the mobility of dislocations is supposedly facilitated, consequently detrimental effects could be expected. So far, there are only a few studies available which take into account the behavior of these materials in high temperatures of exposure, therefore future research is highly required. Importantly, the oxidation behavior of RHEAs is currently being studied by a small number of specialists in HEAs community [89–91] and requires further effort on the properties improvement.

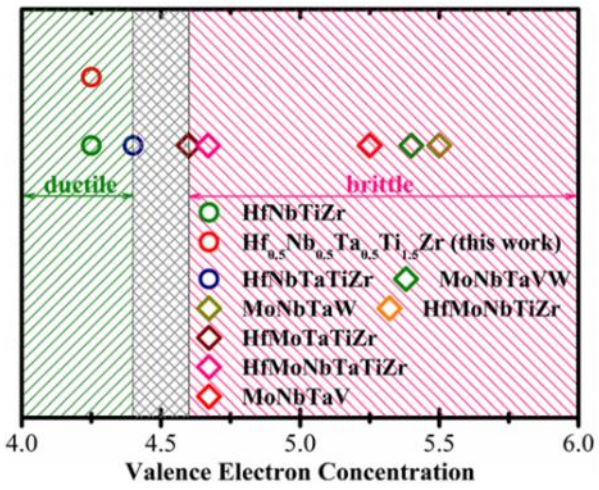

Fig. 12. Separation of ductile and brittle RHEAs by VEC [9].

Recently, several Al-containing RHEAs have been reported to achieve superalloy-like microstructures, such as in $Al_{0.3}NbTaTi_{1.4}Zr_{1.3}$ [83], $Al_{0.5}NbTa_{0.8}Ti_{1.5}V_{0.2}Zr$ [83,92,93], $Al_{0.25}NbTaTiZr$ [94], $Al_{0.5}Mo_{0.5}NbTa_{0.5}TiZr$ [94], $AlMo_{0.5}NbTa_{0.5}TiZr$ [19], with the premise of better high-temperature properties with respect to their single-phase BCC counterparts. They usually have one thing is common: their microstructures possess a BCC (B2) matrix containing coherent disordered BCC precipitates. This resembles the Ɣ (FCC) – Ɣ' (L_{12}) relationships typically encountered in superalloys. In the previously mentioned alloys microstructures, the BCC phase is depleted in Al and Zr, whereas the B2 phase is rich on them. According to Senkov et al. [82], the ordering of the B2 is possibly occurring due to strong interactions of Al and Zr atoms in the presence of other refractory elements.

Despite the very good room and high temperature strengths - exceeding those of single-phase BCC RHEAs - and thermal stability shown by these superalloy-like RHEAs [19,83,92,94], they usually possess poor low-temperature ductility mainly due to the inherent brittleness of the B2 matrix. Additionally, the presence of grain boundary intermetallic phases could also contribute towards such brittleness.

Typical microstructures of superalloy RHEAs are shown in Fig. 13. It depicts the nano-scale structures of $AlMo_{0.5}NbTa_{0.5}TiZr$ (presented in Fig. 13.a,b) and $Al_{0.25}NbTaTiZr$ (Fig. 13.c), respectively. It is evident that the disordered precipitates of the BCC phase are separated by continuous channels of ordered B2 Fig. 13.a,c). Fast Fourier transforms reveal the disordered BCC structure (Fig. 13.b) for the cuboidal precipitates in $AlMo_{0.5}NbTa_{0.5}TiZr$, while it also exposes the ordering in the Al-enriched B2 phase. The first alloy was reported to possess a compressive yield strength of ~750 MPa at 1000 °C, which surpasses the capability of any commercial superalloy.

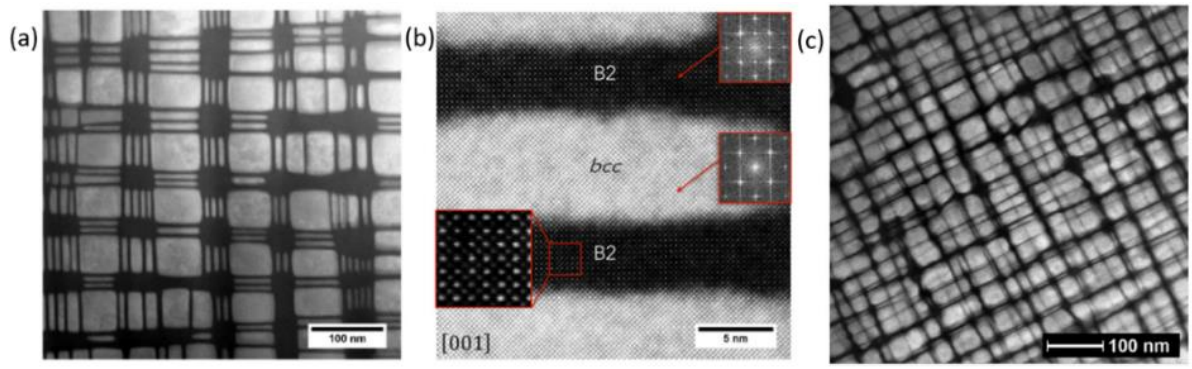

Fig. 13. Typical nano-phase B2/BCC structures: a) STEM-HAADF image of AlMo0.5NbTa0.5TiZr: Cuboidal and plate-like precipitates of a disordered BCC phase are separated by continuous channels of ordered B2. b) STEM-HAADF image of AlMo0.5NbTa0.5TiZr: Fast Fourier transforms exposing an ordered B2 structure for the dark channels and a disordered BCC structure for the cuboidal precipitates. c) STEM-HAADF image of $Al_{0.25}$NbTaTiZr showing a nanoscale two-phase microstructure [94].

The three-dimensional (3D) distribution of the B2 and BCC phases in the cast alloy $Al_{0.5}NbTa_{0.8}Ti_{1.5}V_{0.2}Zr$ alloy, and the elemental partitioning across the interface between these two phases were evaluated [92] using atom probe tomography (APT) as it can be seen in Fig. 14. APT reconstruction of Al- (red) and Ta- (blue) rich regions depicts raw ion mapping of the structure. Evidently, a strong compositional partitioning of the constituent elements is presented within the B2 and BCC phases. The composition profiles indicate that the B2 phase is rich in Al and Zr whereas the BCC phase is rich in Nb and Ta. This alloy has been reported to own a room temperature compressive strength of 2023 MPa in homogenized condition, however with poor ductility.

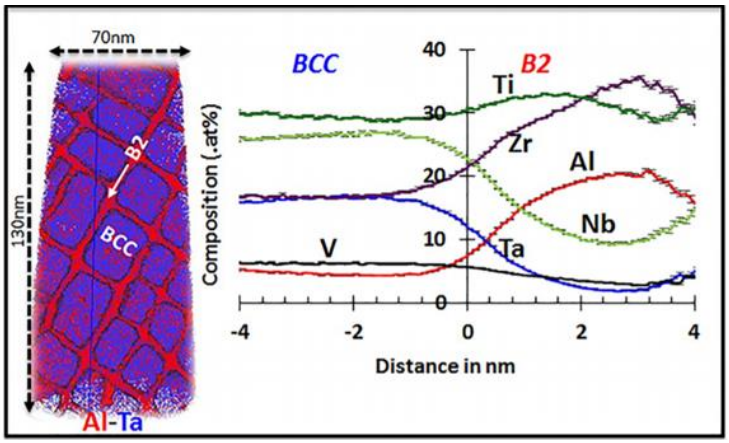

Fig. 14. APT reconstruction of Ta- and Al- rich regions in cast Al0.5NbTa0.8Ti1.5V0.2Zr RHEA (left), with compositional fluctuations across the BCC-B2 interface (right) [92].

The ductility of these RHEAs can be enhanced by microstructure inversion, i.e. a disordered BCC matrix containing ordered B2 precipitates, as shown by Soni and Senkov et al. [92,93], where the controlling of the microstructure was done by “inverting” the original B2 matrix into precipitates by simple heat treatments. The alloy suffers spinodal decomposition from high temperature single-phase field BCC/B2 to a two-phase microstructure of a continuous network of B2 channels around cuboidal BCC precipitates. Up to maximum 5 h of annealing at 600 °C, both phases suffer from compositional changes. Continuous annealing at this temperature provides an inversion in the microstructure in a way that BCC phase becomes continuous,

while B2 gets isolated. This has been shown to successfully improve the ductility, as the room temperature ductility of the alloy increased from 5 % to 55 % by solution annealing.

The origins of the improvement in ductility was suggested recently by Soni et al. [93] (2019). This is possibly caused by a combination of decrease in elastic strain energy due to differences in the modulus of B2 and FCC phases during early stages of annealing (up to 5 h). Additionally, a decrease in the interfacial energy is caused by spheroidization of both phases is the governing mechanism after 5 h.

They propose that a continuous BCC matrix with discrete stiffer B2 precipitates leads to minimization of overall elastic energy of the system, rather than B2 as a matrix. Additionally, the contribution of the minimization of interfacial area between the two phases concomitantly takes place. During annealing times between 1 h up to 5 h, a rise in lattice misfit could lead to loss of coherency between these two phases, generating geometrically necessary misfit dislocations at the interface of these two phases, causing an increase in the interfacial energy. This, in turn, causes a coarsening of the microstructure by bulging/constrictions in the interface, in order to reduce the total interfacial area.

Fig. 15 shows the microstructural evolution of the $Al_{0.5}NbTa_{0.8}Ti_{1.5}V_{0.2}Zr$ RHEA in terms of annealing times. The arrows in Fig. 15.c represent the start of spheroidization. During this phenomenon, the BCC cuboidal particles spheroidize, thus speeding up the dissolution of thinner regions and growth of thicker regions of B2, finally resulting in the microstructure obtained in Fig. 15.f.

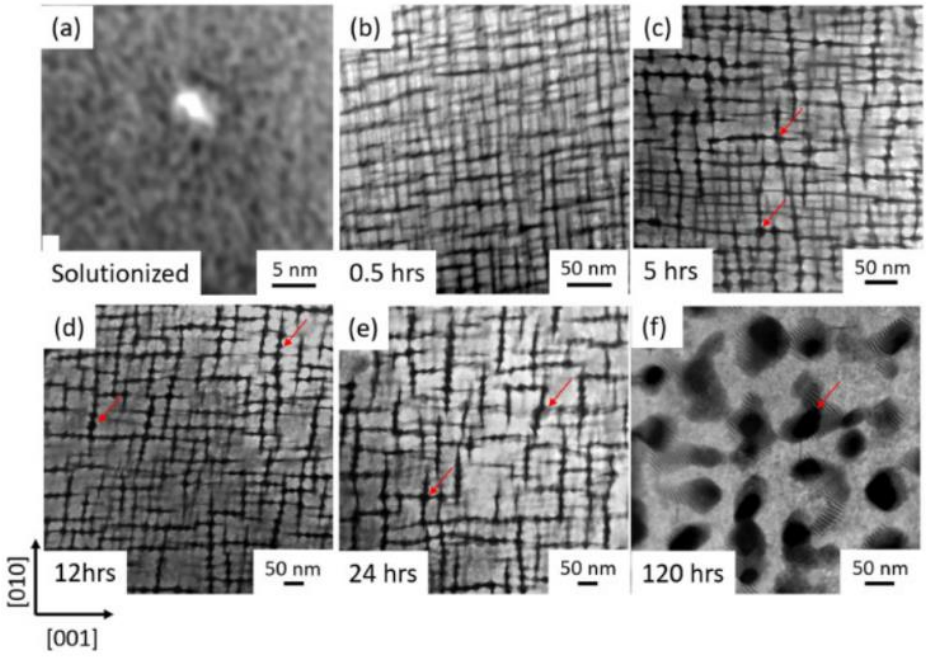

Fig. 15 STEM images show the annealed $Al_{0.5}NbTa_{0.8}Ti_{1.5}V_{0.2}Zr$ at 600°C/x h, where x = (a) 0, (b) 0.5, (c) 5, (d) 12, (e) 24, and (f) 120 [93].

Recently, Wang et al. [95] showed very interesting findings regarding the mechanistic basis for a weak temperature dependence of strength of a single bcc MoNbTi refractory MEA, concomitantly exhibiting high strength and homogeneous plasticity. They report a significant portion of non-screw segments on the gliding dislocations in this alloy at 0.12 T_m, presence of

high order slip planes and a probabilistic description of slip resistance. The dominance of non-screw dislocations and a large fraction of slip planes for dislocation glide account for the excellent mechanical properties of this alloy.

The high strength exhibited by single bcc HEAs is governed by solid solution strengthening. Additionally, chemical fluctuations caused by different atoms contribute to strength level. The authors point out that thermally activated kink nucleation is not the rate-limiting step for dislocation motion, as in usual BCC materials, thus a weak temperature dependence of strength is expected.

For comparison purposes, the authors [95] show the temperature dependence behavior of the yield stress in different refractory alloys tested in compression, as shown in Fig. 16.a. It is clear that the behavior of RHEAs is different than pure single bcc metals.

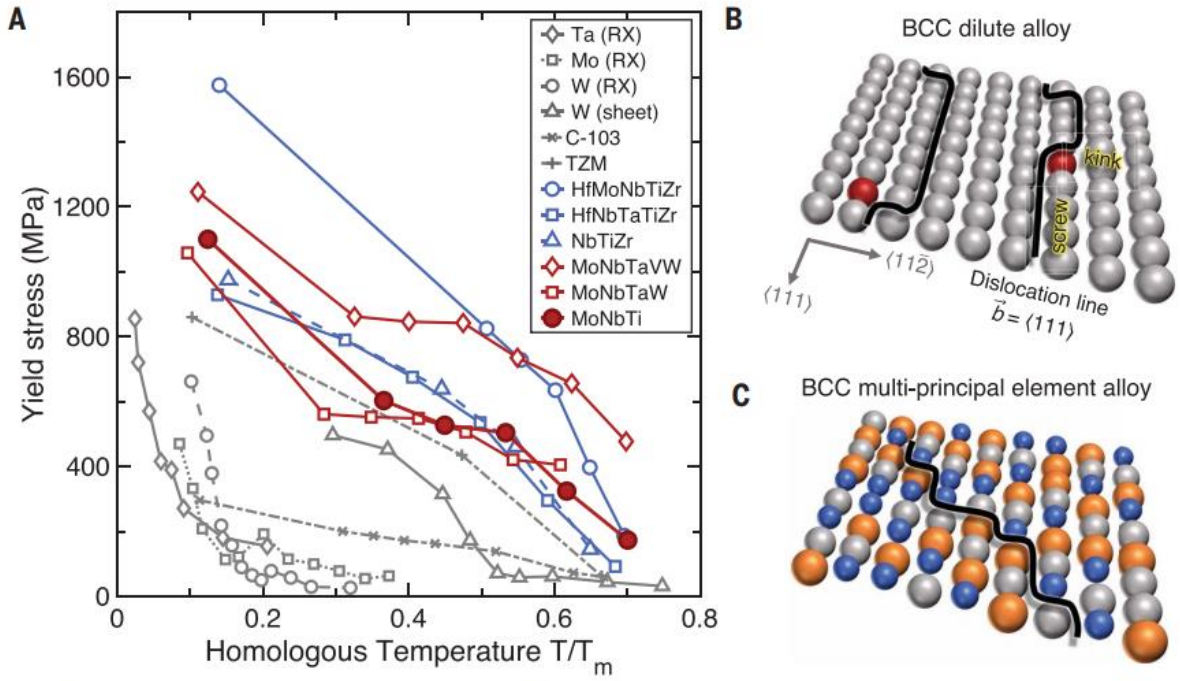

Fig. 16 (a) Diverse RHEAs and pure bcc metals tested in compression. RX and sheet stand for recrystallized and rolled, respectively. C-103 is a Nb based alloy and TZM is MoTiZr. (b) Usual dislocation pathway for bcc metals in {1-10} slip plane. (c) dislocation morphology in BCC HEAs in {1-10} slip plane. Adapted from [95].

Fig. 16.b show dislocation pathways in pure BCC metals, however, in bcc HEAs, dislocations must navigate such as depicted in Fig. 16.c. This rugged atomic arrangement is the underlying reason for simultaneous plasticity and strength, which is thorough discussed in their paper.

2.4 Composites

By definition, composites are a class of materials which combine, at least, two or more distinct materials in an unit [96], namely the matrix - which is considered to be the dominant phase, as its volume fraction is frequently higher than 50% - and the reinforcement - as the guest phase; even at nanoscale [97]. The guest phase can be used in distinct morphologies, depending on the desired application. The final properties of the composite will be significantly influenced by the selected morphology.

Composites may be classified according to the nature of their matrices, as in metal matrix composites (MMCs) – relevant for this work –, polymer matrix composites (PMC), ceramic matrix composites (CMC).
The addition of the reinforcement serves the purpose of improving the properties of the matrix in mechanical, chemical, thermal and even physical behavior [97–99] for a large number of structural and functional applications.

2.4.1 Metal matrix composites

Traditional metallic alloys, in essence, are formed by thermodynamical phase transformations and own, to some extent, chemical similarity. Metal matrix composites, contrarily, can be designed by constituents of dissimilar nature, featuring properties very different from those of the matrix.
The conventional way of introducing reinforcements in MMCs is through simple addition of the guest phase ex-situ by a given processing route to a matrix. Nowadays, it has been frequently shown that composites may be produced in-situ via supplementary routes. The latter refer to methods leading to generation of the guest phase by reactions during the processing, such as chemical vapor deposition [100,101] as gas reactions, even by mechanical alloying and sintering [102] as solid-state reactions.
The MMCs can be produced by liquid processes through melting – often associated with segregation of the reinforcement particles, thus heterogeneously distribution and agglomeration are a very significant issue. This stems from the elevated viscosity of the molten metal and from the increased surface-to-volume ratio of the particles [100]. Efforts from the scientific community have been made to counteract this issue, for example using Disintegrated Melt Deposition [101], a method that uses vibratory feeder while heating up the metal up to the melting temperature and adding ceramic particles; also high-intensity ultrasonic waves, which have been proved useful to disperse the reinforcement, though not solving the problem completely [102]. The feasibility of Selective laser melting (SLM) have been studied as a potential alternative [103]; high-pressure die casting [104]; and others. However, the agglomeration of particles still imposes a challenge.
Another alternative for efficient production of MMCs can be by semi-solid and solid-state processes. The main issue stemming from these processes lies with the fact that their production in large scale may be problematic.
Semi-solid processes are techniques that one can produce partially solid mixtures. For example, rheocasting is a process performed by partial melting of the metal, while mechanically stirring to guarantee that dendrites are fragmented and thus the formation of near-spherical phase is partially ensured [105]. While the metal is agitated, the reinforcement particles are added to the semi-solid mixture and the particles are homogeneously distributed [106].
The solid-state processes are, in general, performed by powder metallurgy routes for the preparation of MMCs [107]. These are frequently realized by mechanical alloying of feedstock

powders by high-energy ball milling and subsequent sintering [108]. An in-situ reaction takes place due to the presence of carbon, nitrogen and oxygen frequently present in the process, forming ceramic particles. Additionally, one may as well add ceramic particles previously on the feedstock powders to obtain homogeneously distributed reinforcements in a metal matrix. The dispersion of the reinforcement is nearly ideal, and it is a very successful technique for production of MMCs.

This work is aimed at metal matrix composites prepared by powder metallurgy route; thus, the details of the manufacturing technique are presented and the state of the art of the method is described in the following sections.

2.5 Production of metal matrix composites by powder metallurgy

As previously mentioned, powder metallurgy may be a very effective way of production of MMCs. This is due to the efficient manufacturing of fine-grained microstructures; homogeneously dispersed particles; its relatively easy and efficient production of a wide scope of advanced materials [107], including high entropy alloys. Refractory alloys, for instance, require very high processing temperatures for melting routes of production; however, when produced by PM, they require much lower temperatures for processing, since it can be produced through solid-state sintering [109,110].

PM materials usually possess higher strengths than their cast counterparts, stemming from extremely fine-grained microstructure, as a result of the nature of PM manufacturing process. This is especially true by mechanical alloying route, as powder particles are heavily deformed during milling. This effect has been shown for HEAs several times [21,22,24,111]. The production of MMCs possessing HEAs as matrices may be thus promising candidates for applications which high strength are required.

Powder Metallurgy comprises a very wide range of techniques and technologies related to powder manufacturing processes to produce final products with specific properties for a specific application or industry. In this work, only the relevant methods for the production of MMCs directly related to this thesis will be described in the next sections.

2.5.1 Mechanical alloying

Mechanical alloying is widely used to produce advanced materials, such as composites, nanocomposites, metal matrix composites, ceramic matrix composites, nanocrystalline materials, quasicrystals, ODS alloys, intermetallic compounds, etc.

This is a solid-state process consisting in repetitively cold welding, fracture and re-welding feedstock powders using high or low energy ball milling and/or rod milling and thus, causing severe plastic deformation to the material. This is the result of the repetitive impact among different feedstock powders, milling balls and milling jar. A substantial rise in hardness of the powders take place due to the increased dislocation density caused by the severe plastic deformation that the powders were submitted to [108]. The plasticity reaches a critical value

in which the powder particles start to fracture, creating new surfaces for cold welding [108,112].

This leads to the production of MMCs and conventional alloys that could be nearly impossible to obtain using conventional melting techniques, such as casting [113,114].

The hardness increase on the powder product can be proportional to four to five times higher than that of the traditional coarse grained counterparts [115,116]. This can be explained by the Hall-Petch relationship describing the strength increasing with hardness due to a decrease in grain size of a final alloy product.

2.5.1.1 Mechanical alloying routine

The feedstock powders are usually placed in a milling jar filled with milling media – could be steel balls (as shown in Fig. 17) or similar abrasive material, such as zirconia balls – or even milling rods. Then the jar is sealed under argon, nitrogen or similar high-purity atmosphere, and subsequently submitted to an intense mechanical alloying accompanied by severe plastic deformation by putting the jar to rotate in a planetary ball mill for a specific amount of cycles. This is usually referred as dry milling.

Fig. 17 Steel milling jar containing steel balls for mechanical alloying of powders fabricated in-house.

The determination of the time of milling, milling media, number of cycles, dwell time, rotations per minute, milling environment, impurities, milling temperature, etc. will greatly affect the final properties of the powder. Generally, though, the behavior of the powders in terms of rate refinement of its structure can be considered logarithmic with the time of milling, thus the initial particles size is not very relevant if milled for long enough, as shown in Fig. 18.

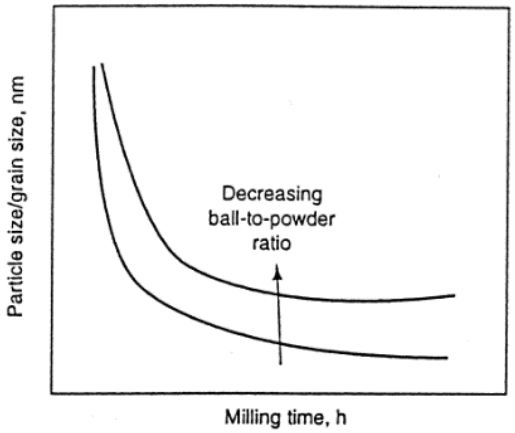

Fig. 18. Dependence of milling time and refinement of particle size/grain size during MA. Adapted from [108].

The rate of refinement is rising with higher ball to powder ratio, milling energy and lower temperatures [112]. For a perfect mechanical alloying, one can expect homogeneous chemical composition of the alloying of all elements inside the final powder particle. For very fine microstructures possibly containing dispersed oxides/carbides, one could mill metallic powders for prolonged times.

When one mills metallic powders, it is often possible to observe that these powders are stuck to the milling jar walls and balls. The use of Process control agents (PCA) helps preventing this phenomenon to happen or can aid on removing these powders from the walls by simply mechanically alloying the powders with them. These PCA could be ethanol, toluene, methanol, stearic acid, wax, etc. PCAs are frequently used during the process to avoid extreme cold welding on the particles as well. PCA agents can be used to perform wet milling.

2.5.2 Contamination due to mechanical alloying

The MA processing route requires a careful preparation to avoid contamination [117], since the feedstock powders are very prone to oxidation, as their very high surface area contributes to a higher level of oxidation as compared to feedstock chunks. The finer the powder, the larger surface area, and higher tendency to oxidation is expected. The reactivity of the powder also could increase due to grain size reduction to nanoscale [118,119]. Additionally, factors such as milling atmosphere (use of inert gases), milling environment (dry milling and wet milling), and other conditions of milling, such as time, may greatly affect the contamination level of the final powders.

The contamination of high entropy alloy equiatomic CoCrFeNi powders from commercial purity during different mechanical alloying times was recently assessed by our group [117,120], in which chemical analysis of the powders were performed in milling times varying from 5 h to 30 h, as well as nitrogen and argon atmospheres were used.

The results shown in Fig. 19 suggest that the carbon and oxygen contamination during dry milling increases with milling time, due to wear of milling jar and media from high-carbon steel. The nitrogen atmosphere is responsible for increased content of nitrogen, as opposed to argon atmosphere, which does not react with the powder and therefore does not significantly influence the contamination level.

The contamination can have a significant impact on the final properties of the material, altering the constitution and stability of the powder product [108]. Nevertheless, the oxidation can be used as an ally to produce ODS alloys and nanocomposite materials.

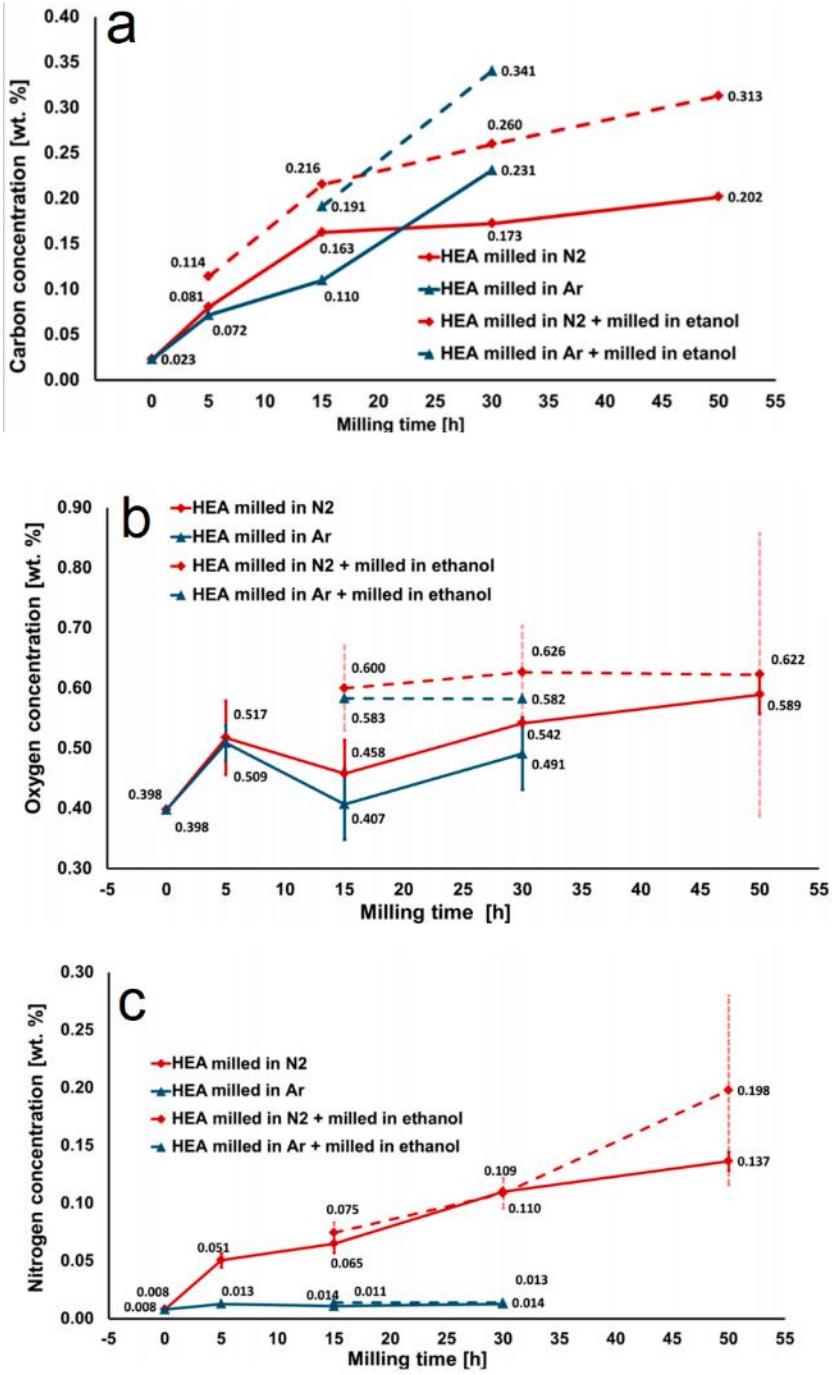

Fig. 19. Concentrations of carbon (a), oxygen (b) and nitrogen (c) in the milled HEA powders in Ar and N_2 atmospheres, respectively. The dashed lines represent powders additionally milled in PCA (ethanol). Adapted from [117,120].

2.5.3 Sintering

The sintering consists on the densification process of the milled powders, to prepare bulk parts. In this work, mainly two sintering technologies were used for densification: hot uniaxial pressing and spark plasma sintering. Therefore, they will be briefly described below.

Hot uniaxial Pressing (HP) is performed in vacuum atmosphere at a constant uniaxial pressure applied by die pistons. The sintering temperature and time are decreased by applying an additional external pressure. The technique is known to be pressure-assisted sintering [121].

For the reduction of potential surface contamination, boron nitride coating is used on a protective graphite foil, which is placed between the powders and the graphite die.
Likewise, spark plasma sintering (SPS) can be applied as well on the milled powders. An external current is utilized in combination with an applied pressure, known as field-assisted sintering technique. The main difference between SPS and HP is the manner that the heat is produced, as for HP it comes from a radiative furnace, whereas for SPS it comes from a pulsed direct current. SPS, however, has the advantage of being a faster sintering technique at lower temperatures than HP, enabling very high densification rates, avoiding unnecessary grain growth [122,123]. The same schematics of boron nitride coating on a protective graphite foil is commonly used in the SPS technique for preventing surface contamination.
By carefully adjusting the parameters, both techniques are able to provide full density and uniform samples [124].
Recently, Dong et al. [125] suggested that, by using a two-step sintering route, one can optimize the sintering to obtain highly uniform full density nanocrystalline materials for structural and functional applications. This may also be achieved for ceramics and powder metallurgy metals, even for very problematic materials for sintering, such as Al_2O_3, which they were able to achieve grain size uniformities exceeding the theoretical limit.

2.6 Strengthening mechanisms

There are several possible strengthening mechanisms in metals and metal matrix composites. For an effective tailoring of the mechanical properties of these materials, it is crucial to understand the fundamentals of the main governing mechanisms responsible for their mechanical behavior. Particularly, for HEAs, due to their compositional complexity, these mechanisms may greatly affect even further the alloys' properties and can be quite useful for designing the mechanical properties of these materials to a specific application. Up to date, the strengthening contributions for HEAs have not been studied extensively.
For metals in general, these mechanisms are a consequence of atomic interactions with different lattice defects and will be described in this section.

2.6.1 The load transfer effect

The load transfer mechanism is an important contribution to the strengthening of the metal matrix composite. Typically, the more ductile matrix transfers the load to the harder dispersed particles under an applied external load increasing the capability of the material to both absorb energy and its load bearing capacity. The predicted strengthening contribution can be calculated [126,127] by:

$$\Delta\sigma_{lt} = f\sigma_m \frac{(l+t)A}{4l} \quad (9)$$

In which f is the volume fraction of the reinforcement, σ_m is the yield strength of the matrix, l is the reinforcement size parallel to the loading axis, t is the thickness of the particles in the perpendicular direction and A is the ratio between l and t. In the case of equiaxial particles:

$$\Delta\sigma_{lt} = \frac{1}{2} f \sigma_m \quad (10)$$

2.6.2 Strengthening caused by E.M. and C.T.E. gradients

The mechanical properties of materials containing two or more very dissimilar phases vary significantly from single-phase materials. In metal matrix composites, for instance, the metal matrix frequently contains ceramic particles as effective reinforcements for improving the mechanical properties of the product, in which the amount of particles and/or secondary phases plays an important role on the materials' final properties.

That is caused by a number of factors, but mostly importantly, the elastic modulus (E.M.) and coefficient of thermal expansion (C.T.E.) of the matrix may differ greatly from the particles and secondary phases, leading to the creation of significant interfacial stresses.

Thermal gradients between a ductile matrix and reinforcement can lead to significantly enhanced dislocation density locally [128,129] on the interface with the reinforcement, thus easing the stress generated due to the mismatch. These are called thermal mismatch dislocations or geometrically necessary dislocations (GND). The stresses around the particles/secondary phases may even induce plastic deformation in the matrix in the vicinity of the interface [127].

In cases which the matrix possesses low plasticity in nature, the locally high residual stresses on the interface near the particle/secondary phase causes strengthening [130].

The increase in dislocation density is directly proportional with the reduction of the particle size of the reinforcement/second phase and increasing reinforcement volume fraction, thus enhancing expressively the strengthening contribution [131].

The increase in dislocations' density [131] locally between the interface of matrix and reinforcement, caused by thermal gradient can be described considering that the particles are cubic [132], as following:

$$\Delta\rho_{CTE} = \frac{12\Delta\alpha\Delta T f}{bd} \quad (11)$$

In which $\Delta\rho$ is the raise in dislocation density, $\Delta\alpha$ is the coefficient of thermal expansion mismatch, f is the volume fraction of the reinforcement, b is the burgers vector, d is particles' size. The variation in the matrix yield strength ($\Delta\sigma$) might be assessed from equation (9).

$$\Delta\sigma_{CTE} \sim Gb\sqrt{\Delta\rho} \quad (12)$$

Here G is the shear modulus.

The elastic modulus (EM) gradient similarly causes strengthening due to the residual interfacial stresses locally present on the vicinity of the particles in a matrix. The generated dislocation density due to this phenomenon is described by the following equation [133]:

$$\rho^{EM} = \frac{6f}{\pi d^3} \varepsilon \quad (13)$$

Please consider that ε assumes a uniform deformation around the particle. The strengthening caused by the EM gradient ($\Delta\sigma_{EM}$) can be assessed as [133]:

$$\Delta\sigma_{EM} = \sqrt{3}\alpha G b\sqrt{\rho^{EM}} \quad , \tag{14}$$

where α is the strengthening coefficient, generally taken as α = 0.5.

The total increment in yield strength due to E.M. and C.T.E. gradients is denoted as [128,133]:

$$\Delta\sigma^2 = \Delta\sigma_{EM}{}^2 + \Delta\sigma_{CTE}{}^2 \tag{15}$$

Therefore, it is possible to estimate the consequences of EM and CTE mismatches on the mechanical behavior of a material containing a matrix with reinforced particles.

2.6.3 Solid solution strengthening

In conventional metals, solid solution strengthening is the mechanism achieved through mobile dislocations that are restricted by the introduction of solute atoms in a solvent. The solvent and solute atoms may have different atomic radii, producing atomic misfit and elastic misfit interaction [134].

This mechanism can be governed by substitutional strengthening – where substitutional atoms occupy sites which are previously occupied by the solvent – or by interstitial strengthening – interstitial atoms occupy interstitial sites among solvent atoms. Usually the last happens due to a much smaller atomic size, such as in solutes of C, N and O.

Substitutional strengthening results in pure hydrostatic stresses, due to the perfectly spherical distortion in the lattice created by the addition of the substitutional element. Since the stress field of edge dislocations is solely hydrostatic, the substitutional atoms interact only with edge dislocations. On the other hand, screw dislocations have zero contribution of hydrostatic stresses, therefore they do not interact with substitutional atoms. A tensile stress field is created and attracts big substitutional atoms and, contrarily, compressive stresses attract smaller substitutional atoms on the opposite side of the dislocation core [134].

Interstitial strengthening is a consequence of impediment of dislocation motion as well, but interstitial atoms produce both hydrostatic and shear stresses due to their intrinsic tetragonal lattice distortion. Thus, interstitial atoms interact with both types of dislocation (edge and screw), providing an increased strengthening effect, caused by a superior inhibition in dislocation motion [26,134].

Different bonding energies of different atoms in a metal could cause changes in elastic properties and may block further the motion of dislocations in certain regions of the crystal, i.e. elastic misfit interaction [134].

Additionally, the contribution of the Portevin – Le Chatelier effect [135] in conventional metals can be a great influence to the final strengthening contribution, as the dislocations are pinned by additional interstitial atoms that could occupy dislocation core sites.

In conventional alloys, the solid solution strengthening is reasoned as [60]:

$$\Delta\sigma_{SSS} = MZGBx^n \tag{16}$$

Here G is the shear modulus; Z is a constant influenced by the nature of the atoms involved; B explains the solute-specific distortion that causes the strengthening by being attractive or repulsive to dislocations; x is the solute atomic concentration and n exponent represents the composition dependence of the yield stress. For dilute solutions, the value n=1/2 can be considered. In more concentrated alloys, the generally used value is n=2/3 [60,136], M is the value of Taylor's factor.

For HEAs, the solid solution strengthening prediction becomes challenging as there is no adequate model to predict it, since there is no differentiation between solute and solvent atoms. At least three contributions (lattice distortion, elastic misfit and a chemical interactions) need to be taken into consideration in a structure where no single element rules [16,36]. However, attempts have been made, good reasoning are shown and satisfactory results were obtained [22,24,60], considering the restrictions.

Additionally, interstitial strengthening on HEAs and MEAs by C or N doping have been shown to be effective and revealed to improve significantly the mechanical properties of the alloys [137,138].

2.6.4 Grain boundary strengthening

The grain boundary strengthening, also known as Hall-Petch or grain size strengthening, is a well-known mechanism for metals. The grain boundaries may act as strong obstacles for dislocation movement in low temperatures. The stress concentration near the boundaries may be caused by a pile up effect of mobile dislocations that could be relaxed by local multiple slip initiation. Accommodation of deformation is realized by multiple slip in the vicinity of the boundaries, causing a high strain-hardening rate [134]. For a given deformation, the work-hardening increases with decreasing grain size due to dislocation interaction.

The stress needed for the pile up dislocations to pass a specific low-angle boundary or to induce dislocation motion in neighboring grains is governed by the Hall-Petch equation. This contribution is expressed as [139]:

$$\sigma_{GBS} = \sigma_0 + kd^{-1/2} \quad , \tag{17}$$

where σ_0 is the lattice friction stress, k is the Hall–Petch coefficient - a constant value for a given material, d is the average grain size.

For FCC HEAs, the strengthening contributions, especially the grain-boundary strengthening have been studied by a few authors, where the Hall-Petch relationship was confirmed [22,29,54], including our group [24].

Regarding RHEAs, the evolution of grain size with annealing time and temperature was investigated for HfNbTaTiZr [140]. Considering different grain sizes, the Hall-Petch relationship was confirmed by tensile testing. It was suggested that the grain boundary strengthening may cause exceptional RT yield stress in nanocrystalline RHEAs [82,110].

One must pay close attention to the fact that, at high temperatures, grain boundary sliding may take place, causing plastic flow or opening up voids along them. Additionally, these act

as preferred locations for source and sinking of vacancy sites, caused by creep mechanisms led by diffusion currents (e.g. Nabarro-Herring creep) [134,141].

2.6.5 Precipitation strengthening

Precipitation strengthening, often called as precipitation hardening or age-hardening, is an important strengthening mechanism and extensively explored for Al alloys and Ni-base superalloys. This mechanism can take place in two different manners, depending on the response of the dislocation to the impediment in movement. In case the dislocation bows when blocked by a precipitate, we will have a classic Orowan-type strengthening; in contrast, in case the dislocation is able to shear the precipitation, a particle-shearing-type strengthening takes place.

On HEAs, this is an important strengthening mechanism, as one often can encounter the presence of intermetallics which significantly contribute to the strength of the alloy.

2.6.6 Orowan-type strengthening

When coarse and/or very hard precipitates are present in a metal matrix, the dislocation has to bow between the precipitates to be able to pass, an effect known as Orowan looping.

The Orowan strengthening contribution can be described as such:

$$\sigma_{ORS} = \frac{0.4MGb}{\pi\sqrt{1-\mu}} \frac{ln\left(2\bar{r}/b\right)}{L_p} \quad , \tag{18}$$

where G is the shear modulus; μ is the Poisson ratio; $L_p = 2\bar{r}(\sqrt{\pi/4f} - 1)$ refers to interparticle spacing obtained from average particle radius (recalculated as $\bar{r}$ on slip plane) and particle volume fraction f; b is Burger's vector. M is the value of Taylor's factor.

This equation was used previously for calculation of Orowan contribution on HEAs [22,24,142].

Please note that, often on HEAs, one could find hard carbides or oxides which act as Orowan-type strengthening and can be reasoned as composite as well. This is particularly effective for HEAs produced by powder metallurgy. An in-situ reaction occurs during mechanical alloying, forming oxides, carbides and/or nitrides compounds and provides enhanced strength to the material [21,24,143]. The inherent contamination of the process may be the driving force of such reaction, since they are present even when feedstock powders are pure elements with very high commercial purity, as shown by our group [117].

The corrosion resistance of specific HEAs, such as in ODS CoCrFeNi HEAs containing Cr_7C_3, Cr_2O_3, $Y_2Hf_2O_7$ and $MnCr_2O_4$ has been shown to improve in comparison to the pure CoCrFeNi [143] due to its passive current density is mainly reduced by the addition of Hf and Y2O3. Therefore, Orowan-type strengthening is a very useful mechanism for generally improving the properties of materials.

2.6.6.1 Particle-shearing

Particle-shearing occur when precipitates do not fully block the movement of dislocations, but dislocations have enough energy to shear them. The overall strengthening by particle shearing strengthening σ_{PSS} is described as:

$$\sigma_{PSS} = \sigma_{CS} + \sigma_{MMS} + \sigma_{OS} \quad (19)$$

These three strengthening components refer to coherency strengthening ($\boldsymbol{\sigma}_{CS}$), moduli mismatch strengthening ($\boldsymbol{\sigma}_{MMS}$) and order strengthening ($\boldsymbol{\sigma}_{OS}$), that are quantitatively described by equations:

$$\sigma_{CS} = 0.85M(G\frac{2}{3}\frac{\Delta a}{a})^{3/2}(rf/(0.5G))^{1/2} \quad (20)$$

$$\sigma_{MMS} = 0.0055M(\Delta G)^{3/2}(2f/G)^{1/2}(r/b)^{(3m/2)-1} \quad (21)$$

$$\sigma_{OS} = (0.81M\gamma_{APB}/2b)(3\pi f/8)^{1/2} \ . \quad (22)$$

Here G is the shear modulus; M is the value of Taylor's factor; $\frac{\Delta a}{a}$ is lattice misfit; r is the particle radius; f is the particle volume fraction; b is the Burger's vector; γ_{APB} is the interfacial energy created by antiphase boundaries between two coherent phases and m is a constant that depends on the crystal structures (for FCC HEAs, m = 0.85 [24]).

2.6.7 Synergetic contribution

The total shear stress necessary for dislocation motion through a material or the critical resolved shear stress (σ_{TS}) for both metals and composites can be defined as the sum of the all the strength contributions. The synergetic contribution is summarized as follows:

$$\sigma_{TS} = \sum \sigma_{GBS} + \sigma_{SSS} + \sigma_{ORS} + \sigma_{PSS} + \sigma_{CTE} + \sigma_{EM} + \sigma_{lt} \quad (23)$$

All these strengthening mechanisms are well known and generally applied in commercial alloys and composites. They have been reported in high and medium entropy alloys as well. The main difference is that contrasting with traditional alloys, in which these mechanisms are followed by a loss in toughness and ductility, in some HEAs these strengthening contributions have been reported to maintain or even concurrently increase the strength and ductility, as specific features of twin and phase boundaries are generated and make some HEAs less prone to embrittlement when their strength are improved [29].

2.7 Toughening mechanisms

Fracture toughness is a measure of the resistance of a material to crack extension under loading [144]. Measurements of the fracture toughness of HEAs have been applied with the use of the fracture toughness parameters K_{IC} (critical stress-Intensity factor $K_{IC} = \sigma_C\sqrt{\pi a}$, where σ_C is the failure stress and a is half of the crack length), J_{IC} integral (measures the critical energy associated with the initiation of the crack growth), and J-R testing (characterizes the resistance to fracture as a function of the crack growth) in a quantitative sense and Charpy-impact testing in a qualitative sense [145].

Toughening mechanisms are an important consideration to be addressed for HEAs, specially for RHEAs, where the ductility is very low at room temperatures. As there are inumerous alloying possibilities in the HEAs compositional space, some HEAs have shown to be ductile and some very brittle - with ductilities tending to zero. By carefully addressing toughness, one could predict the behavior of such brittle HEAs as close to those of ceramics; in contrast, the ductile ones should behave as conventional ductile metals.

W. Li, P.K Liaw and Y. Gao [145,146] addressed the matter dividing the toughening mechanisms of ductile and brittle HEAs in three groups: toughening by dislocation operations; by twinning and by crack bridging.

2.7.1 Toughening by dislocation operations

In metals, dislocation movement is responsible for ductility, while their interaction causes strengthening. The crack tip blunting is believed to be the one of the most important toughening mechanisms responsible for an improved ductility and toughness. The crack present in a material possess a crack tip that becomes blunt due to dislocation plasticity at the edge of the crack tip, which effectively reduces the stress concentration at this region, avoiding further crack propagation [134,144].

For HEAs, particularly for Cantor alloy (FCC CrMnFeCoNi) [13], the stages of deformation in the vicinity of the crack tip were studied and the crack blunting phenomena was observed. The edge crack tip was reported to be blunt (showed in Fig. 20) and providing a significant toughening of the material, resulting in fracture toughness (K_{Jc}) values of 221 MPa.m$^{1/2}$ and 219 MPa.m$^{1/2}$ for temperatures of 200 K and 77 K. Deformation twinning is an important mechanism responsible for the superior toughening values as well, even in cryogenic temperatures, as seen in Fig. 20.b,c. For 77 K, the formation cell structures resulting from dislocation activity is present in the wake of the propagated crack.

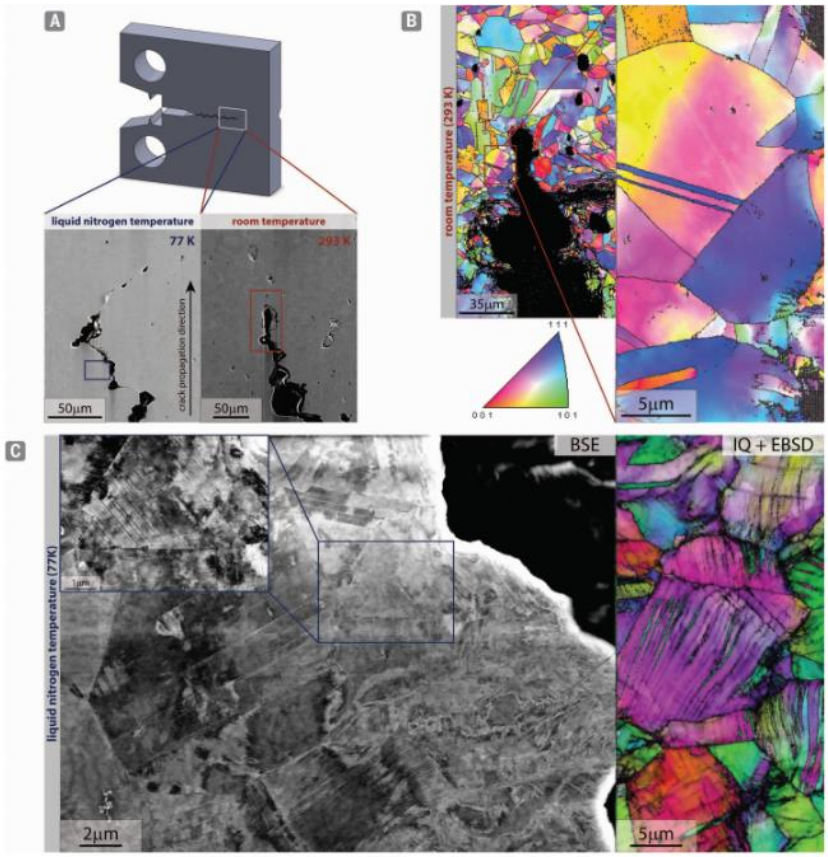

Fig. 20. Deformation mechanisms in the vicinity of the crack tip in the center (plane-strain) section Cantor alloy. a) SEM images of samples tested at 293 K and 77 K display ductile fracture by microvoid coalescence. b) EBSD maps showing twins and grain misorientations due to dislocations – the primary deformation mechanism at 293 K. c) 77 K sample, BSE images in the wake of the propagated crack showing the formation cell structures resulting from dislocation activity [13].

2.7.2 Toughening by TWIP and TRIP effects

Fracture toughness of FCC metals can be improved by deformation-induced twinning (TWIP) and transformation-induced plasticity (TRIP), as these phenomena delay the on-set of plastic instability due to increased strain hardening.

The twinning phenomenon has been extensively reported to occur in FCC HEAs (e.g. CrMnFeCoNi and CrCoNi), and the high fracture toughness exhibited by these alloys has been explicitly associated with twinning [12,13]. Their presence is evident in the cantor alloy (Fig. 20) even at cryogenic temperatures. At room temperatures, twinning is believed to be the primary deformation mechanism of these HEAs.

When occurred, the generation of nano-twinning is responsible for an increased toughness due to the relaxation of stresses in the plastic zone in front of the crack tip [144]. The deformation ability of the metal is improved as the twinning enables deformation in additional slip systems (e.g. in FCC, additional <112> directions are activated compared to normal slip in <110>). As briefly explained before, the stacking fault energy of FCC metals are closely related to the ability to undergo deformation nano-twinning. When ~15 mJ/m^2 < SFE < 50 mJ/m^2, nano-twinning deformation are activated; for SFE < 15 - 18 mJ/m^2, the governing mechanism of deformation is via phase transformation; above 50 mJ/m^2 < SFE, the dislocation

slip-based is the main deformation mechanism [74]. Finally, keeping the other parameters the same, the nano-twinning deformation can simultaneously contribute for an increase in the strength and ductility of the metal.

Twinning is a powerful method to enhance the ductility of alloys [134]. Creation of hierarchical twin architectures in HEAs by the interjunctions of different twin systems further enhances the ductility by producing three-dimensional pathways, therefore facilitating cross-slips of dislocations among twin boundaries [146]. The trade-off between strength and ductility is also overcome in HEAs, as the impediment to dislocation motion may strengthen the material and at the same time ductility is increased.

Following the same fashion, TRIP from FCC to HCP structure has been reported to produce enhanced mechanical properties to avoid the trade-off between strength and ductility (Fig. 9) [11,34,137].

2.7.3 Toughening by crack bridging

Extrinsic toughening mechanisms may be exhibited behind the crack tip while it propagates, eventually providing stabilization of the crack. Generally, crack bridging refers to fibers or lamellas that are formed behind the crack tip and are able to resist catastrophic crack propagation, while keeping fracture resistance in brittle materials. These nanoscale fibers or lamellas bridge the two open fracture surface at the wake of the crack tip and are able to efficiently resist further crack propagation [134,146,147]. This is an important mechanism for brittle FCC and BCC HEAs and, in particular, for RHEAs, as they possess very low ductility at room temperatures. In the case of CrMnFeCoNi HEA, this was observed by in-situ TEM [148] in Fig. 21. The nanofibers bridge the crack, avoiding further crack propagation. Nanotwins can be seen to form in some of the fibers, enhancing ductility of the material and resulting in significant elongation.

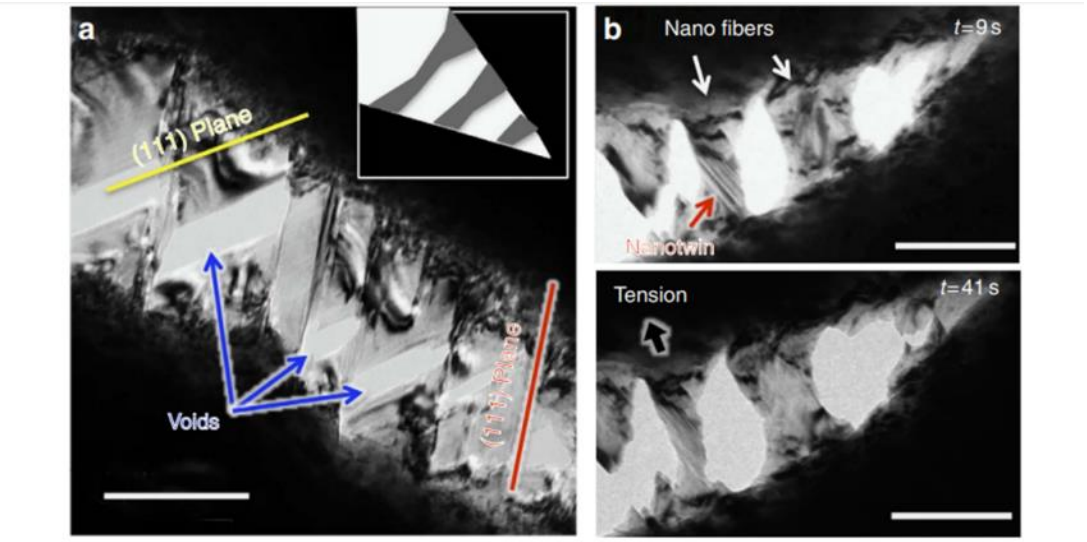

Fig. 21. Crack bridging via near-tip twinned nanobridges in CrMnFeCoNi (scale bar, 200 nm). a) TEM image of a growing crack during in situ straining, showing the formation of nano/submicron voids at the intersection of two slip systems. The crack tip is located 500 nm away from the right-lower corner of this image. (b) TEM images that show the tensile loading of nano 'fibres' that bridge the crack in the near-tip region. [148]

2.7.4 Other toughening mechanisms

There are other important toughening mechanisms that must be mentioned here, such as alloy design approaches for ductilization of HEAs as an attempt of the scientific community to improve the mechanical properties of BCC HEAs, specially RHEAs. The mechanistic approaches were proposed by experts and will be describe below:

Based on trends in compressive ductilities, it was proposed by Sheikh et al. [9] that selecting only elements from groups IV, V and VI, there is a critical VEC ≈ 4.5 which could be calculated to predict ductility of RHEAs. Therefore, this approach would provide a first insight into the ductility potential of a combination of HEAs simply by calculating the VEC values. A word of caution is used here: one cannot take into consideration any other elements out of the mentioned groups; for example, Al-, which is frequently present in RHEAs. The proposal was further explained in detail in section 2.3.2.

This theoretical ductility explored in refractory alloys with bcc lattices for elements from groups IV and V were proposed by [149] based on first-principle calculations. The authors suggested that the intrinsically ductile behavior of these elements was triggered by a shearing instability under tension occurring when the shearing strength of these elements reaches a critical value, which is higher than the tensile strength. Therefore, a preferential orthorhombic path takes place instead of tetragonal, thus leading to a fail in shear under [100] tension - a more ductile behavior, according to their first principles calculations. Normally, certain refractory alloys (such as Mo and W) with perfect bcc lattices under tension along [100] direction, change to a tetragonal symmetry and fail on the tetragonal path on the weakest direction. Above a critical value of strain, though, shear instability occurs, and the cells transform to an orthorrombic structure, leading to a higher theoretical ductility under tension [66]. This phenomenon is illustrated in the figure below.

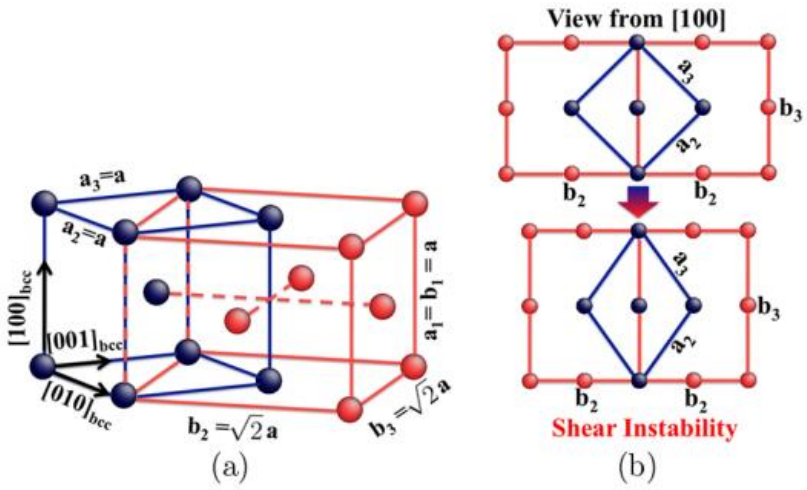

Fig. 22. (a) BCC supercell structure with two atoms represented in blue and tetragonal supercell with four atoms in red. (b) Shear instability takes place when the strain under tension along [100] is higher than a critical value. Thus, the original [001] and [010] directions in bcc become distorted. Adapted from [66].

Additionally, Soni et al. [92,93] proposed an “inverted microstructure” approach for BCC RHEAs with superalloy-like microstructures with continuous B2 matrix and dispersed BCC

precipitates by simple thermal treatments. This was comprehensively discussed in section 2.3.2 as well.

Approaches to lower the temperature of brittle-to-ductile-transition (T_{BDT}) in BCC metals and alloys have been extensively studied in conventional alloys up to date. It was suggested by Senkov et al. [82] that for RHEAs, it would be useful to develop such approach for temperatures below room temperature. However, it may be difficult as several material parameters influence this transition. Therefore, studies on dislocation structure, mobility, interactions with barriers are required for improving RT ductility. Additionally, strengthening mechanisms should be properly clarified for RHEAs.

Other ductilizing approaches such as transformation-induced plasticity in BCC HEAs [150]; tailoring VEC of precipitates by controlled elemental partitioning [151] and size-dependent plasticity of RHEAs [152] were proposed. However, comprehensive and in-depth studies addressing all the influential factors concerning toughening and strengthening are required to confirm the reliability of these methods.

3 Aims of the work

The main goal of this work is to investigate potential alloys that possess a combination of improved mechanical properties for applications where specific high strength is required, with special regard to high-temperature applications. By exploiting the high-entropy alloys approach through the production of HEAs-base metal matrix composites, different compositions are characterized in terms of its microstructures and mechanical properties.

In most of the researches, HEAs have been produced by casting, however, they can also be alternatively produced by powder metallurgy (PM), which may bring additional advantages due to a better microstructural controlling thanks to its solid-state processing [109]. Especially the combination of mechanical milling (MA) of elementary powder mixtures, followed by pressure or field assisted densification, has yielded the most promising results in the preparation of the full density materials [153]. PM has a unique advantage: the ability to effectively produce metal matrix composites with in-situ formed homogeneously dispersed oxides and/or carbide particles for enhanced mechanical properties in comparison to its cast counterpart. Using the same compositions for feedstock materials, one is able to fabricate completely different microstructures by fine-tuning of a selected production technique.

The differences in structure/composition of materials triggered by different processing routes are a topic frequently neglected. That said, the mutual comparison between routes is a useful know-how, particularly for relatively new group of materials such as HEAs. Such knowledge may benefit potential future applications as well as those researchers that are trying to understand the fundamental processes underlying the microstructural and the phase changes.

This doctoral thesis focuses on three HEA compositions: $Al_{0.2}Co_{1.5}CrFeNi_{1.5}Ti$; $Al_{0.5}NbTa_{0.8}Ti_{1.5}V_{0.2}Zr$ and $Al_{0.3}NbTa_{0.8}Ti_{1.5}V_{0.2}Zr$ in stoichiometric ratio. The aim is based on four main pillars: **prediction of present phases** according to thermodynamic calculations of

phase diagrams; **preparation** of alloys by PM and casting; microstructural and mechanical **characterization**; and **thermal treatments**. The goals were achieved by ensuring main objectives that are described as:

1. Microstructural design of the HEAs, based on prediction of phases through CALPHAD.
2. Fabrication of the selected HEAs by solid state processing using powder metallurgy route, by a combination of mechanical alloying and subsequent sintering.
3. Examination of mechanically alloyed powder characteristics by SEM, XRD and hardness tests and their optimization, by varying the milling conditions.
4. Fabrication of the selected HEAs by melting routes, i.e. vacuum induction melting followed by casting for $Al_{0.2}Co_{1.5}CrFeNi_{1.5}Ti$; vacuum arc-melting for $Al_{0.5}NbTa_{0.8}Ti_{1.5}V_{0.2}Zr$ and $Al_{0.3}NbTa_{0.8}Ti_{1.5}V_{0.2}Zr$.
5. Heat treatments for microstructural and mechanical properties optimization, according the combination of results of phase diagrams calculated by CALPHAD and experimental observations.
6. In-depth microstructural characterization of the alloys in all states, by means of SEM, XRD and TEM.
7. Verification of the mechanical properties of the obtained microstructures by means of microhardness tests, nanoindentation hardness, elastic modulus and poisson ratio measurements by ultrasound and vibrational techniques, shear modulus by ultrasonic measurements, flexural tests, density determination by Archimedes principle. Tribological properties at relevant composition, $Al_{0.2}Co_{1.5}CrFeNi_{1.5}Ti$, are assessed by wear tests.
8. A comprehensive assessment of the effect of the two manufacturing techniques regarding their microstructures; phase composition and constitution; mechanical properties and their optimization when necessary.

4 Methodologies

HEA compositions $Al_{0.2}Co_{1.5}CrFeNi_{1.5}Ti$ and $Al_{0.x}NbTa_{0.8}Ti_{1.5}V_{0.2}Zr$ (x = 3 and 5) have been studied in detail during this research. The former is an FCC HEA and the latter are a series of BCC refractory HEAs, which consist of $Al_{0.5}NbTa_{0.8}Ti_{1.5}V_{0.2}Zr$ (Group 1) and $Al_{0.3}NbTa_{0.8}Ti_{1.5}V_{0.2}Zr$ (Group 2).

The experimental methods used on this study to investigate the produced alloys are divided into four categories: thermodynamic calculations; preparation of the alloys; microstructural characterization and mechanical properties. Each one of them will be explained into separated subcategories, as follows:

4.1 Thermodynamic calculations

Calculation of phase and property diagrams were carried out using ThermoCalc software (TCHEA1, TCHEA3 and TCHEA4 databases) for prediction of equilibrium phases of each compositional system.

4.2 Materials preparation

The preparation of the materials was performed by solid state technique (powder metallurgy) and melting routes (casting by vacuum induction melting and vacuum arc melting).

4.2.1 HEAs preparation by powder metallurgy

The alloys in this work were produced by a combination of mechanical alloying and densification process (spark plasma sintering or hot uniaxial pressing). Schematics of a typical powder metallurgy (PM) routine for the prepared alloys on this study can be seen in Fig. 23.

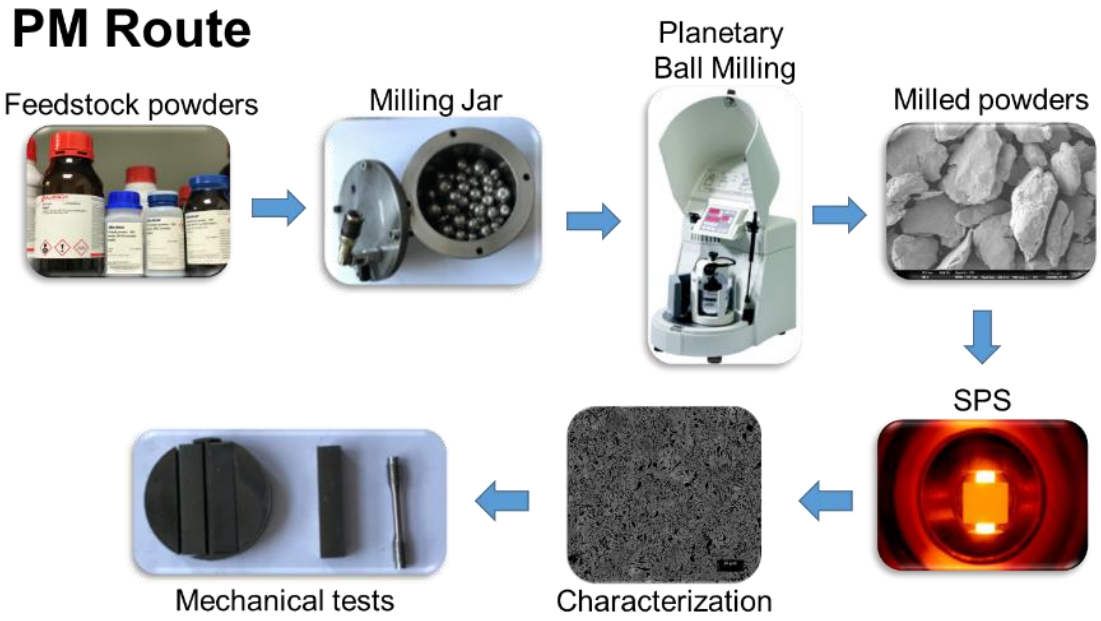

Fig. 23. Typical routine of preparation for PM alloys.

The precursor powders are selected and inserted in a milling jar filled with milling media; subsequently subjected to ball milling; the milled powders are sintered and then prepared to be microstructurally characterized and eventually mechanically tested.

4.2.1.1 $Al_{0.2}Co_{1.5}CrFeNi_{1.5}Ti$ powder metallurgy preparation

$Al_{0.2}Co_{1.5}CrFeNi_{1.5}Ti$ high entropy alloy was prepared by high-energy ball milling of feedstock powders and subsequent spark plasma sintering. Elemental powders of Al, Co, Cr, Fe, Ni and Ti (99.5 wt% purity, Sigma Aldrich) were mixed in stoichiometric ratio. Al powders possess particles sizes under 44 μm; Co with particles size under 150 μm; Cr with particles size under 44 μm; Fe under 5 μm; Ni particle size ranges from 15 to 53 μm; Ti under 44 μm.

- **Mechanical Alloying**

The precursor powders were processed by mechanical alloying in a Fritsch Pulverisette 6 planetary ball mill. The milling was carried out under high-purity nitrogen atmosphere (99.9999%) in a sealed bowl, containing hardened bearing steel balls (AISI 52100 – SUJ2) of 15 mm diameter in a 10:1 ball-to-powder weight ratio (BPR). The milling was conducted with a milling speed of 300 RPM for a total 5 h, comprising of five cycles of 60 min of milling and 30 min idle time. Wet milling in toluene for additional 30 min was necessary in order to remove the powder stuck to the milling balls surfaces.

- **Sintering**

The milled powders were then consolidated by spark plasma sintering technology (Thermal Technology LLC 10-4, USA) using a graphite die with an inner diameter of 30 mm, in vacuum atmosphere at a constant pressure of 30 MPa. The following densification scheme was used: 100 °C·min^{-1} heating rate from RT up to 1000 °C with a 15 min dwell time at 550 °C to remove any organic compounds potentially present. Subsequently, 50 °C·min^{-1} rate was used from 1000 °C up to 1100 °C with the final 10 min dwell time at 1100 °C. After densification, the electric current of the SPS machine was turned off and the sample was spontaneously cooled down to room temperature in a fast rate.
The prepared alloy will be referred in the as-sintered condition as $Al_{0.2}Co_{1.5}CrFeNi_{1.5}Ti$ as-sintered HEA, or as-sintered FCC PM-HEA.

4.2.1.2 $Al_{0.5}NbTa_{0.8}Ti_{1.5}V_{0.2}Zr$ powder metallurgy preparation

The $Al_{0.5}NbTa_{0.8}Ti_{1.5}V_{0.2}Zr$ alloy (stoichiometric ratio) was prepared by mechanical alloying and subsequent sintering by hot uniaxial pressing.
The feedstock powders (handled under argon atmosphere in glovebox) are divided in two categories: Precursors-A and Precursors-B.

- Precursors-A: are elemental powders of Al (99.9 wt.% purity, Sigma Aldrich, particle size under 44 μm); Ti, Nb, V (over 99.8 wt.% purity, Alfa Aesar, all elements with particles size under 44 μm); Ta (99.9 wt.% purity, CRM, particles size under 60 μm) were used as feedstock powders. Due to difficulties on finding pure Zr elemental powder, Zr **sponge** (≥99% trace metals basis, Sigma Aldrich) was firstly **milled to**

powder - significantly reducing the particle size - by high-energy ball milling (referred herein as milled Zr powder) and then used as one of the feedstock powders together with Al, Ti, Nb, Ta and V during mechanical alloying to produce the **alloyed** powders with desired $Al_{0.5}NbTa_{0.8}Ti_{1.5}V_{0.2}Zr$ composition. A special subsection describes the reduction of Zr sponge to powder.

- Precursors-B: elemental powders of Al (99.9 wt.% purity, Sigma Aldrich, particle size under 44 μm); Ti, Nb, V (over 99.5 wt.% purity, Alfa Aesar, all particles size under 44 μm); Ta (99.9 wt.% purity, CRM, particles size under 60 μm); **Zr elemental powder** (99.5 wt.% purity, TLS Technik, particles size from 45 to 150 μm). Compared to **Precursors-A**, purchased Zr powder was used instead of Zr sponge.

The only difference between Precursors-A and Precursors-B powders is the source of the Zr powder. The morphology of commercially available Zr powders (particles size from 45 to 150 μm) and milled Zr powders from Zr sponge (particles size under approximately 45 μm) can be seen in Fig. 24.

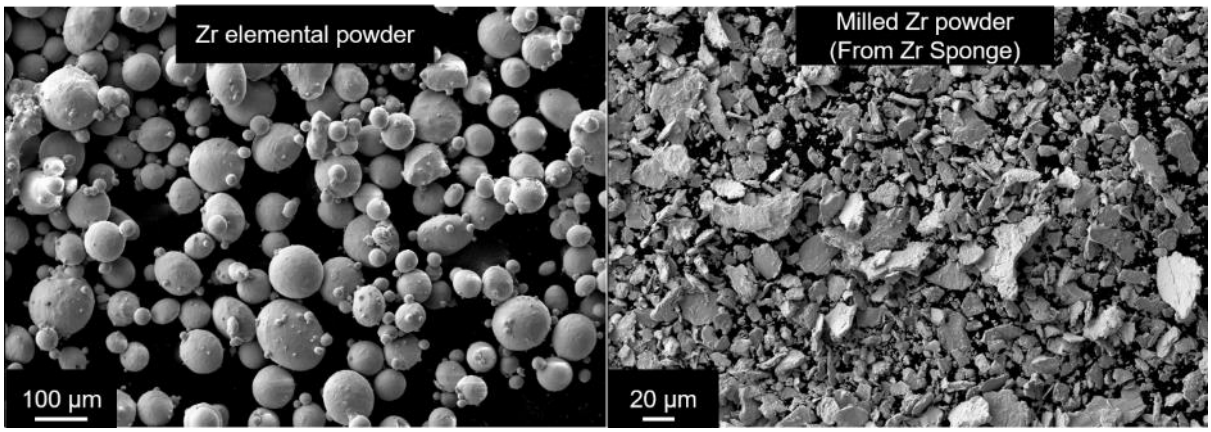

Fig. 24. Commercially available Zr powder (TLS Technik) and milled Zr powder (Sponge from Sigma Aldrich).

Both precursors were submitted to the same conditions of mechanical alloying and sintering, separately. However, since the Zr feedstock powders were different, the produced bulks were expected to be different. Therefore, they were named distinctly as PM1-mZr (Precursors-A) and PM1 (Precursors-B), respectively. The “mZr” stands for milled sponge of Zr.

- **Milling of Zr sponge into powder**

The powder preparation was done by firstly milling Zr sponge – commercial purity of 99 % into powder in a hardened steel milling bowl filled with high purity argon atmosphere together with hardened bearing steel balls (100Cr6) of 20 mm and 15 mm diameter (1:1 ratio of the diameter of the balls), in a 10:1 ball-to-powder weight ratio (BPR) for 6 h in ethanol. The milled Zr powders were dried in argon atmosphere. These milled Zr powders were, then, mixed with Al, Nb, Ta, Ti and V. This mixture of powders was named as Precursors-A.

- **Mechanical alloying**

The precursor powders Precursors-A and, separately, Precursors-B were milled by mechanical alloying in a Fritsch Pulverisette 6 planetary ball mill. Both millings were carried out under high-purity argon atmosphere (99.9999%) in a sealed bowl, containing hardened bearing steel balls (AISI 52100) of 15 mm diameter in a 10:1 ball-to-powder weight ratio (BPR). The milling was conducted with a milling speed of 250 RPM for a milling time of 10 h, comprising of 40 cycles of 15 min of milling and 1 h idle time. Wet milling in toluene for additional 25 min was necessary to remove the powder stuck to the milling balls surfaces.

- **Sintering optimization**

Milled Precursors-A were used as the feedstock milled powders. Three separate samples were prepared for optimization of the sintering conditions. These are RHEA1-1200, RHEA1-1300, RHEA1-1600, named according to the maximum sintering temperature of testing: 1200 °C, 1300 °C and 1600 °C, respectively. The sintering maximum temperatures were varied, while the other sintering conditions were kept the same.

The hot pressing (Experimental inductive hot-press IHP, AIT 2009, Austria) was carried out at a constant uniaxial pressure of 50 MPa applied by die pistons, heating rate of 100 °C.min^{-1} up to 50 °C from the maximum sintering temperatures of 1200 °C, 1300 °C and 1600 °C for each sample. On the last 50 °C, a heating rate of 25 °C.min^{-1} was used with a dwell time of 10 min. After sintering, the machine was turned off, the samples naturally cooled down in the vacuum chamber. The specimens had 3 mm thickness with 15 mm diameter in a cylindrical shape.

- **Final (optimized) sintering conditions**

The sintering was performed by Hot Pressing (HP) (Experimental inductive hot-press IHP, AIT 2009, Austria) in vacuum atmosphere. This procedure was carried out for Precursors-A and Precursors-B, named after sintering as $PM1_A$ and $PM1_B$, respectively. The sintering was carried out at a constant uniaxial pressure of 50 MPa applied by die pistons, at a maximum temperature of 1200 °C, heating rate of 100 °C.min^{-1} up to 50 °C from the maximum sintering temperatures. On the last 50 °C, a heating rate of 25 °C.min^{-1} was used with a dwell time of 10 min. After sintering, the machine was turned off, the samples naturally cooled down in the vacuum chamber. The specimens had 6 mm thickness and 50 mm diameter in a cylinder.

- **Diagram of RHEAs bulks preparation**

For better elucidation of the samples' preparation, a diagram for this group of samples and their resulting products was prepared and can be seen below.

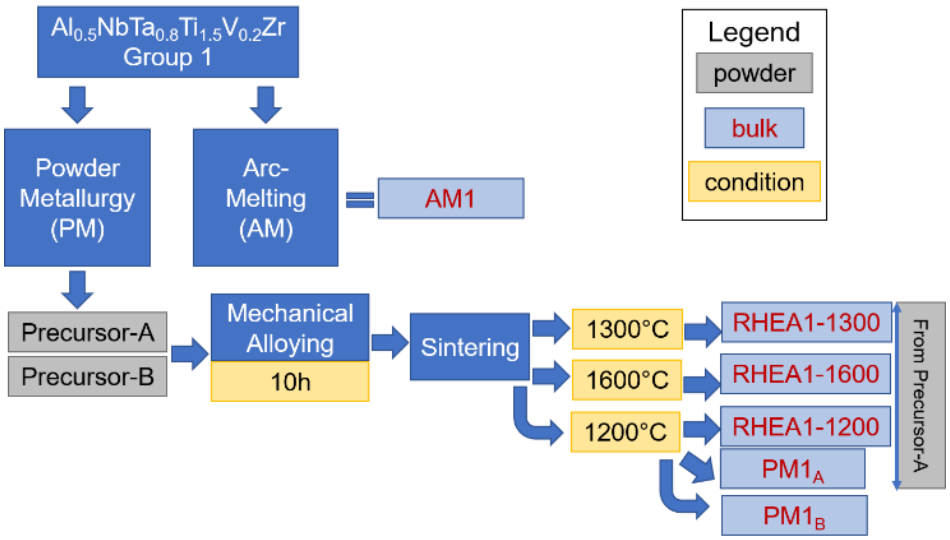

Fig. 25. Samples preparation diagram for $Al_{0.5}NbTa_{0.8}Ti_{1.5}V_{0.2}Zr$ RHEA. Precursor-A contains milled Zr powder from Sponge feedstock (sintered bulks RHEA1-1300, RHEA1-1600, RHEA1-1200, PM_A). Precursor-B consists of all elements from commercially available powders (sintered bulk $PM1_B$).

4.2.1.3 $Al_{0.3}NbTa_{0.8}Ti_{1.5}V_{0.2}Zr$ powder metallurgy preparation

The $Al_{0.3}NbTa_{0.8}Ti_{1.5}V_{0.2}Zr$ alloy (stoichiometric ratio) was prepared by a combination of mechanical alloying and hot pressing. The elemental powders with commercial purity were used as feedstock: Al (99.9 wt.% purity, Sigma Aldrich); Ti, Nb, V (over 99.5 wt.% purity, Alfa Aesar); Ta (99.9 wt.% purity, CRM) and Zr powders (99.5 wt.% purity, TLS Technik). The powders were handled before MA under argon in high-purity atmosphere in glovebox.

- **Mechanical alloying optimization**

Precursor powders were mechanically alloyed under different milling times to evaluate the evolution of the powders with the time of milling. The selected milling times were 0 hours (only mixed, not milled); 1 h; 3 h; 5 h; 10 h; 20 h; 30 h; 40 h; 50 h. These powders were named as RMA-0; RMA-1; RMA-3; RMA-5; RMA-10; RMA-20; RMA-30; RMA-40; RMA-50, respectively. RMA stands for Refractory Mechanically Alloyed powders. Other conditions of milling were kept constant, as described below.

The precursor powders were mixed by mechanical alloying in a Fritsch Pulverisette 6 planetary ball mill. The milling was carried out under high-purity argon atmosphere (99.9999%) in a sealed bowl, containing hardened bearing steel balls (AISI 52100) of 15 mm diameter in a 10:1 ball-to-powder weight ratio (BPR). The milling was conducted with a milling speed of 250 RPM, in cycles of 15 min of milling and 1 h idle time until the maximum milling time was reached. Wet milling in toluene for additional 20 min was necessary to remove the powder stuck to the milling balls surfaces.

- **Final mechanical alloying conditions**

The precursor powders were mixed by mechanical alloying in a Fritsch Pulverisette 6 planetary ball mill. The milling was carried out under high-purity argon atmosphere (99.9999%) in a

sealed bowl, containing hardened bearing steel balls (AISI 52100) of 15 mm diameter in a 10:1 ball-to-powder weight ratio (BPR). The milling was conducted with a milling speed of 250 RPM for 10 h of effective milling, in 40 cycles of 15 min of milling and 1 h idle time. Wet milling in toluene for additional 20 min was necessary to remove the powder stuck to the surfaces.

- **Sintering**

The final sintering condition was carried out by hot pressing (Experimental inductive hot-press IHP, AIT 2009, Austria) for the milled Precursor, named after sintering as PM2.

The sintering was carried out at a constant uniaxial pressure of 50 MPa applied by die pistons, at a maximum temperature of 1200°C, heating rate of 100 °C.min^{-1} up to 50 °C from the maximum sintering temperatures. On the last 50 °C, a heating rate of 25 °C.min^{-1} was used with a dwell time of 15 min. After sintering, the machine was turned off and the samples naturally cooled down in the vacuum chamber. The resulting bulk specimens had 6 mm thickness and 50 mm diameter in a cylindrical shape.

Additional sintering was performed on selected powders subject to different milling times, namely RMA-3, RMA-10, RMA-30 and RMA-50. After densification, the sintered bulks were named as SRMA-3, SRMA-10, SRMA-30 and SRMA-50. “SRMA” stands for Sintered Refractory Mechanically Alloys. This was performed to evaluate the effect of the milling time into the sintered bulks final properties. The milled powders were consolidated by spark plasma sintering technology (Sumitomo Coal Mining, Dr. Sinter SPS machine) using a graphite die with an inner diameter of 12 mm, in vacuum atmosphere. The other parameters and sintering scheme were kept the same as for the hot pressing, for comparability purposes.

- **Diagram of RHEAs bulks preparation**

For better elucidation of the samples’ preparation, a diagram for this group of samples and their resulting products was prepared and are depicted below.

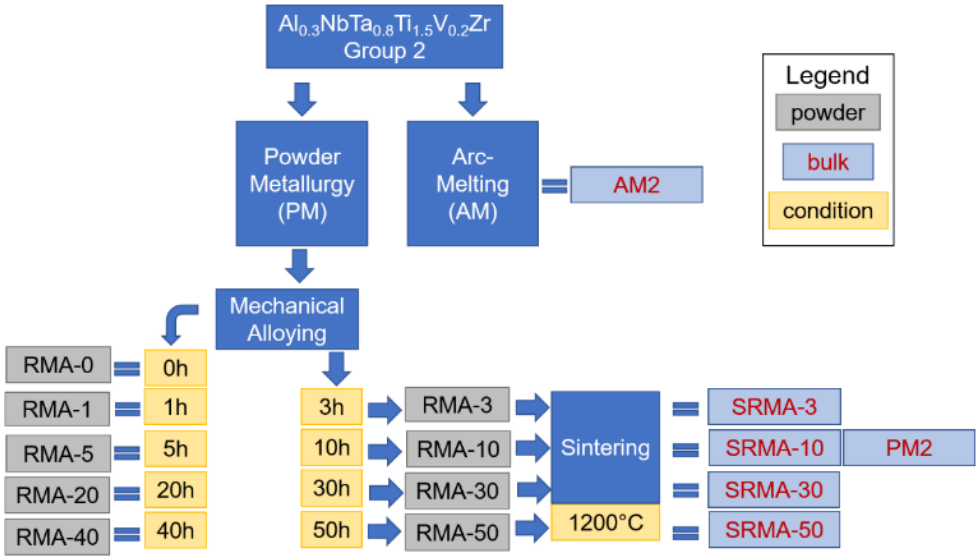

Fig. 26. Samples preparation diagram for $Al_{0.3}NbTa_{0.8}Ti_{1.5}V_{0.2}Zr$ RHEA.

4.2.2 HEAs preparation by casting

The alloys were produced by vacuum arc-melting or, alternatively, vacuum induction-melting followed by casting into a crucible. In case of arc-melting, chunks of each element are heated via an electric arc created by a tungsten electrode and the feedstock metals [154]. In induction-melting, the heating is created by an electric current that passes through a set of induction coils. The passage of current through the coils creates a magnetic field, inducing current [155].

- **$Al_{0.2}Co_{1.5}CrFeNi_{1.5}Ti$ preparation by vacuum induction melting**

The $Al_{0.2}Co_{1.5}CrFeNi_{1.5}Ti$ HEA studied on this research was prepared by vacuum induction melting. The ingot was cast under argon atmosphere from elemental constituents with purities higher than 99.5 wt%. The melting process was repeated at least six times for a guaranteed homogenization of the ingot. The prepared alloy will be referred in the cast condition, i.e. before heat treatments, as $Al_{0.2}Co_{1.5}CrFeNi_{1.5}Ti$ as-cast HEA, or FCC as-cast C-HEA.

- **$Al_{0.x}Nb_{1.y}Ta_{0.8}Ti_{1.5}V_{0.2}Zr$ preparation by vacuum arc melting**

The $Al_{0.5}NbTa_{0.8}Ti_{1.5}V_{0.2}Zr$ and $Al_{0.3}NbTa_{0.8}Ti_{1.5}V_{0.2}Zr$ RHEAs were produced exclusively by vacuum arc-melting (AM), and named as AM1 and AM2. The difficulties of preparation became a challenge, due to the alloys very high melting temperatures, requiring extremely high operation temperatures for their fabrication, which it is not possible to achieve in the case of induction melting furnaces. The melting took place at least six times for a guaranteed homogenization of the materials.
Casting was not possible in any of the alloys, as the pieces solidified immediately as soon as the arc was elevated, hindering the possibility of pouring the melted elements into a crucible.

4.2.3 Heat treatments

Heat treatments were performed in the studied alloys to evaluate the microstructural stability; remove possible segregation; improve the microstructures and mechanical properties; and analyze the phase transformations of each composition. These are described in subsections.

- **$Al_{0.2}Co_{1.5}CrFeNi_{1.5}Ti$**

The $Al_{0.2}Co_{1.5}CrFeNi_{1.5}Ti$ alloy in as-cast and as-sintered states, namely FCC C-HEA and FCC PM-HEA were subject to heat treatments. Both materials were heat treated for 5 h at 1000 ºC in a heating rate of 20 ºC/min, in air atmosphere and then air cooled. The obtained materials were named as FCC C-HEA1000 and PM-HEA1000 for the alloys prepared by cast and powder metallurgy, respectively. The pieces of each heat-treated material were divided in two parts, one for microstructural analysis and the second was subjected to a subsequent heat treatment. A second heat treatment was performed for additional 5 h at 750 ºC in a heating rate of 20 ºC/min, under air atmosphere, and air cooled again. The obtained materials were named as FCC C-HEA750 and FCC PM-HEA750. The schematics are depicted below.

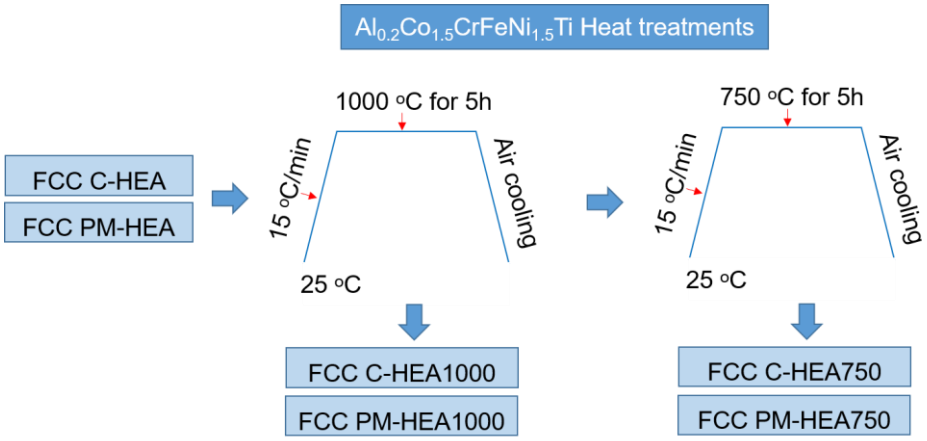

Fig. 27 Diagram of heat treatments performed on $Al_{0.2}Co_{1.5}CrFeNi_{1.5}Ti$ HEAs produced by PM and cast.

- **$Al_{0.x}Nb_{1.y}Ta_{0.8}Ti_{1.5}V_{0.2}Zr$**

The series of $Al_{0.x}Nb_{1.y}Ta_{0.8}Ti_{1.5}V_{0.2}Zr$, a group of RHEAs composed of $Al_{0.5}NbTa_{0.8}Ti_{1.5}V_{0.2}Zr$ (Group 1) and $Al_{0.3}NbTa_{0.8}Ti_{1.5}V_{0.2}Zr$ (Group 2), were subject to heat treatments in appropriate furnace of highly protective atmospheres. The conditions for each alloy of the same state were kept constant for comparability purposes. The description is as follows:

The arc melted and powder metallurgy RHEAs of Groups 1 and 2 ($Al_{0.5}NbTa_{0.8}Ti_{1.5}V_{0.2}Zr$ and $Al_{0.3}NbTa_{0.8}Ti_{1.5}V_{0.2}Zr$, respectively) were submitted to an alternative heat treatment as well using a high vacuum furnace and with pumped argon to insure the absence of external contamination. The cooling was done by furnace cooling from the maximum temperature, as:

- Heat treatment at 1400 ºC – from room temperature up to 1300 ºC in a rate of 15 ºC/min; from 1300 ºC up to 1400 ºC in a heating rate of 5 ºC/min; 1400 ºC for 1 h; furnace cooling.

The heat treatment at 1400 ºC was performed with the intention of homogenization of the alloys and is the start point for all the following heat treatments. The samples AM4, PM4 (Group 1) and AM5, PM5 (Group 2) were produced. Subsequently, additional heat treatments were performed as described below.

- Aging at 1050 ºC - after homogenization, aging took place following the scheme: from room temperature up to 1050 ºC in a rate of 15 ºC/min; 1050 ºC for 30 h; furnace cooling. The samples AM7, PM7 (Group 1) and AM8, PM8 (Group 2) were produced.
- Aging at 800 ºC - after homogenization, aging took place following the scheme: from room temperature up to 800 ºC in a rate of 15 ºC/min; 800 ºC for 30 h; furnace cooling. The samples AM10, PM10 (Group 1) and AM11, PM11 (Group 2) were produced.
- Aging at 600 ºC – after homogenization, aging took place following the scheme: from room temperature up to 600 ºC in a rate of 15 ºC/min; 600 ºC for 30 h; furnace cooling. The samples AM13, PM13 (Group 1); AM14 and PM14 (Group 2) were produced.

The heat treatments performed by furnace cooled conditions are depicted in Fig. 28.

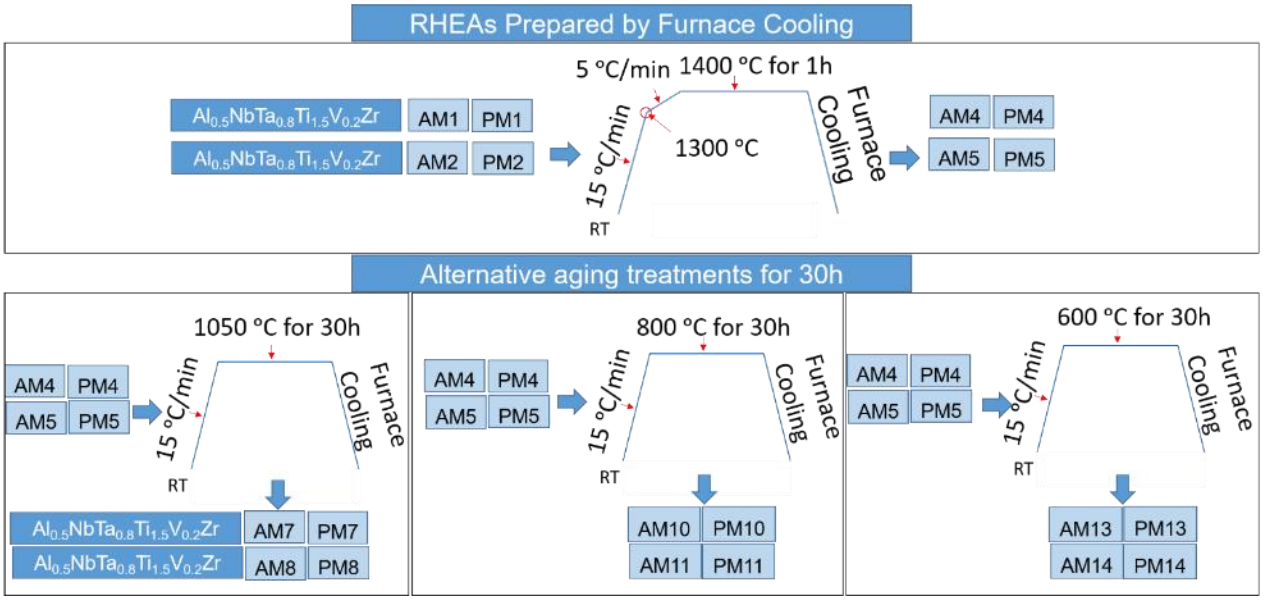

Fig. 28 Diagram of furnace cooled heat treatments performed on the studied RHEAs. All alloys were subjected to these treatments; subscripts are not shown.

4.3 Microstructural characterization

The HEA samples studied on this work for microstructural observations were prepared by hot mounting in conductive resin and mechanically ground with SiC abrasive papers down to #2400 grit. The samples were polished using 3 µm and 1 µm diamond paste. The last steps of sample preparation are mechano-chemical polishing using Struers OPS colloidal silica suspension and vibration polishing for minimum 4 h using Eposil M colloidal silica suspension of 0.06 µm.

4.3.1 Scanning electron microscopy

Scanning electron microscopy (SEM) using ZEISS Ultra Plus FEG microscope was performed in all materials for analyses of the microstructural features, using secondary electrons (SE) detector, backscattered electrons (BSE) detector and electron channeling contrast (ECCI) modes. For chemical composition, Energy-dispersive X-ray spectroscopy (EDX) mode was used. The values presented here are an average of at least three measurements, where the error is the standard deviation. Electron backscatter diffraction (EBSD) was utilized for obtaining information about the structure, crystal orientation, phase, grain size average and other structural parameters. Additionally, Zeiss Merlin, Gemini and Zeiss-Crossbeam XB 1540 FIB were used for a few analyses in BSE and SE modes.

4.3.2 Transmission electron microscopy

Thin foil specimens of $Al_{0.2}Co_{1.5}CrFeNi_{1.5}Ti$ in as-cast and as-sintered states were prepared for Transmission electron microscopy (TEM) (Jeol 2200FS) observation of the microstructure by Focused Ion Beam (FIB) micromachining inside ZEISS Auriga SEM chamber, to observe

features in nanometric scale and ultra-high-resolution atomic scale, with the support of Scanning TEM imaging (STEM) and EDX.

4.3.3 X-ray diffraction

X-ray diffraction (XRD) analysis for detailed structural characterization, phases, chemical composition and geometrical parameters was performed in all materials.
This was performed mainly using Philips X'Pert Pro diffractometer operated at 40 kV voltage with the current of 30 mA. A continuous scanning was usually performed with 2θ between 30° and 100° using a speed of 0.02°·min^{-1} and a step size of 0.0167°. The radiation used was Cu-Kα with λ = 1.54056 Å. Additional XRD measurements were carried out using diffractometer XRD ISO-DEBYEFLEX 3003 equipped with Co Kα (λ = 1.788965 Å) radiation source operated at 40 kV and 30 mA.

4.4 Mechanical properties

The mechanical response of the produced alloys was tested as described below.

4.4.1 Hardness

Vickers hardness was assessed for all materials using microhardness testing according to ISO 6507-1:2005, using LECO LM 274 AT hardness tester, with applied loads of 0.2 kg. The individual results for materials represent an average of at least 15 measurements and the error is the standard deviation. In the specific case of $Al_{0.2}Co_{1.5}CrFeNi_{1.5}Ti$ in as-cast and as-sintered states, after tribological tests, hardness measurements were taken using Vickers indenter with 0.2 kg load, on the same surface of the test in a perpendicular direction to the worn track. The results for each material are taken from at least five perpendicular lines to the track containing 15 measurements and the error is the standard deviation.
Nanoindentation hardness testing was carried out in all materials according to Oliver & Pharr method [156]. CSM Instruments NHT2 nanoindentation tester equipped with a Berkovich diamond indenter was used at acquisition rate of 10 Hz, maximum load of 100 mN, loading and unloading rates of 200 mN.min-1, and dwell time of 10 s. Averages were taken from at least 15 indents for each sample, where the error is the standard deviation of the values.

4.4.2 Flexural tests

Flexural strength (R_{mo}) determination was performed on samples that were manufactured by electric discharge machining (EDM). To decrease the influence of surface roughness, the samples were polished to mirror finish. $Al_{0.2}Co_{1.5}CrFeNi_{1.5}Ti$ HEA was tested using three-point bending jig of Zwick Z020 universal tensile test machine, with the loading span of 18 mm and a crosshead speed of 1 mm·min^{-1}. The materials had dimensions of 3 × 4 × 20 mm^3. Four specimens were used for each material and the results were taken as an average of the measurements. The calculated error represents the standard deviation. The 4 × 18 mm^2 face

of these samples corresponded to the direction perpendicular to the SPS pressing direction for the PM HEAs.

In the case of $Al_{0.3}NbTa_{0.8}Ti_{1.5}V_{0.2}Zr$ RHEAs, three-point bending was performed using Instron 8862 equipment with a loading span of 20 mm and crosshead speed of 0.1 $mm \cdot min^{-1}$. The specimens' dimensions were 3 × 4 × 23 mm^3. The 4 × 23 mm^2 face of these samples corresponded to the direction perpendicular to the SPS pressing direction for the PM RHEAs. Three specimens were used for each material and the results were taken as an average of the measurements. The calculated error represents the standard deviation.

4.4.3 Elastic modulus and Poisson ratio determination

Elastic modulus was determined for selected samples of $Al_{0.3}NbTa_{0.8}Ti_{1.5}V_{0.2}Zr$ RHEA by excitation method on the RFDA System 24-3 machine according to standard E1876-15. The elastic modulus was calculated by an average of 10 measurements taken on each sample.

Ultrassound (US) measurements were carried out for $Al_{0.5}NbTa_{0.8}Ti_{1.5}V_{0.2}Zr$ RHEA composition on the PM alloy, in order to investigate the influence of the sintering times into its final properties. They were performed using Olympus 38DL Plus system for Elastic Modulus and Poisson Ratio calculations. The probe used for calculation of elastic modulus was M112 10MHz Longitudinal wave transducer; and the probe used for calculation of Poisson ratio and Shear Moduli was V156 5 MHz Shear wave transducer.

4.5 Tribological properties

In the case of $Al_{0.2}Co_{1.5}CrFeNi_{1.5}Ti$ HEA as-cast and as-sintered states, tribological properties have been measured. The wear testing was done on the commercial UMT TriboLab tribometer using the reciprocal ball-on-plate scheme. During testing, the samples performed a reciprocating movement under dry sliding conditions, while a 9.51 mm-diameter bearing steel (AISI 52100 – SUJ2) counterpart ball was fixed stationary on the top of the plate under an applied normal load.

As a reference material, a high-speed bearing steel (AISI 52100 – SUJ2) bar was chosen due to its exceptional mechanical properties in terms of wear, and also to facilitate a direct comparison with a previous study on cast high-entropy alloys [157]. As a second reference material, as-cast Inconel 713 was used due to its crystallographic similarity to the PM-HEA as-sintered alloy (FCC matrix with dispersed coherent precipitates). The reference materials and the HEAs were tested under identical conditions. The used parameters of the wear testing were normal loads of 1.2 N and 5 N, stroke length of 10 mm, stroke frequency of 2 Hz and test duration of 30 min (corresponding to a total sliding distance of 36 m). The samples were

machined to dimensions of 5 × 5 × 28 mm^3 and successively ground with #250-2000 grit SiC papers, followed by polishing with 3 mm and 1 mm diamond paste using a linen disc.

The friction force was monitored and recorded in-situ, while the specific wear rates of the studied materials were quantified according to the Archard's model equation [158]:

$$(Specific\ wear\ rate) = \frac{wear\ volume}{load*distance} \quad , \tag{24}$$

where the wear volume was calculated as the product of the worn cross-sectional area measured with the optical profilometer Contour GT, and the total sliding distance.

The maximum contact pressure p_{max} under the selected load was calculated according to the Hertzian contact stress theory for spheres in contact with flat surface, which gives a description of the stress within mating parts following the model's equation [159]:

$$p_{max} = \frac{1}{\pi}\left(\frac{6FE^{*2}}{R^2}\right)^{1/3}, \tag{25}$$

where F is the applied normal force, R is the radius of the sphere and E* relates the elastic moduli of the ball (E_1) and the tested materials (E_2) and its respective Poisson ratios (μ_1, μ_2) according to:

$$\frac{1}{E^*} = \frac{1-\mu_1^2}{E_1} + \frac{1-\mu_2^2}{E_2}. \tag{26}$$

The corresponding coefficients of friction (COF) were calculated as a ratio between the applied normal and friction forces and their respective errors are the standard deviation of the measurement.

5 Results

5.1 $Al_{0.2}Co_{1.5}CrFeNi_{1.5}Ti$ high entropy alloy

The $Al_{0.2}Co_{1.5}CrFeNi_{1.5}Ti$ high-entropy alloy produced by powder metallurgy (PM) and casting have been subject to investigation [160] in this work. The next subsections will deal with each aspect of the studied alloy.

5.1.1 Phase prediction

To discuss the experimental findings of this study, thermodynamic calculation of phase diagrams (CALPHAD) for $Al_{0.2}Co_{1.5}CrFeNi_{1.5}Ti$ (stoichiometric ratio) high-entropy alloy was computed using TCHEA1. The respective diagram is shown in Fig. 29. The alloy designed in this study possesses Al content equal to 3.2 at. % (denoted by the red arrow in Fig. 29a).
For this alloy, the predicted melting temperature is approximately 1130 ºC. Between temperatures (t) 1130 ºC and approximately 1120 ºC, nucleation of the BCC phase should occur. For temperatures (t) between 1120 ºC < t < 1090 ºC, nucleation of the FCC phase is initiated. The liquid phase is completely absent below 1090 ºC and a concurrent nucleation and growth of BCC and FCC takes place. From a temperature of approximately 985 ºC,

FCC#2 should nucleate and grow. Further temperature reduction induces the subsequent formation of sigma (at 885 ºC) and Laves phases (at 795 ºC) approximately.

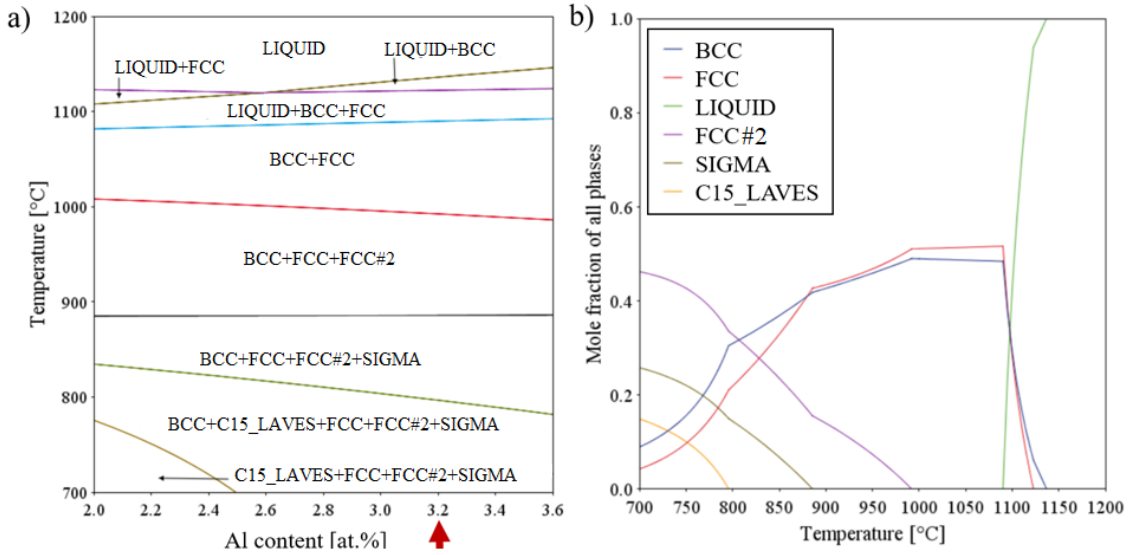

Fig. 29. CALPHAD calculations for the studied HEA. a) AlxCo1.5CrFeNi1.5Ti calculated phase diagram in the range from 2.0 < x < 3.6. The investigated composition (x = 3.2%) is marked with the red arrow. b) Property diagram of Al0.2Co1.5CrFeNi1.5Ti as mole fraction of all phases vs. temperature.

5.1.2 Microstructural characterization (as-cast and as-sintered states)

The XRD pattern analyses of the two $Al_{0.2}Co_{1.5}CrFeNi_{1.5}Ti$ alloys produced by powder metallurgy and casting are provided in Fig. 30, in their as-sintered and as-cast states, respectively. The lattice constants of the alloys were determined by XRD and by selected area electron diffraction patterns (SAEDP) from TEM analysis (Table 1). The comparison shows analogous FCC matrices and BCC phases in common and a major FCC solid solution matrix.

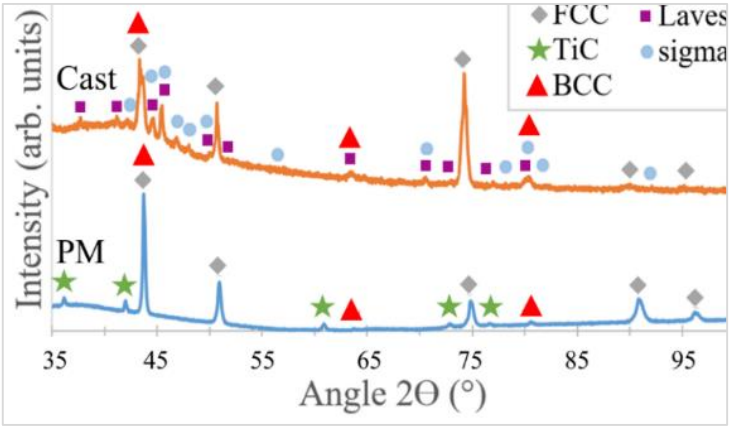

Fig. 30. XRD patterns and phase composition of PM HEA after the SPS densification (blue – PM) and Cast HEA (orange – Cast) in as-sintered and as-cast states.

PM HEA [Å]					
	a_{XRD}	c_{XRD}	a_{SAED}	c_{SAED}	vol.%
FCC matrix	3.58	-	3.61	-	**89.3**
TiC	4.30	-	4.38	-	**8.0**
BCC	2.93	-	2.95	-	**2.7**

Cast HEA [Å]					
FCC matrix	3.63	-	3.67	-	**47.8**
Laves	4.79	7.79	4.75	7.73	**30.6**
sigma (σ)	8.88	4.57	8.82	4.61	**11.5**
BCC	2.93	-	2.92	-	**10.1**

Table 1. Comparison of lattice parameters of PM and Cast HEA measured by XRD and selected area electron diffraction (SAEDP) in their in as-sintered and as-cast states.

The microstructure of the PM alloy is presented in Fig. 31 (FCC matrix and its features) and Fig. 32 (BCC and carbides). The FCC solid solution matrix can be seen in Fig. 31a, combined with its respective SAEDP (Fig. 31b) along the [011] zone axis, confirming the lattice constant as a = 3.61 Å, i.e., in good agreement with the XRD results (Table 1). The EDX point analysis indicates a matrix rich in Fe, Ni and Co (Table 2).

Chemical composition [at.%]									
Phase	FCC Matrix		BCC		TiC	Laves	σ phase	Map Sum Spectrum	
Alloy	PM	Cast	PM	Cast	PM	Cast	Cast	PM	Cast
Al	9.2	7.4	4.1	7.0	0.5	1.3	5.4	3.8	3.3
Ti	3.6	16.8	**19.3**	**23.5**	**92.6**	**28.0**	7.1	15.4	15.0
Cr	10.1	15.4	3.7	4.4	1.4	1.2	**28.2**	14.5	14.5
Fe	**20.3**	**17.1**	9.8	10.9	2.2	1.9	**24.1**	15.8	16.1
Co	**28.1**	**24.4**	**31.2**	**25.8**	1.8	**21.4**	**20.2**	24.4	24.4
Ni	**28.6**	**19.1**	**32.0**	**28.5**	1.5	**46.2**	14.9	26.1	26.7

Table 2. Comparison of the EDX chemical composition of the PM and cast alloys in their as-sintered and as-cast states, respectively.

Annealing twins have been observed within the FCC matrix (Fig. 31c) and further confirmed by SAEDP (Fig. 31d). The additional spots of the SAEDP correspond to patterns simulated for FCC twins with 60º misorientation to the matrix. The twins are represented by blue dots through the reflection planes on the <011> direction by 70.53° [161,162].

The presence of nano-sized coherent precipitates within the FCC matrix in the PM alloy is documented in Fig. 31e and confirmed by the SAED patterns along the zone axis [011] in Fig. 31f. The coherent ordered FCC phase is represented by a simulation of the supercell reflections (yellow dots) surrounding the reflection of the FCC matrix (red dot) in Fig. 31g inset. The supercell has a lattice constant about five times larger than the matrix. The coherent precipitates should correspond to Ni_3Ti precipitates with L12-type ordered lattice structure.

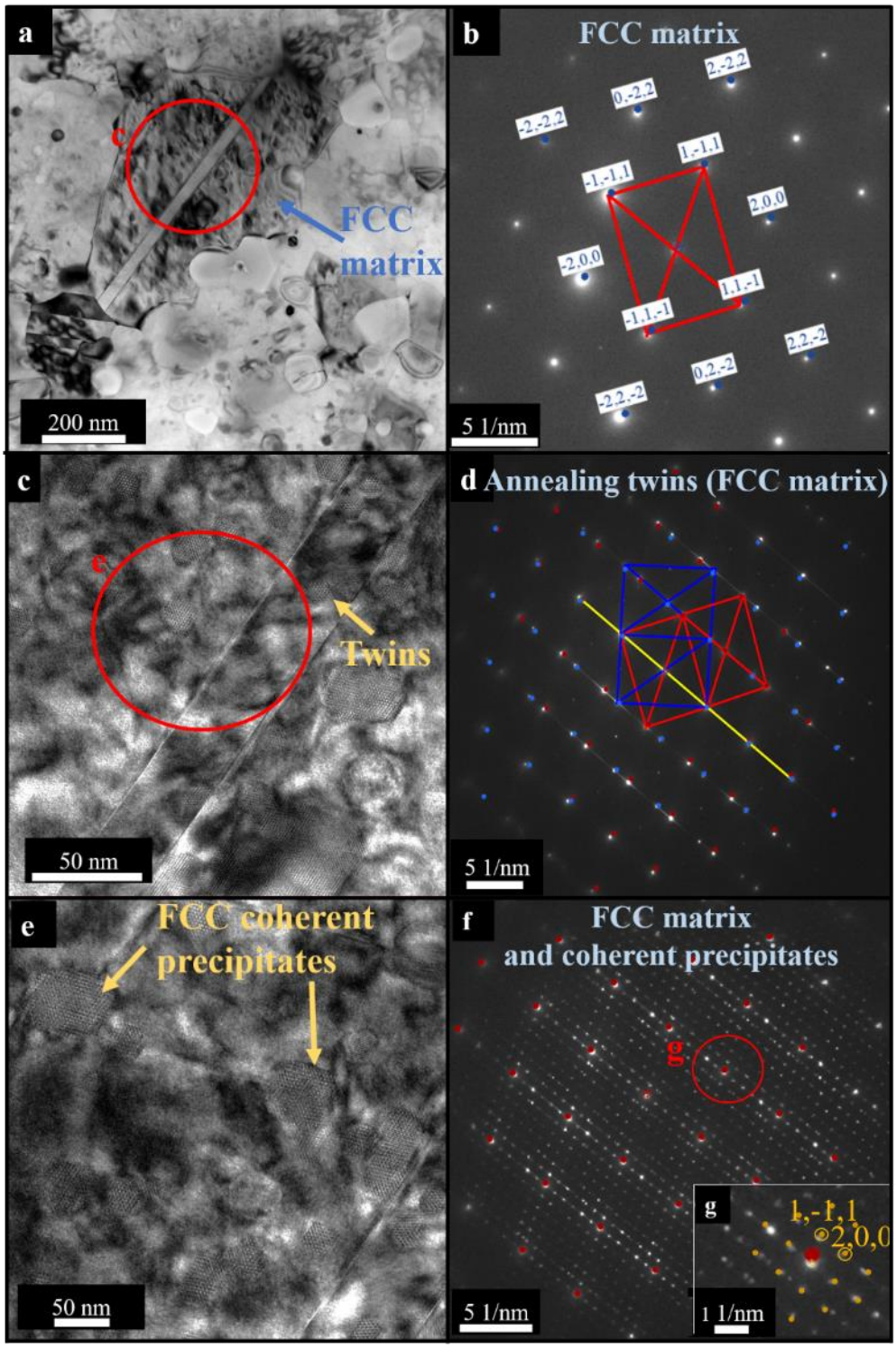

Fig. 31. Bright-field TEM image of the Al0.2Co1.5CrFeNi1.5Ti as-sintered PM HEA on the left side and SAED patterns of the respective phases on the right side. a) FCC matrix. b) SAEDP along the [011] zone axis. c) Twin boundary representation within the FCC matrix. d) SAEDP of a twin - the red dots are a simulation of the corresponding planes along the zone axis [011]. The blue dots are the representation of twins through reflection planes. e) Nano-precipitates coherent with FCC matrix. f) SAEDP of the FCC matrix showing coherent precipitates along zone axis [011]. A schematic simulation of the pattern of FCC matrix is represented by red dots. g) Coherent ordered FCC phase represented by yellow dots surrounding the reflection from the FCC matrix (red dot).

CALPHAD predictions showed formation of a second FCC (Fig. 29), mostly likely ordered. Nano-sized coherent precipitates were formed by precipitation from the FCC matrix while cooling after sintering. The mentioned precipitation phenomena can be related to the coherent

L12 phase formation (γ') in the matrix, which may eventually be transformed to η-phase as previously reported on similar HEAs [15,24], forming a γ/ γ′ relationship with the matrix. This phenomenon is analogous to one observed in traditional Ni-base superalloys.

The presence of nano-sized coherent precipitates within the FCC matrix in the PM alloy is documented in Fig. 31e and confirmed by the SAED patterns along the zone axis [011] in Fig. 31f. The coherent ordered FCC phase is represented by a simulation of the supercell reflections (yellow dots) surrounding the reflection of the FCC matrix (red dot) in Fig. 31g inset. The supercell has a lattice constant about five times larger than the matrix. The coherent precipitates should correspond to Ni_3Ti precipitates with L12-type ordered lattice structure. CALPHAD predictions showed formation of a second FCC (Fig. 29), mostly likely ordered.

Nano-sized coherent precipitates were formed by precipitation from the FCC matrix while cooling after sintering. The mentioned precipitation phenomena can be related to the coherent L12 phase formation (γ') in the matrix, which may eventually be transformed to η-phase as previously reported on similar HEAs [15,24], forming a γ/ γ′ relationship with the matrix. This phenomenon is analogous to one observed in traditional Ni-base superalloys.

The globular TiC particles formed in-situ during milling are characterized in Fig. 32a and b. The SAEDP along the [011] zone axis shows an ordered FCC structure with lattice parameter a = 4.38 Å, corroborating the a = 4.30 Å values obtained by XRD (Table 1). The TiC structure was first reported in [163], in which the lattice constant was found to be smaller, a = 3.32 Å, according to the Inorganic Crystal Structure Database (ICSD) collection code 44494. The EDX point analysis has confirmed that the phase is Ti-rich (Table 2). This was further supported by the mapping presented in Fig. 35, clearly showing globular-like areas rich in Ti.

The minor BCC phase (2.7 vol.% fraction) in the PM alloy is shown in Fig. 32c and its respective SAEDP along the [-111] zone axis is shown in Fig. 32d with the calculated lattice parameter of a = 2.95 Å comparable to the results extracted from XRD (Table 1). The phase is rich in Ni, Co and Ti (Table 2 and additional EDX map provided in Fig. 36).

The microstructures of the Cast HEA variant and their respective SAEDPs are presented in Fig. 33 (patterns of the major FCC and Laves phases) and Fig. 34 (minor phases: σ and BCC). Fig. 33a shows typical microstructural features of the cast alloy, in which the FCC matrix surrounded by elongated needle-like Laves and σ phases, and very fine dispersed globular BCC precipitates can be observed.

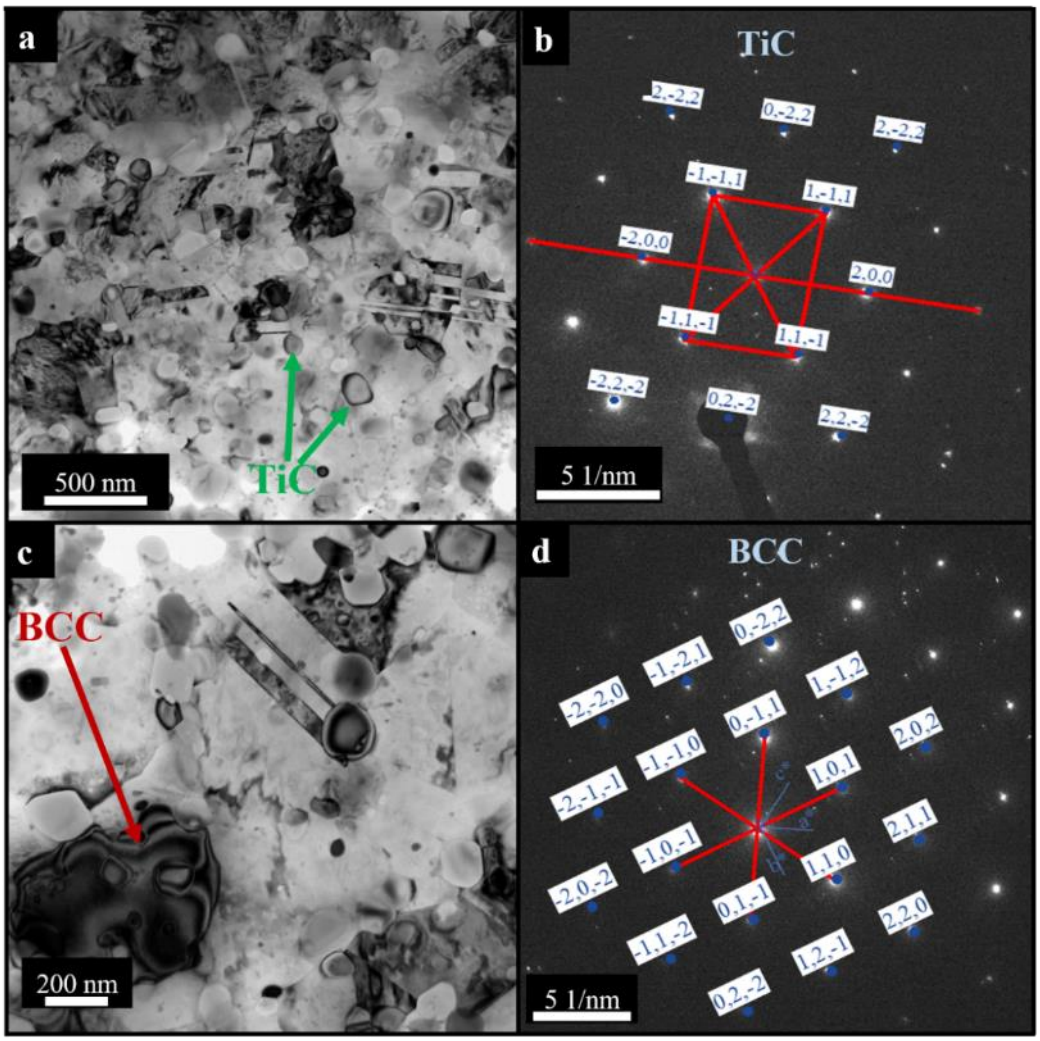

Fig. 32. Bright-field TEM image of Al0.2Co1.5CrFeNi1.5Ti as-sintered PM HEA on the left side and SAEDP of the respective phase on the right side. a) Dispersed TiC within the matrix. b) SAEDP from PM HEA of TiC along [011] zone axis. c) Representation of BCC phase. d) SAEDP from PM HEA along [-111] zone axis of BCC.

The SAED patterns of the FCC matrix along [-110] zone axis in the Cast HEA are displayed in Fig. 33b. The phase is (Fe, Ni, Co)-rich and with a calculated lattice parameter a = 3.67 Å, confirming the values from XRD peaks (Table 1).

The Laves phase was only present in the cast alloy and is depicted in Fig. 33c. Its SAEDP along the [11-20] zone axis is shown in Fig. 33d. The lattice constant for this topologically close-packed (TCP) phase was calculated to be a = 4.75 Å and c = 7.73 Å, in accordance with the XRD results, a = 4.79 Å and c = 7.79 Å, presented in Table 1. The phase is rich in Co, Ni and Ti corresponding to a ratio $(Co,Ni)_2Ti$, as shown in Table 2 and confirmed by EDX maps of the corresponding areas marked by red arrows in Fig. 37.

The σ phase (11.5 at. %) found only in the Cast HEA is denoted by the green arrow in Fig. 34a. Its SAEDP together with the simulated pattern along the [100] zone axis for the phase depicted in Fig. 34b have lattice constants a = 8.82 Å and c = 4.61 Å. Similar results were obtained by XRD diffraction peaks (Table 1). This phase is rich in Cr, Co and Fe (Table 2). The EDX maps (Fig. 37) also show the presence of the same elements in the indicated areas pertaining to the σ phase, as marked by the blue arrows.

The minor BCC phase (10.1 at. %) also present in the Cast HEA is depicted in Fig. 34c, marked with the blue arrow. Its lattice constant was measured by SAEDP (Fig. 34d) along the [111] zone axis, showing a = 2.92 Å, i.e., matching the equivalent result of a = 2.93 Å found by XRD, and the same BCC minor phase as in the PM counterpart (Table 1). The similarities between the BCC phase in the PM and cast alloys are also evidenced by the analogous chemical compositions shown in Table 2, both being Ni-, Co- and Ti-rich.

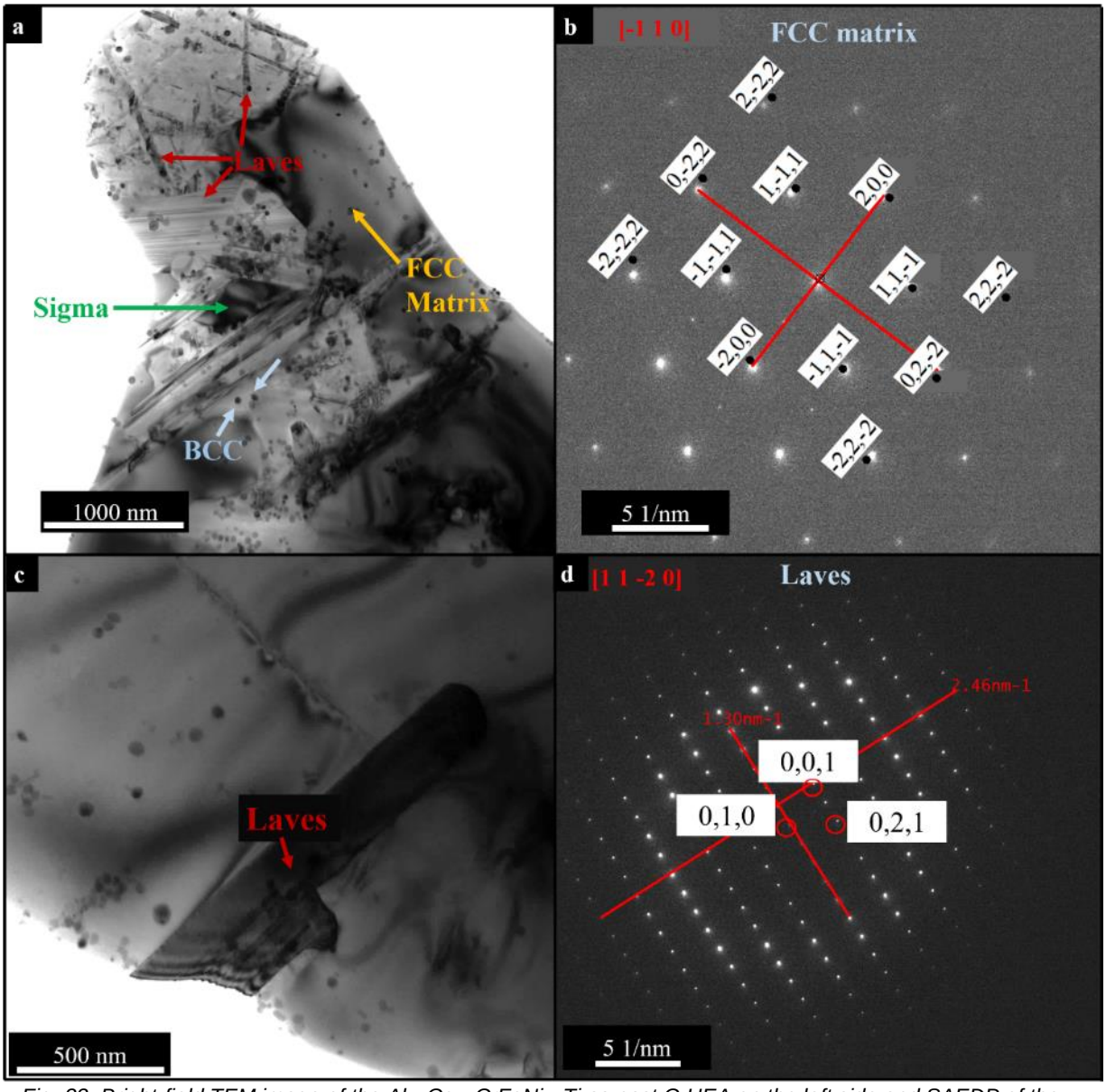

Fig. 33. Bright-field TEM image of the $Al_{0.2}Co_{1.5}CrFeNi_{1.5}Ti$ as-cast C-HEA on the left side and SAEDP of the respective phase on the right side. a) representative microstructure showing all phases present in the alloy. b) SAEDP of the FCC matrix along [-110] zone axis. c) Needle-like Laves phase. d) SAEDP of the Laves phase along [11-20] zone axis.

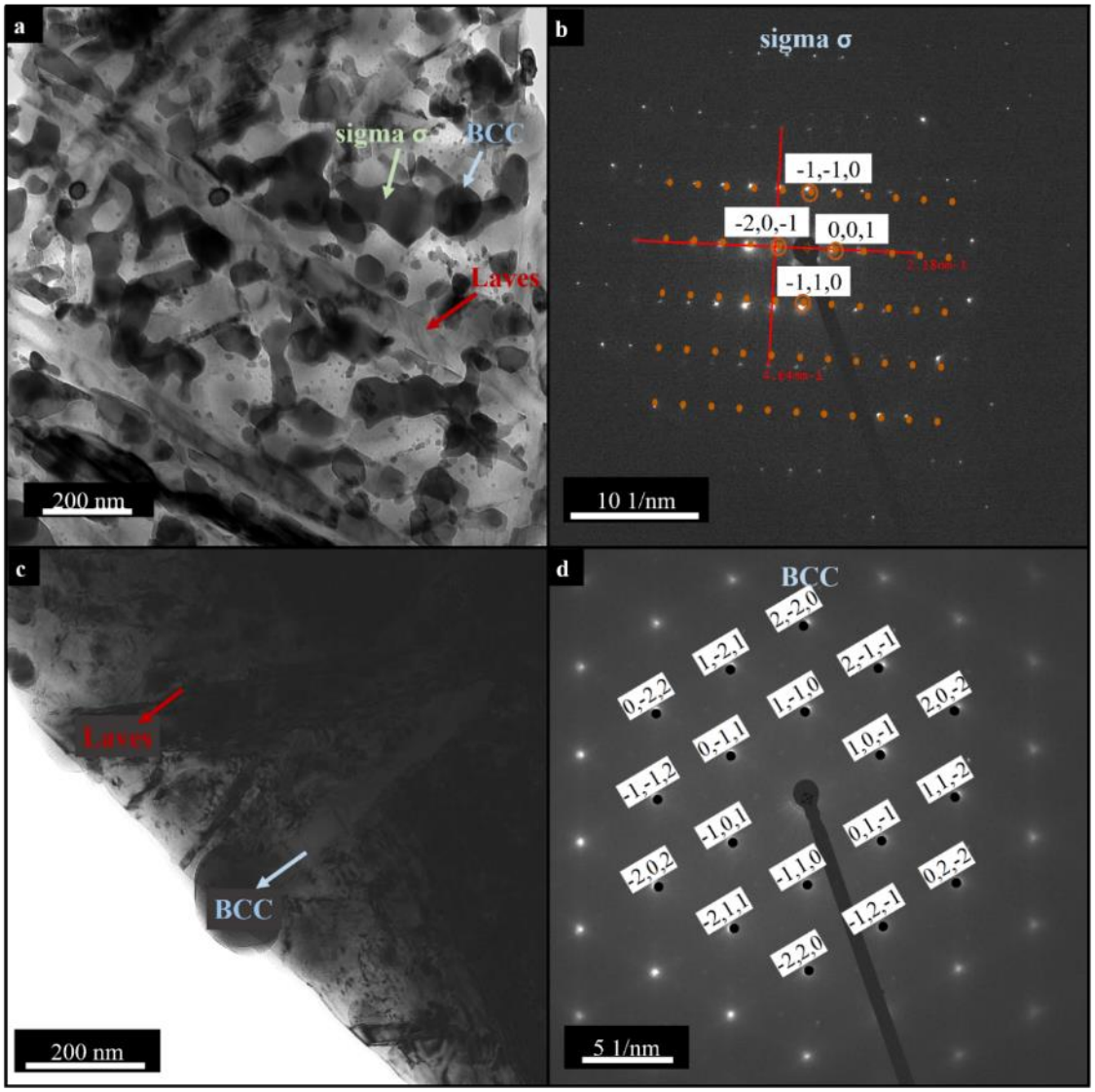

Fig. 34. Bright-field TEM image of the $Al_{0.2}Co_{1.5}CrFeNi_{1.5}Ti$ as-Cast C-HEA on the left side and SAED patterns of the denoted phase on the right side. a) representative TEM image showing Laves, σ and BCC phases. b) SAEDP of σ phase along [100] zone axis. c) Typical microstructure for needle-like Laves and BCC phases. d) SAEDP of BCC along [111] zone axis.

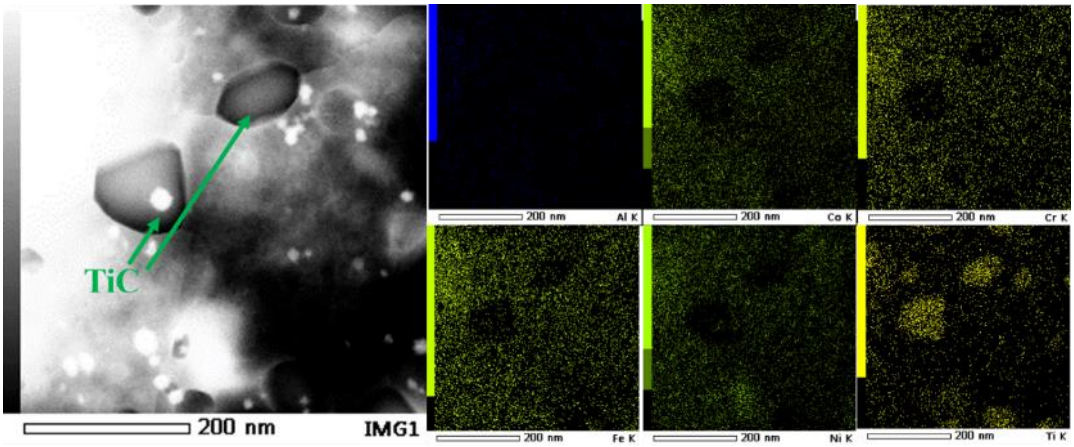

Fig. 35. TEM/EDX mapping showing that the FCC is a Ti-rich phase, corresponding to TiC particles from the microstructure of the as-sintered PM HEA.

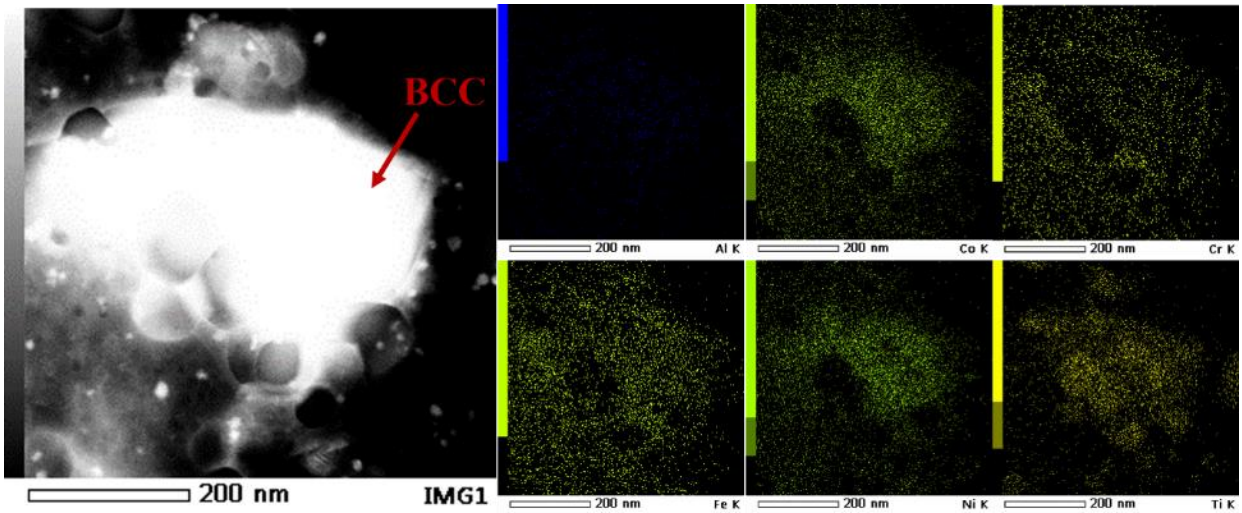

Fig. 36. TEM/EDX mapping of the BCC phase in the as-sintered PM HEA.

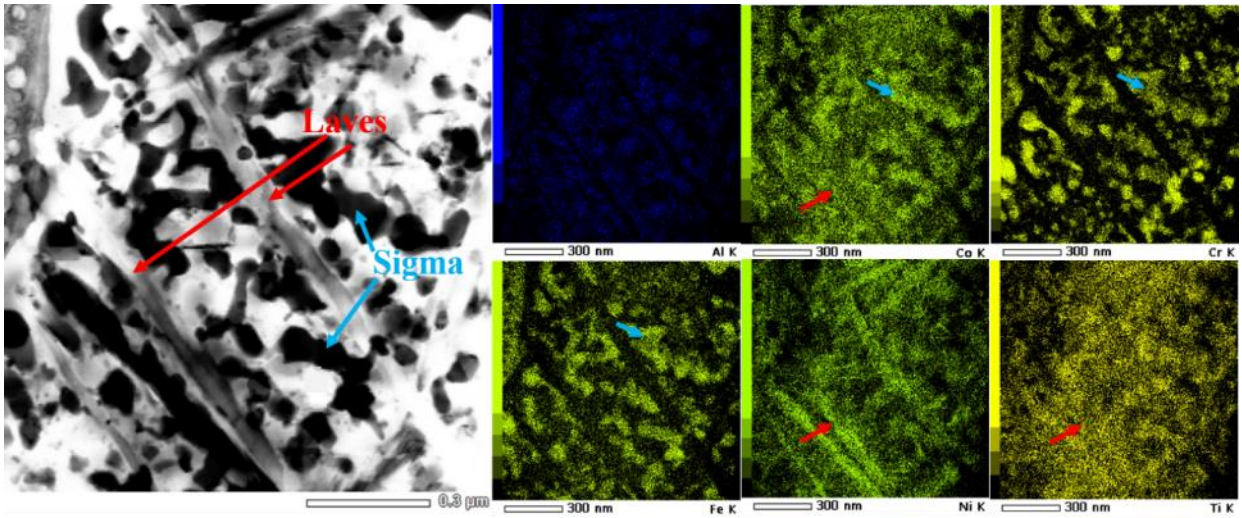

Fig. 37. TEM/EDX mapping of the as-Cast HEA alloy. The Laves phase is denoted by the red arrows, the σ phase is marked by blue arrows.

For quantitative evaluation of the microstructure, EBSD analyses have been performed, with results concerning the phase distribution, orientation and grain sizes of the PM and cast alloys presented in Fig. 38 and Fig. 39, respectively.

With the SPS-process, full density fine-grained samples can be produced, even at relatively short sintering periods (10 minutes). The PM alloy possesses a distribution of fine nano-sized grains of both FCC and TiC (Fig. 38a,c,d). The average grain sizes of the FCC matrix and TiC are 0.42 µm and 0.40 µm, respectively.

One can perceive the random orientation of both FCC and TiC grains despite the uniaxial pressing during the SPS of the PM alloy, as any type of preferential crystallographic texture cannot be detected in Fig. 38b. Due to EBSD resolution constraints, the BCC phase is not visible.

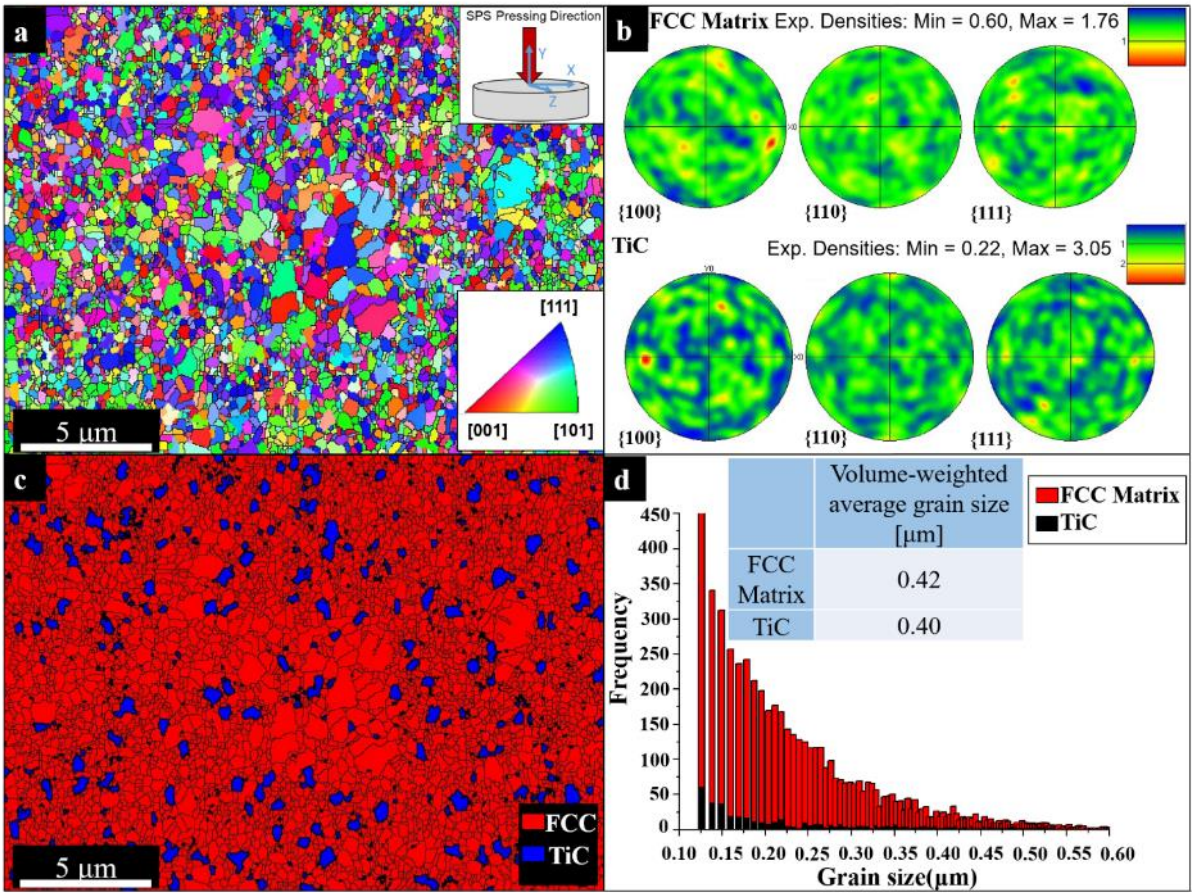

Fig. 38. Representative SEM EBSD analysis of the as-sintered PM HEA. a) inverse pole figure showing grain orientation maps with reference direction perpendicular to the SPS compaction direction denoted as Z in the image. b) Pole figures of FCC and TiC phases. c) Phase map showing distribution of TiC in FCC matrix. d) Grain size distribution of respective phases with average grain size and volume fraction.

The quantitative analysis of the FCC matrix and Laves phases shows that their average grain size is 42.8 µm and 5.4 µm, respectively. The large-sized grains of the cast alloy essentially show one preferential crystallographic orientation due to dendritic solidification (Fig. 39a).

The white regions in the EBSD maps correspond to non-indexed areas that were impossible to resolve accurately due to the resolution threshold of the method. They may possibly correspond to a mixture of nano-sized phases already identified in the TEM images (namely σ, BCC, or the needle-like nano-sized Laves phase, documented in Fig. 34a).

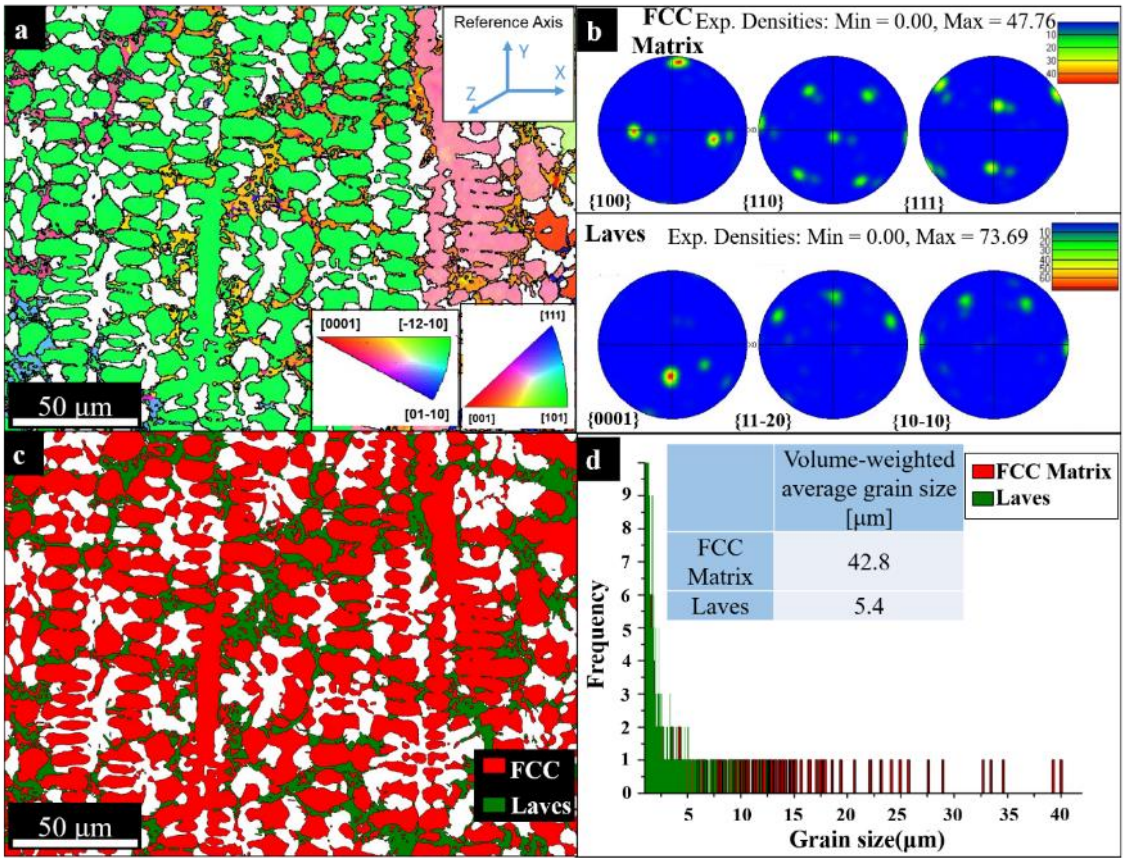

Fig. 39. Representative SEM EBSD analysis of the as-cast C-HEA. a) Inverse pole figure orientation map with reference direction Z denoted in the image. b) Pole figures of FCC and Laves phases. c) Phase map showing distribution of Laves in FCC matrix. d) Grain size distribution of respective phases with average grain size and volume fraction.

5.1.3 Mechanical properties (as-cast and as-sintered states)

The results of mechanical characterization by means of hardness and bending testing are presented in Table 3. The hardness values obtained by Vickers test for PM and Cast HEAs were found to be 712 ± 3 HV and 682 ± 10 HV, respectively. The elastic modulus *E* of each material was measured by nanoindentation test. The results show that the PM HEA possesses *E* modulus of 258 ± 10 GPa, while the cast counterpart shows a value of *E* = 210 ± 20 GPa. The bending strength (R_{mo}) of the PM material was exceptionally high, with values exceeding 2 GPa (averaging 2018 ± 65 MPa). These values are almost double compared to the Cast HEA, which has an average R_{mo} of 1101 ± 42 MPa.

	Hardness [HV]	E [GPa]	R_{mo} [MPa]
Cast	682 ± 10	210 ± 20	1101 ± 42
PM	712 ± 3	258 ± 10	2018 ± 65

Table 3. Average hardness, elastic modulus and flexural strength for the PM and Cast HEAs in as-cast and as-sintered states.

PM HEA exhibits a much smaller grain size in all phases, with nanosized grains (0.42 µm) of the FCC matrix holding 89.3% of the total volume and additional TiC particles pinning the grain

boundaries. Neither materials showed any significant plastic strain, i.e., their failure occurred immediately after the initial elastic loading.

The results of the fractographic analysis of the ruptured bending test specimens are presented in Fig. 40. The morphology of the fracture surface of the PM alloy is a mixture of ductile and brittle fracture mechanisms. The presence of very fine and shallow ductile dimples, shown in Fig. 40a, is attributed to the small grain size of the ductile FCC matrix present in a high volume fraction. No visible inclusions or other particles were detected inside the dimples, suggesting a strong metallurgical bonding of the TiC particles with the matrix (Fig. 40b).

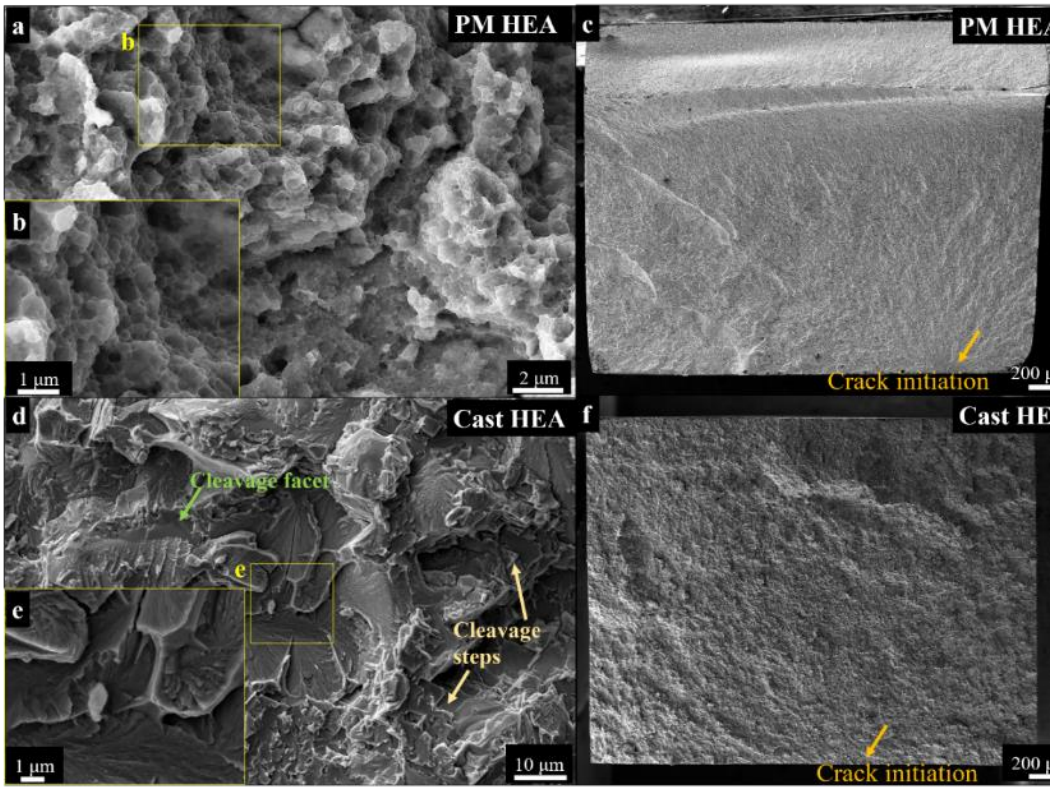

Fig. 40. SEM micrographs of fracture surfaces of $Al_{0.2}Co_{1.5}CrFeNi_{1.5}Ti$ bending specimens. a) Typical PM HEA fracture surface morphology with fine ductile dimples in the as-sintered state. b) Enlarged view of the area denoted by yellow rectangle showing typical fine ductile dimples. c) PM HEA fracture surface overview with crack initiation site denoted by yellow arrow. d) Typical as-Cast HEA fracture surface having predominantly brittle morphology. Brittle cleavage facets denoted by the green arrow and steps by yellow ones. e) Enlarged view of the area denoted by the yellow rectangle showing typical cleavage separation and river patterns. f) Cast HEA: fracture surface overview.

The Cast HEA manifested a significant brittle nature of the fracture surface morphology, with large cleavage facets corresponding to brittle phases cracking (Fig. 40d). The green arrow shows a typical total cleavage separation of a brittle phase. Some of the brittle facets are surrounded by ductile fracture of the FCC matrix (Fig. 40e), in which the deformation creates a ductile bridge between the facets, preceding the fracture by cleavage.

The yellow arrows in Fig. 40d point to the formation of cleavage steps in the crack propagation along different crystallographic planes for dissipation of deformation energy. This is a consequence of the presence of different nano-sized particles within the matrix, interacting with the crack tip and changing the cleavage step mechanism. The cast material does not

exhibit a major initiation site (Fig. 40f) but rather evidences multiple initiation sites from the surface. A typical initiation site is marked in yellow.

5.1.4 Tribological properties

The specific wear rates of the PM and Cast HEAs in the as-sintered and as-cast states were compared with the reference AISI 52100 (conventional wear-resistant steel) and Inconel 713. The latter possesses a microstructure similar to that of PM HEA, containing fine coherent precipitates dispersed within the FCC matrix. The results are shown in Fig. 41.

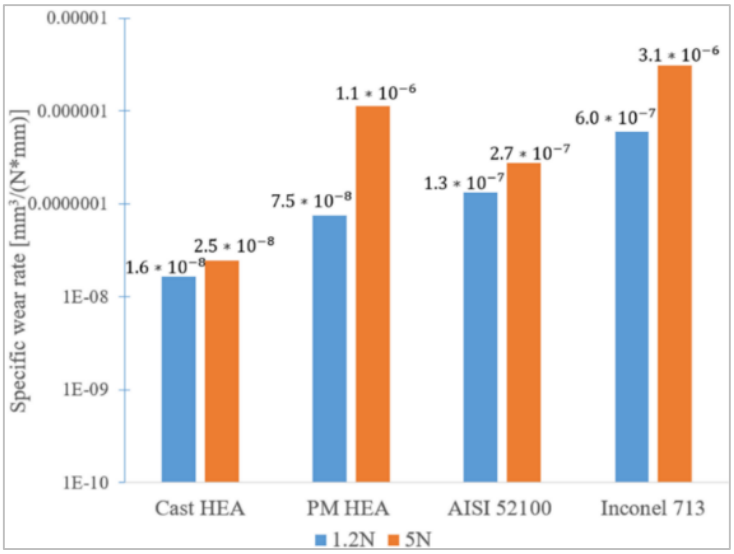

Fig. 41. Specific wear rates of the cast and the PM HEAs in comparison with reference materials (AISI 52100 and Inconel 713) under different load conditions, 1.2 N and 5 N.

The corresponding values of the worn volumes, as well as the average coefficients of friction (COF) recorded in-situ, are provided in Table 4. The variations in the specific wear rates are directionally proportional to the worn volume of material and inversely proportional to the force applied; both values will, therefore, be provided.

Material	Worn volume [µm³]		COF	
	1.2 N	5 N	1.2 N	5 N
Cast HEA	0.71	1.07	0.67 ± 0.11	0.66 ± 0.04
PM HEA	3.25	48.57	0.74 ± 0.08	0.60 ± 0.04
AISI 52100	5.7	11.85	0.80 ± 0.04	0.67 ± 0.07
Inconel 713	25.96	134.47	0.81 ± 0.05	0.74 ± 0.04

Table 4. Total worn volume of each material and corresponding coefficients of friction under 1.2 N and 5 N loads.

Among all tested materials, the Cast HEA had the best performance under both loading conditions, showing specific wear rates of 1.6×10-8 $mm^2.N^{-1}$ for 1.2 N (corresponding to a worn volume of material of 0.71 µm³ and COF = 0.67 ± 0.11) and 2.5×10^{-8} $mm^2.N^{-1}$ for 5 N (a

worn volume of 1.07 μm³ and COF = 0.67 ± 0.04). The maximum contact pressures between the sphere and the flat surface were calculated to be 0.51 GPa and 0.83 GPa, respectively.

Surprisingly, in comparison with the traditionally used wear-resistant AISI 52100, the performance of the Cast HEA was remarkably higher, achieving a specific wear rate ten times lower than AISI 52100.

The PM HEA exhibited results slightly superior to the traditional AISI 52100 under 1.2 N load, as its specific wear rate was found to be 7.5×10^{-8} $mm^2.N^{-1}$ and COF = 0.74 ± 0.08. The worn volume was calculated to be 3.25 μm^3, i.e., about 4.6 times higher than the worn volume of its cast counterpart.

Under higher loads, the PM material seems to become more fragile. The contact pressures under the two loads were calculated to be 0.55 GPa and 0.88 GPa, respectively, i.e., values similar to the ones encountered for the Cast HEA. Above 0.55 GPa, the microstructure can no longer withstand higher loads and the wear rate substantially increases from 7.5×10^{-8} $mm^2.N^{-1}$ up to 1.1×10^{-6} $mm^2.N^{-1}$, a value almost 15 times higher. Consequently, the corresponding wear volume exhibited a significant increase to 48.57 μm^3. The respective COF equals 0.60 ± 0.04, i.e., lower than that at 1.2 N load.

In general, both PM and Cast HEAs showed very good wear resistance under a 1.2 N load, superior to the commercially available AISI 52100 or Inconel 713 materials.

The overall morphology of the wear surface for both PM and cast alloys can be seen in Fig. 42. Three-dimensional optical profilometry images of the worn tracks show the individual grooves and plastic deformation. Those features represent broken adhesive junctions on the worn surface.

EDX analyses on the worn surface features of broken adhesive junctions (Fig. 43, Fig. 44 and Table 5) reveal a high content of iron oxides, which, together with the test conditions, indicates a mild-oxidational wear regime [164]. A relatively high Fe content suggests that the material partially originates from the counterpart ball.

The morphology of the worn track area presents grooves in both as-cast and as-sintered alloys (Fig. 42). They may be associated with delamination wear [164,165] that originates from severe plastic deformation in the contact of asperities. The resulting plastic shear strain is accumulated in the subsurface layer, and when it reaches a certain value, cracks are formed, and material is removed in the form of flake-like particles.

Cast HEA exhibits only a negligible amount of non-metallic inclusions typically seen in cast materials. These should not influence the tribological properties of the Cast HEA, as these impurities are not even detected by XRD technique Fig. 30.

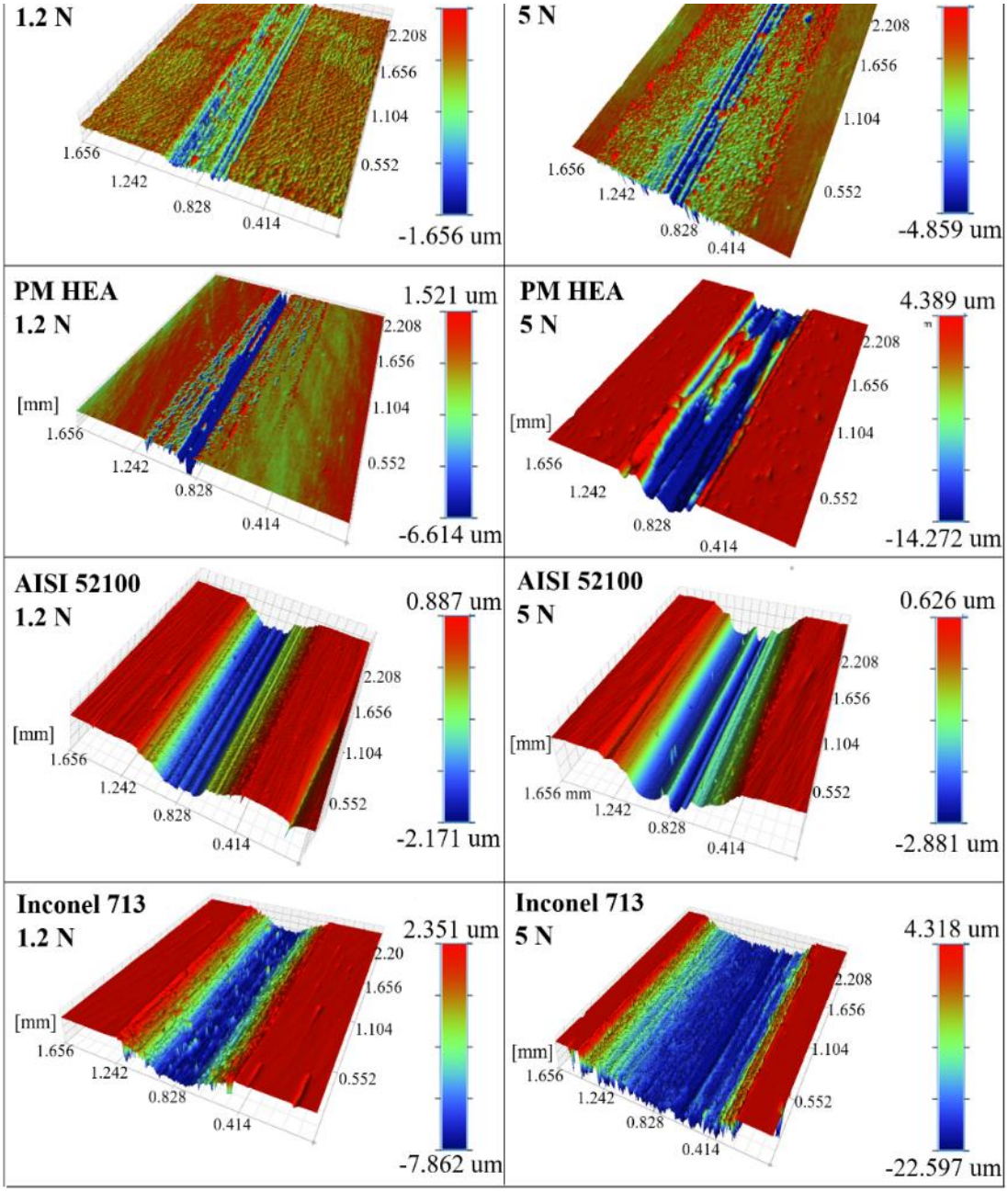

Fig. 42. Three-dimensional wear track profiles of the Cast HEA, PM HEA, AISI 52100 and Inconel 713 formed under 1.2 N and 5 N load forces. Note that the colored scales actually refer to different values in µm.

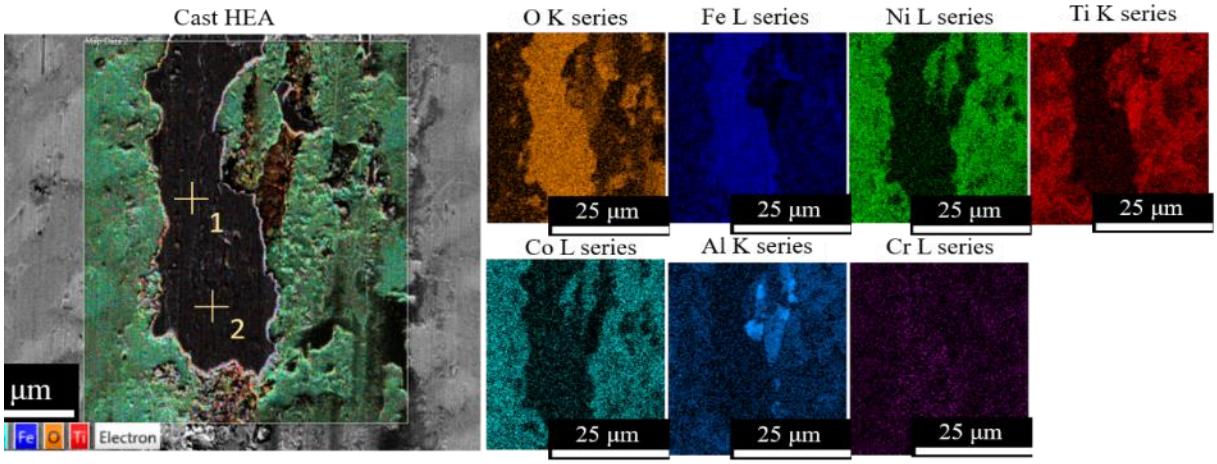

Fig. 43. EDS map on wear track of Cast HEA under 1.2N load.

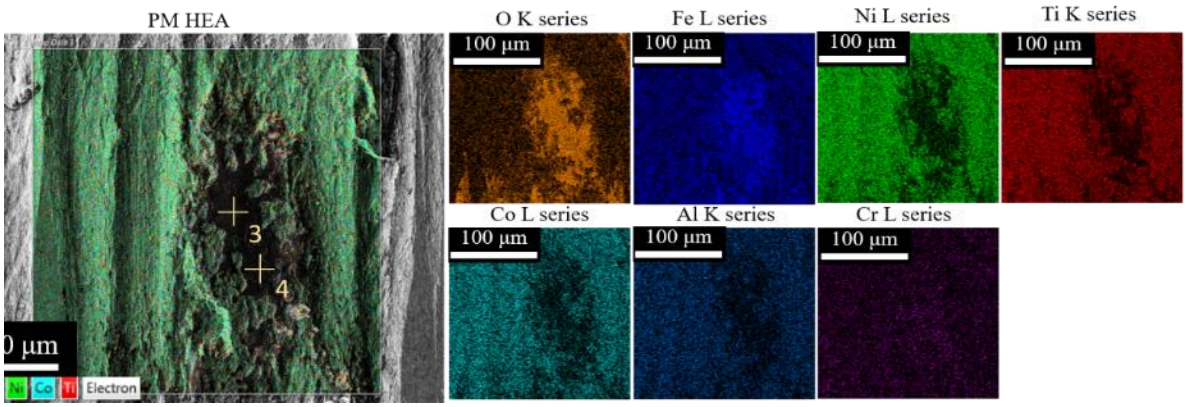

Fig. 44. EDS map on wear track of PM HEA under 5N load.

	Average point analysis	
Element	Cast HEA (Points 1 and 2)	PM HEA (Points 3 and 4)
O	**57.8 ± 1.2**	**58.3 ± 1.0**
Fe	**40.7 ± 1.1**	**38.9 ± 0.5**
Cr	1.0 ± 0.1	1.9 ± 0.4
Ti	0.5 ± 0.0	0.9 ± 0.3

Table 5. Average point analysis of adhesive features on wear track of Cast and PM HEAs.

The hardness profiles of the worn surfaces after tribological tests in as-sintered and as-cast HEAs were investigated to analyze possible strain hardening effects. This is shown in Fig. 45. These might play a role on the tribological properties and will be discussed.

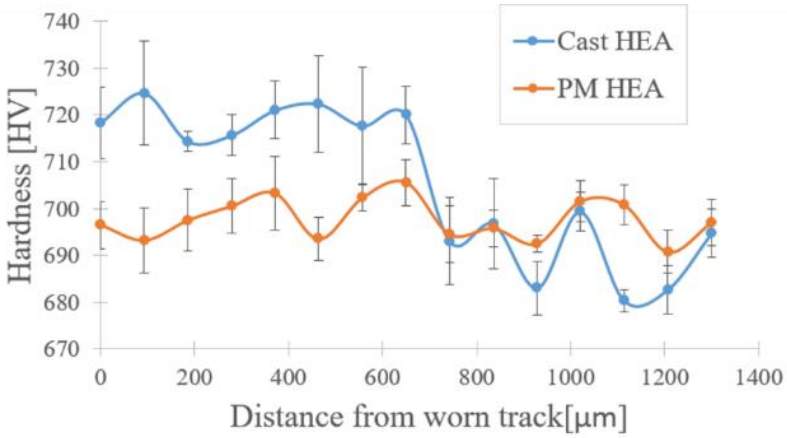

Fig. 45 Plot showing microhardness profiles after wear tests on 5 N load for PM and Cast HEAs. The local hardness under the worn track of Cast HEA increased compared to base material (higher distances) due to local strain hardening.

As can be seen in Fig. 46, PM HEA possesses an interesting combination of low specific wear rate under 1.2 N load and high flexural strength allied with high hardness. The PM HEA is superior in terms of mechanical bending strength, presenting a significant increase in strength, as compared to its cast counterpart, while retaining an identical wear rate at 1.2 N. The results of PM HEA's flexural strength are still superior to traditional tool steels, such as AISI 52100 [166], AISI A681 O1 [167] and AISI M2 [157,168]. Increasing the load to 5 N during the wear

test causes a significant reduction in its wear properties, whereas the Cast HEA wear rate remains relatively unchanged, maintaining its enhanced tribological properties.

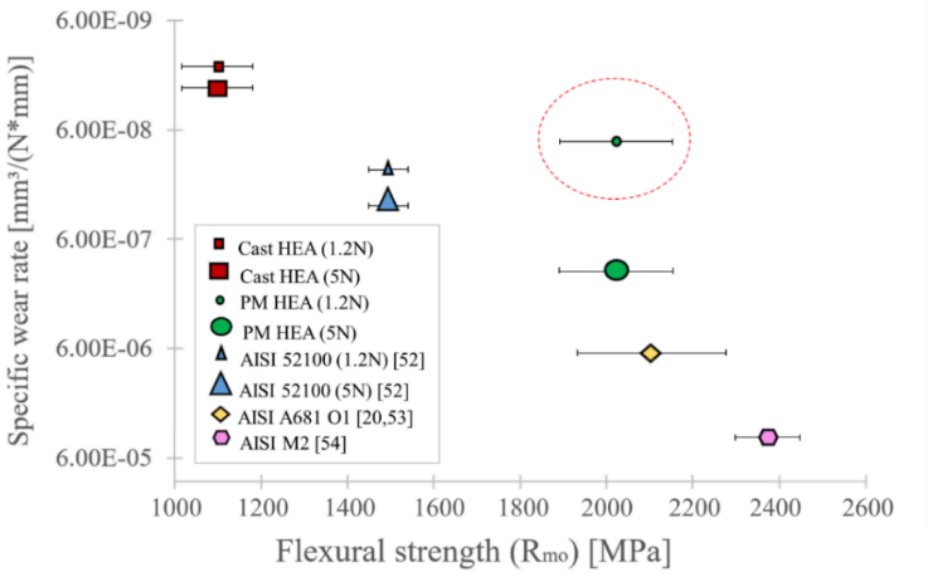

Fig. 46. Specific wear rates vs. flexural strengths (R_{mo}) of both the PM and the Cast HEA in comparison with conventional tool steels. Data for tool steels are taken from [157,166–168].

5.1.5 Microstructures and basic mechanical properties after heat treatments

The microstructural evolution upon heat treatments of the PM and Cast HEAs were studied. The alloys were submitted to heat treatments at 1000 °C for 5 h, and, subsequentially, at 750 °C for further 5 h. The XRD analyses of the $Al_{0.2}Co_{1.5}CrFeNi_{1.5}Ti$ produced by PM and casting and after each heat treatment are exhibited in Fig. 47. The results are summarized in Table 6 for better elucidation.

PM HEA [Å]									
	as-sintered PM			PM HEA 1000 °C			PM HEA 1000 °C+750 °C		
	a_{XRD}	c_{XRD}	vol.%	a_{XRD}	c_{XRD}	vol.%	a_{XRD}	c_{XRD}	vol.%
FCC matrix	3.58	-	89.3	3.59	-	81.8	3.59	-	73.3
TiC	4.30	-	8.0	4.30	-	11.9	4.31	-	13.4
BCC	2.93	-	2.7	2.91	-	6.3	2.92	-	11.5
η-Ni_3Ti	-	-	-	-	-	-	5.10	8.31	1.8
Cast HEA [Å]									
	as-cast			Cast HEA 1000 °C			Cast HEA 1000 °C+750 °C		
FCC matrix	3.63	-	47.8	3.61	-	67.1	3.62	-	48.2
Laves	4.79	7.79	30.6	4.79	7.79	10.5	4.79	7.79	25.4
sigma (σ)	8.88	4.57	11.5	8.87	4.55	2.8	8.86	4.54	5.9
BCC	2.93	-	10.1	2.94	-	17	2.95	-	18.1
η-Ni_3Ti	-	-	-	5.1	8.31	2.6	5.09	8.30	2.4

Table 6. Lattice parameters of HEAs before and after heat treatments taken by XRD analyses.

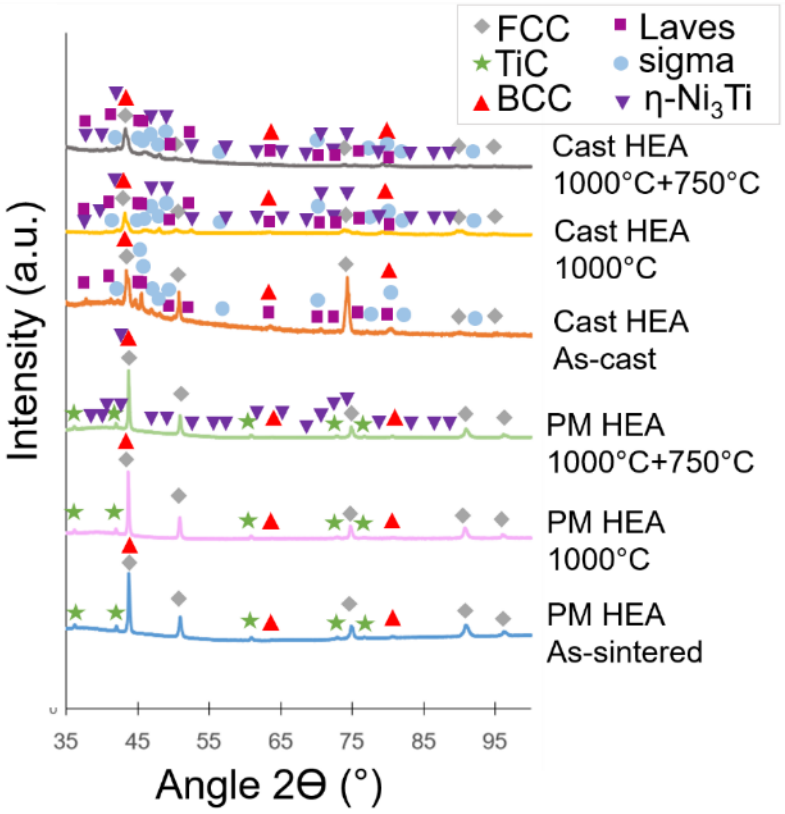

Fig. 47. XRD patterns and phase composition of PM HEA and Cast HEA in all states.

The microstructures of as-sintered PM HEA and correspondent microstructures upon following heat treatments are shown in Fig. 48.

The PM alloy, even after both heat treatments, maintains a nano-sized microstructure and stable grain size of all phases (as evidenced later by EBSD).

In contrast, microstructures of the cast counterpart and respective microstructures after heat treatments are exhibited in Fig. 49 and show significantly larger grain sizes of the FCC matrix, and distribution of the remaining phases in smaller grain sizes, such as for BCC, Laves, sigma, and η-Ni_3Ti detected by XRD. The phases are identified by arrows on the SEM images. The dendritic microstructure is partially present even after 10 h of heat treatments. The presence of needle-like phase and globular precipitates in interdendritic areas are visible in Fig. 49c,e. The phase composition and grain size average of each phase present in all states were assessed by EBSD.

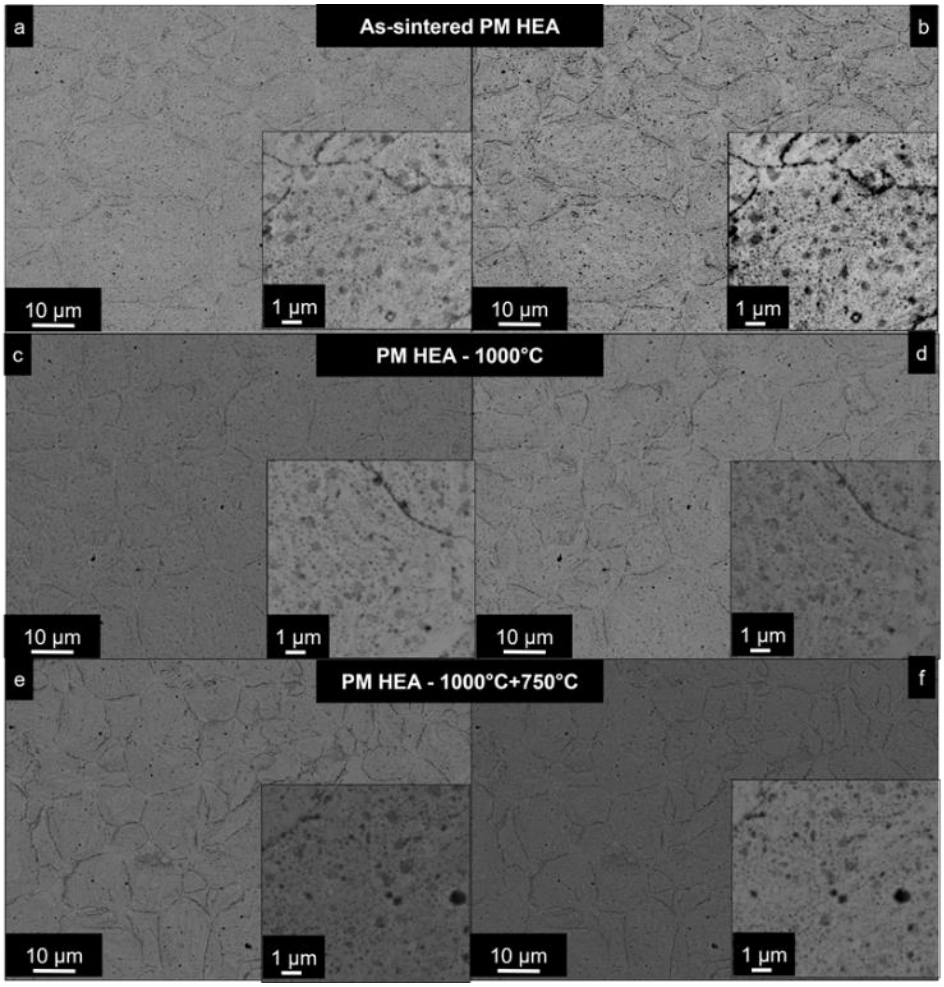

Fig. 48 SEM images of microstructures of PM HEAs. a,b) micrographs of as-sintered state in SE and BSE modes, respectively. c,d) PM HEA subjected to 1000 °C for 5h in SE and BSE detectors. e,f) PM HEA after additional 750 °C for 5 h (in order: SE and BSE modes).

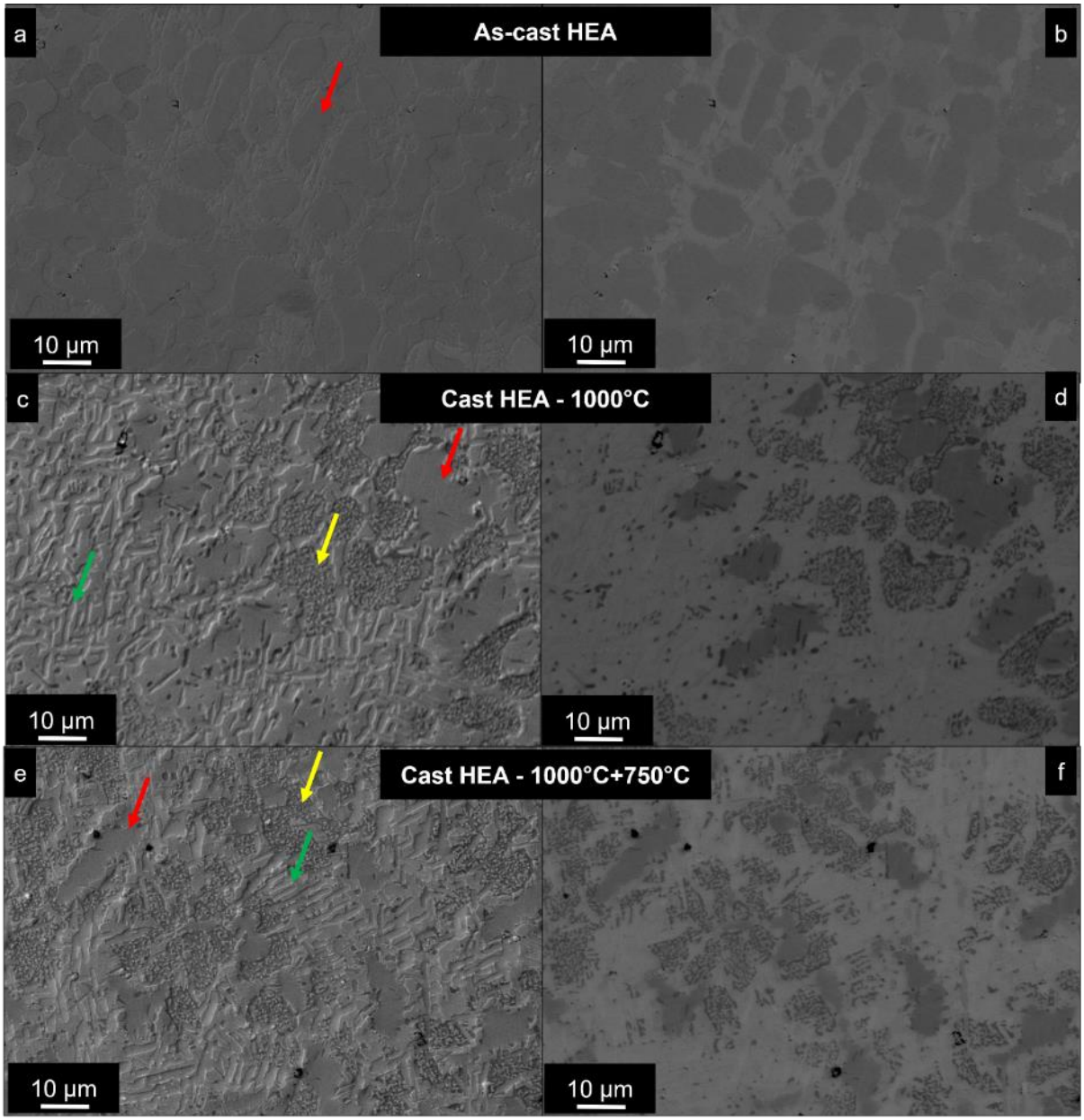

Fig. 49 SEM images of microstructures of Cast HEAs. a,b) images of as-cast HEA in SE and BSE modes, respectively. c,d) Cast HEA subjected to 1000 °C for 5 h (SE and BSE modes). e,f) Images of cast HEA upon additional heat treatment at 750 °C for 5 h (SE and BSE detectors, in order). Red arrows represent the dendritic phase and green arrows the needle-like phase. The yellow arrows point to globular-like phases.

For quantitative assessment of the microstructures in each state after heat treatments for both PM and Cast materials, EBSD analyses have been performed. The results regarding the phase distribution, orientation and grain sizes of the PM and cast alloys are exhibited in Fig. 50 and Fig. 51, respectively.

Upon heat treatment at 1000 °C for 5 h, the PM alloy possesses a distribution of fine nano-sized grains of FCC, BCC and TiC. The average grain size of the FCC matrix is 0.88 µm. The BCC phase's correspondent average grain size was measured to be 0.64 µm. Since it is clear that there are only three phases on this PM HEA-1000, confirmed by XRD and SEM analysis, the white areas correspond TiC and were calculated to possess average size of 0.55 µm. The random orientation of the grains, despite the uniaxial pressing during SPS, is clearly maintained.

After additional heat treatments at 750 °C for more 5 h, the PM alloy exhibits a very fine matrix with average size of FCC grains of 1.4 µm, as evidenced by EBSD analysis and SEM images. The BCC phase possesses an average grain size of 0.68 µm. The TiC is expected to possess and average grain size of 1.3 µm. Due to EBSD resolution constraints, the η-Ni_3Ti phase found by XRD is not visible.

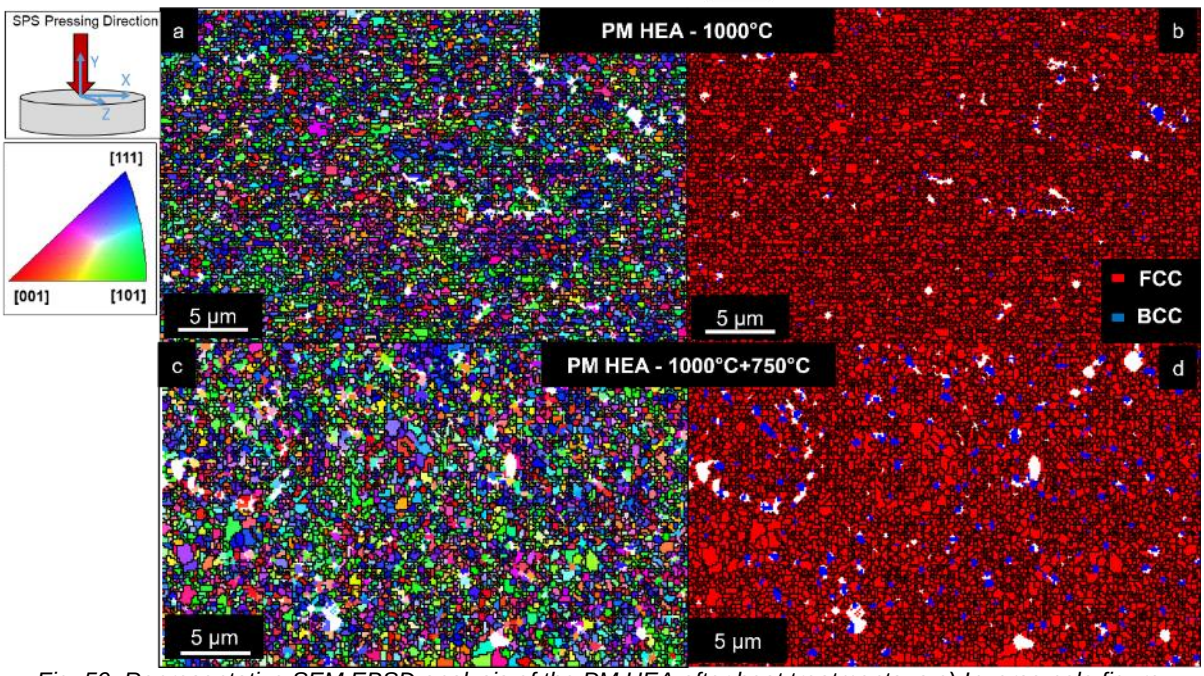

Fig. 50. Representative SEM EBSD analysis of the PM HEA after heat treatments. a,c) Inverse pole figure showing grain orientation maps with reference direction perpendicular to the SPS compaction direction denoted as Z in the image for PM HEA-1000 and PM-HEA-750,respectively. b,d) Phase map showing distribution of BCC in FCC matrix. The white regions correspond to TiC.

The EBSD analyses of present phases in Cast HEA after heat treatments are shown in Fig. 51.

Upon heating at 1000 °C for 5 h, the Cast HEA-1000 possesses the same FCC phase present in the as-cast state (confirmed by crystallographic properties already identified by XRD), with grain size average of 22.3 µm. The BCC phase significantly grew compared to the as-cast state, now exhibiting an average grain size of 21.5 µm. In the as-cast state, the BCC grain size was not possible to be assessed by EBSD due to the resolution constraints of the EBSD method. The nano-sized phase was only possible to be identified by TEM (Fig. 34 and Fig. 37). The Laves phase average grain size was calculated to be 8.2 µm.

The white regions in the EBSD maps correspond to non-indexed areas that were impossible to resolve accurately due to the resolution threshold of the method. They may possibly correspond to a mixture of nano-sized phases already identified in the TEM images (namely σ, or the needle-like nano-sized Laves phase, documented in Fig. 34a and additionally η-Ni_3Ti phase identified by XRD).

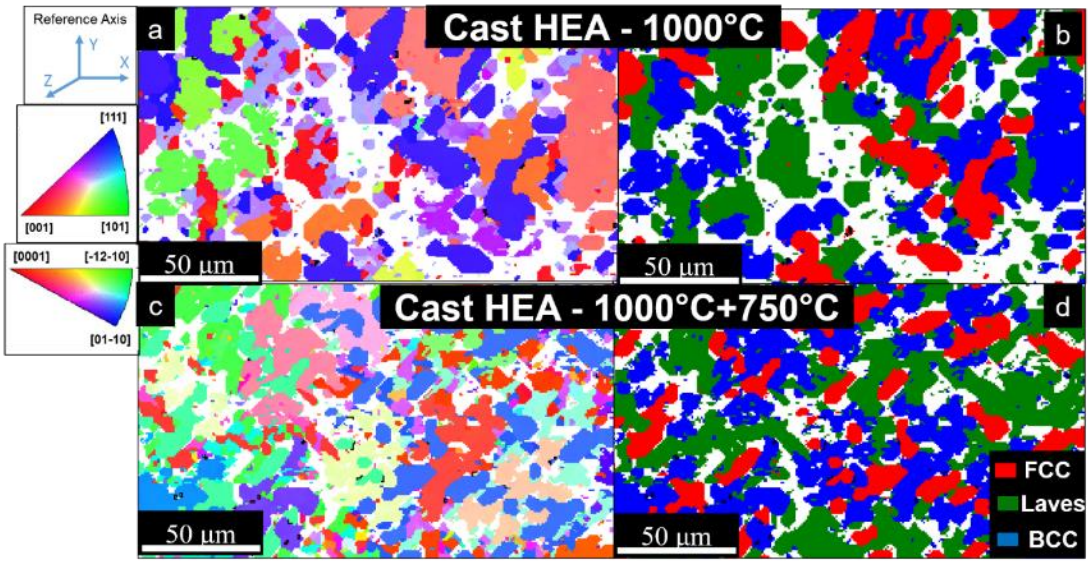

Fig. 51. Representative SEM EBSD analysis of the PM HEA after heat treatments. a,c) Inverse pole figure orientation map with reference direction Z denoted in the image for Cast HEA-1000 and Cast HEA-750, respectively. b,d) Phase map showing distribution of Laves and BCC phases in FCC matrix for Cast HEA-1000 and Cast HEA-750, respectively.

After additional heating at 750 °C for more 5 h, the FCC phase exhibits an average grain size of 15.3 µm. The BCC phase shows an increase average grain size of 23.17 µm. The Laves phase shows a relatively stable average grain size of approximately 9.1 µm.

After both heat treatments, the FCC phase still shows a preferential orientation due to the remaining effects from the casting process, explained on the previous section for the as-cast state. The chemical composition of each phase in the cast alloys were done by point analyses using SEM/EDS method. The results are shown in Table 7.

Cast HEA after heat treatments								
Phase	**FCC**		**BCC**		**Needle-like phase**		**Globular phase**	
Alloy	**1000°C**	**1000°C +750°C**	**1000°C**	**1000°C +750°C**	**1000°C**	**- 1000°C +750°C**	**1000°C**	**1000°C +750°C**
Al	9.1	9.1	10.4	5.3	1.3	1	1.5	2.2
Ti	15.8	14.4	19.9	**17.5**	**19.4**	**18.1**	8.3	8.6
Cr	10.3	11.2	6.6	10.3	4.7	7.3	**22.7**	**21.2**
Fe	**16.1**	**14.6**	8.7	12.7	8.5	10.9	**23.1**	**23.2**
Co	**23**	**25.3**	25.4	**25**	**22.9**	**22.9**	**25.1**	**26.1**
Ni	**25.7**	**25.4**	29	**29.2**	**43.2**	**39.8**	19.3	18.7

Table 7. Chemical composition of each phase present in the Cast HEA after heat treatments.

Both FCC and BCC chemical compositions correspond to very similar values exhibited before in the as-cast state (Table 2). The needle-like phases shown in Fig. 49 are rich in Ti, Co and Ni, and possess very similar chemical composition of the Laves needle-like phase present in the as-cast state. The globular phases, also exhibited in Fig. 49, are Cr-, Fe- and Co- rich, similar to the ones of sigma phase present in the as-cast state (Table 2).

The composition of each phase in the PM alloy was not possible to be measured due to their very fine grain sizes, below the resolution limit of the EDS method. However, they were

analyzed already by TEM in the as-sintered state. The XRD results together with SEM and EBSD characterization confirm that the same phases are present after heat treatments, therefore suppressing the need to further investigation by EDS/TEM. The only additional peak from XRD corresponds to η-Ni_3Ti, which also has a nano-sized scale, since it was not detected by SEM imaging and sequential EBSDs.

The basic mechanical properties were assessed by Vickers hardness and nanoindentation hardness (for calculation of elastic modulus). The results are exhibited in Table 8.

	Hardness [HV]	E [GPa]
As-Cast	682 ± 10	210 ± 20
Cast HEA - 1000°C	606 ± 11	236 ± 15
Cast HEA - 1000°C+750°C	641 ± 5	245 ± 14
As-sintered PM HEA	712 ± 3	258 ± 10
PM HEA - 1000°C	675 ± 6	252 ± 6
PM HEA - 1000°C+750°C	706 ± 7	266 ± 7

Table 8. Average hardness and elastic modulus of PM and Cast HEAs before and after heat treatments.

There is an evident decrease in hardness of both PM and Cast HEAs after being submitted to 1000 °C, followed by an increase in hardness after 750 °C. The elastic modulus of the PM HEA is shown to be steady before and after heat treatments. In contrast, Cast HEA shows a lower elastic modulus (210 GPa) in the as-cast state than compared to all other samples, but after both heat treatments, the elastic modulus is increased to almost the same values of the PM alloys. The underlying reasons for these results are further discussed in the discussion.

5.2 Optimization of mechanical alloying parameters of refractory high entropy alloys

An effective mechanical alloying of different powders is achieved upon selecting optimum conditions for powder milling. By varying milling times, the powder may be evaluated in terms of its mechanical alloying efficiency, powder characteristics and even possible contamination levels. The next section will deal with the results of the effect of milling times variation on the aspects of selected powders' morphology.

5.2.1 Influence of the milling time on the powders properties

The RHEA $Al_{0.3}NbTa_{0.8}Ti_{1.5}V_{0.2}Zr$ (in stoichiometric ratio) was subject to different milling times – while keeping the same milling setup conditions. Milling was carried out for 1 h, 3 h, 5 h, 10 h, 20 h, 30 h, 40 h and 50 h (hence, the samples are named RMA-x, where x is the specific time used for milling). The non-milled powders (RMA-0h) are used for comparison. XRD patterns of all conditions can be seen in Fig. 52.

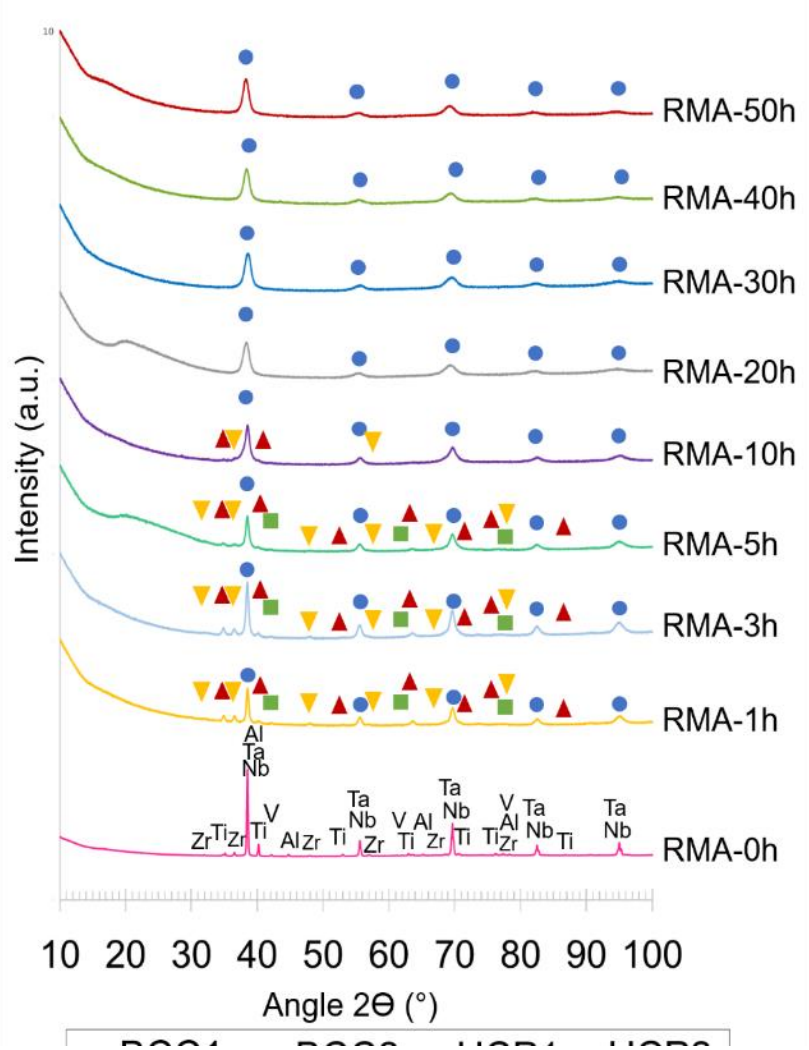

Fig. 52. XRD patterns of $Al_{0.3}NbTa_{0.8}Ti_{1.5}V_{0.2}Zr$ powders after different milling times.

The lattice parameters of the mechanically alloyed powders are shown in the table below.

	RMA_1h			RMA_3h			RMA_5h		
	a_{XRD}	c_{XRD}	wt.%	a_{XRD}	c_{XRD}	wt.%	a_{XRD}	c_{XRD}	wt.%
BCC1	3.3	-	56.2	3.31	-	58.6	3.31	-	87.7
BCC2	3.03	-	2.9	3.03	-	3.3	3.03	-	0.4
HCP1	3.23	5.14	23.1	3.24	5.14	20.7	3.24	5.13	10.8
HCP2	2.95	4.68	17.8	2.95	4.68	17.4	2.94	4.68	1.1
	RMA_10h			RMA_20h			RMA_30h		
BCC1	3.31	-	94.3	3.31	-	100.0	3.32	-	100.0
HCP1	3.24	5.13	4.9	-	-	-	-	-	-
HCP2	2.95	4.68	0.8	-	-	-	-	-	-
	RMA_40h			RMA_50h					
BCC1	3.32	-	100.0	3.33	-	100.0			

Table 9. Lattice parameters of the mechanically alloyed powders detected by XRD analysis.

RMA-0h show peaks relative to the non-milled powders. These are Al, possessing a = 4.05 Å, space group Fm-3m, in 1.9 wt. %; Nb with a = 3.30 Å, space group Im-3m, in 22.2 wt. %; Ta with a = 3.31 Å, space group Im-3m, in 34.6 wt. %; Ti with a = 2.95 Å, c = 4.68 Å, space group

P63/mmc, in 17.1 wt. %; V with a = 3.03 Å, space group Im-3m, in 2.4 wt. %; Zr owning a = 3.23 Å, c = 5.15 Å, space group P63/mmc, in 21.8 wt. %. This is in good agreement with the values in wt. % for this alloy. Solid solution forming reactions should occur upon the start of the milling process of the mixed powders [169].

After 1 h of mechanical milling, RMA-1h exhibits the development of four different phases: BCC1, BCC2, HCP1 and HCP2. The major phase is BCC1 solid solution, relating to the peaks of Nb and Ta before mechanical alloying. After milling, these peaks completely overlap due to the very similar crystal structures of both elements; and probably dissolution of these elements in the lattices of one another, at some extent, caused by mechanical alloying. TEM analysis would prove helpful to evaluate if this corresponds to a single BCC solid solution, as shown by XRD analysis after Rietveld refinements.

The second most abundant phase is the HCP1, which its peaks are related to the ones of the pure non-milled Zr, however the peaks are called differently due to the fact that the present crystal structure after milling might contain elements which were mechanically alloyed to the crystal lattices, changing the nature of the powder, which now is deformed and owns a different chemical composition than the pure powder. Note that even the wt.% referent to HCP1 is different than that of pure Zr. HCP2 appears as well. It is clear that the Al element was successfully mechanically alloyed to the other powders in its total content already after 1 h, due to the absence of peaks' referent to this element.

After 3 h of milling, BCC1, HCP2 and BCC2 are present. After 5 h of milling, BCC1 is significantly increased its content. Concurrently, the remaining phases substantially decreased. After 10 h of milling, the BCC1 is clearly dominant, reaching almost the total weight of the alloy; BCC2 is completely dissolved in the lattices of the other phases. HCP1 is present. After 20 h of milling, a single BCC1 is achieved. Subsequent milling for 30 h, 40 h and 50 h does not induce any phase changes.

The SEM analyses of the milled powders are shown in Fig. 53 for milling times from 0 to 10 h, and Fig. 54 for 20 to 50 h. The respective EDS maps taken from the cross-section of each milled powder is shown in the last column of the set of micrographs.

Prior to mechanical alloying, the powders exhibited diverse morphologies and sizes, as visible in Fig. 53.a,b,c,1. However, after only 1 h of milling, the powders start to acquire similar particle sizes, and are effectively being mechanically alloyed, with significant deformation and alloying of all elements, which is visible by the EDS maps of the cross section of these powders in 1 h of milling (Fig. 53.2).

Further 3 and 5 h of milling bring significant alloying of all elements and homogenization, however it is possible to still observe segregation of elements, specially Zr and Ti, which possess HCP crystal structures.

After 10 h of milling, one can observe that the powders start to have internal cracks (Fig. 53.5) and fracture into smaller particles (Fig. 53.o). Concurrently, the powders are virtually fully homogeneously alloyed, and no significant segregation can be noticed (Fig. 53.5).

From 20 h milling, one can expect again a more homogeneous distribution of particle sizes in a globular morphology (Fig. 54.a,b,c,1), with significant decrease in size as compared to the 10 h state.

Milling times of 30 and 40 h do not show significant variations in powder morphology and sizes, while the obvious homogenization of the fully mechanically alloyed powders is guaranteed.

After 50 h of milling, it is possible to see that some particles were elongated (Fig. 54.l), but the powders are mostly of globular morphology.

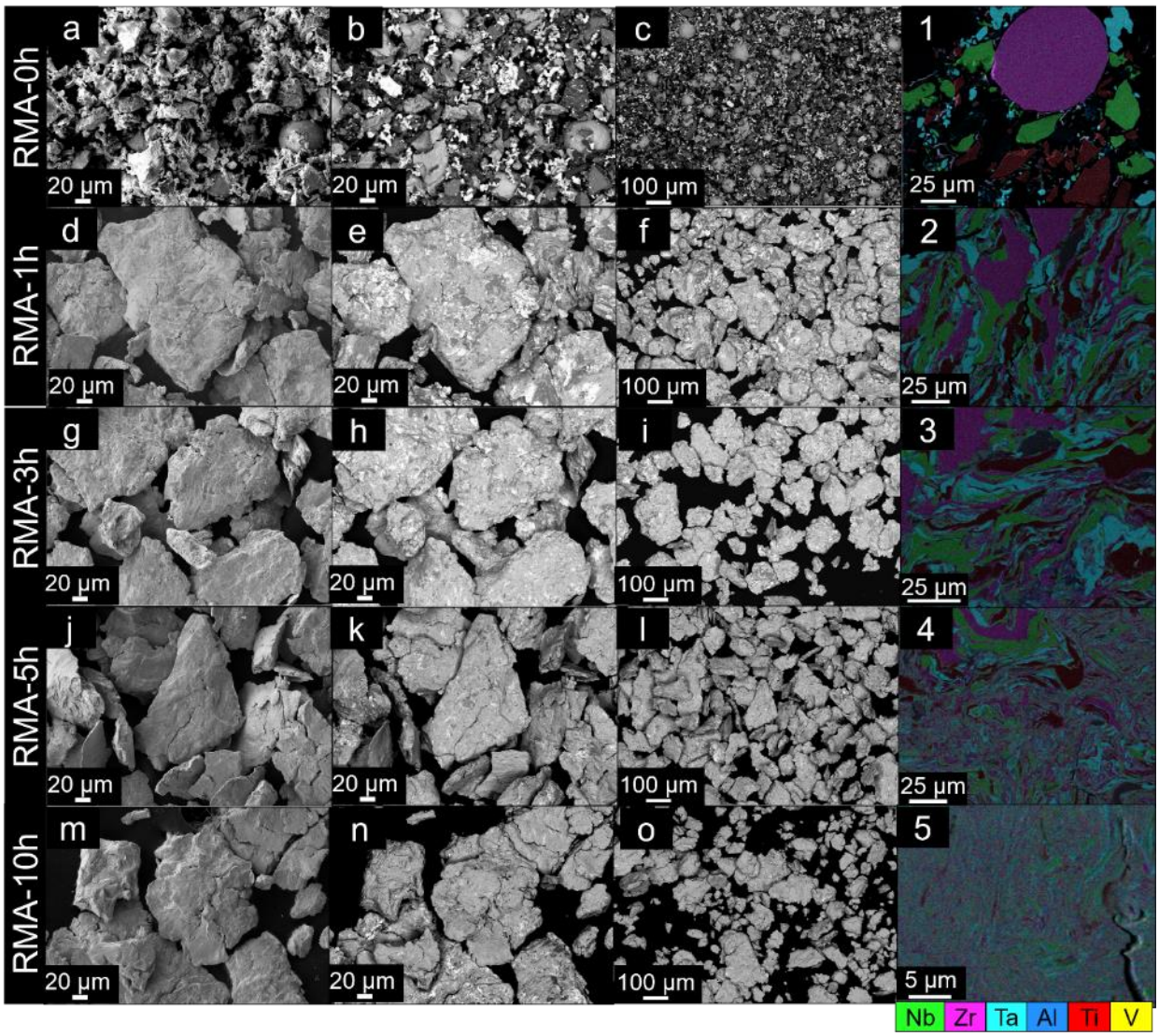

Fig. 53. SEM images of $Al_{0.3}NbTa_{0.8}Ti_{1.5}V_{0.2}Zr$ powders after different milling times from 0 to 10. The milling times are described in the beginning of each row of images. a,d,g,j,m) SEM micrographs using SE detector showing powders in detail after each milling from 0 to 10 h, in order. b,e,h,k,n) Corresponding SEM images using BSE detector showing powders in detail after each milling. c,f,i,l,o) SEM images using BSE mode to exhibit an overview of the powders in lower magnifications. 1,2,3,4,5) EDS maps with all elements in color are shown, taken from the cross-section of each powder milled from 0 to 10 h, respectively.

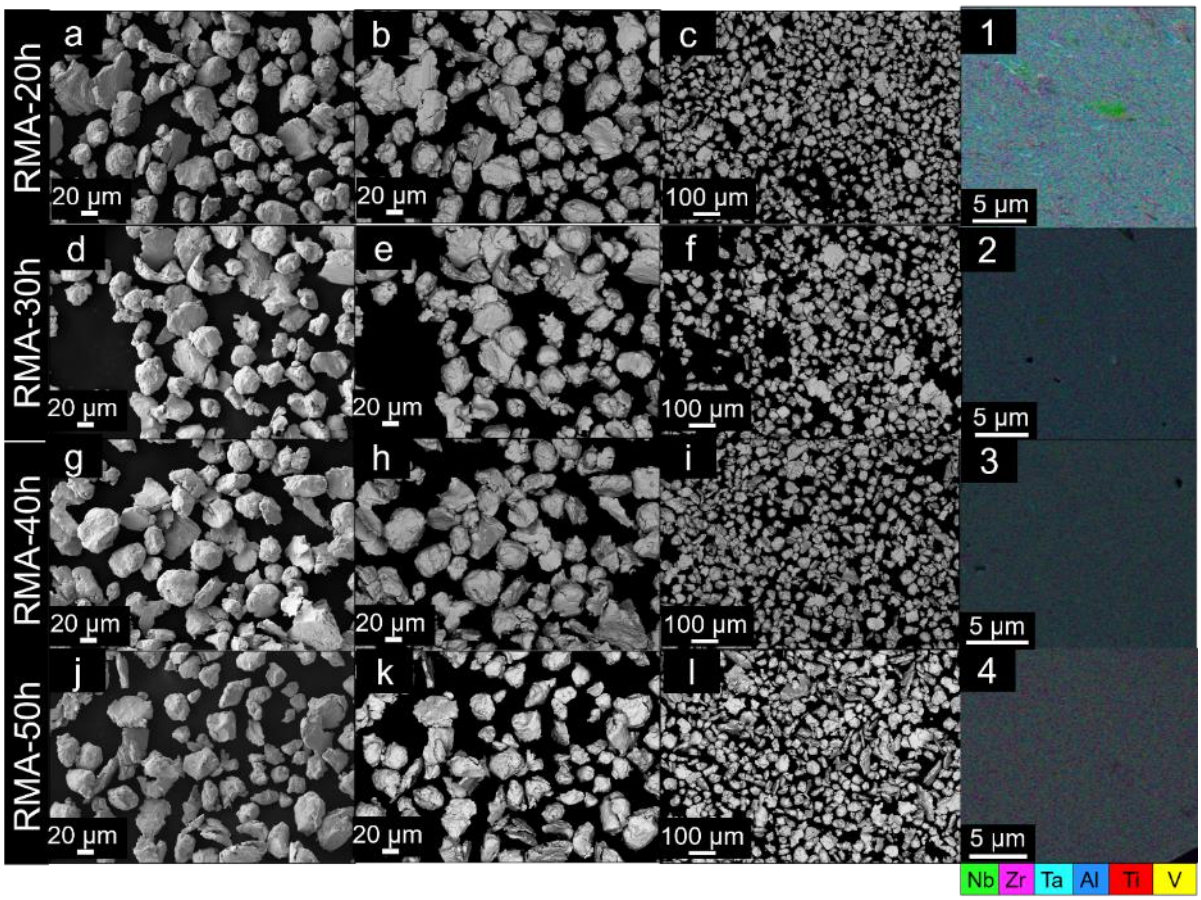

Fig. 54. SEM images of $Al_{0.3}NbTa_{0.8}Ti_{1.5}V_{0.2}Zr$ powders after different milling times from 20 to 50. The milling times are described in the beginning of each row of images. a,d,g,j) SEM micrographs using SE detector showing powders in detail after each milling from 20 to 50 h, in order. b,e,h,k) Corresponding SEM images using BSE detector showing powders in detail after each milling. c,f,i,l) SEM images using BSE mode to exhibit an overview of the powders in lower magnifications. 1,2,3,4) EDS maps taken from the cross-section of each powder milled from 20 to 50 h, respectively.

5.3 Optimization of sintering process parameters of refractory high entropy alloys

After mechanical alloying by ball milling, sintering is the following step for densification of the material in solid state. The **optimization** of the sintering process is discussed below.

5.3.1 Effect of the milling time variation on the sintered bulks

The RHEA $Al_{0.3}NbTa_{0.8}Ti_{1.5}V_{0.2}Zr$ was milled for different times (section 5.2.1) and different milled powders were selected in order to analyze the effect of the milling time variation in the spark plasma sintered bulks, while keeping the same conditions of sintering, such as heating rates, vacuum level, dwell times at the maximum temperature and cooling rates.

The selected milling times were 3 h, 10 h, 30 h and 50 h. The bulks were named as SRMA-3h, SRMA-10h, SRMA-30h, SRMA-50h. XRD patterns of the bulks are shown in Fig. 55.

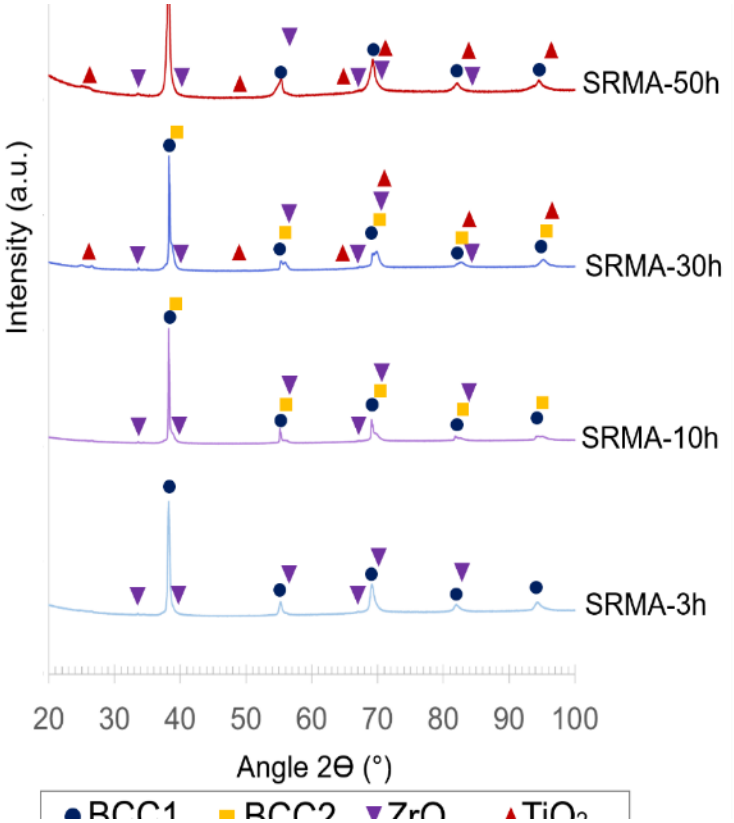

Fig. 55. XRD patterns of sintered bulks using powders subject to different times of milling.

The sintered bulk SRMA-3h show a main BCC1 phase and a small fraction belonging to the crystal structure of ZrO. On the other hand, SRMA-10h exhibit two BCC phases, instead of one. This is evidenced by the additional peaks in very close angles from those of BCC1 - thus owning very close lattice parameters to the ones of the BCC1 - depicted by the yellow squares in Fig. 55. The exact lattice constants of each phase are found in the table below.

	BCC1		BCC2		ZrO (Fm-3m)		TiO2 (I41/amd)		
	a_{XRD}	wt.%	a_{XRD}	wt.%	a_{XRD}	wt.%	a_{XRD}	c_{XRD}	wt.%
SRMA-3h	3.32	98	-	-	4.62	2	-	-	-
SRMA-10h	3.32	52.7	3.3	43.3	4.62	4	-	-	-
SRMA-30h	3.32	74.6	3.29	20.7	4.61	4.3	3.8	9.56	0.4
SRMA-50h	3.31	88.7	-	-	4.6	6.8	3.79	9.55	4.5

Table 10. Lattice parameters of the sintered bulks utilizing powders with different times of milling.

SRMA-30h shows BCC1 matrix; the ZrO fraction remains relatively unchanged. Additionally, the crystal structure of Ti_2O appears, belonging to the tetragonal crystal system and I41/amd space group. Finally, SRMA-50h shows the main BCC1, while BCC2 is interestingly absent. The remaining fraction corresponds to oxides formation. The ZrO fraction increases.

The microstructures of the sintered bulks are revealed in Fig. 56. The micrographs reveal a BCC matrix with dispersed oxides on all materials, especially around the grain boundaries, denoted by the darker particles. The SRMA-3 shows fewer oxides than all other conditions, in agreement with XRD results. Further milling significantly increases the oxides content,

especially for 30 h and 50 h, where two crystal structures composed of oxides are present (from cubic and tetragonal systems). EDS performed in the BCC matrix are shown below.

[at. %]	**SRMA-3h (BCC1)**	**SRMA-10h (BCC1)**	**SRMA-30h (BCC1)**	**SRMA-50h (BCC1)**
Al	5.4 +- 0.2	6.1 +- 0.1	6.0 +- 0.2	6.1 +- 0.1
Ti	29.4 +- 1.2	31.0 +- 0.2	30.3 +- 0.1	29.8 +- 0.3
V	3.9 +- 0.6	4.0 +- 0.4	4.5 +- 0.1	4.8 +- 0.1
Zr	18.9 +- 1.2	20.5 +- 0.3	19.3 +- 0.3	20.5 +- 0.1
Nb	23.0 +- 0.8	20.2 +- 0.1	19.9 +- 0.1	19.7 +- 0.3
Ta	19.4 +- 1.2	18.3 +- 0.1	18.3 +- 0.1	18.0 +- 0.3
Fe	-	-	1.8 +- 0.1	2.2 +-0.1

Table 11. Chemical compositions in at. % of the BCC matrix of sintered bulks subject to different milling times performed by SEM/EDS.

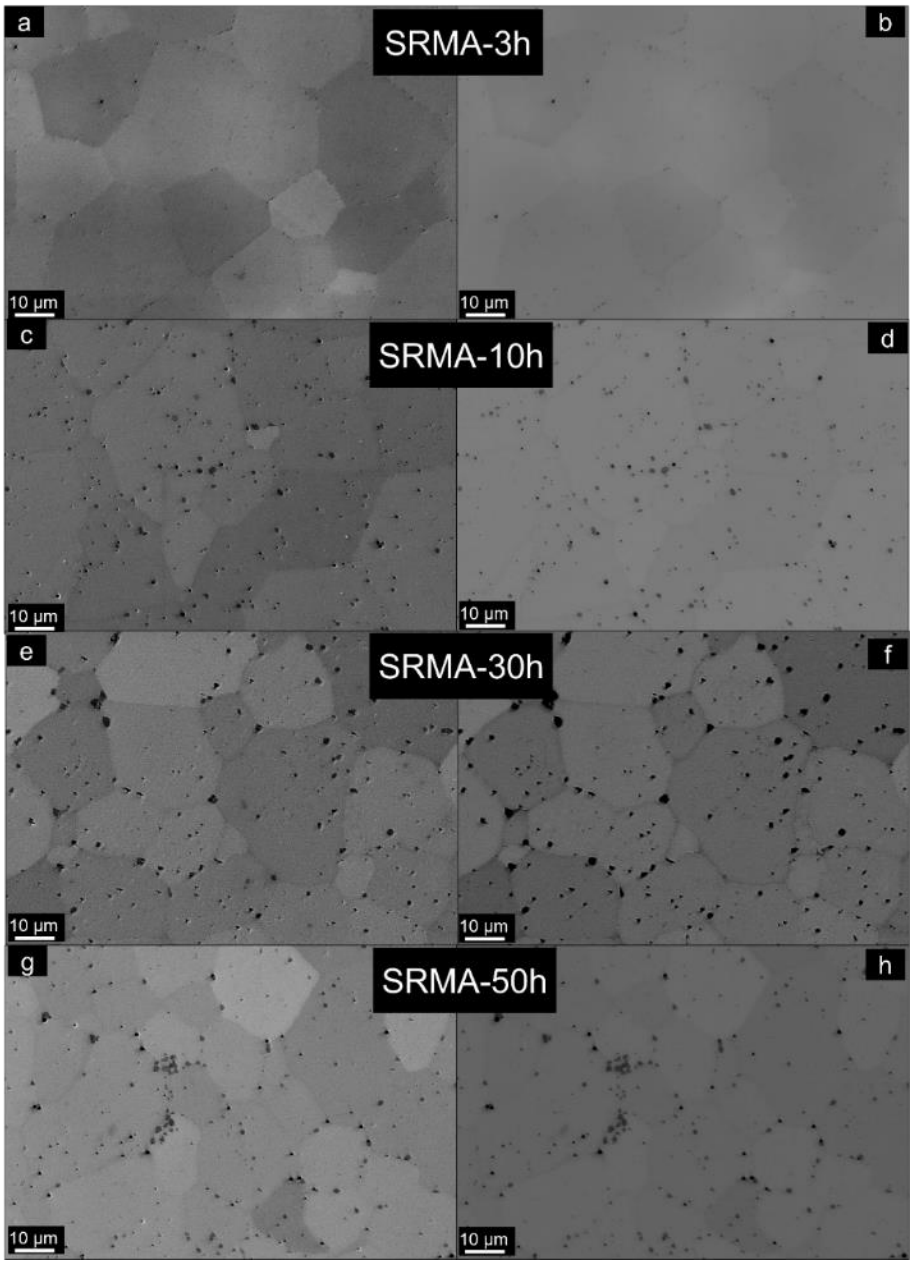

Fig. 56. SEM micrographs of the $Al_{0.3}NbTa_{0.8}Ti_{1.5}V_{0.2}Zr$ sintered bulks subject to different powder milling times in SE and BSE modes, respectively. a,b) SRMA-3h. c,d) SRMA-10h. e,f) SRMA-30h. g,h) SRMA-50h.

It is evident that the BCC1 phase possesses similar compositions for all sintered bulks. However, the presence of Fe in 1.8 at. % is manifested after 30 h of milling. The presence of Fe increases to 2.2 at. % for 50 h of milling times.

For quantitative results, EBSD was performed in all samples and can be seen in Fig. 57.

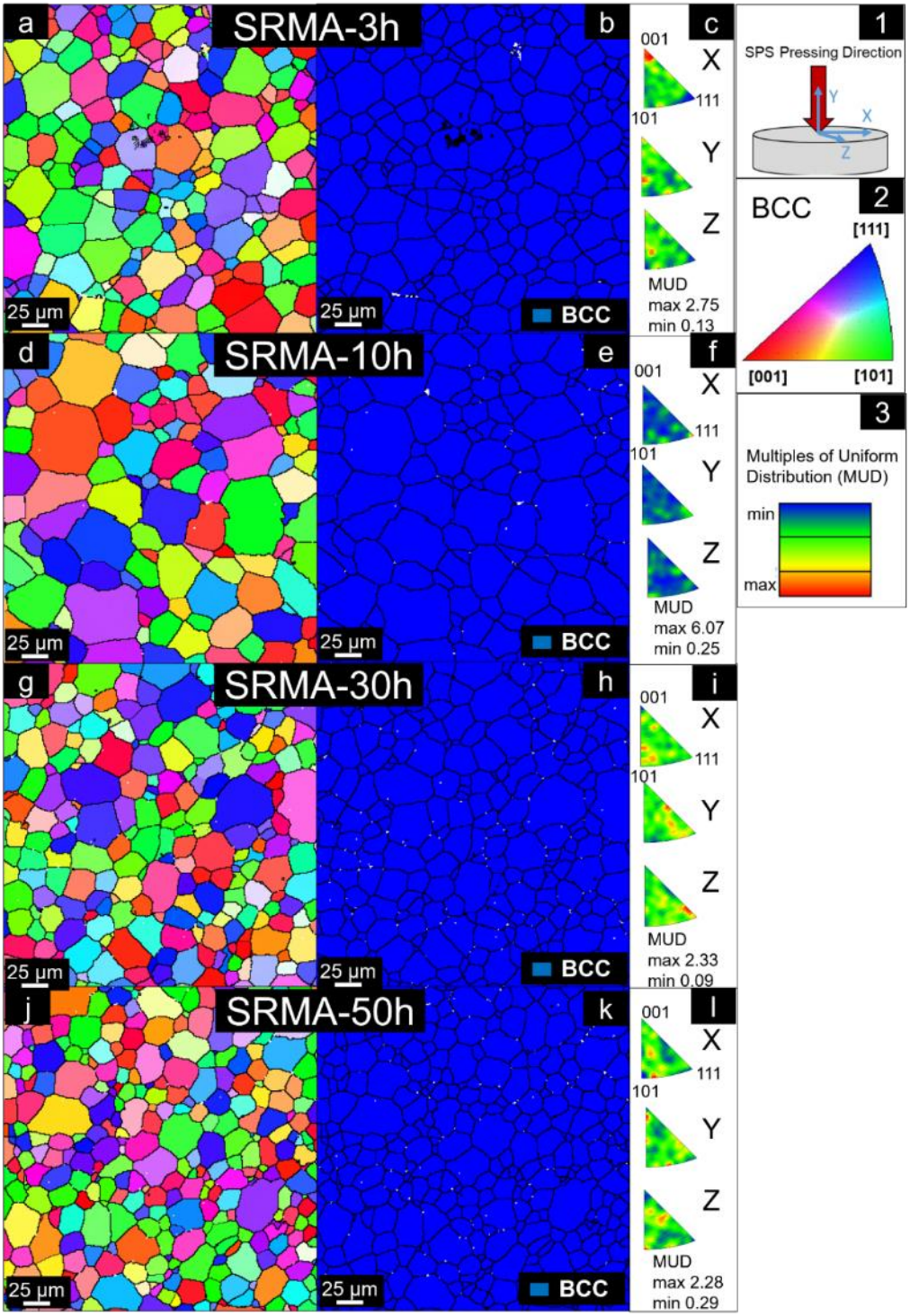

Fig. 57. Representative EBSD results of $Al_{0.3}NbTa_{0.8}Ti_{1.5}V_{0.2}Zr$ sintered bulks subject to different powder milling times. a,d,g,j) Inverse pole figure showing grain orientation maps with reference direction perpendicular to the SPS compaction direction denoted as Z in (1), for SRMA-3,10,30 and 50h, respectively. The colors represent the directions shown in (2). b,e,h,k) Phase map showing distribution of BCC grains (white regions represent dispersed oxides), for SRMA-3,10,30 and 50h, respectively. c,f,i,l) Inverse pole figures of BCC phase. MUD reference is shown in (3).

The sintered bulk SRMA-3h shows a BCC matrix possessing average grain size of 33.8 µm. The white regions shown in Fig. 58 represent the secondary phase shown in XRD, namely the ZrO. Its calculated average grain size is 1.8 µm according to four EBSD measurements in different areas. The sintered bulk SRMA-10h also exhibits a BCC matrix, with an average grain size of 37.7 µm and dispersed oxides in the white areas. The calculated average grain size of these regions corresponds to 3.3 µm. The second BCC phase shown in XRD is not possible to be assessed due to the resolution limit of the EBSD. SRMA-30h and SRMA-50h show refined microstructures in comparison with the previous states. The average grain sizes of the BCC phase in both materials are calculated to be 28.3 µm and 25.2 µm, respectively. There is a weak preferential orientation in [001] in X axis for the SRMA-3h, caused probably due to a slight plastic flow during pressing, locally in this specific region of the EBSD map. However, it is not strong enough to be relevant nor to be considered texture (as its maximum MUD is too low, in the same level of that of the other samples). The random orientation of the grains, despite the uniaxial pressing during SPS, is clearly maintained in all samples.

5.3.2 The influence of sintering temperatures on the properties of the bulks

Induced changes into the microstructure of the low-density $Al_{0.5}NbTa_{0.8}Ti_{1.5}V_{0.2}Zr$ (in stoichiometric ratio) prepared by mechanical alloying combined with hot uniaxial pressing (HP) was investigated. The RHEA was studied in terms of sintering temperature variation (at the maximum temperatures of 1200 °C, 1300 °C, up to 1600 °C), while keeping constant densification times and rates under protective atmosphere. Note that this is a different alloy than shown previously in 5.3.1. Additionally, the precursor powders of this alloy are more contaminated due to milling of Zr sponge into Zr powders (please refer to 4.2.1 section for further details). Nevertheless, the results are described here as these outcomes are part of the sintering process optimization.

The influence of the increase in sintering temperatures on the RHEAs' microstructural features, composition and basic mechanical properties was explored.

5.3.2.1 Phase prediction and microstructural characterization

Thermodynamic calculation of property diagram for $Al_{0.5}NbTa_{0.8}Ti_{1.5}V_{0.2}Zr$ (stoichiometric ratio) refractory high-entropy alloy (RHEA) was computed using ThermoCalc software in order to relate the theoretical phase changes with the experimental findings of this study. The diagram shown in Fig. 58 marks the three sintering temperatures (T_s) used for sintering by red arrows; namely 1200 °C, 1300 °C and 1600 °C. The alloys were named after the chosen sintering temperatures, as RHEA-1200, RHEA-1300 and RHEA-1600.

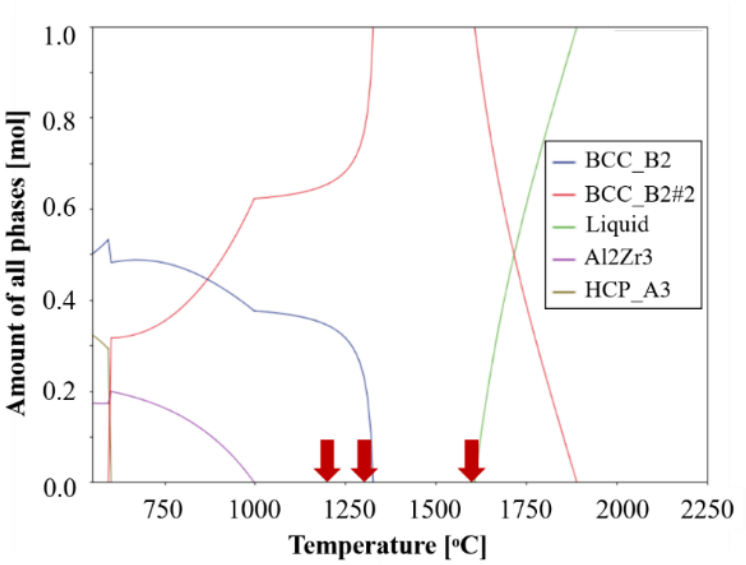

Fig. 58. Property diagram of Al0.5NbTa0.8Ti1.5V0.2Zr as mole fraction of all phases vs. temperature. TCHEA3 database from ThermoCalc software was used.

For this alloy, the melting is initiated at approximately 1600 °C. A full melting predicted to be achieved at 1875 °C. The preparation of the alloys consisted of heating the solid powders with already homogenous chemical composition to the sintering temperature, short dwell time and relatively rapid cooling. The XRD patterns of the sintered bulks at different maximum temperatures are shown in Fig. 59.

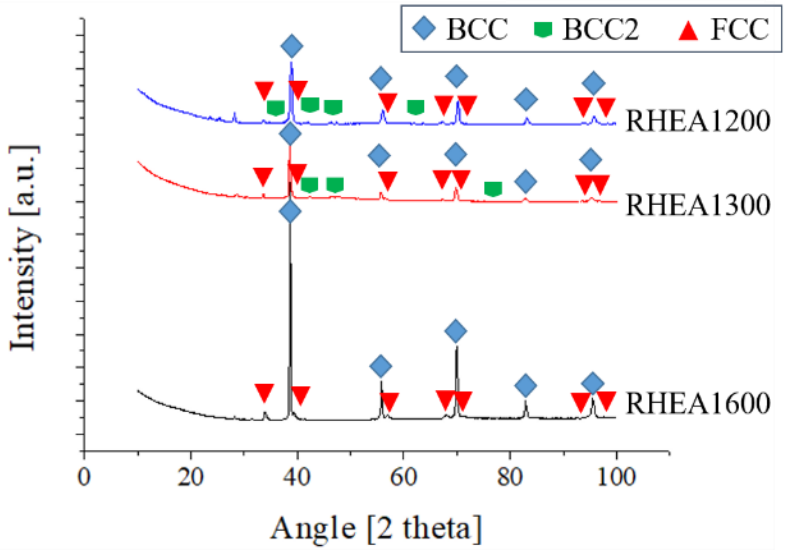

Fig. 59. XRD patterns and phase composition of $Al_{0.5}NbTa_{0.8}Ti_{1.5}V_{0.2}Zr$ RHEA after sintering under different maximum temperatures of 1200 °C, 1300 °C and 1600 °C. The FCC phase corresponds to in-situ formed carbides.

Despite the predicted liquid phase present at 1600 °C (Fig. 58), no melting was observed during sintering of RHEA-1600. The absence of liquid phase at 1600 °C, could be a consequence of short sintering time and high pressure which may increase the melting temperature [160], especially considering that the melting is only initiated at this temperature. The BCC phase formed at 1600 °C was then retained to room temperature due to relatively

rapid cooling after sintering, preventing nucleation and growth of other phases. This is in accordance to the XRD results in Fig. 59.

	BCC		BCC2		FCC	
	a_{XRD}	wt.%	a_{XRD}	wt.%	a_{XRD}	wt.%
RHEA_1600 °C	3.291	85.6	-	-	4.563	14.4
RHEA_1300 °C	3.298	89.1	3.013	6.5	4.613	4.4
RHEA_1200 °C	3.288	90.7	2.776	3.8	4.623	5.5

Table 12.Lattice parameters of the phases detected by XRD analysis.

RHEA-1600 possesses BCC matrix. FCC phase has been identified also in the alloy as having the crystal structure of a carbide, namely ZrC, from Fm-3m space group.

According to the CALPHAD prediction, for the sintering temperature of 1300 °C, the expected phase composition present in RHEA-1300 should be two BCC phases, which is in accordance with the XRD results. The alloy possesses a main BCC1 phase and, additionally, it exhibits another BCC2 phase. The carbide particles ZrC are also present on this alloy, regarded as the FCC phase. Similarly, RHEA-1200 is predicted to contain two BCC phases according to the ThermoCalc property diagram. The XRD shows that this alloy possesses a main BCC phase, a secondary BCC2, and carbides (ZrCr) regarded as FCC phase.

The SEM images of the microstructures of the alloys are exhibited in Fig. 60.a-c using SE mode and EBSD mode (Fig. 60.d-i). The average grain size are displayed in the images of each corresponding alloy (Fig. 60.g,h,i). Equivalent EDS point analysis referring to points marked in Fig. 60.a-c are shown in Table 13.

	RHEA-1200		**RHEA-1300**		**RHEA-1600**		
	Point 1	**Point 2**	**Point 1**	**Point 2**	**Point 1**	**Point 2**	**Point 3**
Al	7.8	-	9.9	-	9.0	-	-
Nb	24.5	-	21.4	-	16.0	-	20.2
Ta	25.9	-	19	-	14.3	-	51.2
Ti	30.3	1.1	32.5	1.2	42.1	0.8	24.2
V	4.3	-	4.6	-	4.6	-	4.4
Zr	7.2	49.8	12.6	41.0	14	50.0	-
C	-	49.1	-	57.8		49.2	-

Table 13. Chemical compositions taken from EDS/SEM point analysis of sintered RHEAs. The points correspond to the ones shown in Fig. 60.

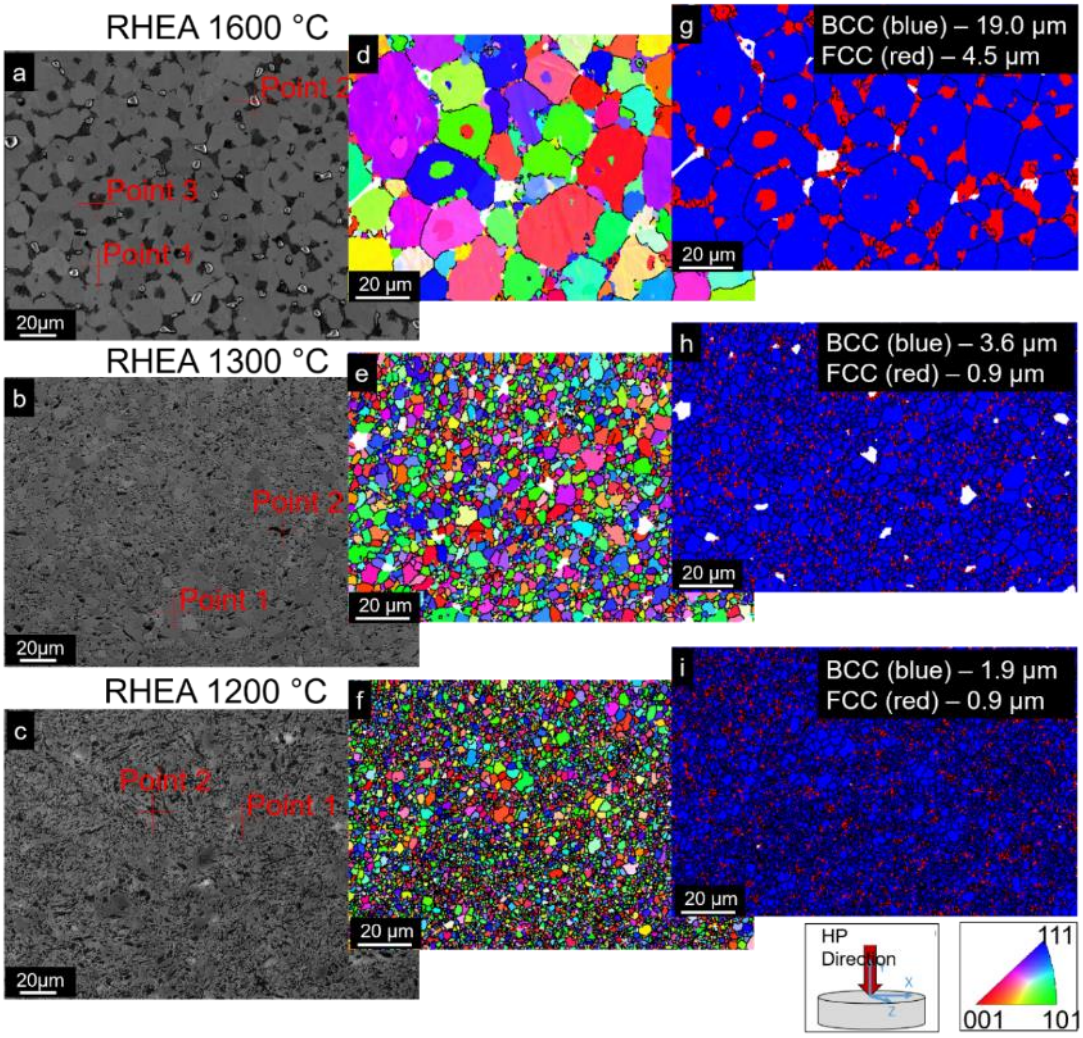

Fig. 60. SEM/EBSD analysis of RHEA1600, RHEA1300 and RHEA1200, respectively: a,b,c) typical microstructures using SE detector. d,e,f) Inverse pole figure orientation maps with reference direction Z. g,h,i) Phase maps for phase distribution of BCC matrix (blue) and FCC carbides (red).

Point 1 appears to show the chemical composition of the main BCC phase in all alloys, this corresponds to a phase mostly rich in Ti, Ta and Nb. This phase is shown as blue grains in Fig. 60.g,h,i. Point 2 seems to correspond to the chemical composition of the FCC carbide, Zr-, C- and Ti- rich. This phase is present in all alloys as well. White regions belonging to non-indexed areas is evident in EBSD maps (Fig. 60.g,h,i) in RHEA-1600 and RHEA-1300. These regions most likely correspond to the BCC2, identified by XRD, and rich in Ta, Ti and Nb as well (RHEA-1600, Point 3 in Table 13). Note that BCC1 is rich on similar elements, however in different proportions. One can notice the random orientation of BCC and FCC carbide grains despite the uniaxial pressing during the HP, as any type of preferential crystallographic texture cannot be detected in Fig. 60.d-f.

5.3.2.2 **Basic mechanical properties**

The basic mechanical properties of the three RHEAs are summarized in Table 14. The elastic modulus, Shear Modulus and Poisson ratio were measured by ultrasound method as described in the appropriate section. The theoretical density is based on the rule of mixtures.

	Hardness [HV 0.2]	Elastic Modulus [GPa]	Poisson Ratio	Shear Modulus [GPa]	Theoretical density [g.cm-3]	Archimedes density [g.cm-3]	% density
1200 °C	639 ± 16	148	0.328	56	7.56	7.63	100.0
1300 °C	660 ± 18	141	0.326	53	7.56	7.63	100.0
1600 °C	569 ± 23	160	0.318	61	7.56	7.64	100.0

Table 14. Summary of basic mechanical properties: hardness, elastic moduli, Poisson ratio, shear modulus and density of bulk RHEAs submitted to different maximum temperatures of sintering.

Full density alloys were achieved using all three different sintering temperatures. The hardness of RHEA-1200 (639 HV) and RHEA-1300 (660 HV) are similar, while there is a significant decrease in hardness for higher temperatures of sintering, as 1600 °C exhibits hardness values of 569 HV. It seems that the elastic modulus results go inversely, RHEA-1200 and -1300 have similar elastic modulus (148 and 145 GPa, respectively), which are lower in comparison to the ones of RHEA-1600 (160 GPa). Poisson ratio and shear moduli of RHEA-1200, RHEA-1300 and RHEA-1600 were calculated to be 0.328 and 56 GPa; 0.326 and 53 GPa; 0.318 and 61 GPa, respectively.

5.4 $Al_{0.5}NbTa_{0.8}Ti_{1.5}V_{0.2}Zr$ refractory high entropy alloy

The $Al_{0.5}NbTa_{0.8}Ti_{1.5}V_{0.2}Zr$ refractory high-entropy alloy produced by both powder metallurgy (PM) and casting have been subject to investigation in this work, due to its unique properties previously reported in the literature [92,93,170], as a potential RHEA for high temperature applications. After specific processing, this alloy resembles a superalloy-like microstructure, possessing a B2 matrix with dispersed BCC precipitates.

The novelty of our work is that we are studying this composition in a varied range of heat treatments allied with compositional variation of Al and Nb (sections 5.5 and 5.6, respectively). Additionally, the manufacturing method will be discussed and the consequences of producing the alloys by either powder metallurgy or casting will be presented. The next subsections will deal with each aspect of the studied alloy.

5.4.1 Phase prediction

The calculated phase and property diagrams of $Al_{0.5}NbTa_{0.8}Ti_{1.5}V_{0.2}Zr$ RHEA performed by ThermoCalc using TCHEA3 database are exhibited in the figure below. Fig. 61.a shows the phase diagram for Al content varying from 5.0 to 12.5 at. %. The red arrow indicates the correspondent at. % for this alloy, i.e. 10 at. %. Fig. 61.b shows the property diagram of this specific composition. The red arrows indicate the temperatures used for heat treatments in this work.

One can see that the temperature of nucleation of BCC phase from liquid during cooling start at around 1875 °C up to approximately 1600 °C. At this temperature, the phase amount equivalent to 100 % of BCC is expected to be present. At about 1300 °C, the second BCC type of structure nucleates. At about 1000 °C, aluminides start forming, followed by the

precipitation of HCP phase at about 550 °C. Note that depending on the heating and cooling rates, these secondary phases may be avoided by rapid heating/cooling.

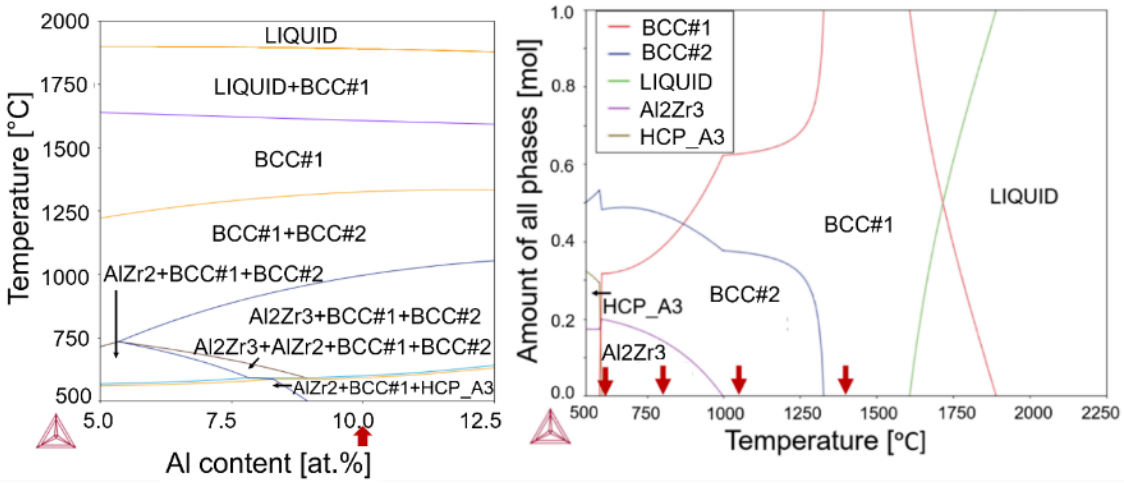

Fig. 61. CALPHAD predictions for $Al_{0.5}NbTa_{0.8}Ti_{1.5}V_{0.2}Zr$ RHEA. a) Calculated phase diagram varying Al content in the range from 5.0 up to 12.5 at. %. The investigated composition (Al in 10.0 at. %) is marked with the red arrow. b) Property diagram of amount of all phases vs. temperature. (TCHEA3 database).

The set of heat treatments selected to be performed on this work will be compared with the results calculated by ThermoCalc from the property diagrams.

Homogenization at 1400 °C was particularly chosen to be performed due to the formation of a predicted pure BCC type of structure. Following heat treatments were sequentially performed to evaluate the transformations happening in each phase field. These were chosen to be 1050 °C, 800 °C and 600 °C. At 1050 °C, a potential formation of two BCC phases (possibly corresponding to BCC/B2 shown by [93]) is expected. At temperatures below 1000 °C, a three-phase field is expected to be retained with BCC/B2 type of structures and addition of aluminides. Below 600 °C, HCP phase should form. The experimental results will be compared and shown in the next sections.

5.4.2 Microstructural characterization of powder metallurgy and arc-melted alloys

The $Al_{0.5}NbTa_{0.8}Ti_{1.5}V_{0.2}Zr$ RHEA was produced by milling of feedstock powders (Precursors-A – please refer to 4.2.1 section) via mechanical alloying. Subsequent hot pressing (HP) was performed for densification of the bulk. The as-sintered bulk is called $PM1_A$. The RHEA composition was also produced by arc-melting of elemental chunks. The arc-melted material is called AM1. The first heat treatment was completed at 1400 °C, as an attempt of homogenization of the alloys into a BCC single-phase field (as predicted by CALPHAD calculations). The obtained samples are named as $PM4_A$ and AM4. This was chosen to be the starting point of the following heat treatments performed separately, which are: 1050 °C ($PM7_A$ and AM7); 800 °C ($PM10_A$ and AM10); and 600 °C ($PM13_A$ and AM13). A simplified scheme of heat treatments is exhibited in Fig. 62. For a detailed diagram, one can refer to Fig. 28).

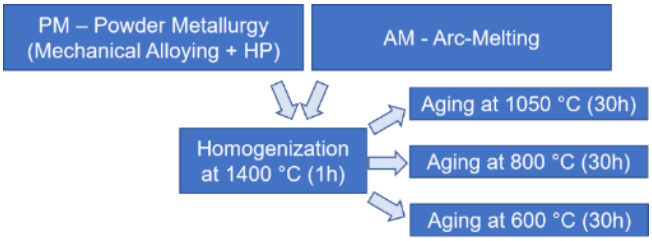

Fig. 62. Simplified heat treatments scheme for $Al_{0.5}NbTa_{0.8}Ti_{1.5}V_{0.2}Zr$.

The XRD results before and after heat treatments for PM alloys are displayed in Fig. 63. The lattice parameters of the phases found by XRD patterns are shown in the table below.

	PM1A - as sintered			PM4A - 1400 °C					
	a_{XRD}	c_{XRD}	wt.%	a_{XRD}	c_{XRD}	wt.%	a_{XRD}	c_{XRD}	wt.%
BCC1	3.29	-	85.5	3.29	-	83.9			
Al3Zr (I4/mmm)	4.02	17.38	0.4	-	-	-			
ZrO	4.62	-	13.9	4.62	-	16.1			
Ta2C (P-3m1)	3.11	4.95	0.2	-	-	-			
	PM7A - 1050 °C			PM10A - 800 °C			PM13A - 600 °C		
BCC1	3.28	-	79.8	3.28	3.28	81.3	3.28	-	93.0
Al3Zr (I4/mmm)	4.01	17.37	6	4.01	17.37	3.1	-	-	-
ZrO	4.62	-	11.2	4.61	4.61	14.1	4.59	-	7
HCP	2.93	4.92	2.4	2.94	4.92	1.5	-	-	-
Al_2Ti_3 (P63/mmc)	2.93	4.37	3	-	-	-	-	-	-

Table 15. Lattice parameters calculated by XRD analysis of PM RHEAs before and after heat treatments.

The XRD results of the arc-melted counterparts before and after heat treatments are presented in Fig. 64. The lattice parameters of the samples are exhibited in the table below.

	AM1 - arc-melted			AM4 - 1400 °C		
	a_{XRD}	c_{XRD}	wt.%	a_{XRD}	c_{XRD}	wt.%
BCC1	3.33	-	75.0	3.31	-	87.3
BCC2	3.32	-	25.0	3.32	-	12.7

	AM7 - 1050 °C				AM10 - 800 °C				AM13 - 600 °C		
	a_{XRD}	b_{XRD}	c_{XRD}	wt.%	a_{XRD}	b_{XRD}	c_{XRD}	wt.%	a_{XRD}	c_{XRD}	wt.%
BCC1	3.29	-	-	74.1	3.31	-	-	81.6	3.37	-	71.5
BCC2	3.3	-	-	19.5	3.37	-	-	9.1	3.29	-	26.2
Al3Zr (I4/mmm)	3.98	3.98	17.35	6.0	-	-	-	-	-	-	-
Al3Zr2 (Fdd2)	9.59	13.88	5.62	0.4	9.59	13.88	5.62	2	-	-	-
$AlTi_2Zr$(P63/mmc)	-	-	-	-	5.95	5.95	4.78	4.4	-	-	-
Al_2Zr(P63/mmc)	-	-	-	-	5.29	5.29	8.79	2.9	-	-	-
Ti2Zr(P63/mmc)	-	-	-	-	-	-	-	-	3.06	4.9	2.3

Table 16. Lattice parameters calculated by XRD analysis of arc melted RHEAs before and after heat treatments.

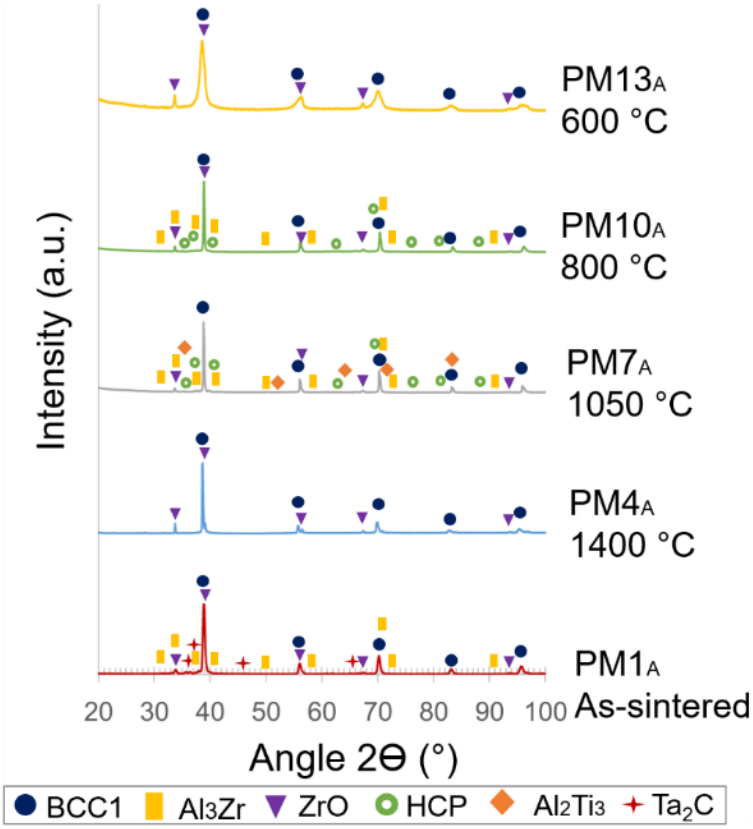

Fig. 63. XRD patterns of PMA $Al_{0.5}NbTa_{0.8}Ti_{1.5}V_{0.2}Zr$ RHEA before and after heat treatments.

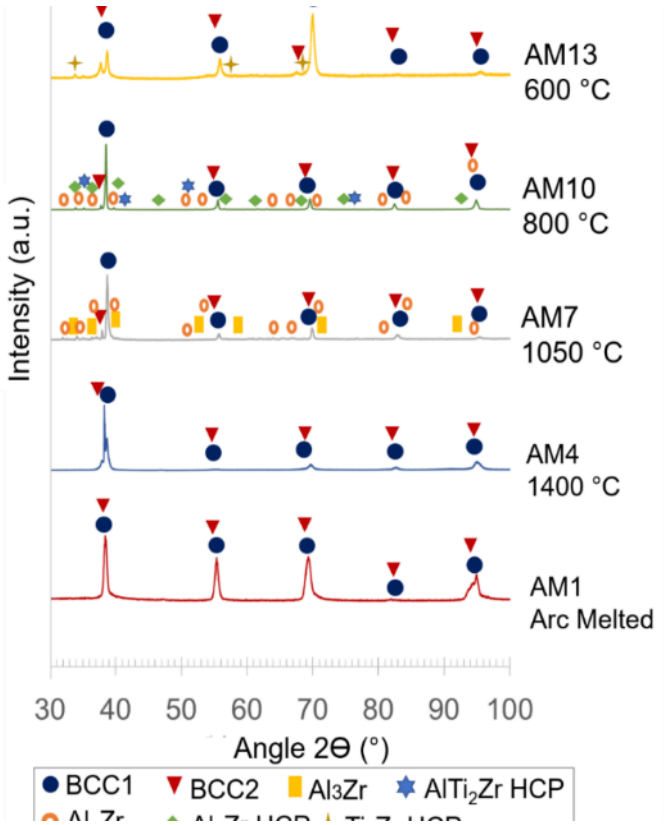

Fig. 64. XRD patterns for all conditions of heat treatments of the arc-melted $Al_{0.5}NbTa_{0.8}Ti_{1.5}V_{0.2}Zr$ RHEA.

The microstructure of the as-sintered $Al_{0.5}NbTa_{0.8}Ti_{1.5}V_{0.2}Zr$ RHEA ($PM1_A$) can be seen in Fig. 65a,a.1 in SE mode for an overview of the microstructure and enlarged view of the microstructure, respectively. Fig. 65b,b.1 show the corresponding images in BSE mode.

The microstructure of the alloy after heat treatment at 1400 °C for 1 h is displayed in Fig. 65c,c.1 for an overview of the microstructure and its enlarged view in SE mode, respectively. The corresponding BSE images are shown in Fig. 65d,d.1, respectively.

The alloys, after different heat treatments for 30 h at 1050 °C, 800 °C and 600 °C, exhibit diverse microstructures, as visible in Fig. 66a,b, Fig. 66c,d and Fig. 66e,f, respectively.

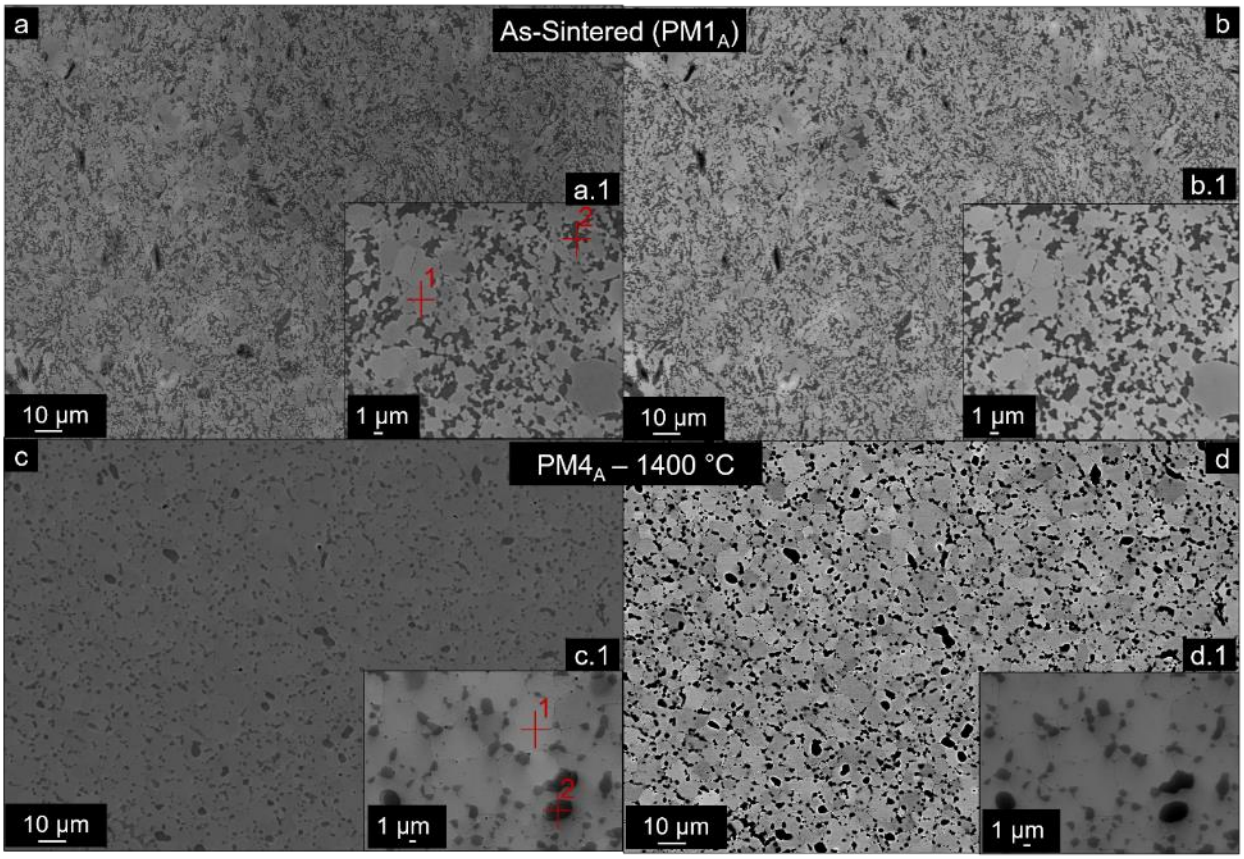

Fig. 65. SEM images of microstructures of $Al_{0.5}NbTa_{0.8}Ti_{1.5}V_{0.2}Zr$ RHEA produced by powder metallurgy using precursor A: a) Overview of $PM1_A$ (as-sintered state) using SE mode. a.1) Details of $PM1_A$ microstructure in higher magnification (SE mode). b,b.1) Corresponding overview and details of $PM1_A$ utilizing BSE detector, respectively. c) Overview of the RHEA after heat treatment at 1400 °C for 1 h ($PM4_A$). c.1) Details of $PM4_A$ in higher magnification (SE mode). d,d.1) Respective overview and details of $PM4_A$ using BSE detector, in order. The red crosses represent EDS point analyses on each sample.

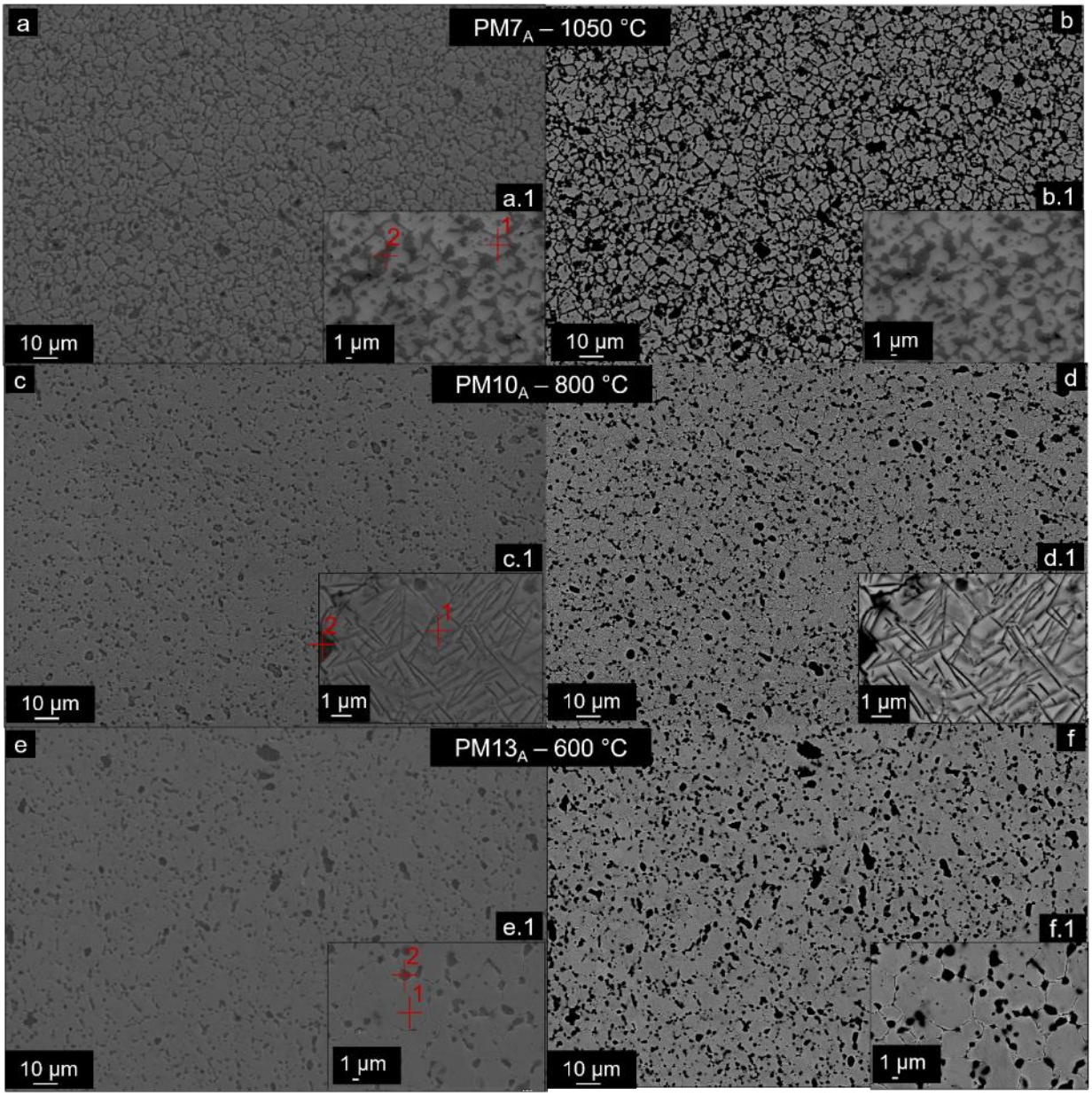

Fig. 66. SEM images of microstructures of $Al_{0.5}NbTa_{0.8}Ti_{1.5}V_{0.2}Zr$ RHEA produced by powder metallurgy using precursor A: a) Overview of $PM7_A$ using SE mode. a.1) Details of $PM7_A$ microstructure in higher magnification (SE mode). b,b.1) Corresponding overview and details of $PM7_A$ using BSE detector, respectively. c) Overview of $PM10_A$ RHEA after heat treatment at 800 °C for 30 h ($PM4_A$). c.1) Details of $PM10_A$ in higher magnification (SE mode). d,d.1) Respective overview and details of $PM10_A$ using BSE detector, in order. e, f) Overview of $PM13_A$ after 30 h of heat treatment at 600ºC in SE and BSE modes. e.1,f.1) Respective microstructure of $PM13_A$ in higher magnification in SE and BSE modes. The red crosses represent EDS point analyses on each sample.

The chemical composition of the RHEA before and after heat treatments were measured and can be seen in Table 17 and Table 18. The oxygen content shown by EDS is a rough approximation of its amount, it is shown for reference, since the this is not the most suitable method to calculate elements of low characteristic x-ray energies, such as O, N and C.

The chemical composition of the material, before heat treatments, shown as the column corresponding to the map sum spectrum, exhibits the equivalent amount of all elements in $Al_{0.5}NbTa_{0.8}Ti_{1.5}V_{0.2}Zr$ (stoichiometric ratio).

	$PM1_A$ - As-sintered			$PM4_A$ - 1400 °C	
[at.%]	Point 1 (BCC)	Point 2	Map Sum Spectrum	Point 1 (BCC)	Point 2
Al	9.3 +- 0.1	1.7 +- 0.4	9.6 +- 0.6	8.9 +- 1.2	1.6 +- 1
Ti	34.4 +- 0.2	7.5 +- 1.1	29.8 +- 1.0	33.7 +- 1.4	6 +- 1.4
V	4.7 +- 0.1	3.1 +- 0.7	3.8 +- 0.4	4.3 +- 0.5	0.9+-0.3
Zr	9.6 +- 0.3	35.0 +- 1.4	19.7 +- 0.7	12.2 +- 1.0	33.9 +- 1.2
Nb	23.7 +- 0.9	4.0 +-2.1	20.2 +- 0.3	22.5 +- 1.1	3.1 +- 0.8
Ta	19.3 +- 0.4	3.1 +- 0.5	16.9 +- 1.2	18.4 +- 0.8	3.4 +- 0.9
O	-	45.6 +- 1.0	-	-	51.1 +- 2.5

Table 17. SEM/EDS point analysis of the PM RHEA before ($PM1_A$) and after heat treatment at 1400 °C ($PM4_A$). The points correspond to the crosses exhibited in Fig. 65.

	$PM7_A$ - 1050 °C		$PM10_A$ - 800 °C		$PM13_A$ - 600 °C	
[at.%]	Point 1 (BCC)	Point 2	Point 1 (BCC)	Point 2	Point 1 (BCC)	Point 2
Al	8.1 +- 0.4	4.8 +- 1.0	9.8 +- 0.4	1 +- 0.2	9.9 +- 0.1	1.3 +- 0.3
Ti	30.0 +- 0.2	15.4 +- 2.1	33.1 +- 1.7	5.5 +- 0.4	31.8 +- 0.2	5.4 +- 1.0
V	5.2 +- 0.1	2.3 +- 0.5	4.2 +- 0.3	0.3 +- 0.1	5.2 +- 0.4	0.8 +- 0.1
Zr	8.9+-0.6	38.5 +- 2.2	9.1+- 1.0	35.5 +- 0.8	13.4 +- 0.5	34.6 +- 0.6
Nb	24.8 +- 0.7	7.1 +- 1.8	22.5+-2.2	0.3 +- 0.4	20.7 +- 0.1	2.9 +- 0.5
Ta	23 +- 0.6	6.0 +- 1.0	21.4 +- 1.1	0.9 +- 0.2	19.0 +- 0.2	3.0 +- 0.5
O	-	25.9 +- 2.5	-	56.5 +- 3.5		52.0 +- 1.7

Table 18. SEM/EDS point analysis of PM RHEA after heat treatment at 1050 °C ($PM7_A$), 800 °C ($PM10_A$) and 600 °C ($PM10_A$). The points correspond to the crosses displayed in Fig. 66.

It is possible to affirm that the main BCC phase is exhibited by Point 1 in all PM alloys, and this phase is rich in Ti, Nb and Ta before and after heat treatments. Additionally, one can notice that point 2 corresponds to Zr-rich oxides as a second major phase in all PM alloys. The ZrO crystal structure was confirmed by XRD. The other elements are probably present in the point analysis as a consequence of the spot size of the SEM during EDS acquisition. One must be aware that, for an effective chemical analysis of these RHEAs, a combination 10kV and 60 µm aperture was used. The spot size is, therefore, influenced by these parameters and most likely reached the vicinity of the particle, i.e. collected data from the BCC matrix.

Due to the resolution limit of SEM, only the chemical compositions of BCC and oxides were possible to be measured by point analysis. Nonetheless, the $PM10_A$ exhibits a needle-like phase, displayed in Fig. 66c,d. This phase's chemical composition was qualitatively assessed by EDS through an element profile plot and the result is shown in Fig. 67.

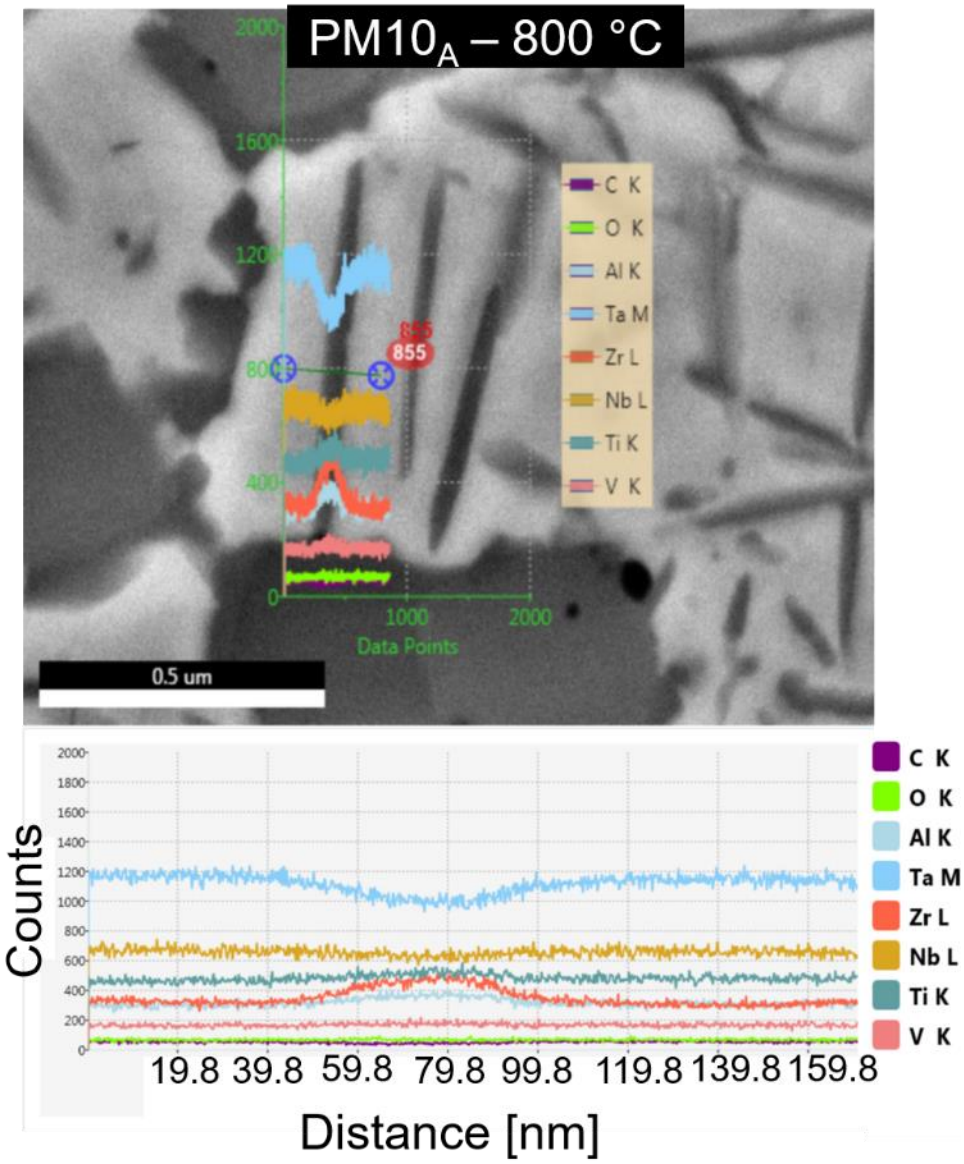

Fig. 67. SEM/EDS element profile plot of PM10A exhibiting needle-like precipitates rich in Zr and Al.

The profile plot of the elements present in the alloy reveals that this needle-like phase is Al- and Zr-rich. This is in good agreement with the XRD analysis, as it is shown in Fig. 63 that this heat treatment of 800 °C for 30 h leads to precipitation of Al_3Zr crystal structure, which most likely corresponds to this phase.

The arc-melted counterpart of $Al_{0.5}NbTa_{0.8}Ti_{1.5}V_{0.2}Zr$ RHEA exhibits a very dissimilar microstructure as compared to the ones exhibited by powder metallurgy. This was anticipated, owing the intrinsic differences of both manufacturing methods. The microstructure of the arc melted alloy (AM1) is shown in Fig. 68.a using SE mode, and Fig. 68.b shows the same image in BSE mode. AM1 evidences a microstructure composed of dendritic and interdendritic area. On the other hand, after heat treatment at 1400 °C for 1 h, the dendrites were successfully dissolved (Fig. 68.c and .d exhibit the SEM images of the microstructure after, in SE and BSE modes). The enlarged views of the area marked with yellow rectangle are depicted in Fig. 68c.1,d.1 utilizing SE and BSE detectors, respectively.

The images reveal very fine nano-sized precipitates dispersed into large grains of the main BCC phase. These are in good agreement with the obtained results from XRD.

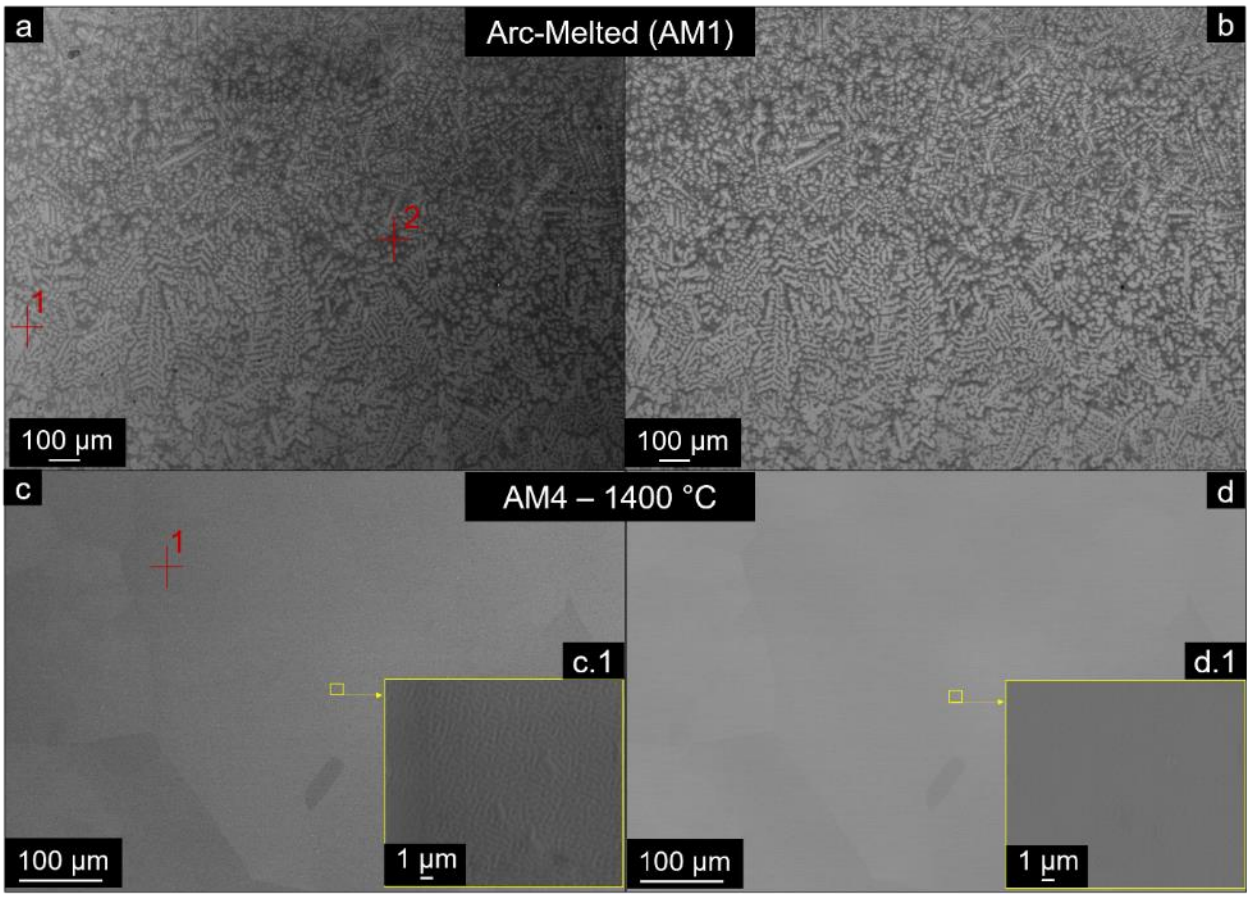

Fig. 68. SEM images of microstructures of $Al_{0.5}NbTa_{0.8}Ti_{1.5}V_{0.2}Zr$ RHEA produced by arc-melting. a) Microstructure of AM1 prepared by arc-melting – SE detector. b) Corresponding microstructure of AM1 using BSE detector. c) AM4 microstructure after heat treatment at 1400 °C for 1 h (SE mode). c.1) Enlarged view of AM4 exhibiting nano-sized precipitates (SE Mode). d,d.1) Corresponding images of the exactly same regions as in c and c.1, respectively, using BSE mode. The red crosses represent EDS point analyses on each sample.

After being submitted to 1050 °C for 30 h, AM7 reveals a different microstructure as compared to the previous states, as shown in Fig. 69.

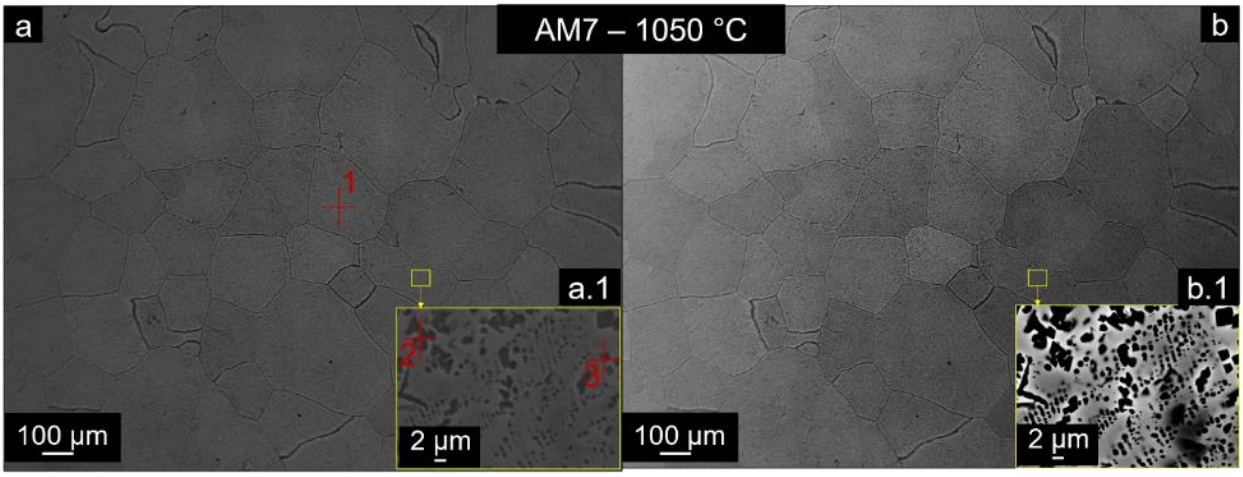

Fig. 69. SEM images of microstructures of $Al_{0.5}NbTa_{0.8}Ti_{1.5}V_{0.2}Zr$ RHEA produced by arc-melting. a) AM7 microstructure after 30 h of heat treatment at 1050°C in SE mode. a.1) Enlarged view of the area marked by the yellow rectangle in SE mode. b) Same image as shown by a. in BSE mode. b.1) Corresponding image of a.1. in BSE mode. The red crosses show the location of EDS point analyses.

The enlarged view reveals fine precipitates within the BCC matrix, probably corresponding to the secondary phases exhibited by XRD, such as a secondary BCC2 and different kinds of aluminides (Al_3Zr and Al_3Zr_2).

Alternatively, heat treatments at 800 °C for 30 h were performed after the homogenization process. This sample is named AM10 and the resulting microstructure is shown in Fig. 70.

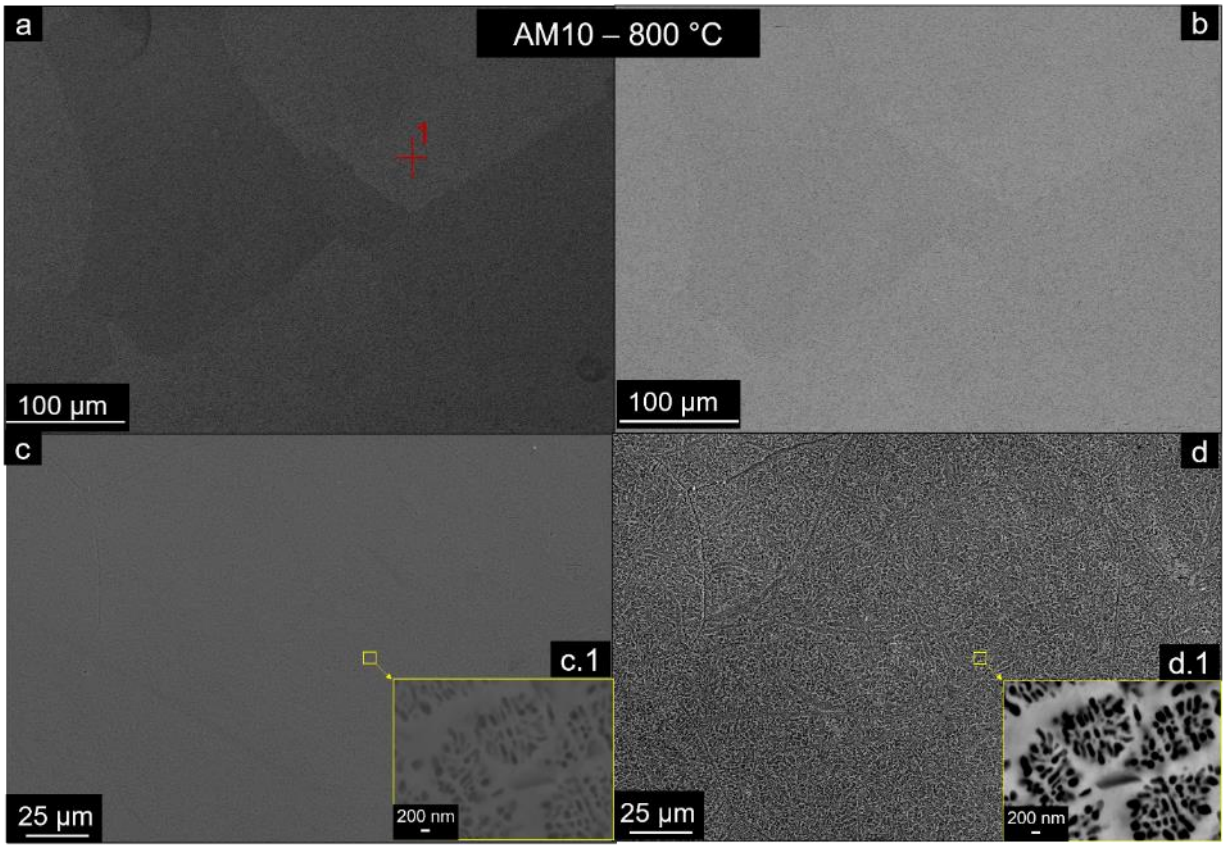

Fig. 70. SEM images of microstructures of $Al_{0.5}NbTa_{0.8}Ti_{1.5}V_{0.2}Zr$ RHEA produced by arc-melting. a) AM7 microstructure after 30 h of heat treatment at 800 °C in SE mode. b) Same image as shown by a. in BSE mode. c) AM7 in enlarged view using SE detector. d) Same image as shown by c. using BSE detector. c.1) Further enlarged area of AM7, corresponding to the area marked by the yellow rectangle (SE mode). b.1) Equivalent image of c.1. in BSE mode. The red crosses show the location of EDS point analyses.

The enlarged view of AM10 reveals a BCC main phase with very fine dispersed precipitates, similarly, as exhibited in the state of 1050 °C. However, in comparison with AM7, AM10 exhibits finer precipitates of B2 and aluminides with dissimilar morphology due to the lower processing temperature. Additionally, according to XRD, AM10 shows the presence of $AlTi_2Zr$ nanoprecipitates.

Heat treatment at 600 °C for 30 h, nonetheless, exhibits a very different microstructure as compared to those of 1050 °C and 800 °C states. The SEM images in Fig. 71 display the microstructure corresponding to AM13. It seems that this temperature was not enough to provoke the precipitation of the aluminides visible in the previous states, however nano-sized precipitates most likely corresponding to BCC2 phase within the main BCC phase are visible.

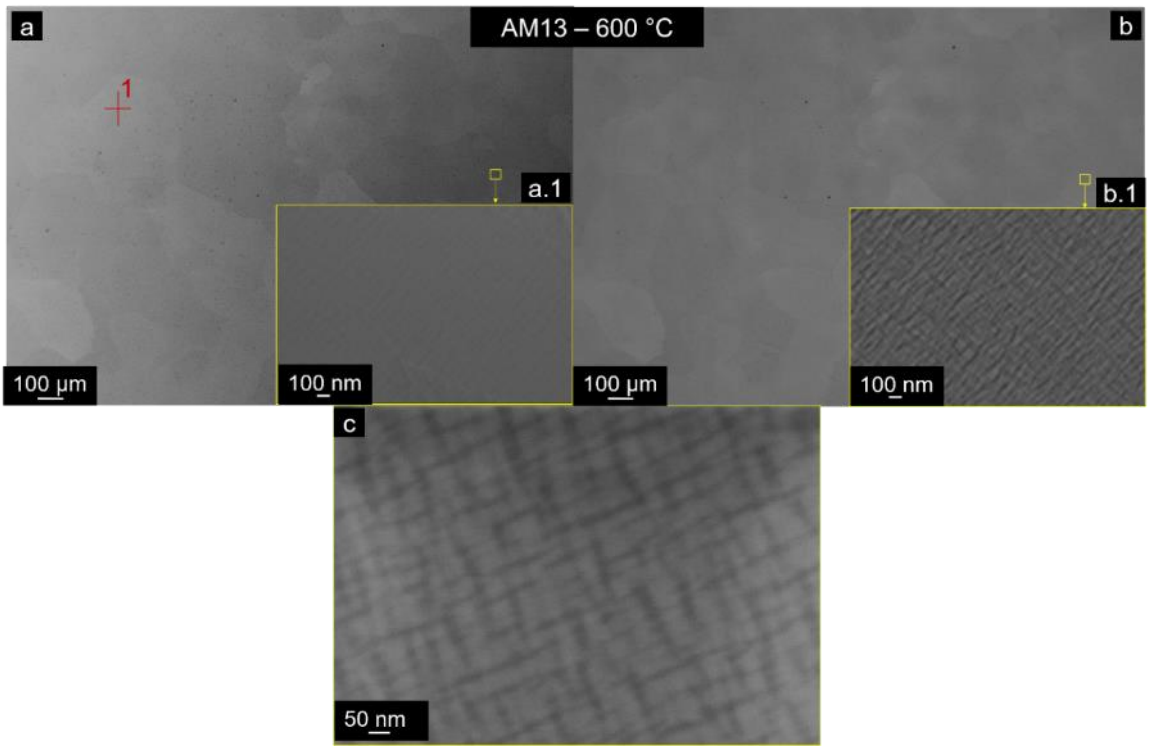

Fig. 71. SEM images of microstructures of $Al_{0.5}NbTa_{0.8}Ti_{1.5}V_{0.2}Zr$ RHEA produced by arc-melting. a) AM13 microstructure after 30 h of heat treatment at 600 ºC in SE mode. a.1) Enlarged view of the area marked by the yellow rectangle in SE mode. b) Same image as shown by a. in BSE mode. b.1) Equivalent image shown in a.1. using BSE mode. c) Enlarged view of the microstructure, exhibiting nano-sized precipitates. The red cross shows the location of EDS point analysis.

The chemical composition of the arc-melted alloys was assessed by EDS maps, point analyses and line spectrum. Please note that not all phases shown in XRD results were possible to be measured by SEM/EDS due to the resolution constraints of the machine.

The point analyses results of all alloys produced by arc-melting are shown in Table 19 and Table 20. The respective locations of EDS analyses are exhibited in the previous SEM images, corresponding to AM1 and AM4 (Fig. 68); AM7 (Fig. 69); AM10 (Fig. 70) and AM13 (Fig. 71). The results suggest that the arc-melted AM1 exhibits two phases in interdendritic and dendritic regions. The interdendritic area is –Ti, -Zr and –Al rich. Conversely, the dendrites are rich in –Ta, -Nb and -Ti. The two regions were assessed by EDS element profile plot (Fig. 72).

	AM1 - Arc-Melted			AM4 - 1400 ºC
[at.%]	Point 1 (Interdendrites)	Point 2 (Dendrites)	Map Sum Spectrum	Point 1 (BCC)
Al	13.8 +- 1.7	5.4 +- 0.3	9.5 +- 0.6	10.1 +- 0.1
Ti	29.6 +- 1.7	26.4 +- 0.5	29.7 +- 1.1	28.6 +- 1.5
V	3.9 +- 0.2	3.3 +- 0.2	4.0 +- 0.2	3.6 +- 0.1
Zr	30.6 +- 1.4	11.3 +- 0.3	20.3 +- 0.4	19.0 +- 0.2
Nb	13.3 +- 0.8	24.7 +- 0.2	19.5 +- 1.3	18.7 +- 0.2
Ta	8.7 +- 0.5	28.9 +- 1.2	17.0 +- 1.0	19.8 +- 1.5

Table 19. SEM/EDS chemical composition of AM RHEA before (AM1) and after heat treatment at 1400 ºC (AM4). The point analyses correspond to the crosses exhibited in Fig. 68.

	AM7 - 1050 ºC			AM10 - 800 ºC	AM13 - 600 ºC
[at.%]	Point 1 (BCC)	Point 2	Point 3	Point 1 (BCC)	Point 1 (BCC)
Al	9.3 +- 0.2	24.6 +- 2.0	23.2 +- 1.0	6.3 +- 1.4	9.1 +- 0.3
Ti	29.6 +- 0.3	10.8 +- 0.6	19.9 +- 0.5	34.0 +- 2.1	29.3 +- 0.6
V	3.9 +- 0.1	3.9 +- 0.8	1.6 +- 0.3	4.4 +- 0.2	4.2 +- 0.1
Zr	19.6 +- 0.5	50 +- 1.3	33.1 +- 1.2	16.3 +- 1.3	20.1 +- 0.7
Nb	19.5 +- 0.4	4.8 +- 0.4	12 +- 0.3	20.5 +- 0.5	19.6 +- 0.5
Ta	18.2 +- 0.5	5.9 +- 1.9	10.2 +- 0.4	18.5 +- 1.0	18.4 +- 0.9

Table 20. SEM/EDS chemical composition of the AM RHEA heat treatments at 1050 ºC (AM7); 800 ºC (AM10) and 600 ºC (AM13). The point analyses correspond to the crosses exhibited in Fig. 68, Fig. 69, Fig. 70 and Fig. 71, respectively.

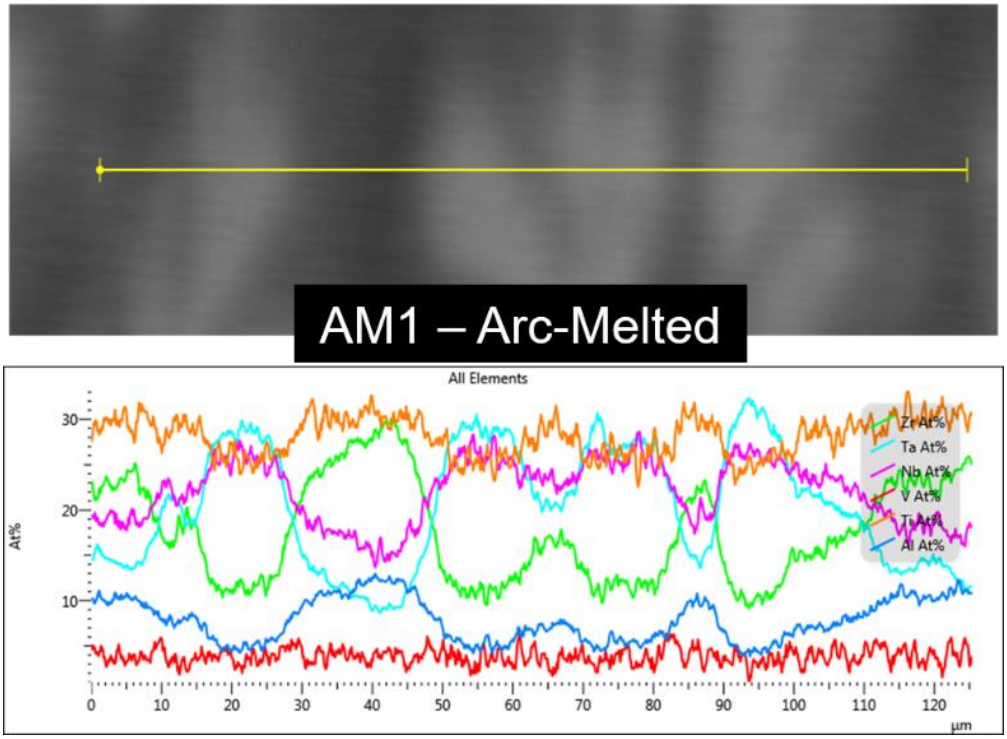

Fig. 72. SEM/EDS element profile plot of at. % vs. distance on the dendritic/interdendritic interface of AM1.

The line spectrum confirms the point analyses' results of the arc-melted sample, showing that the interdendrites are rich in Ti, Zr and Al; the dendrites are especially rich in Nb, Ta. Additionally, the occurrence of a slight decrease in the at. % of Ti is observed when one goes from interdendritic to dendritic regions, however Ti is still a major element in the dendritic areas. The map sum spectrum confirms the stoichiometric ratio of $Al_{0.5}NbTa_{0.8}Ti_{1.5}V_{0.2}Zr$ RHEA.

After homogenization at 1400 ºC, the main BCC phase is rich in –Ti, -Zr, -Ta and –Nb. Additional heat treatments show the same trend in chemical composition of the main BCC phase. The chemical compositions of secondary phases exhibited by the alloy subjected to 1050 ºC (AM7) were possible to be assessed. It is clear that the chemical composition of the precipitate selected by point 2 (Fig. 69) corresponds to a –Zr, -Al rich precipitate. They probably match the aluminides detected by XRD (Al_3Zr and Al_3Zr_2). Point 3 exhibits a very similar chemical composition, -Zr and –Al rich, however also –Ti appears expressively. This

could correspond to the $AlTi_2Zr$ precipitates detected when the alloy is subjected to 800 ºC for 30 h. Additionally, the chemical composition of the phases identified by point 2 and 3 may be slightly influenced by the ones of the phases in the very close vicinity. This is caused by the limited spot size of the EDS method.

After heat treatment at 800 ºC for 30 h, the main BCC exhibits a –Ti, -Zr, -Ta and –Nb rich phase, in a similar fashion as other heat treatments results. The slight variations in chemical composition will be explained in the discussion section. This heat treatment results in formation of several aluminides, confirmed by XRD. These aluminides were not possible to be assessed by EDS point analysis, due to its nano-size character of the precipitates as visible in Fig. 70d.1, and limited resolution of SEM/EDS. However, these were qualitatively assessed by EDS maps, as shown in Fig. 73.

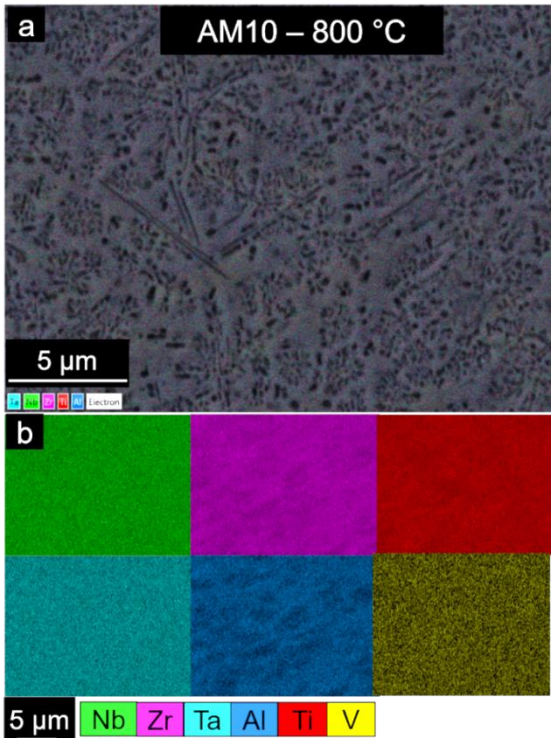

Fig. 73. EDS maps of AM10. a) Overlay map of elements present in the alloy. c) Single maps of Nb, Zr, Ta, Al, Ti and V elements.

From the mapping, it is visible that the dark areas are rich in -Al and –Zr elements. Therefore, the dark areas are probably the referred aluminides.

After 600 ºC for 30 h, on the other hand, the $Al_{0.5}NbTa_{0.8}Ti_{1.5}V_{0.2}Zr$ RHEA exhibits mainly a BCC matrix with similar composition as the others, and additionally BCC2 nano-sized precipitates which could not be assessed by EDS due to its resolution limit. XRD detects minor amounts of other HCP phase (1.3 wt. %) which is not visible by SEM/EDS. For quantitative evaluation of the microstructure, EBSD analyses have been performed, with results concerning the phase distribution, orientation and grain sizes of the PM and arc-melted alloys presented in Fig. 74 and Fig. 75, respectively.

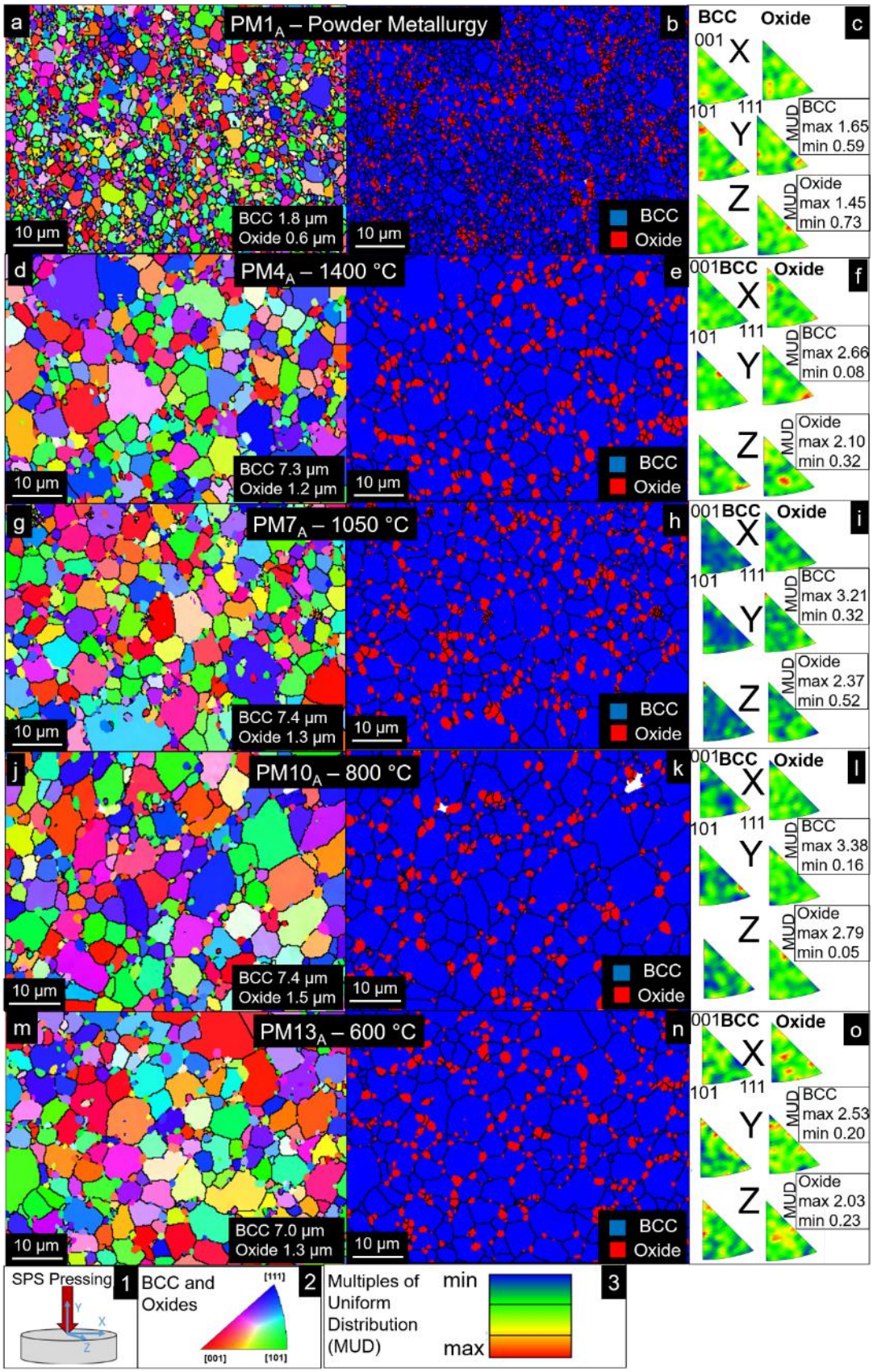

Fig. 74. SEM EBSD analysis of the PM RHEA. a,d,g,j,m) Grain orientation maps of PM1A, PM4A, PM7A, PM10A and PM13A with reference direction Z denoted in 1, the grain orientation reference is shown in 2. b,e,h,k,n) Phase map showing distribution of BCC and Oxide phases in PM1A, PM4A, PM7A, PM10A and PM13A. c,f,i,l,o) Respective inverse pole figures denoting orientation in X, Y and Z direction with respective MUD reference in 3.

Through solid state sintering, it is possible to manufacture full-density very fine-grained alloys. The EBSD analysis of the as-sintered state ($PM1_A$) evidences the BCC matrix with average grain size distribution of (1.8 ± 0.1) μm and the oxide particles exhibit (0.6 ± 0.1) μm grain sizes in a homogeneously distributed manner within the matrix. The oxide particles were indexed as crystals of Fm-3m space group, with crystal structure of ZrO, according to the data obtained by XRD. The other phases present were not possible to be indexed due to the EBSD resolution constraints regarding their nano-sized grain character. One can notice the random orientation of both BCC and oxide grains despite the uniaxial pressing during the SPS of the PM alloy. Even though some red areas appear in the inverse pole figures for the BCC, their MUD values are very low, therefore no preferential orientation is determined.

After being subjected to the very high temperature of 1400 °C for 1 h, the RHEA exhibited an increase in grain size up to (7.3 ± 0.7) μm and the oxides suffered an increase up to (1.2 ± 0.1) μm. No important crystallographic orientation relationship of the grains is detected.

Additional heat treatment at 1050 °C for 30 h, surprisingly, does not bring any important grain growth to the BCC matrix, evidencing a BCC average grain size of (7.4 ± 1.0) μm and dispersed oxides presenting (1.3 ± 0.1) μm. No preferential orientation is visible.

Alternative heat treatment at 800 °C for 30 h does not impose any significant changes as well in the BCC grain size average (7.4 ± 1.0) μm nor to the oxides grain size average, which is calculated to be (1.5 ± 0.2) μm. White regions appear, pertaining to non-indexed EBSD areas, probably corresponding to regions with high concentration of aluminides shown by SEM and XRD. When the material is subjected to 600 °C for 30 h, the BCC matrix is comprised of grains possessing average grain size of (7.0 ± 0.6) μm and homogeneously dispersed oxides of (1.3 ± 0.1) μm.

The EBSD maps performed on the arc-melted alloys are exhibited in Fig. 75. In contrast, the material before heat treatments - in the arc-melted state - possesses a major BCC phase of grain size average of (166.0 ± 20.0) μm. The preferential crystallographic orientation shown in [001] Z of the BCC is caused by the dendritic solidification. However, this orientation is not very pronounced as it is evidenced by the low MUD values.

After homogenization at 1400 °C for 1 h, the grain size of the main BCC phase increases significantly up to (225.9 ± 9.0) μm. The other elements present are too small in size to be detected by such magnification in EBSD. At this state, no important preferential orientation is visible, as the maximum MUD values remain very low. The morphology of the grains changes as compared to the previous state, and it is clear that the homogenization and recrystallization took place – evidenced by SEM as well.

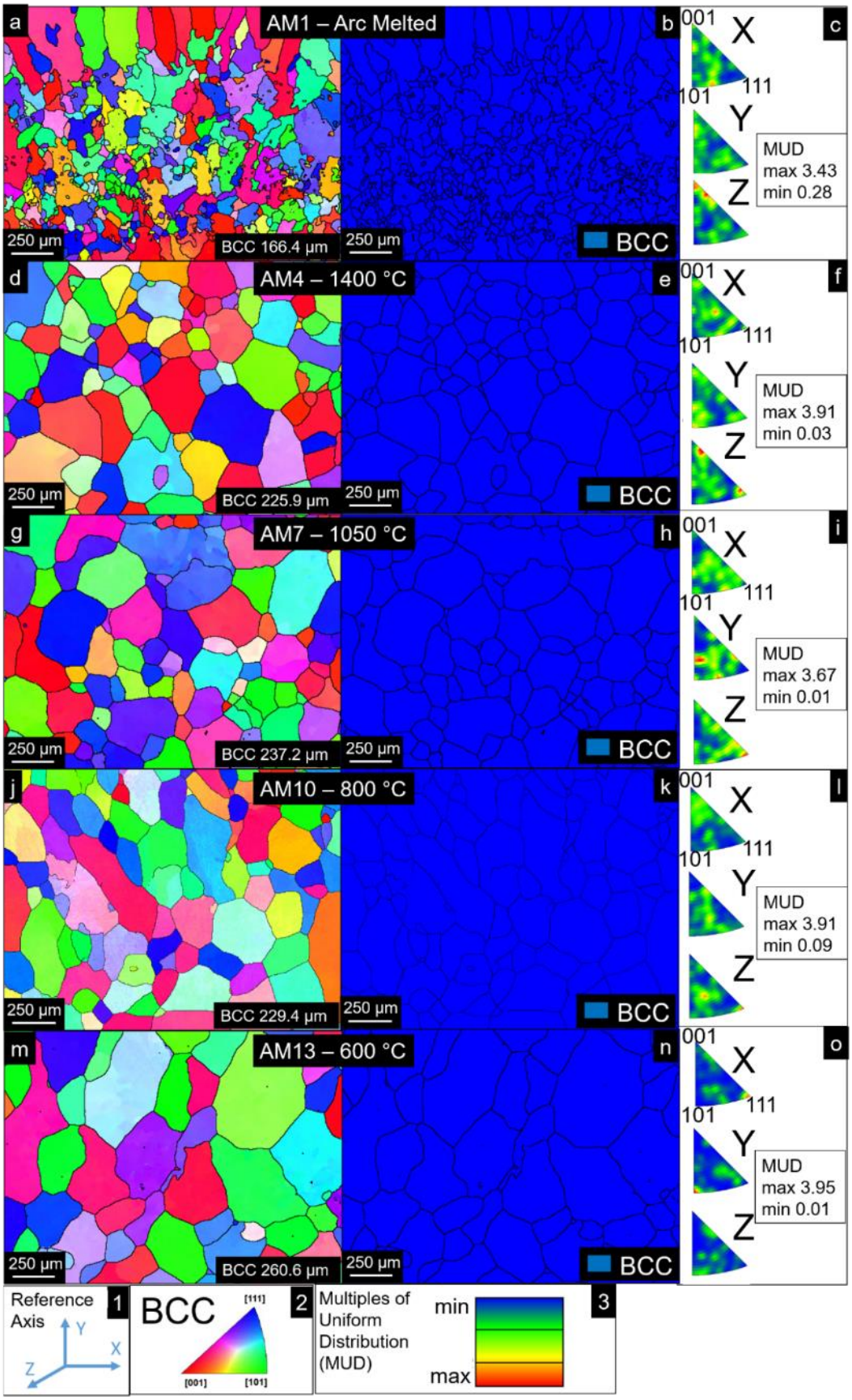

Fig. 75. *SEM EBSD analysis of the AM RHEA. a,d,g,j,m) Grain orientation maps of AM1, AM4, AM7, AM10 and AM13 with reference direction Z denoted in 1, the grain orientation reference is shown in 2. b,e,h,k,n) Phase map showing distribution of BCC and Oxide phases in AM1, AM4, AM7, AM10 and AM13. c,f,i,l,o) Respective inverse pole figures denoting orientation in X, Y and Z direction with respective MUD reference in 3.*

When subjected to 1050 °C for 30 h, the RHEA does not suffer a significant grain growth, presenting a BCC phase of (237.2 ± 1.7) μm grain size. Alternatively, at 800 °C for 30 h, the alloy exhibits grains of (229.4 ± 2.1) μm, reasoning with the slightly smaller grain size with the lower temperature of processing, as compared to those of 1050 °C. When subjected to 600 °C for 30 h, the BCC grains show an average grain size of (260.6 ± 5.3) μm. No preferential crystallographic orientation is noticeable.

These results presented above are the ones using milled Zr sponge, which were milled into powder particles (Precursors-A; sintered bulk **PM_A**). The use of commercially available Zr powders (TLS Technik) together with other available commercial powders (Precursors-B; sintered bulk **PM_B**) was assessed for comparison and the results of microstructural characterization are shown in Appendix A.

5.4.3 Basic mechanical properties

The Vickers hardness and elastic modulus (taken from nanoindentation tests) of all samples were measured and a summary of the results is exhibited in Table 21.

	Hardness [HV]	Elastic Modulus [GPa]
AM1- Arc-Melted RHEA	529 +- 10	111.5 +- 3.4
AM4 - RHEA after 1400°C	542 +- 11	127.6 +- 7.6
AM7 - RHEA after 1050°C	603 +- 9	141.9 +- 8.3
AM10 - RHEA after 800°C	607 +- 5	137.6 +- 2.4
AM13 - RHEA after 600°C	554 +- 6	145.9 +- 3.3
$PM1_A$- As-sintered RHEA	602 +-7	145.2 +- 5.1
$PM4_A$ - RHEA after 1400°C	564 +- 10	143 +-2.8
$PM7_A$ - RHEA after 1050°C	616 +-9	150.1 +- 5.4
$PM10_A$ - RHEA after 800°C	605 +- 5	149.2 +- 4.0
$PM13_A$ - RHEA after 600°C	571 +- 8	138.2 +- 5.7
$PM1_B$ - As-sintered RHEA	570 +- 4	132.9 +- 5.6
$PM4_B$ - RHEA after 1400°C	561 +- 8	123.3 +- 4.8
$PM7_B$ - RHEA after 1050°C	576 +- 5	134.5 +- 3.8
$PM13_B$ - RHEA after 600°C	555 +- 4	123.4 +- 5.4

Table 21. Average hardness and elastic modulus of PM and Arc-Melted HEAs before and after heat treatments.

The results show that the PM_A RHEA, in any state, exhibits superior average hardness and elastic modulus values than any of those exhibited by the other materials. This is due to the increased amount of ZrO homogeneously dispersed in the material in all states.

On the other hand, the PM_B RHEA does not contain an expressive amount of ZrO, therefore its hardness and elastic modulus are relatively lower. This is explained by the avoidance of contamination during the powder metallurgy process. This corresponds to the group that was prepared with only commercially available pure powders.

The arc-melted RHEA does not process a significantly lower hardness values than the other PM states. This can be explained by its microstructural features. The variation in hardness

and elastic modulus values of each of the alloys will be discussed in detail in the Discussion section.

5.5 $Al_{0.3}NbTa_{0.8}Ti_{1.5}V_{0.2}Zr$

The Refractory High Entropy Alloy studied in the last section was also subject of study in terms of varying the aluminum content. The variant $Al_{0.3}NbTa_{0.8}Ti_{1.5}V_{0.2}Zr$ was chosen to possess less Al content due to a potential enhancement in ductility caused by this fluctuation. The reasoning is that Al is a strong BCC_B2 former on the original alloy (as depicted in Fig. 14 in the literature review). This is composed of ordered BCC lattices and its presence is evidenced to decrease the ductility of RHEAs, especially at low temperatures [92,93]. Thus, potentially reducing the formation of BCC_B2, might potentially contribute for a higher ductility.

The intent of this research is to study the phase evolution and their corresponding compositions by several solution and aging treatments on the $Al_{0.3}NbTa_{0.8}Ti_{1.5}V_{0.2}Zr$ RHEA, as well as their effect into the mechanical properties of this alloy. The next sections will deal with the corresponding results.

5.5.1 Microstructural characterization of arc-melted and PM alloys

The material was produced by powder metallurgy, with a careful preparation by using glovebox for powders' handling with protective atmosphere to avoid excessive formation of oxides. Additionally, arc-melting samples were produced. The samples in the as-sintered and as-arc-melted states were named PM2 and AM2. Heat treatments were performed according to the scheme below.

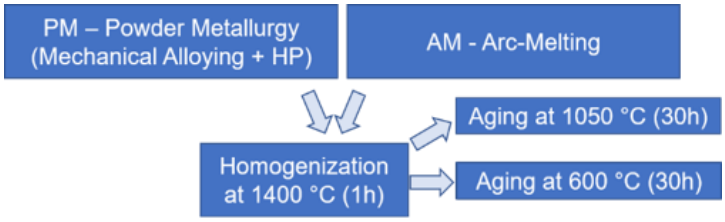

Fig. 76. Preparation scheme for $Al_{0.3}NbTa_{0.8}Ti_{1.5}V_{0.2}Zr$.

The XRD patterns of both powder metallurgy and arc-melted RHEAs and their respective heat treatments are exhibited in Fig. 77.

The as-sintered material (PM2) exhibits a microstructure composed of a main BCC crystal structure (BCC1) in 74.7 wt.% and a second BCC, referred as BCC2 in 24.3 wt.%. Additional peaks correspond to a minor phase corresponding to oxide (and thus named Oxide herein), of ZrO crystal structure in only 1.0 wt.%, space group Fm-3m and cubic crystal system. Please note, this ZrO crystal type possesses similar lattice constants and crystallographic characteristics as ZrC and ZrN.

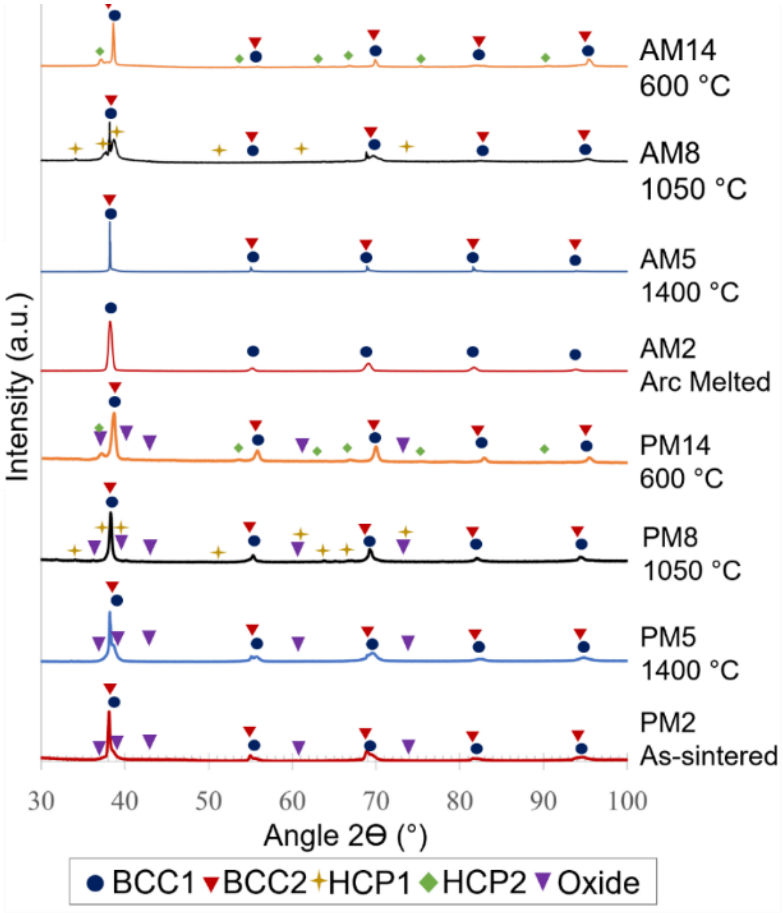

Fig. 77. XRD patterns of $Al_{0.3}NbTa_{0.8}Ti_{1.5}V_{0.2}Zr$ RHEA.

The lattice parameters of each detected phase and its content are found in Table 22.

		PM2		PM5		PM8		PM14	
Phase	Lattice	Lattice [Å]	wt. %	Lattice [Å]	wt. %	Lattice [Å]	wt. %	Lattice [Å]	wt. %
BCC1	a	3.32	74.7	3.31	76.8	3.32	76.3	3.29	71.4
BCC2	a	3.34	24.3	3.33	19.4	3.33	13.4	3.33	20
Oxide	a	4.62	1	4.62	3.8	4.56	5.5	4.64	4.6
HCP1	a	-	-	-	-	3.02	4.8	-	-
	c	-	-	-	-	4.72	-	-	-
HCP2	a	-	-	-	-	-	-	4.85	4.0
	c	-	-	-	-	-	-	5.90	-
		AM2		AM5		AM8		AM14	
Phase	Lattice	Lattice [Å]	wt. %	Lattice [Å]	wt. %	Lattice [Å]	wt. %	Lattice [Å]	wt. %
BCC1	a	3.34	100	3.32	88.3	3.31	74.2	3.36	70.2
BCC2	a	-	-	3.34	11.7	3.39	15.1	3.29	25.5
HCP1	a	-	-	-	-	3.07	10.7	-	-
	c	-	-	-	-	4.87		-	-
HCP2	a	-	-	-	-	-	-	4.85	4.3
	c	-	-	-	-	-	-	5.90	

Table 22. Lattice parameters from XRD patterns and respective phase content.

The microstructure of the PM RHEA before heat treatments is exhibited in Fig. 78. The red crosses represent EDS point analyses shown in Table 23.

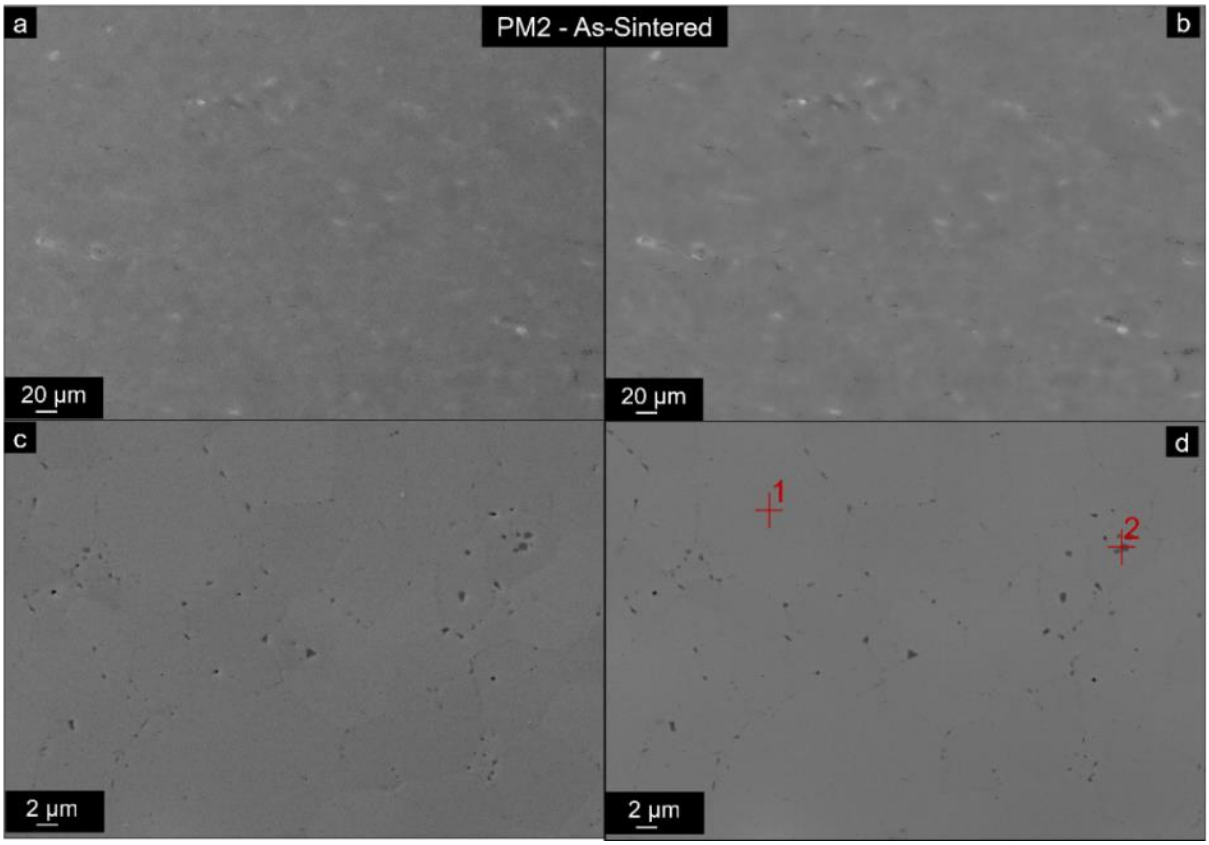

Fig. 78. Microstructure of PM2 RHEA in the as-sintered state. a,b) Overview in SE and BSE modes, respectively. c,d) Detail in higher magnification in SE and BSE modes, respectively. The red crosses denote EDS analyses.

The SEM images exhibit a nearly full-density microstructure, with virtually almost no pores evidenced. The BCC main phase is rich in -Ti, -Nb, -Ta and -Zr. There is a second phase –O rich on the grain boundaries, which probably correspond to the oxide particles detected by XRD. Please note that the phase is rather small, therefore the chemical composition of the surrounding BCC phase is probably being measured, due to the limited spot size of the EDS.

	PM2-As-sintered		PM5-1400 ºC		PM8-1050 ºC	PM14-600 ºC
[at.%]	Point 1 (BCC)	Point 2	Point 1 (BCC)	Point 2	Point 1 (BCC)	Point 1 (BCC)
Al	6.2 ± 0.1	0.4 ± 0.2	5.2 ± 0.1	4.0 ± 1.0	5.2 ± 0.1	4.4 ± 1.3
Ti	31.1 ± 0.6	4.6 ± 3.0	31.5 ± 0.4	14.5 ± 0.7	32.3 ± 0.1	35.3 ± 1.4
V	4.4 ± 0.2	-	4.3 ± 0.3	0.8 ± 0.9	4.7 ± 0.1	4.5 ± 0.4
Zr	21.7 ± 2.5	52.8 ± 6.7	20.5 ± 0.2	13.4 ± 3.4	18.5 ± 0.1	15.9 ± 1.0
Nb	19.1 ± 1.1	1.1 ± 0.3	20.0 ± 0.4	12.3 ± 2.1	20.8 ± 0.2	21.80 ± 2.2
Ta	17.4 ± 1.6	21.2 ± 1.1	18.5 ± 0.1	20.4 ± 2.5	18.6 ± 0.3	18.1 ± 0.5
O	-	19.9 ± 3.5	-	34.6 ± 4.0	-	-

Table 23. Chemical composition of the PM RHEA before and after heat treatments. These values correspond to the points exhibited in the SEM images.

After exposed to 1400 °C for 1h, the microstructure significantly changed, as visible in Fig. 79. The alloy exhibits a BCC matrix rich in Ti, Nb, Ta and Zr, and substantially more oxides especially present in the grain boundaries. These oxides are exhibited in Fig. 79c,d. According

to EDS point analysis, these are -O, -Ta and -Zr rich. The excessive formation of oxides appears to have taken place in the microstructure during the heat treatments. These seem to have been detached from the microstructure during polishing.

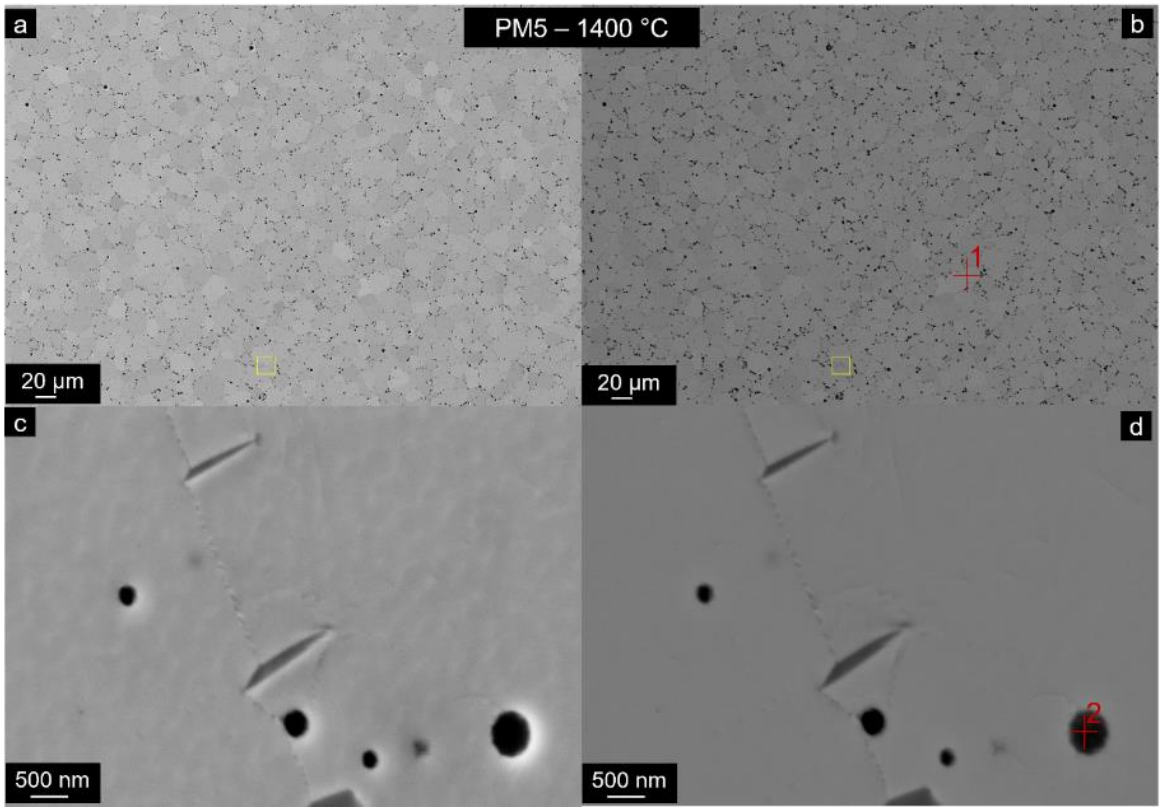

Fig. 79. Microstructure of PM5 RHEA after exposed to 1400 °C for 1h. a,b) Overview in SE and BSE modes, respectively. c,d) Detail in higher magnification in SE and BSE modes. The red crosses are EDS analyses.

EDS map and line spectrum were performed on the material – shown in Fig. 80 and Fig. 81, respectively, to qualitatively confirm the abundance of certain elements in these particles. The EDS images confirm the abundance of -O and -Ta elements on these areas.

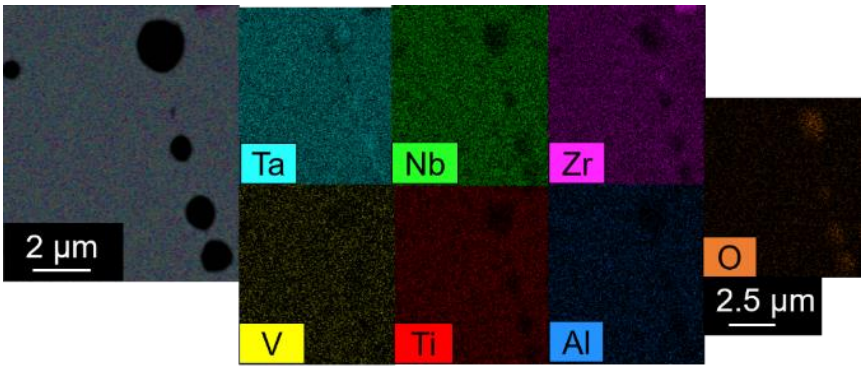

Fig. 80. EDS maps on PM5 exhibiting the presence of oxides.

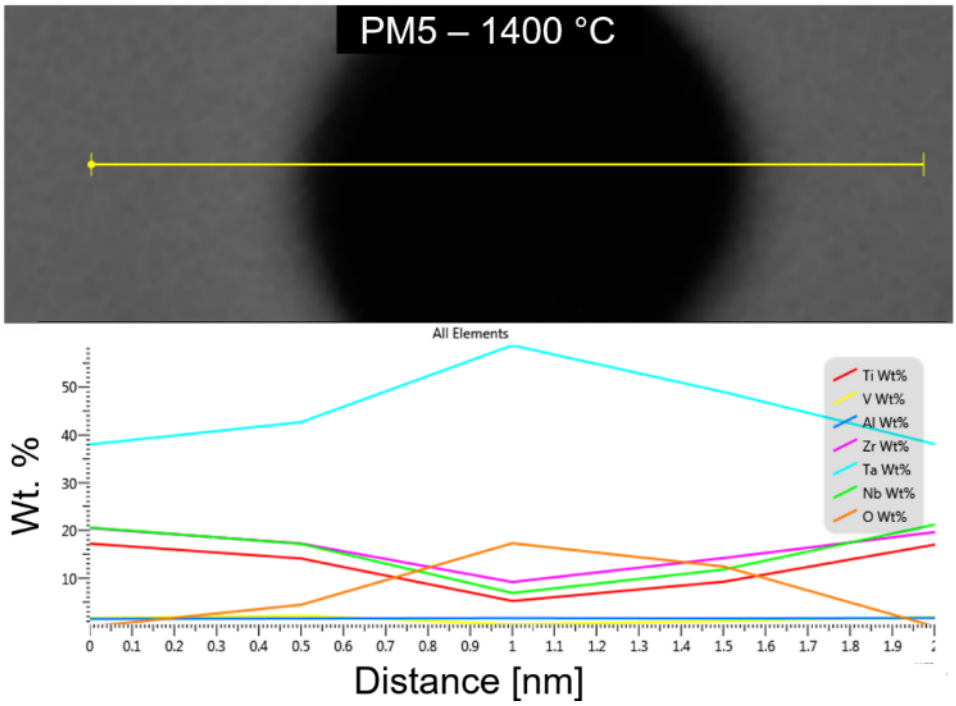

Fig. 81. EDS line spectrum on PM5 showing the increase in wt. % of Ta and O in the black areas.

The SEM images in Fig. 79c,d also display another phase growing in the grain boundaries region. These were too small to be detected by point analysis, therefore qualitative EDS maps were performed (Fig. 82). They show that these regions are Zr rich.

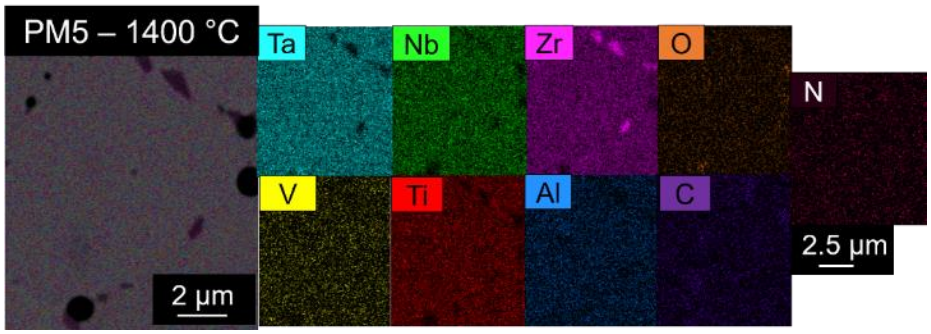

Fig. 82. EDS maps on PM5 exhibiting the presence of Zr rich phase precipitating in the grain boundaries.

After exposed to 1050 °C for 30 h, PM8 exhibits a BCC matrix with similar grain morphologies and chemical composition as the others, as seem in Fig. 83 and Table 23.

Additionally, the oxides are present and the occurrence of a phase growth in the grain boundaries region preferentially took place. This phase is too small to be assessed by EDS point analysis. Therefore, EDS maps (shown in Fig. 84) detect that this is a Zr- rich phase.

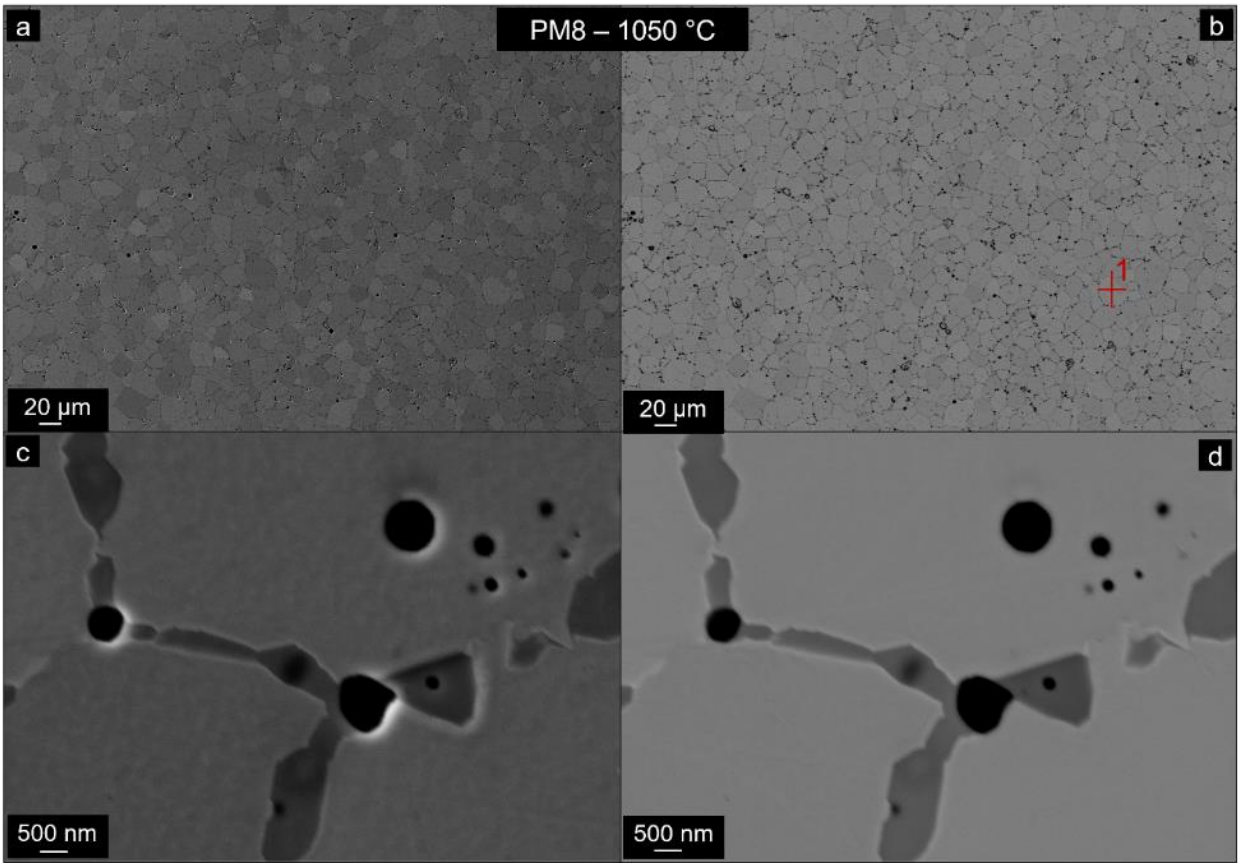

Fig. 83. Microstructure of PM8 RHEA after exposed to 1050 °C for 30h. a,b) Overview in SE and BSE modes, respectively. c,d) Detail in higher magnification in SE and BSE modes. The red crosses are EDS analyses.

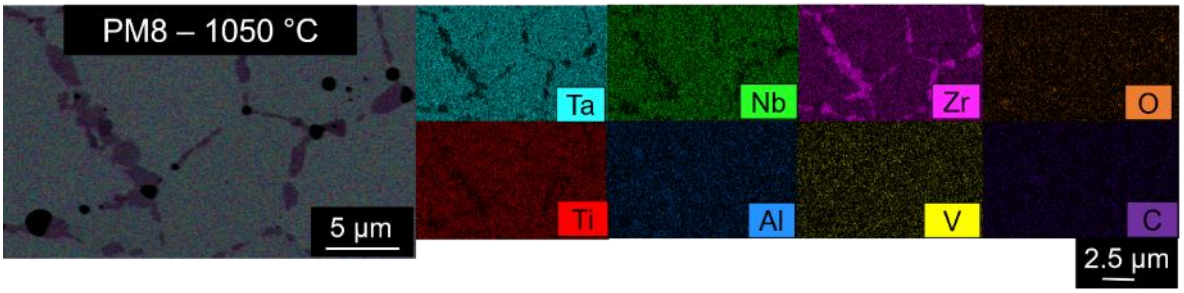

Fig. 84. EDS maps on PM8 exhibiting the presence of Zr rich phase growing in the grain boundaries.

Finally, after submitted to 600 °C for 30 h, the PM14 RHEA displays a quite interesting microstructure as shown in Fig. 85, composed of BCC grains and very fine nano-sized precipitates within the BCC matrix. The oxides are visible in the grain boundaries.

The arc-melted RHEA in the as-melted state (AM2), on the other hand, is exhibited in Fig. 86a,b. Its chemical composition along with the ones of the other samples is shown in Table 24. AM2 displays a dendritic microstructure caused by the solidification from the melting. The interdendritic region is rich in Ti, Nb and Ta; the dendritic region is Zr-, Ti-, Al-, Nb- rich.

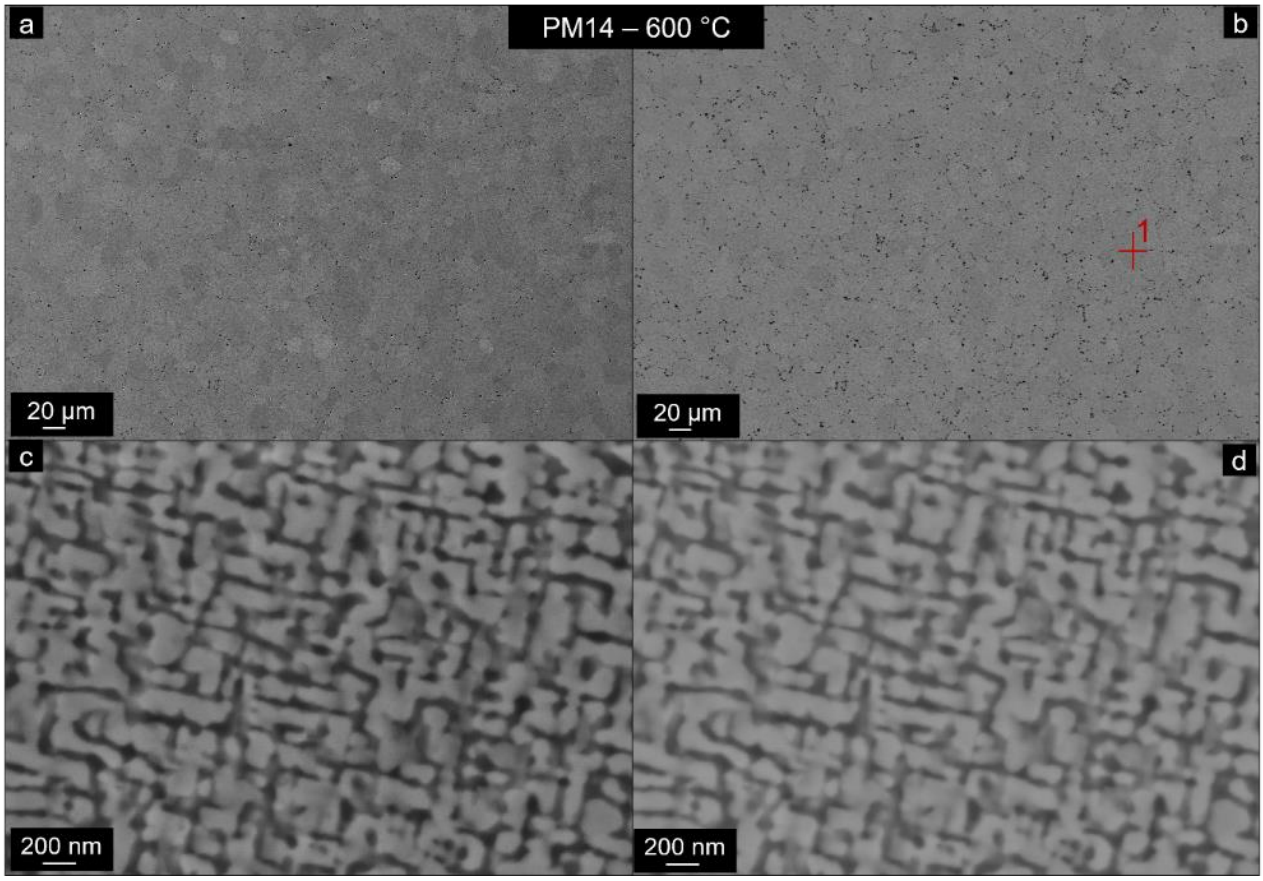

Fig. 85. Microstructure of PM14 RHEA after exposed to 600 °C for 30h. a,b) Overview in SE and BSE modes, respectively. c,d) Detail in higher magnification in SE and BSE modes. The cross is EDS analysis.

	AM1 - Arc-melted		AM5 - 1400 °C	AM8 - 1050 °C		AM14 - 600 °C
[at.%]	Point 1 Dendrites	Point 2 Interdendrites	Point 1 (BCC)	Point 1 (BCC)	Point 2	Point 1 (BCC)
Al	4.5 ± 0.1	11.4 ± 0.1	5.7 ± 0.1	5.7 ± 0.2	16.5 ± 2.6	5.8 ± 0.1
Ti	29.8 ± 0.4	32.2 ± 0.1	31.3 ± 1.0	32.3 ± 0.5	14.8 ± 0.7	31.4 ± 0.4
V	4.2 ± 0.1	4.3 ± 0.1	3.8 ± 0.2	4.1 ± 0.3	3.4 ± 0.3	4.1 ± 0.2
Zr	16.3 ± 0.7	26.4 ± 0.1	20.5 ± 0.1	12.1 ± 0.5	58.9 ± 3.2	20.8 ± 0.3
Nb	22.4 ± 0.3	12.7 ± 0.2	20.6 ± 0.2	26.4 ± 0.17	3.8 ± 0.7	20.2 ± 0.2
Ta	22.8 ± 0.8	13.0 ± 0.1	18.1 ± 18.2	19.3 ± 0.2	2.6 ± 0.2	17.7 ± 0.8

Table 24. EDS point analyses of phases present in the arc-melted alloy before and after heat treatments. The measurements correspond to the red crosses exhibited in the SEM images.

The alloy (AM5), after subjected to 1400 °C for 1h, shows dissolution of the dendrites and exhibits large BCC grains rich in Ti, Zr, Nb and Ta. The SEM images are shown in Fig. 86c,d. After 30 h at 1050 °C, on the other hand, AM8 displays a more complex microstructure, with intragranular precipitates within the main BCC phase (Fig. 87), as well as along the grain boundaries. According to EDS analyses, these precipitates are rich especially in Zr and Al. The BCC phase is consequently depleted of Zr.

Alternatively, after submitting the alloy to a temperature of 600 °C for 30 h directly from the homogenization treatment at 1400 °C, very fine nano-sized precipitates appear within the BCC main phase.

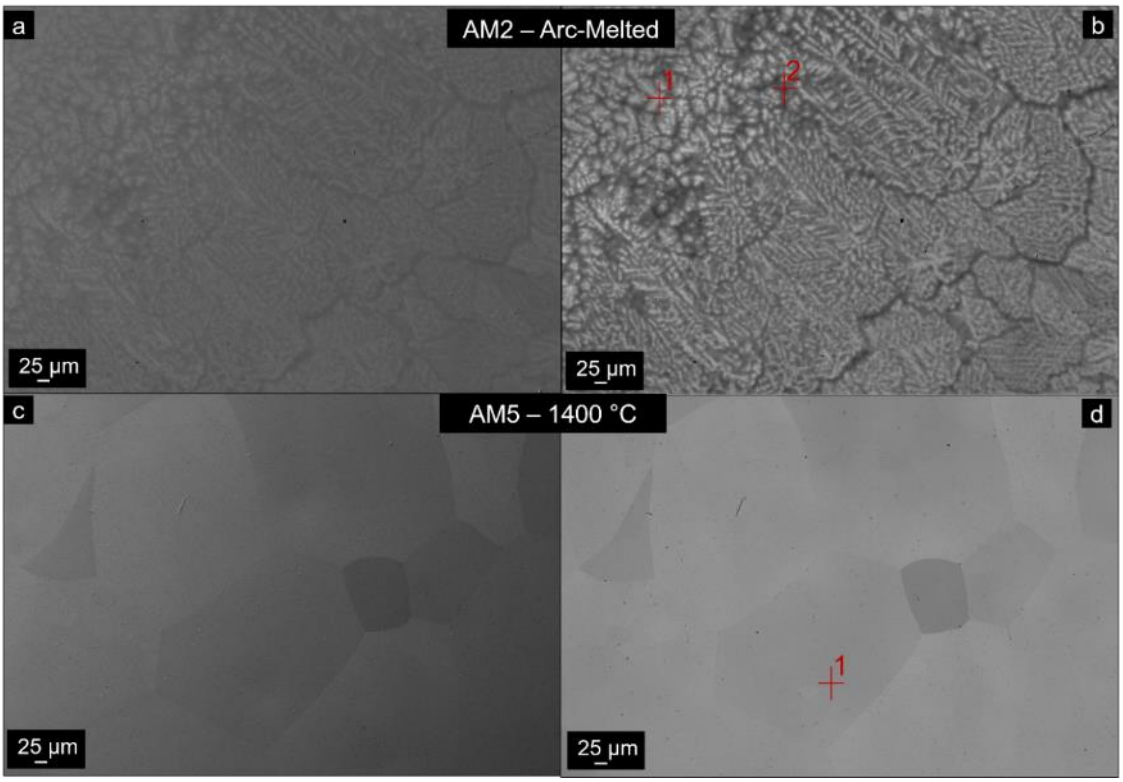

Fig. 86. Microstructure of arc-melted RHEAs. a,b) SEM images of as-melted state in SE and BSE modes, respectively. c,d) SEM images of AM5 in SE and BSE modes. The red crosses are EDS analyses.

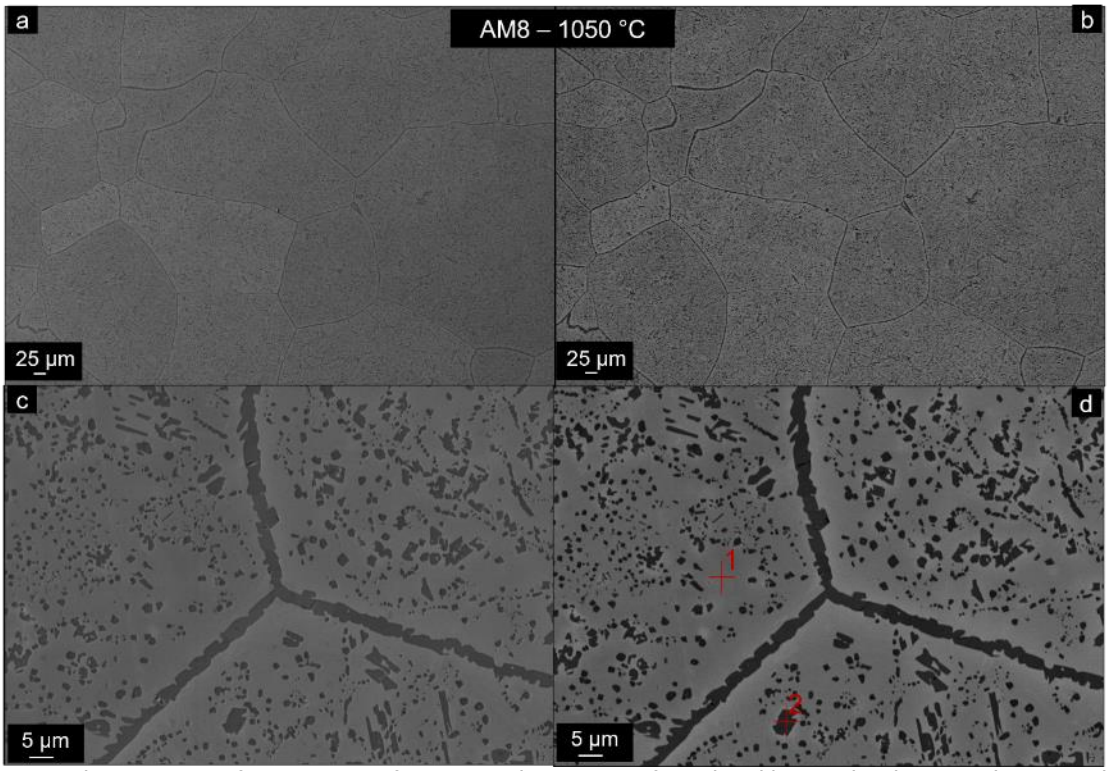

Fig. 87. Microstructure of AM8 RHEA after exposed to 1050 °C for 30h. a,b) Overview in SE and BSE modes, respectively. c,d) Detail in higher magnification in SE and BSE modes. The red crosses are EDS analyses.

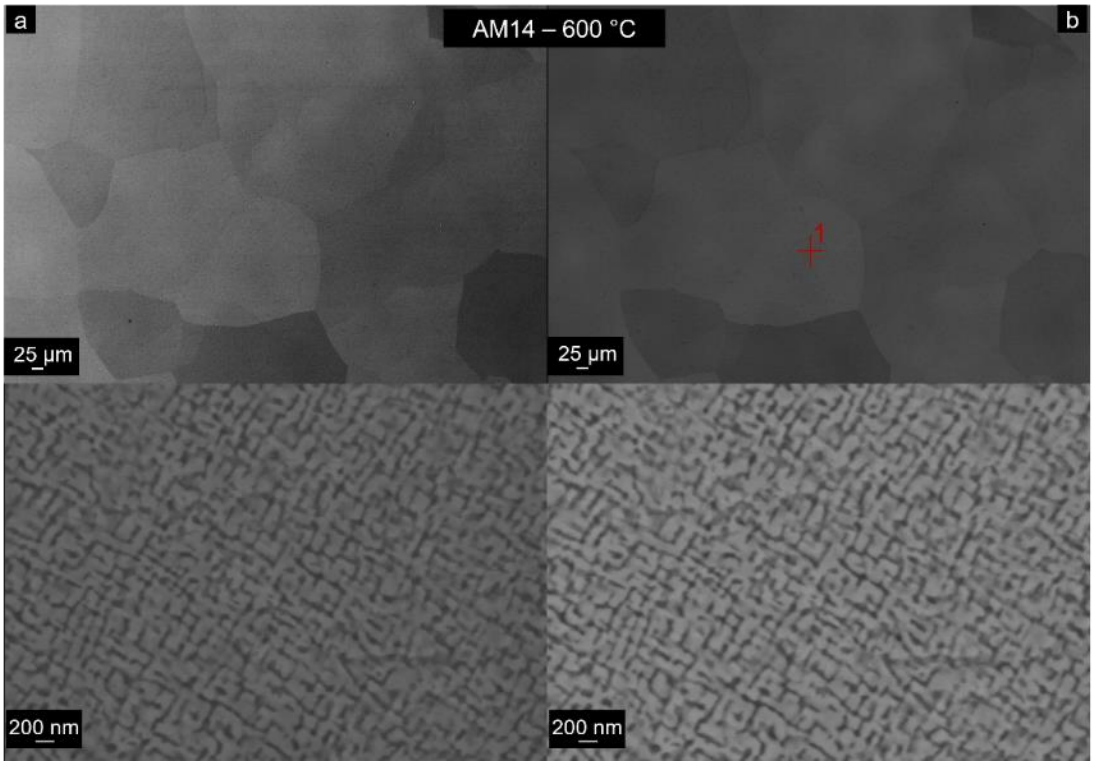

Fig. 88. Microstructure of AM8 RHEA after exposed to 1050 °C for 30h. a,b) Overview in SE and BSE modes, respectively. c,d) Detail in higher magnification in SE and BSE modes. The cross is EDS analysis.

For quantitative evaluation of the microstructure, EBSD analyses have been performed, with results concerning the phase distribution, orientation and grain sizes of the PM and arc-melted alloys presented in Fig. 89 and Fig. 90, respectively.

None of the phases comprised in PM RHEA before and after heat treatments show any important preferential orientation, as evidenced by their low MUD values.

The PM RHEA in the as-sintered state (PM2) exhibits very fine BCC matrix with average grain sizes of (5.87 ± 0.4) µm. The oxides were measured to possess sizes of (0.89 ± 0.10) µm. They are mainly dispersed along the grain boundaries of the matrix.

After being submitted to heat treatment of 1 h at 1400 °C, the BCC matrix suffers significant grain growth, showing an average grain size of (18.01 ± 1.27) µm. The oxides do not grow substantially in size, with an average of (0.93 ± 0.21) µm.

Additional heat treatment at 1050 °C for 30 h induces only a slight further growth of the BCC matrix, showing average grain sizes of (18.76 ± 0.54) µm. The oxides here exhibit an average grain size of (1.31 ± 0.11) µm.

Alternative heat treatment at 600 °C for 30 h directly from the heat treatment at 1400 °C evidences similar grain sizes as in the previous state, with BCC matrix showing an average of (17.93 ± 0.42) µm grain size. The oxides display sizes of (1.14 ± 0.16) µm.

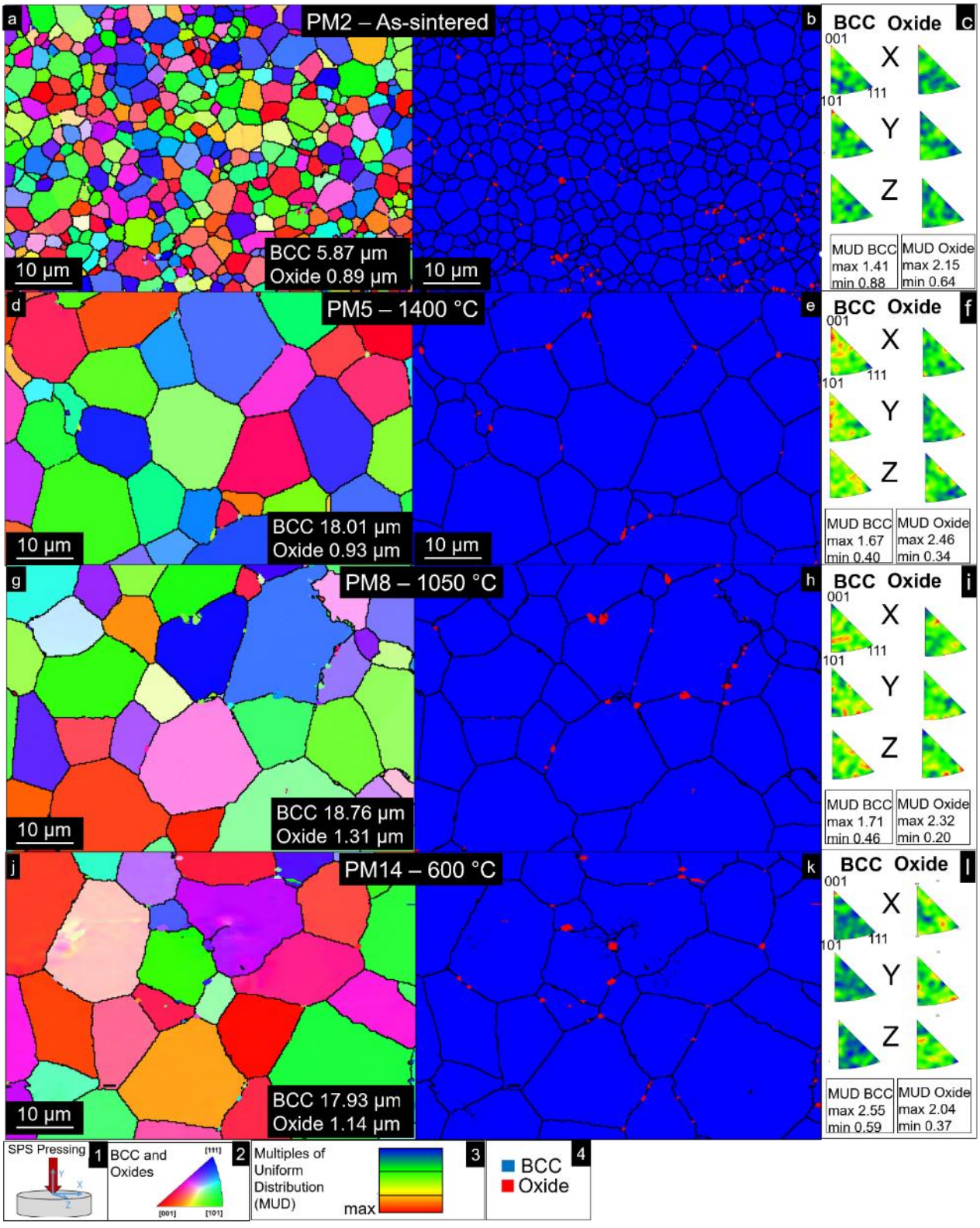

Fig. 89. Representative SEM EBSD analysis of the PM RHEA. a,d,g,j) Grain orientation maps of PM2, PM5, PM8 and PM14 with reference direction Z denoted in 1, the grain orientation reference is shown in 2. b,e,h,k) Phase map showing distribution of BCC and Oxide phases in PM2, PM5, PM8 and PM14. The corresponding legend is shown in 4. c,f,i,l) Respective inverse pole figures denoting orientation in X, Y and Z direction with MUD reference in 3.

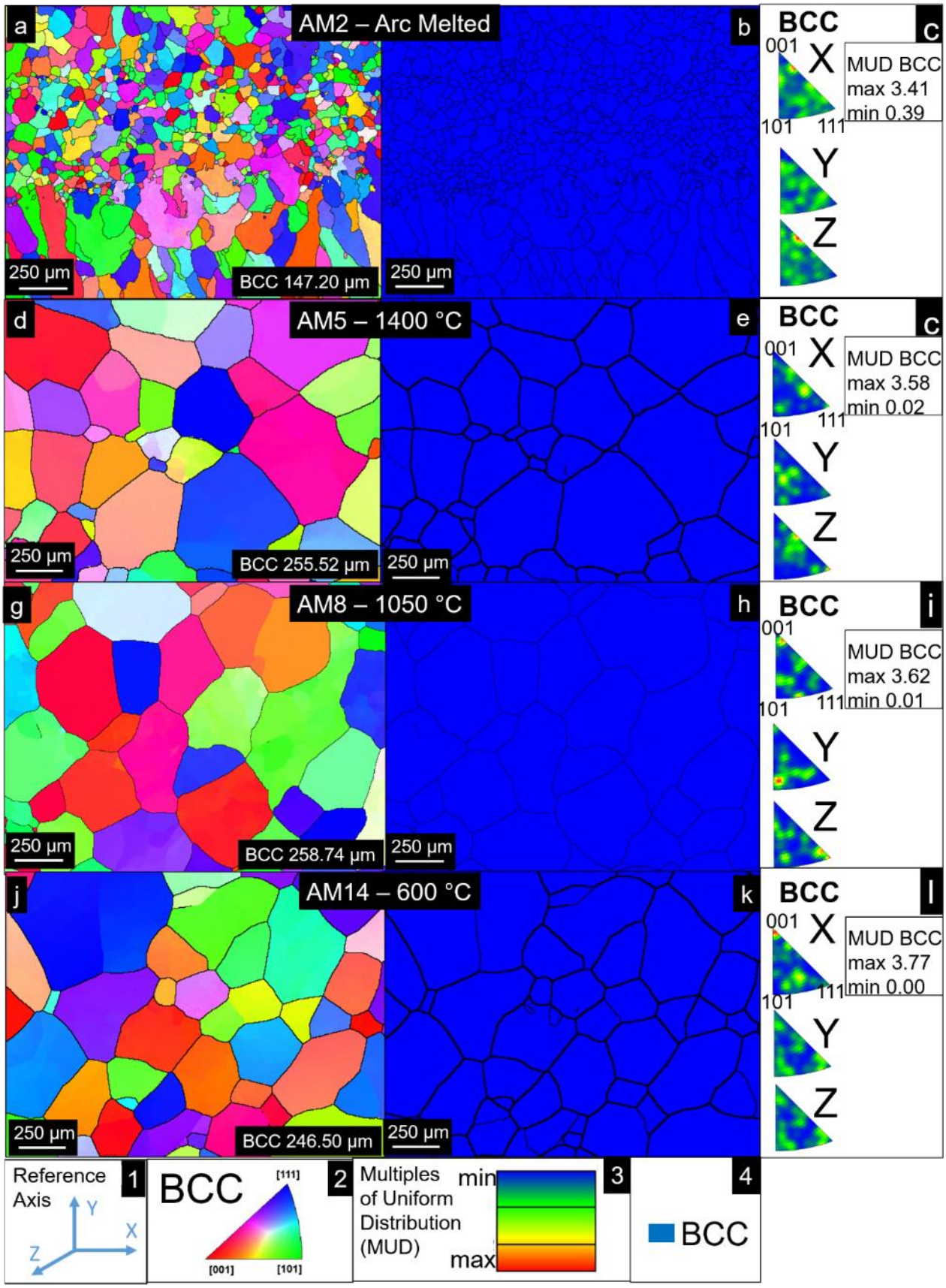

Fig. 90. Representative SEM EBSD analysis of the AM RHEA. a,d,g,j) Grain orientation maps of AM2, AM5, AM8 and AM14 with reference direction Z denoted in 1, the grain orientation reference is shown in 2. b,e,h,k) Phase map showing distribution of BCC and Oxide phases in AM1, AM4, AM7, AM10 and AM13 with legend in 4. c,f,i,l) Respective inverse pole figures denoting orientation in X, Y and Z direction with MUD reference in 3.

The arc-melted RHEA, contrarily, exhibits importantly larger grain sizes in all states. The as-melted state (AM2) shows a slight preferential crystallographic orientation due to the formation of the dendrites caused by the solidification development. However, its MUD is low and comparable to the other states, therefore this preference is not strong. The grain sizes exhibited by the BCC phase in this state averages (147.20 ± 25.8) µm. The large uncertainty is resulting from the large grains pertaining to the preferential orientation.

After heat treatments, the AM RHEA do not show any significant crystallographic texture as evidenced by Fig. 90a,d,g,j and their respective inverse pole figures. The homogenization at 1400 °C for 1 h, induces significant growth in AM5 alloy's BCC grain size, showing an average of (255.52 ± 6.16) µm. Additional heat treatment at 1050 °C for 30 h induces a slight grain size increase in AM8, with an average of (258.74 ± 8.01) µm. Alternatively, with aging at 600 °C for 30 h, AM14 do not suffer any important increase in grain size of the BCC phase, exhibiting average sizes of (246.50 ± 6.23) µm.

5.5.2 Mechanical properties

The mechanical behaviour of the RHEAs produced by arc-melting and powder metallurgy were assessed by Vickers microhardness and nanoindentation hardness for calculation of elastic modulus in all materials. After heat treatments, excitation method for measuring the elastic modulus and flexural tests were performed on the aged samples. The results are shown in Table 25.

	Hardness [HV]	E. Modulus (Indentation) [GPa]	E. Modulus (Excitation Method) [GPa]	Stress at Maximum Load [MPa]
AM2 – Arc-Melted	495 ± 4	121 ± 1	-	-
AM5 - 1400°C	502 ± 9	117 ± 2	99.91 ± 0.01	294.2 ± 37.6
AM8 - 1050°C	585 ± 7	125 ± 1	105.25 ± 0.12	414.1 ± 22.1
AM14 - 600°C	498 ± 9	128 ± 4	110.75 ± 0.25	701.9 ± 51.4
PM2 – As-sintered	556 ± 4	127 ± 3	-	-
PM5 - 1400°C	574 ± 11	119 ± 4	103.47 ± 0.15	599.5 ± 87.0
PM8 - 1050°C	620 ± 7	127 ± 3	106.21 ± 0.28	564.3
PM14 - 600°C	612 ± 5	129 ± 2	109.32 ± 0.22	1128.2 ± 74.4

Table 25. Results of PM and AM RHEAs exposed to heat treatments in terms of hardness, elastic modulus and flexural tests.

The PM material before and after heat treatments possesses hardness and elastic modulus with values higher than their arc-melted counterparts. The results of flexural tests show that AM14 and PM14 exhibit the highest values of stresses at maximum load. This is attributed to their unique microstructural features. An appropriate discussion of the relationship between the mechanical behaviour of the materials and their microstructures is elaborated in the Discussion section.

The respective curves from flexural test results performed at room temperature are exhibited in Fig. 91.

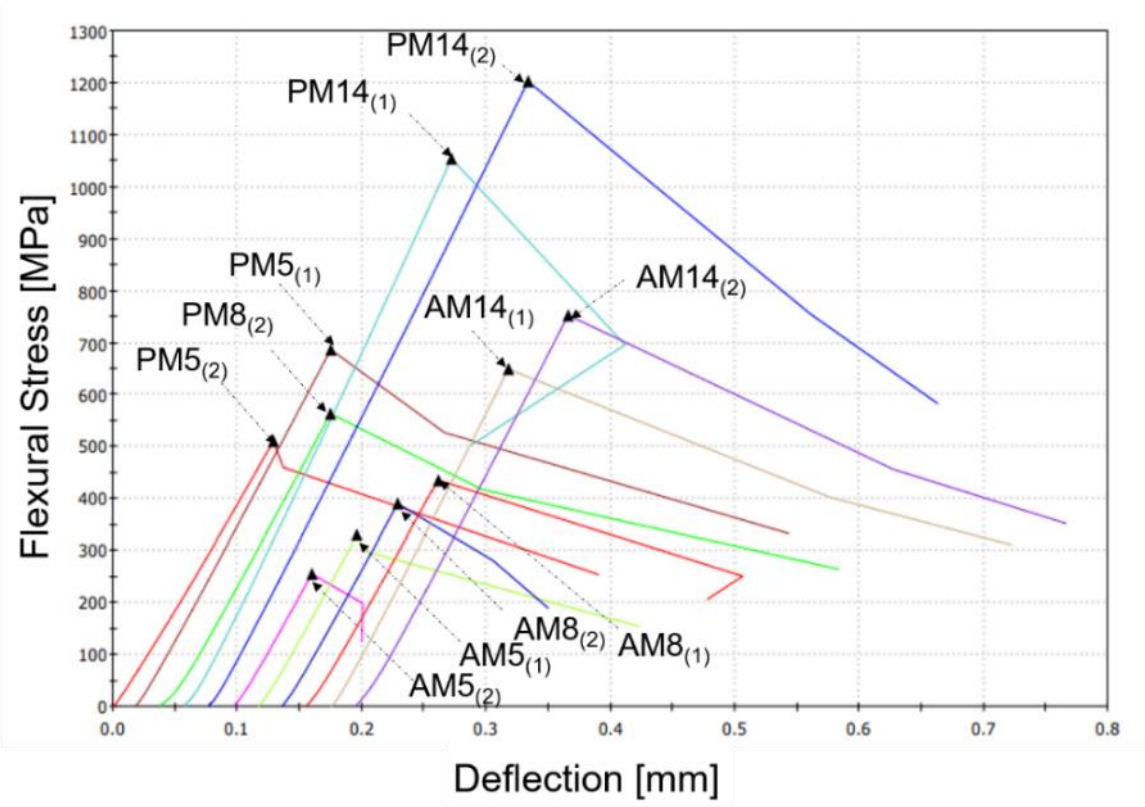

Fig. 91. Curves taken from flexural tests displaying flexural stress vs deflection.

It is possible to see that, from macroscopic point of view, all materials behave in a brittle manner, as significant strain is not observed.

For a more detailed assessment, after the fracture, the materials were analyzed by SEM in order to evaluate the fractographic features of the ruptured specimens on their cross section. The results of the fractographic analysis of the arc-melted alloy submitted to 1400 °C for 1h (AM5) are shown in Fig. 92. The other arc-melted alloys exposed to 1050 °C and 600 °C for 30h (AM8 and AM14, respectively) are shown in Fig. 99 and Fig. 100, in order.

The arc-melted alloys exhibit a typical brittle fracture surface morphology in all states, with large cleavage facets corresponding to the cracking of brittle phases with multiple initiation sites. For instance, in Fig. 92c,d is possible to observe typical total cleavage separation of brittle phase. These are exhibited for all arc-melted alloys.

The results of PM RHEA exposed to 1400 °C for 1h is shown in Fig. 95; to 1050 °C for 30h is shown in Fig. 96 and at °C for 30h is shown in Fig. 97.

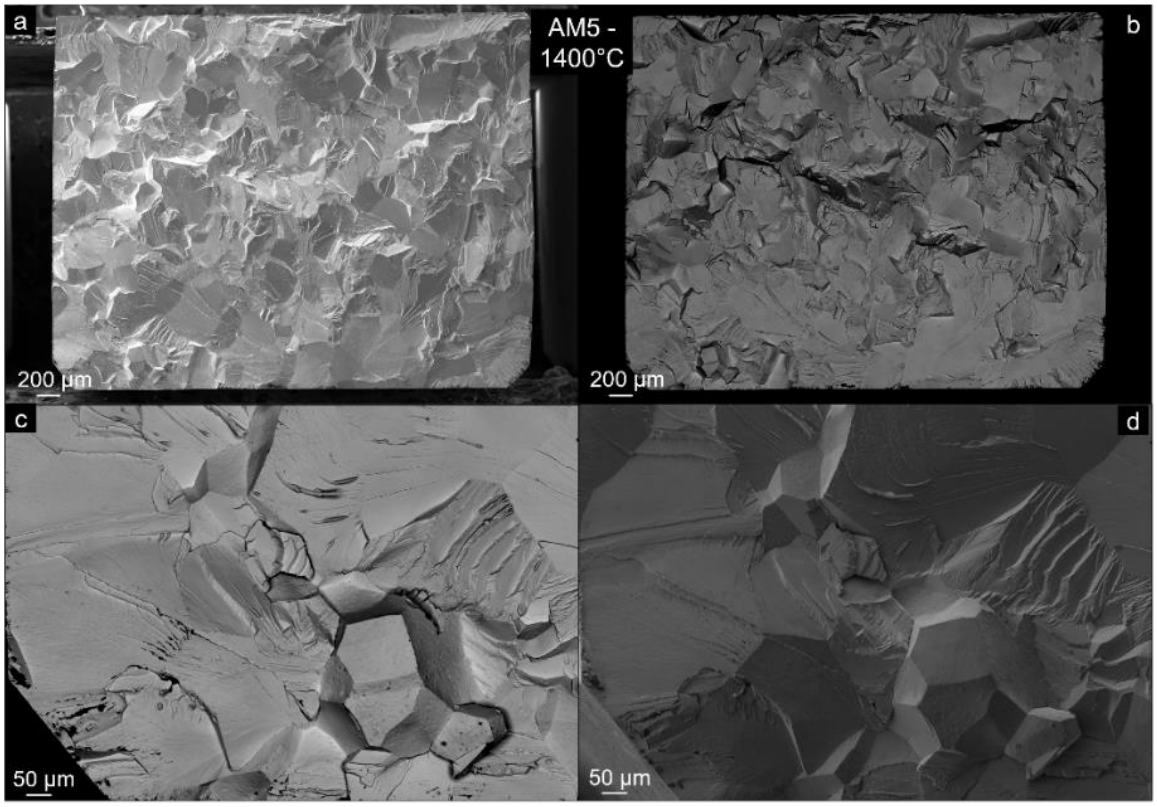

Fig. 92. SEM micrographs of fracture surfaces of AM5 bending specimens. The compression side is upwards, while the tension side is downwards and has grinded edges. a,b) Typical fracture surface morphology using SE and BSE detectors, respectively. c,d) Enlarged view of the microstructure in SE and BSE modes.

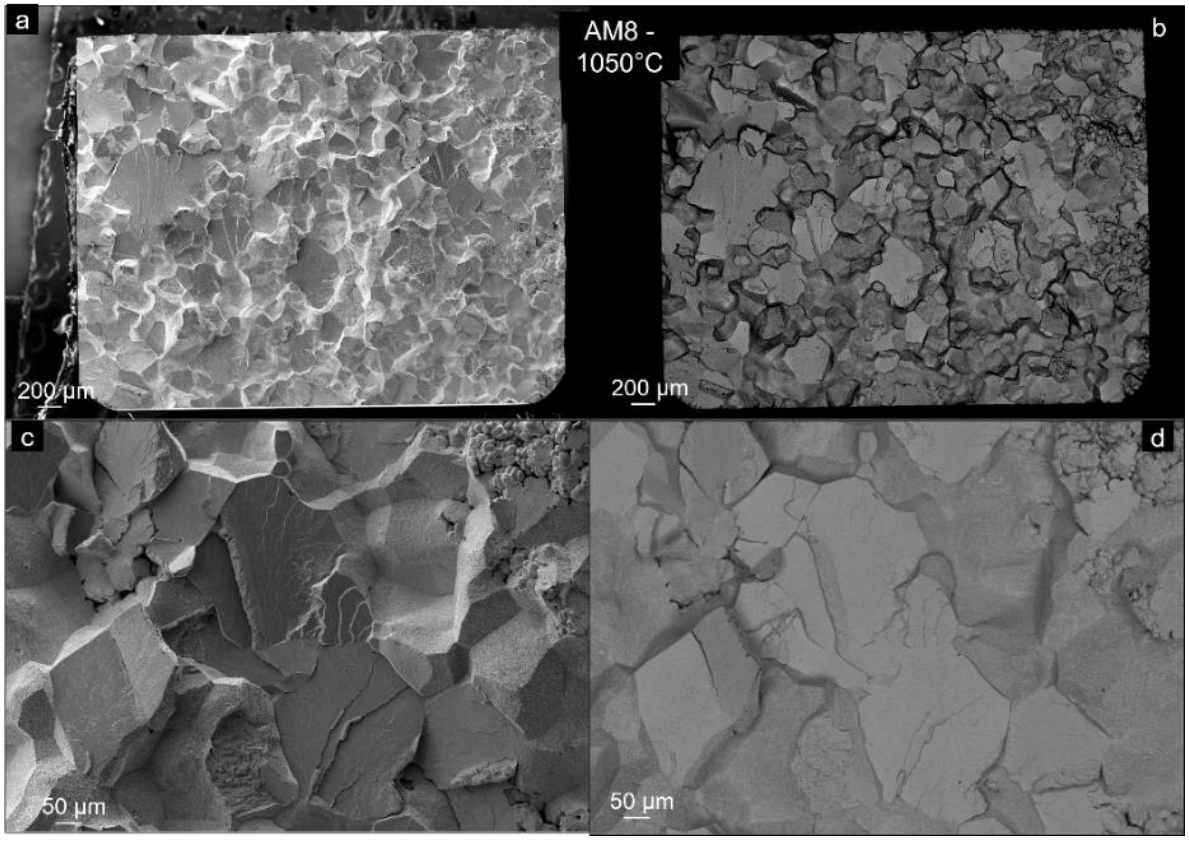

Fig. 93. SEM micrographs of fracture surfaces of AM8 bending specimens. The compression side is upwards, while the tension side is downwards and has grinded edges. a,b) Typical fracture surface morphology using SE and BSE detectors, respectively. c,d) Enlarged view of the in SE and BSE modes.

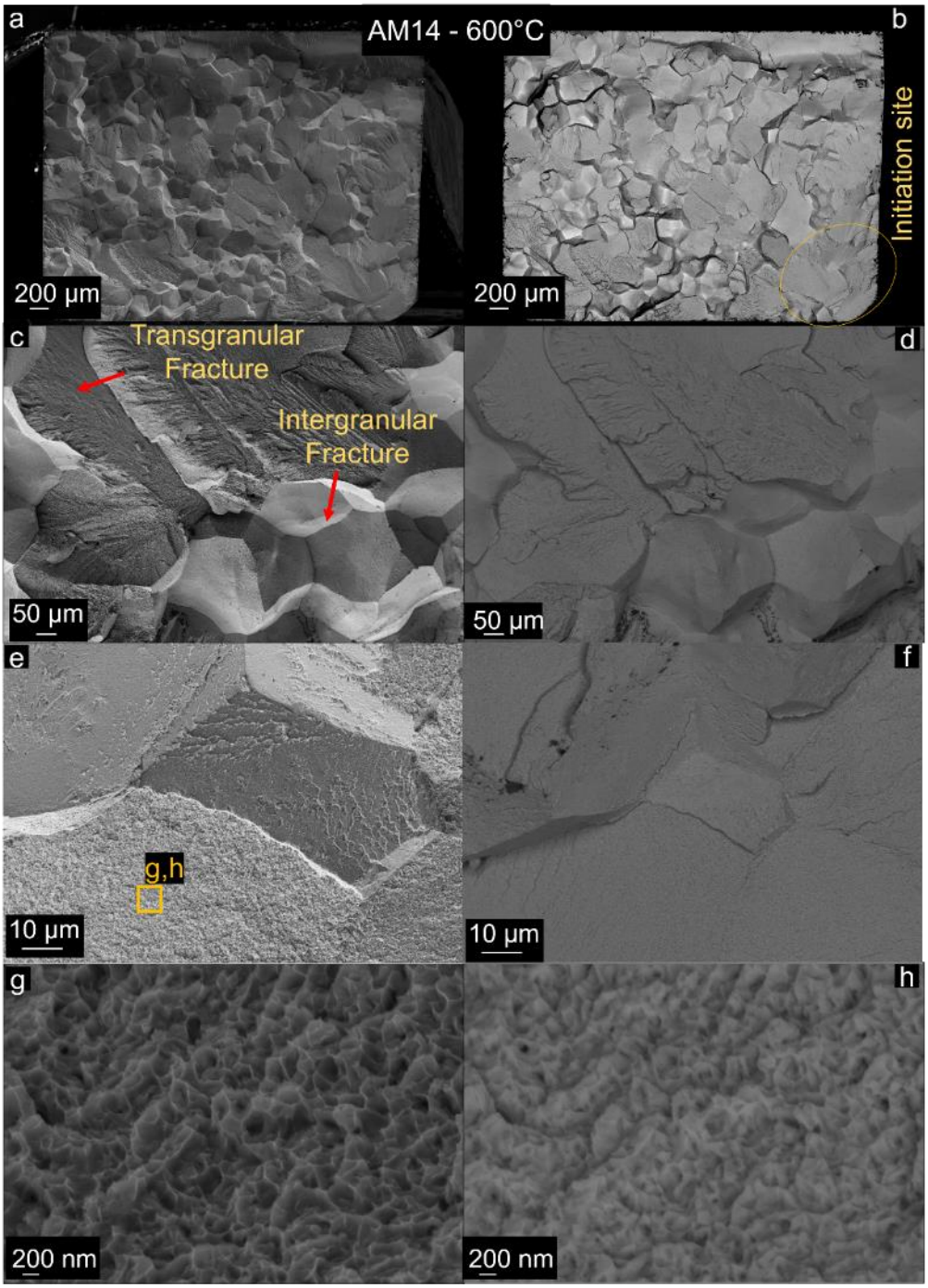

Fig. 94. SEM micrographs of fracture surfaces of AM14 bending specimens. The compression side is upwards, while the tension side is downwards and has grinded edges. a,b) Typical fracture surface morphology using SE and BSE detectors, respectively. c,d) Enlarged view of the microstructure in SE and BSE modes. e,f) Highly-magnified views, using SE and BSE modes, respectively. g,h) Enlarged view of the rectangle shown in (e), in SE and BSE modes.

The PM material exhibits also brittle fracture mechanisms in all states with cleavage facets present, however several differences are shown in comparison with AM counterparts. Firstly, the grain sizes are much smaller for the powder metallurgy materials. Additionally, a large amount of areas pertaining to oxide particles mostly along the grain boundaries are seen. These were detached from the matrix, indicating a weak metallurgical bonding of the oxides

with the matrix. These alloys evidence multiple initiation sites from the surface. Typical initiation sites are marked in red arrows. A thorough discussion is found in the Discussion.

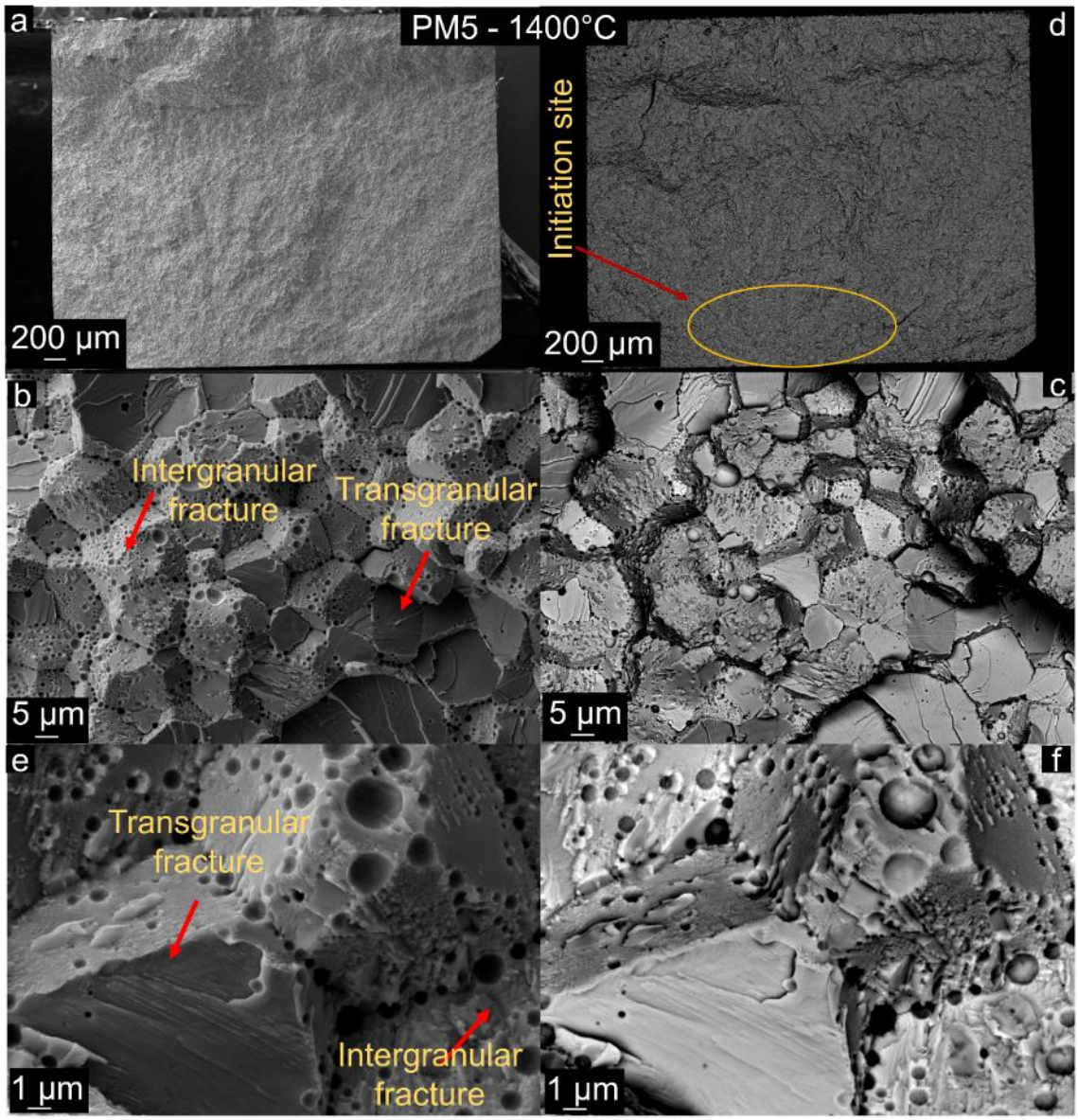

Fig. 95. SEM micrographs of fracture surfaces of PM5 bending specimens. The compression side is upwards, while the tension side is downwards and has grinded edges. a,b) Typical fracture surface morphology using SE and BSE detectors, respectively. c,d) Enlarged view of the micromorphology in SE and BSE modes. e,f) Further enlarged views of the microstructure in SE and BSE modes, respectively.

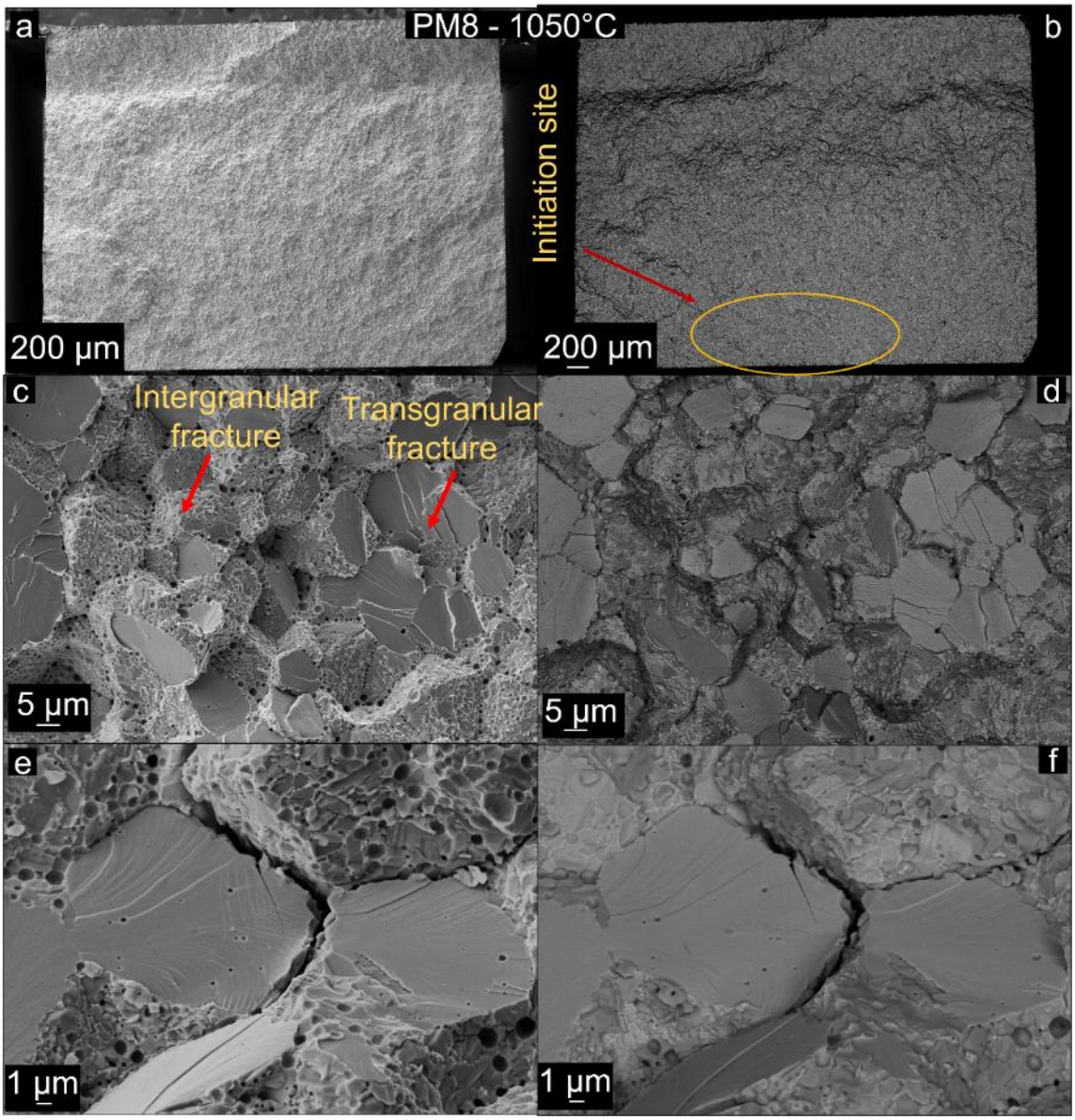

Fig. 96. SEM micrographs of fracture surfaces of PM8 bending specimens. The compression side is upwards, while the tension side is downwards and has grinded edges. a,d) Typical fracture surface morphology using SE and BSE detectors, respectively. b,c) Enlarged view of the microstructure in SE and BSE modes. e,f)Further enlarged views of the microstructure in SE and BSE modes, respectively.

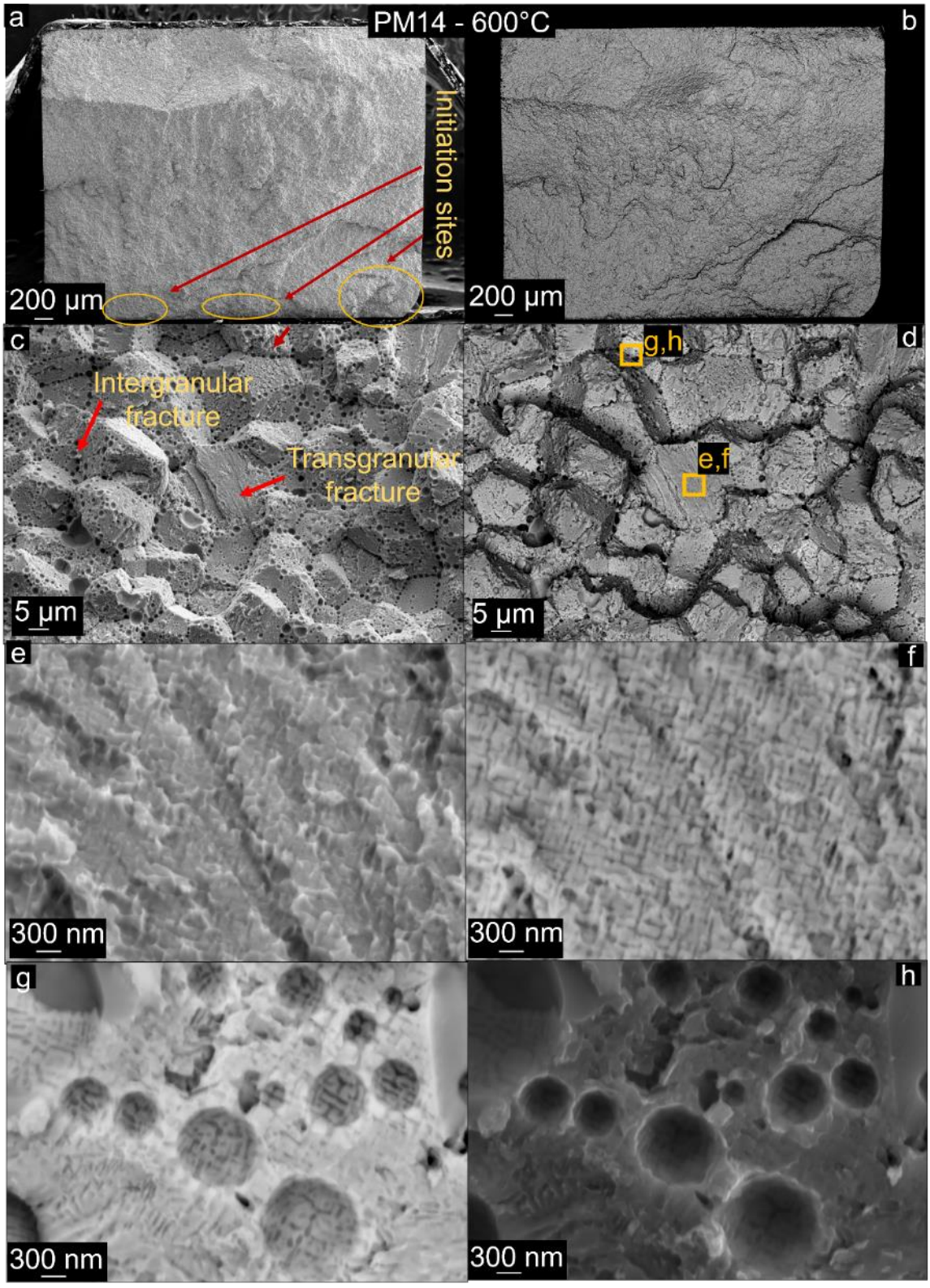

Fig. 97. SEM micrographs of fracture surfaces of PM14 bending specimens. The compression side is upwards, while the tension side is downwards and has grinded edges. a,b) Typical fracture surface morphology using SE and BSE detectors, respectively. c,d) Enlarged view of the microstructure in SE and BSE modes. e,f) Further enlarged views of the micromorphology of the area shown by the rectangle in (d) in SE and BSE modes, respectively. g,h) Area exhibited by the rectangle in (d) in SE and BSE modes, respectively.

6 Discussion

6.1 $Al_{0.2}Co_{1.5}CrFeNi_{1.5}Ti$ high entropy alloy

6.1.1 Microstructural characterization (as-sintered and as-cast states)

The prediction of phases by CALPHAD is in good agreement with the experimental observations on the as-sintered and as-cast states of $Al_{0.2}Co_{1.5}CrFeNi_{1.5}Ti$, even using the first HEA database in ThermoCalc (TCHEA1).

Due to the large negative enthalpy of mixing of Al-containing HEAs, intermetallics are expected to be formed on this $Al_{0.2}Co_{1.5}CrFeNi_{1.5}Ti$ composition, leading to a multi-phase structure in which the relative volumes of FCC and BCC phases are strongly dependent on the cooling rates [171]. The high molar ratios of Co and Ni, known as being efficient FCC formers, guarantee that FCC remains the dominant phase.

The preparation of PM alloy consisted from heating the solid powders with already homogenous chemical composition to 1100 °C sintering temperature, short dwell time and relatively rapid cooling. In accordance with the thermodynamic prediction, FCC solid solution, ordered FCC L12 and BCC were experimentally observed in the powder metallurgy (PM) HEA (confirmed by TEM), in which the solid-state sintering took place at 1100 °C.

Despite the predicted liquid phase present at 1100 °C, no melting was observed during sintering. This could be a consequence of short sintering time and high pressure which may increase the melting temperature. The phase composition formed at 1100 °C was then retained to room temperature due to relatively rapid cooling after sintering, preventing nucleation and growth of Laves and sigma (σ) precipitates. As seen in Fig. 29b, the temperature of the first stable equilibrium occurrence of sigma (σ) phase of this particular alloy during cooling is 883 °C. However, our sintering temperature was carried out in a rapid heating rate of 100 °C.min^{-1} up to 1000 °C, and then slowed down to 50 °C.min^{-1} up to the final temperature of 1100 °C, followed by a relatively rapid cooling after the sintering.

Due to the short processing times (fast heating and cooling), the nucleation of sigma (σ) phase in the PM alloy was avoided; in other words, the time spent in the temperature range where effective diffusion would allow for sigma phase nucleation and growth was not sufficiently long. This is in accordance with other studies: the kinetics of nucleation of the sigma phase was observed to be extremely slow in HEAs [172], particularly in FCC ones containing Ni. Here, the nickel acts as a strong stabilizer of the FCC solid solution, suppressing the formation of the Cr-rich σ phase. In fact, the σ phase was shown to be formed in the $CrMnFeCoNi_x$ alloy only after annealing at 700 – 900 °C for more than 1000 h.

Similarly, the temperature for formation of Laves phase during cooling is about 793 °C. Therefore, the formation of Laves phase did not take place as well. On the other hand, the nucleation of ordered FCC L12 phase took place due to the slower heating rate (50 °C.min^{-1}) from 1000 °C up to the maximum temperature of 1100 °C.

The thermodynamic calculation was also in good agreement with the phases detected in the Cast HEA: FCC disordered, BCC, Laves and σ. The latter two phases most likely precipitated during cooling at temperatures below 800 ºC. In HEAs, Cr has been repeatedly reported to promote the formation of the σ sigma phase, particularly in the presence of Fe, Co, and Ni [173]. The ordered FCC L12 might either not have formed in the structure or may not have been detected in the alloy due to having content below the detection threshold of the techniques used for phase analysis (XRD + EBSD). It should be noted that the occurrence of a certain segregation is expected in the cast alloy due to liquid-solid transformation. On the other hand, segregation effects are completely omitted in PM HEA due to solid-phase processing.

It should be noted that some discrepancies between calculations and experiments may always arise due to the real nature of the materials' experimental conditions—as they may be in a state close to equilibrium but may also contain metastable phases. The phase diagrams are essentially calculated for a thermodynamic equilibrium state characterized by a global minimum of Gibbs energy [174]. Experimentally, this could only be reached by extremely slow cooling conditions or prolonged annealing times [175]. On the other hand, our experimental materials were cooled rapidly, avoiding the formation of some phases.

The predicted phases were confirmed in our alloys by TEM - selected area electron diffraction patterns (SAED) and XRD. A lattice-parameters comparison of the respective phases of each alloy from XRD and SAED indicates that they possess analogous FCC matrices and BCC phase in common.

The XRD peaks for TiC were detected only for the PM HEA, as expected, demonstrating that carbide formation is thermodynamically favourable during the powder milling process due to the nature of the technique, as previously reported in [176]. As carbon was not initially present in the feedstock powders, the decomposition of the toluene used as a milling agent for preparing powders for PM HEA should be regarded as its source. Consequently, an in-situ reaction of carbon and titanium took place, owing to their having the highest chemical affinity among the used elements.

The occurrence of annealing twins formed due to the high-temperature exposure of the PM HEA during SPS points out to the low stacking fault energy (SFE) of the FCC matrix, as the twinning boundary represents a long stacking fault (analogous to FCC austenitic steels [177]). The annealing twins are generated during recrystallization of the mechanically alloyed powder microstructures [22,178] at the sintering temperature.

The PM and Cast HEAs possess identical overall chemical compositions, as established by area EDX TEM mapping (Table 2), matching the $Al_{0.2}Co_{1.5}CrFeNi_{1.5}Ti$ stoichiometric ratio. Both the PM and cast FCC matrices are Fe-, Ni- and Co-rich (Table 2). The difference in the chemical composition of both alloys lies in the Ti partitioning. In the cast alloy, the FCC matrix phase is rich in Ti, while in the PM alloy, Ti is depleted. In the PM HEA, Ti reacted with C to form TiC, thereby depleting the FCC matrix of Ti. These said, the differences in microstructures must be solely a result of different processing routes and temperature profiles.

The fine grain size of the as-sintered PM-HEA (Fig. 38) is attributed to the high thermal stability of the TiC particles, which prevented grain growth of the FCC matrix by grain boundary pinning and a consequence of the SPS rapid densification (short sintering time) of the severely plastically deformed (i.e., grain refined) mechanically alloyed powders.
In contrast to the PM alloy, the cast alloy presents a much larger average grain size distribution (Fig. 39). The preferential orientation of the cast alloy is attributed to the heterogeneous nucleation, the dendrites crystalize in specific directions of heat dissipation at the ingot mould sides, a phenomenon seen often in metallic castings. Consequently, the FCC phase has a very strong orientation texture, as opposed to the essentially texture-free PM alloy. The same strong crystallographic orientation applies to the Laves phase.
In an overall comparison of the PM and Cast HEAs microstructures, combining mechanical alloying and SPS seems to deliver better results than casting, even considering the presence of carbide particles. The PM process produced a significantly more refined, uniform and chemically homogenous microstructure essentially without preferential orientation and porosity. To obtain a comparably uniform microstructure, the Cast HEA would have to be subjected to additional procedures (homogenization combined with hot working or cold working). However, such methods would further complicate the materials' processing due to the needed plastic deformation (change of shape) and would unnecessarily increase the cost of production. Additionally, the hot and cold workability of this Cast HEA with such a significant volume of brittle TCP phases is questionable.
Therefore, heat treatments were applied to analyze the effects of into the phase evolution and constitution of this HEA composition and a proper discussion will be present in this work.

6.1.2 Mechanical properties (as-sintered and as-cast states)

The as-sintered PM HEA shows only a slight increase in hardness in comparison to its cast counterpart - measured to be 712 HV in comparison to 682 HV, respectively.
An enhancement in elastic modulus of approximately 22% higher value was exhibited in the as-sintered PM HEA as compared to as-cast HEA. The higher PM HEA E modulus can be attributed to the presence of very stiff TiC and their good cohesion with the matrix, which possesses alone an E modulus = 400 GPa [179]; therefore, contributing for the overall E of the material. The bending strength (R_{mo}) of the PM material was remarkably high, with values exceeding 2 GPa. These values are almost double compared to as-cast HEA.
The reasons for the great differences in mechanical response between both materials are primarily explained by their microstructural characteristics. Except for TiC formation in the PM alloy, no significant inclusions, segregation of elements or porosity were detected in both alloys, suggesting these do not play a role in the mechanical properties. The better mechanical properties of PM HEA stem from the advantages of a more uniform microstructure. Additionally, the remarkably high strength is attributed to Hall-Petch strengthening.
On the other hand, the cast alloy's mechanical performance was inferior to the PM HEA, due to a much more heterogeneous microstructure. Even though the cast alloy's larger FCC matrix

grains (42.8 μm) should be more ductile (compared to the nano-grained PM HEA), a brittle behaviour was observed. This is caused by a high-volume fraction of brittle σ and Laves phases (52.4%) in the Cast HEA, possessing very brittle TCP crystal structures combined with minor BCC nanoparticles - which in turn have a significant detrimental effect on the mechanical response.

Neither materials showed any significant plastic strain, i.e., their failure occurred immediately after the initial elastic loading. In the case of PM, this occurred due to its extremely high strength and therefore insufficient plasticity, while, for the cast counterpart, due to the intrinsic brittleness caused by intermetallic phases.

Upon bending, it was observed an absence of particles inside the dimples for the PM HEA. This suggests that, most likely, the crack initiated and propagated by ductile tearing inside the FCC matrix, forming a dimple-like surface morphology formed by adjacent microvoid coalescence [147].

Considering that no significant ductility was present during the bending in any of the materials at room temperature, the fracture possesses a transgranular character and should be referred to as brittle in nature, frequently called low-energy tearing [147,180], despite the presence of ductile dimples. The fracture surface contains ridges retracting towards the fracture initiation site as shown in Fig. 40, a typical morphology for brittle fracture behaviour.

The lack of macroscopic ductility for the PM HEA might be explained by the severely strengthened microstructure. Nano-grains are a consequence of the high strains that the material was subjected to during its milling in powder state, followed by incomplete recrystallization during the sintering processing times. The grains were further pinned by an in-situ formation of the TiC particles. This effect is common for high-strength alloys, where dislocation motion is severely restricted [181,182], even though ductile fracture by micro-void coalescence with ductile dimples of various sizes occurs.

Compared to PM HEA, the Cast HEA manifested a considerably pronounced brittle damage of the fracture surface morphology. The existence of a high-volume fraction of brittle secondary phases (52.4% of the total volume calculated from XRD patterns) is responsible for the exceptionally brittle character of the Cast HEA fracture.

6.1.3 Tribological properties (as-sintered and as-cast states)

There are significant differences in the wear rate between the PM and the Cast HEA. As shown in Fig. 42, especially at higher load, the wear track of the PM HEA is much more deeply grooved and the adhesive material transfer process is more evident. In contrast, the wear track is much narrower. This indicates very severe adhesive wear in a smaller area due to the significant material transfer in the initial point contact.

Important variations in friction response for each material may be triggered by large differences in microstructures; average grain sizes and distribution; phase composition and respective volume fractions caused by dissimilar states of preparation, even though they possess the same overall chemical composition (Table 2).

The TiC hard particles exhibited by PM HEA may have a substantial effect on the tribological properties of the material, as the PM alloy acts as a metal matrix composite, enhancing the wear resistance of the material to some extent. This fact possibly contributes for the enhanced results when subjected to 1.2 N load compared to those of the AISI 52100. This is in accordance with other studies suggesting that some metal-matrix composites may have improved response over traditional wear-resistant steels when subjected to specific conditions [183–186].

Under higher loads, the tribological performance of the PM alloy decreases. It is assumed that, when the load is increased to 5 N, microcracks are initiated on the very hard TiC. They can block the motion of mobile dislocations during shearing, thus, leading to early crack nucleation and propagation and more severe delamination wear. These microcracks essentially lead to inferior results in wear properties at 5 N load.

The combined effect of higher stress intensity (compared to 1.2 N load) and cracking regions leads to wear rate increase in the PM alloy, in agreement with other studies evidencing identical effect upon the same wear conditions for PM alloys [187]. In contrast, there is no evidence of microcracking regions in the Cast HEA even when subjected to high load.

Additionally, since the PM alloy is mostly composed of FCC structure, dislocation slip is facilitated due to lower friction stress compared to, e.g. BCC or other type of structures; i.e. it facilitates the material deposition in form of adhesive wear [188]. Furthermore, the ductile FCC phase is more susceptible to forming adhesive bonds, i.e. the material with the highest amount of FCC has a stronger tendency to wear at certain conditions.

Since the wear process under 1.2 N with PM HEA is realized in much smaller contact area as compared to the Cast HEA while the COFs are similar, much higher flash temperature is expected. Higher temperature could further facilitate the formation of adhesive bonds.

The enhanced wear of the Cast HEA may be especially attributed to the exceptionally hard coarse precipitates of the TCP phases and large mixed areas of Laves, σ, and BCC phases. The material possesses only about half of the volume of the FCC phase compared to PM HEA, therefore reducing the tendency for adhesive wear. Moreover, the coarse brittle phases in the Cast HEA serve as barriers to delamination wear.

Up to some extent, local strain hardening caused by plastic deformation might play a role on the tribological properties of the Cast HEA, as coarse-grained microstructures have sufficient space for dislocation glide [189]. This is evidenced by the hardness of the Cast HEA worn surface, which increases after the wear test. This effect might contribute for the improved wear resistance of the part. In contrast, nanoscale FCC grains present in PM HEA have very limited space for dislocation glide; consequently, no local strain hardening was observed after the wear test, thus exhibiting an inferior performance in comparison with the Cast HEA.

The combination of the aforementioned features leads the Cast HEA to perform exceptionally better than any other under both loading conditions, considering the particular differences between the two states.

In conclusion, as-sintered PM HEA is superior in terms of mechanical bending strength, presenting a strength increase of ~80%, relative to its cast counterpart, while retaining an identical wear rate at 1.2 N (Fig. 46). A load increase in cast HEA does not compromise its performance in wear, maintaining enhanced tribological properties almost intact.

6.1.4 Microstructures and basic mechanical properties after heat treatments

The microstructural evolution of the PM and Cast HEAs were observed in terms of heating temperature and heating times, in order to analyze the phase transformations in each alloy and the differences among the resulting microstructures. The alloys were submitted to heat treatments at 1000 °C for 5 h, and, subsequentially, at 750 °C for further 5 h.

After 1000 °C for 5 h, PM HEA remains as nanosized composite, comprising a main FCC matrix with similar lattice parameter as shown in the as-sintered state. The average grain size of the matrix remains in the nanoscale level (0.88 µm) as compared to as-sintered state (0.42 µm), even when subjected to temperatures very close to the predicted melting point for this alloy (1130 ºC).

The BCC phase remains present, as predicted by CALPHAD and confirmed by XRD (Fig. 47). At this temperature, the phase field is calculated by ThermoCalc to belong to FCC and BCC, in good agreement with experimental observation. The BCC content, in fact, increases in volume from 2.7 % to 6.3 % and also suffered an increase in average grain size, which is clear from the EBSD maps (Fig. 50), now evidencing a BCC microstructure of average grain size of 0.64 µm, as opposed to the as-sintered state, where only FCC and TiC were visible due to the very small grain sizes of the BCC precipitates before.

Additionally, TiC is present since it is a very thermally stable carbide. Heat treatment at 1000 °C is not sufficient for dissolving it, as its melting temperature is expected to be about 3160 °C [179]. The amount of TiC was increased from 8 % to 11.9 %, this is caused by the fact that the heat treatment was performed in air. The average grain size of the TiC in the as-sintered state was measured to be 0.40 µm, and after 1000 °C for 5 h, it does not show significant growth, with an average of 0.55 µm.

Upon additional 5 h of heat treatment at 750 °C, the FCC matrix does not lose its very fine character of grain size, possessing an average grain size of 1.4 µm. The BCC phase is further increased in volume up to 11.5 %. TiC also increases up to 13.4 % due to the heat treatment being performed in air. The remaining fraction belongs to a crystal structure of η-Ni_3Ti, as XRD results suggest. This phase was not predicted by CALPHAD. However, it has been shown to appear in similar alloys [157,190]. The PM alloy does not exhibit any significant changes in phase distribution and microstructural composition even after 10 h of heat treatments, except for the precipitation of the η-Ni_3Ti.

The nano-scale nature of the PM alloy, even after 10 h of heat treatments in temperatures close to the theoretical melting point of this alloy stems from the thermally stable TiC homogeneously dispersed in the FCC matrix, playing the role of pinning the grain boundaries

and thus, avoiding grain growth and presumably increasing the thermal stability of the material as a whole.

In contrast, the cast HEA, when submitted to a heat treatment of 1000 °C for 5 h, has significantly larger grains as compared to PM, due to the very nature of the different manufacturing processes and lack of carbides on the former. The FCC phase suffers an increase in volume (67.1 %) compared to the as-cast state (47.8 %), due to the dissolution of secondary phases. The average grain size of this phase had a reduction to 22.3 µm, mostly likely at the expenses of increasing the grain sizes of the BCC phase. CALPHAD predicts that the phase field of 1000 °C belongs to FCC and BCC phases (Fig. 29), however 5 h was clearly not enough for dissolving all the secondary phases. This might be due to the slow kinetics of some particular HEAs, specially FCC HEAs, caused by an sluggish diffusion due to an increased lattice distortion [54], in comparison to conventional alloys. That said, the BCC phase was increased from 10.1 % to 17 %, with no significant changes in lattice parameter. The average grain size of the BCC phase increased substantially, up to 21.5 µm. On the contrary, in the as-cast state, the BCC grain size was not possible to be assessed by EBSD due to the resolution constraints of the EBSD method. The nano-sized phase was only possible to be identified by TEM previously in the as-cast state (Fig. 34 and Fig. 37).

The Laves phase was not fully dissolved, however suffered a significant reduction in volume from 30.6 % up to 10.5 %, with an average grain size of 8.2 µm. This was identified to be the needle-like phase, similarly as of in the-cast states morphology. The sigma phase is also present in a decreased amount (2.8 %) as compared to as-cast state (11.5 %). This phase was identified to possess a globular morphology (Fig. 49 - marked by an yellow arrow), confirmed by comparing EDS compositions (Table 7) from as-cast state and after heat treatments. Additionally, the η-Ni3Ti was identified by XRD to precipitate even at 1000 °C, even though owning only a very minor amount of the total volume (2.6 %). This phase was not predicted at all by ThermoCalc, even using the latest database TCHEA4.

The selected heat treatment of 1000 °C for 5 h was not enough to fully recrystallize the material, as evident by the remaining preferential orientation of the FCC phase caused by the casting processing, visible by EBSD measurements before and after heat treatments (Fig. 39 and Fig. 51).

Upon further heat treatment at 750 °C for 5 h, the cast HEA presents an increase in volume of FCC phase up to 48.2 %, owning an average grain size of 15.3 µm, which is slightly decreased from the previous state. This is probably due to new FCC phases concomitantly precipitating and growing at a given temperature. The lattice parameter of this phase remains constant. The BCC phase did not have such significant increase in volume (18.1 %) from the previous state (15 %), nor increased substantially in grain size (23.2 µm), indicating that the BCC phase achieved an equilibrium window at the range of these temperatures. The Laves phase increased again in volume significantly up to 25.4 % with a grain size of approximately 9.1 µm, in good agreement with CALPHAD predictions. Sigma phase is present in 5.9 %,

however the grain size is so small that it was not detected by the EBSD scanning at the set conditions. The η-Ni_3Ti remained present with the steady content of 2.4 %.

ThermoCalc calculations predict that, at 750 °C, the phase field belongs to FCC, BCC, Laves and Sigma phases. Exceptionally, a second FCC phase is expected to nucleate, however it was not seen experimentally.

Even after 10 h in total of heat treatments, preferential orientation is still evident due to dendritic solidification during the casting. This fact is rather surprising, considering that the theoretical melting temperature of this alloy is about 1130 °C. This is probably caused by the, previously mentioned, supposed slow kinetics of HEAs as compared to conventional alloys.

The mechanical properties of the alloys produced by PM and casting and subjected to heat treatments were evaluated by Vickers hardness and nanoindentation hardness (to assess the elastic modulus of the materials).

After 1000 °C, both materials show a trend in decreasing the hardness. This is caused by the dissolution, at some extent, of some secondary phases, such as the brittle and hard Laves and sigma phases, and increase in FCC and BCC phases; therefore, decreasing the total hardness of the materials.

After further heat treatment at 750 °C for additional 5 h, one can see a trend in an increased hardness. According to ThermoCalc prediction and experimental observations, this phase field relates to a precipitation of new sigma and Laves phases. It was experimentally proven that these phases precipitate and increase in content. Additionally, the η-Ni_3Ti is present in both alloys at this stage. Therefore, all these new phases contribute to the increase in hardness of the materials.

The elastic modulus of the PM HEA is relatively constant for all states – before and after heat treatments. This is due to the formed stable microstructure caused by the presence of TiC, pinning the grain boundaries and guaranteeing similar grain sizes for all conditions, even after 10 h at high temperatures. The low elastic modulus present by as-cast HEA is presumably attributed to the very brittle character of the Laves and sigma phases present in high amount in this material. After heat treatments, the values of elastic modulus reach similar values of those of PM HEA.

Additional effects may be taken into consideration for a careful evaluation of the properties by nanoindentation hardness. The variation in values of elastic modulus for Cast HEA may be furthermore explained due to the nature of the nanoindentation measurement. Each indent measures a different grain, which may correspond to very different phases and thus, different properties. In the case of the Cast HEA it is especially problematic, since the grain sizes are so large, particularly in the case of Laves phase, BCC and FCC. Therefore, a considerable number of indents must be made to guarantee an accurate value of elastic modulus. This was carefully done for both alloys and the slightly higher standard deviation of Cast HEA is reflected by this phenomenon.

6.2 Optimization of mechanical alloying parameters of refractory HEAs

6.2.1 Influence of the milling time on the powders properties

The consequences of the variation in the milling time on the properties of $Al_{0.3}NbTa_{0.8}Ti_{1.5}V_{0.2}Zr$ RHEA powder (in stoichiometric ratio) have been assessed by changing the time of milling from 0 h up to 50 h, while keeping the rotations per minute constant (250 RPM) under argon atmosphere.

The XRD results show that after only 1 h of milling, the powders formed four phases; a main BCC1 phase and secondary BCC2, HCP1 and HCP2. The powder microstructures are also significantly altered, as evidenced by SEM and EDS images, even though the segregation of all elements is very pronounced. After milling for 1 h, the Al element was fully dissolved into the other powders, due to higher ductility of its FCC crystal structure, compared to rest of elements.

By increasing the milling time from 1 h to 5 h, the total amount of of the secondary phases decreases significantly, thus increasing the main BCC1 fraction. The particles become increasingly more homogeneous with longer mechanical alloying. However, elemental segregation is still pertinent. Similar particles sizes are observed up to 5 h, even though the feedstock powders possessed very different morphologies before milling.

After 10 h of milling, it is possible to achieve powders comprising 95 wt. % of BCC phase. The additional 5% relates to HCP phases. The particle size is rapidly decreased at 10 h of milling time. This is due to the achievement of a critical value of plasticity in which the powder particles begin to fracture, thus generating new surfaces for cold welding [108].

From 20 h onwards, the powders are comprised of pure BCC phase, acquire a globular morphology and show significant decrease in size induced by the mechanical alloying process. However, it was previously shown that such long times of mechanical alloying may provoke contamination of the powders with C and O [117,120]. Therefore, one must compromise and select parameters which avoid unnecessarily long times of milling while achieving an appropriate microstructure.

The powders after 40 h of milling did not show any significant changes in comparison to those of 20 h and 30 h, as the powder morphologies are comparable, and sizes only slightly reduced. Few elongated particles are visible (Fig. 58.l) after 50 h of milling, but the powders are mostly of globular morphology.

Subsequent milling from 1 h up to 50 h induces an important broadening of the XRD peaks, as the consequence of refining the powder crystallite size by increasing plastic strains caused by repeated cold deformation from milling.

From these results, it is possible to conclude that 10h of milling seems to provide sufficiently homogeneous particles comprising an almost single-phase BCC structure, with satisfactory powder size and morphologies, and no significant segregation. At the same time, possible powder contamination induced by unnecessarily longer mechanical alloying can be avoided by choosing 10 h of milling.

6.3 Optimization of sintering parameters of refractory HEAs

6.3.1 Effect of the milling time variation on the sintered bulks

The influence of the changes in milling times on the properties of the sintered $Al_{0.3}NbTa_{0.8}Ti_{1.5}V_{0.2}Zr$ RHEA bulks (in stoichiometric ratio) by SPS has been evaluated. The precursor powders have been submitted to various milling times, and powders from selected milling times of 3 h, 10 h, 30 h and 50 h were sintered by SPS. The sintered bulks – namely SRMA-3h, SRMA-10h, SRMA-30h, SRMA-50h - have been evaluated in terms of their microstructural features and basic mechanical properties.

The BCC phase is the predominant structure present in all sintered bulks, with similar lattice parameters as of those shown by the main BCC in the RMA powders. Despite the HCP phase formed on the powders during milling, this phase was not exhibited in the sintered alloys. A second BCC2 phase was detected for SRMA-10h and SRMA-30h. Two BCC phases were proven to exist in similar alloys in a BCC/B2 relationship, fruit of spinodal decomposition [92,93].

Before sintering, the powders did not present peaks corresponding to ZrO structure, as opposed to the sintered alloys, which ZrO appeared in all cases. Despite this fact, increased milling times of the powders lead to the formation of a higher fraction of ZrO after sintering, indicating that contamination might be associated with prolonged milling times. For instance, the powders milled for 3 h showed less ZrO formation (2.0 wt. %) after sintering than powders milled for 50 h (6.8 wt. % after sintering), while all the sintering conditions were guaranteed to be the same. This is in agreement with other studies [117]. The sintering seems to promote the formation of the cubic structure Fm-3m of ZrO; and possibly contributes to further contamination due to the use of graphite dies.

In the cases of SRMA-30h and SRMA-50h, additional formation of Ti_2O crystal structure, belonging to the tetragonal crystal system, was observed after sintering. This structure was not observed in the powder forms also.

The BCC1 predominant phase owns comparable chemical compositions for all bulks. Nevertheless, the occurrence of Fe is revealed after 30 h of milling in 1.8 at. %. The presence of Fe increases for 50 h of milling up to 2.2 at. %. This contamination is caused during the mechanical alloying process, due to the worn surfaces of the milling balls and jar after the powders being submitted to long milling times.

Additionally, the increasing in time of milling is directly proportional to the increase in microstructural refinement. This is caused since the powders' particles sizes were reduced for longer milling times, therefore forming microstructures with lower average grain sizes. This is evident by comparing the matrices grain sizes of SRMA-3h (33.8 μm) and SRMA-50h (25.2 μm). Other studies [108] already suggested that the behaviour of the powders in terms of rate refinement of its structure can be considered logarithmic with the time of milling.

In conclusion, it is possible to suggest that for the case of $Al_{0.3}NbTa_{0.8}Ti_{1.5}V_{0.2}Zr$ RHEA sintered bulks, the longer is the milling time, the more refined will be the microstructure comprising a higher content of oxides dispersed into the BCC matrix.

6.3.2 The influence of sintering temperatures on the properties of the bulks

The low-density $Al_{0.5}NbTa_{0.8}Ti_{1.5}V_{0.2}Zr$ RHEA prepared by mechanical alloying combined with hot uniaxial pressing (HP) was investigated. The influence of increasing the sintering maximum temperatures, while keeping other conditions constant, on the RHEAs' microstructural features, composition and basic mechanical properties was evaluated. This investigation aimed on selecting an optimum sintering temperature for this particular RHEA composition. The maximum sintering temperatures of 1600 ºC, 1300 ºC and 1200 ºC were studied.

Full-density samples were achieved utilizing all three sintering temperatures: 1200 °C, 1300 °C and 1600 °C at a constant uniaxial pressure of 50 MPa and 10 min dwell time.

According to XRD results, and supported by CALPHAD predictions, RHEA-1600 possesses a single BCC phase with FCC carbides (crystal structure of ZrC, Fm-3m space group) dispersed into the matrix. The ZrC has similar lattice parameter as ZrO and ZrN, therefore an atom probe tomography would have proven useful for accurate determination. A second BCC2 phase was not detected on this alloy by XRD, in accordance to ThermoCalc, which predicts the formation of a secondary BCC below temperatures corresponding to 1300 ºC. On the other hand, RHEA-1200 and RHEA-1300 detected two BCCs and FCC carbides.

The FCC carbides detected by XRD are probably originated from the milling of the commercially available Zr sponge into Zr powder by mechanical milling. The obtained Zr powder was mixed together with commercially available powders of Al, Nb, Ta, Ti and V (high purity powders) in a stoichiometric ratio of $Al_{0.5}NbTa_{0.8}Ti_{1.5}V_{0.2}Zr$. These powders were milled by mechanical alloying as described in Methods. Mechanical alloying has been proven to contribute on the contamination of the powders elsewhere [120]. The influence of the use of Zr sponge or use of commercially available high purity powder in the production of RHEAs by powder metallurgy was assessed and a separate chapter is dedicated to it. This will be discussed with further detail in the appropriate section.

All three RHEAs possess fine-grained microstructures with homogeneously dispersed carbides.

When subjected to the lowest sintering temperature of 1200 ºC, the BCC matrix owns an average grain size of 1.9 μm with dispersed carbides (FCC) mainly along the grain boundaries with an average grain size of 0.9 μm. Increasing the temperature to 1300 °C, results in ≈ 1.8 times larger BCC matrix with grain sizes of 3.6 μm, while the FCC carbides are stable and do not suffer any grain growth.

With further increase in the sintering temperature to 1600 °C, the BCC matrix grain size average increases to 19.0 μm - ten times larger as compared to the ones of 1200 °C - and the FCC carbides to only 4.5 μm – five times increase as compared to the ones of 1200 °C, due

to its high stability. Even though the average BCC grain size is ten times higher here than at the lowest sintering temperature (RHEA-1200), the grain size is still considerably small compared to materials that do not contain dispersed carbides.

The fine grain sizes of the matrix, even at very high temperatures of exposure, are attributed to the high thermal stability of the FCC carbide particles, playing the role of pinning the grain boundaries and avoiding excessive grain growth. Additionally, the rapid HP densification, i.e. short sintering times, of the severe plastically deformed mechanically alloyed powders contributed to the grain refinement of the microstructures.

The white regions on EBSD maps (Fig. 60) correspond to non-indexed areas which possibly relate to the secondary BCC2 phase identified by XRD as BCC2 that was still not fully dissolved at 1600 °C (due to relatively short sintering time upon heating). The BCC2 phase was detected on the other alloys, however it was not detected by XRD for RHEA-1600. This may be attributed to several reasons. For instance, it could be attributed to the phase's too low weight fraction or simply because diffraction patterns may overlap, being difficult to resolve only based on XRD. The background noise of the XRD pattern could have hidden some peaks as well. TEM would have been proven useful to confirm the existence of a secondary BCC2 phase upon sintering at 1600 °C.

Regarding the mechanical properties, there is ≈ 12 % increase in hardness and 3 % increase in Poisson ratio with a decrease in the sintering temperatures from 1600 °C to 1200 °C. The hardness and Poisson ratio increase may be explained by the grain size refinement of the microstructures and higher amount of secondary BCC phase present at the lowest temperatures of sintering. The shear modulus seems to slightly decrease proportionally with the decrease of the temperature from 1600 °C to 1200 °C from 61 to 56 GPa. The elastic moduli of the three alloys vary proportionally with the content of in-situ formed FCC carbides. RHEA-1600 exhibits the highest fraction of FCC carbides (14.4 %) and highest elastic modulus (160 GPa). Following the same reasoning, RHEA-1300 presents 4.4 % in vol. of FCC carbides and the lowest elastic modulus (145 GPa), showing similar results as RHEA-1200 with FCC carbides in 5.5 wt.% and elastic modulus of 148 GPa.

In summary, the achievement of full density bulks (100 %, calculated experimentally) is possible for all the selected sintering temperatures of 1200 °C, 1300 °C and 1600 °C. All alloys have shown homogeneous distribution of phases, with presence of in-situ formed homogeneously dispersed carbides, which are responsible for a grain-boundary pinning effect and stabilization of fine-grained microstructures even at very high temperatures of exposure.

6.4 $Al_{0.5}NbTa_{0.8}Ti_{1.5}V_{0.2}Zr$ refractory high entropy alloy

6.4.1 Microstructural characterization of powder metallurgy and arc-melted alloys

The $Al_{0.5}NbTa_{0.8}Ti_{1.5}V_{0.2}Zr$ RHEA was subject to study through the production of two manufacturing routes: powder metallurgy (by a combination of mechanical alloying and sintering) and arc-melting.

The RHEA arc-melted counterpart was proven to be rather challenging to be produced, due to the difficulties in liquid state preparation by melting routes associated with very different melting temperature of different elements, such as Al - with temperature of melting (T_m) of about 660 °C; Nb (T_m = 2477 °C) and Ta (T_m=3017 °C). At first, the Ta and Nb were segregated in interdendritic areas. The alloys needed to be remelted several times to obtain successfully homogenous microstructures. Additionally, the casting was absolutely not viable because the solidification rapidly took place, as soon as the arc was distanced from the material, therefore making it impossible to pour the liquid into a copper mould in order to shape the alloy as an ingot. Therefore, the resulting material was a big chunk of $Al_{0.5}NbTa_{0.8}Ti_{1.5}V_{0.2}Zr$ in stoichiometric ratio – the correct chemical composition was assured.

In contrast, the PM route offers an easy solution: sintering in the solid state. Cylindrical shaped samples are possible to be manufactured by a combination of mechanical alloying through ball milling, and subsequent sintering. No segregation of specific elements was observed, as the materials were not melted. Segregation can occur only in the case of insufficient milling and sintering times, but it could be easily solved by a previous optimization of the parameters. However, one must pay close attention to avoid contamination during the entire production method, since oxygen can easily contaminate the powders when entering in contact with air; also the presence of oxygen/carbon is revealed during mechanical alloying and sintering. Nevertheless, this can be used as an advantage for specific applications, since it has been proven as useful and effective way to produce oxide/carbides/nitrides dispersed particles into a metal matrix.

The differences in microstructural characterization and consequential basic mechanical properties were evaluated and are discussed in detail in this section. The theoretical results obtained by CALPHAD are also included in the discussion.

With the SPS-process, full density fine-grained RHEAs can be produced, even at relatively short sintering periods at the maximum temperature (10 minutes).

The as-sintered $PM1_A$ exhibits a BCC1 phase in 85.5 wt. %, rich in Ti, Nb and Ta, owning a grain size average of 1.8 μm. The crystal structure pertaining to ZrO was observed in 13.9 wt.%. Please, note that the ZrC and ZrN crystals possess similar lattice parameters and the same crystal system. For an exact determination of the chemical composition, APT would have been proven useful. EDS confirmed to be rich in Zr and O by EDS analysis, therefore we will suppose it is ZrO. This phase is shown to possess grain size of 0.6 μm. Additional Al_3Zr in 0.4 wt.% was detected by XRD, as well as Ta_2C-type of crystal in 0.2 wt.%. These minor phases were not possible to be evaluated by SEM/EDS/EBSD due to the resolution constraints of the methods.

The arc-melted AM1 exhibits a dendritic/interdendritic microstructure as two BCC phases. This morphology is caused by the solidification process from melting. The interdendritic area is rich in Ti, Zr and Al. Conversely, the dendrites are rich especially in Ta, Nb and Ti.

This is in agreement with a study performed by Soni et al. [92], which the authors investigated the relationship between the two BCC phases by TEM in cast $Al_{0.5}NbTa_{0.8}Ti_{1.5}V_{0.2}Zr$ under

different conditions of preparation. One BCC was found to be, in fact, ordered (B2) and the second disordered solid solution (BCC). The authors examined an APT reconstruction on the interface between BCC/B2 particles (Fig. 14 present on this thesis). It is clear that there is a correlation between the APT performed by the other group and the results found for AM1 present herein (EDS line spectrum Fig. 72). The interdendritic area is rich on Ti, Zr and Al, which according to their research, the BCC_B2 phase is rich on these elements. The dendritic area corresponds to BCC, which according to Soni et al., it is a phase that is rich in Ta, Nb and Ti.

The main BCC comprises 75 wt. % of the alloy with an average grain size of 166.4 μm, while BCC2 comprises 25 wt.%. These two phases cannot be distinguished on the EBSD analysis. This is due to the very similar lattice parameters of both phases, as well as both of them pertain in the same cubic crystal system (BCC). The difference is the occupation of the atoms in the BCC lattices, as one of them is ordered (B2) and the second is disordered (BCC).

Subsequent heat treatments were done in both materials in order to analyze the evolution of different phases and potential improvement in mechanical properties.

The first one was performed at 1400 °C for 1 h. The calculated phase and property diagrams for $Al_{0.5}NbTa_{0.8}Ti_{1.5}V_{0.2}Zr$ predicted that, at 1400 °C, a single BCC phase field would be present. The predicted phase was good agreement with the results obtained by $PM4_A$; a single BCC was present in 83.9 wt.%. This phase is rich in Ti, Nb and Ta.

Additionally, ZrO (16.1 wt.%) homogeneously dispersed into the matrix. The ZrO cannot be dissolved at this temperature, as it owns an extremely high melting temperature. A substantial increase in ZrO content was observed from the previous as-sintered state.

The Ta_2C previously evidenced in $PM1_A$ did not appear on the XRD of any heat treatment, probably due to being hidden by the pattern background, as it contained only 0.2 % of the total weight. This phase was not even detected by other methods, such as EDS and EBSD, probably due to its very low amount combined with fine grain size.

For the arc-melted counterpart, except for the main BCC phase, the material exhibited very fine precipitates of a secondary BCC phase in 12.7 wt.%. CALPHAD did not predict the presence of the second BCC at this temperature. One possible explanation could be due to insufficient time at the mentioned temperature for a full dissolution of the BCC2 precipitates.

A full dissolution of the dendrites occurred even with only 1 h of heat treatment at 1400 °C. The BCC1 grains considerably grow at this temperature, up to sizes of 225.9 μm, and are rich in Ti, Nb, Ta and Zr.

One may notice that the Zr content in the BCC phase of the arc-melted alloys is significantly higher as compared to the one exhibited for the powder metallurgy counterpart. The reduced Zr content in the latter is caused by the ZrO presence, therefore depleting the BCC matrix.

Further heat treatment at 1050 °C for 30 h was performed. CALPHAD predicts that this corresponds to two BCC phase field. However, several aluminides are present in both PM and AM materials, therefore the predictions do not relate to the experimental observations. This might be caused, at some extent, to the precipitation of aluminides during cooling, as

aluminides were predicted at lower temperatures. The heat treatment furnace was turned off and the samples were cooled down naturally.

The $PM7_A$ exhibits a main BCC present in 79.8 wt. % of 7.4 μm grain size average. ZrO presents a content of 11.2 wt. % and grain size of 1.3 μm. No additional grain growth was observed in both phases of the material, even after exposure for 30 h at such high temperature, indicating thermal stability in terms of grain size. The lack of the second BCC phase may be explained due to the presence of ZrO, since the metallic matrix is depleted in Zr content at the expenses of the oxide formation. The Zr phase was shown elsewhere [93] to belong to the chemical composition of the BCC_B2 precipitates. Aluminides are present in Al_3Zr crystal structure in 6.0 wt.% and Al_2Ti_3 in 0.4 wt.% Additionally, an HCP phase is evident in 2.4 wt.%. This HCP phase probably results from the furnace cooling.

The arc-melted counterpart, on the other hand, indeed exhibit two BCC phases; additional aluminides are detected as well. BCC1 is present in 74.1 wt.% with the grain size kept relatively constant from the previous state, with 237.2 μm average grain size. BCC2 phase comprises 19.5 wt.%. Al_3Zr is present in 6.0 wt.% - the same amount of this phase was obtained in the PM RHEA. Al_3Zr_2 precipitates are also present in 0.4 wt.%.

Alternatively, heat treatment at 800 °C for 30 h was performed after the solution treatment at 1400 °C. CALPHAD predicts that a three-phase field is present: two BCCs and formation of aluminides of crystal type Al_2Zr_3. The experimental results of the arc melted material indeed indicate the presence of two BCCs and aluminides, however not the crystal structure type predicted by CALPHAD. The exact phases for each material are described as follows:

On the PM material, a main BCC phase was experimentally observed in 81.3 wt.%, with grain size average of 7.4 μm. Note that the size of the BCC grains was kept constant either at 1050 or 800 °C. ZrO is present in 14.1 wt. % with average grain size of 1.5 μm. Additionally, Al_3Zr in a nano-sized needle-like morphology is exhibited in 3.1 wt.%. HCP precipitates are present in 1.5 wt.%.

On the AM alloy, on the other hand, a complex microstructure composed of two BCC phases and different kinds of aluminides is exhibited. A main BCC phase is present in 81.6 wt.% with average grain size of 229.4 μm. Note that this fraction of BCC is higher than the one observed at 1050 °C. This is explained because less precipitates were detected at 800 °C and following that the kinetics of phase transformations are accelerated at higher temperatures, thus the amount of precipitates at higher temperatures is higher belonging to the same phases field. Additional phases are: BCC2 in 9.1 wt.%; $AlTi_2Zr$ is present in 4.4 wt.%; Al_2Zr in 2.9 wt.% and Al_3Zr_2 in 2 wt. %.

Finally, heat treatment at 600 °C for 30 h performed subsequently after solution treatment at 1400 °C should induce the precipitation of additional HCP phase, according to CALPHAD. The HCP precipitates were, indeed, present in the arc-melted alloy as Ti_2Zr HCP crystal type. In the PM alloy it either might not have precipitated, or the amount was too low to be detected by XRD. The depletion of Zr into the average chemical composition of the other phases due

to formation of ZrO might be a consequence of differences in phase prediction and experimental observations.

In the PM RHEA, a BCC present in 93.0 wt. % with grain sizes of 7.0 μm are shown. Additionally, ZrO is present in 7.0 wt. % with grain sizes of 1.3 μm. On the other hand, AM alloy shows a main BCC1 phase in 71.5 wt.%, possessing grain sizes of 260.6 μm. Very fine nano sized BCC2 precipitates are visible, with 26.2 wt. % of content. Additionally, HCP phase is shown in 1.3 wt.%, in good agreement with CALPHAD.

No important crystallographic orientation preference is detected in any of the PM RHEAs. On the other hand, the AM counterpart presents a slight orientation on the arc-melted state before heat treatments. This is caused by the dendritic solidification. Further heat treatment at 1400 °C for only one hour is enough to eliminate any preferential orientation.

The very fine grains of the RHEA produced by powder metallurgy are attributed to the presence of oxides distributed homogeneously within the BCC matrix. These oxides play the role of pinning the grain boundaries. Consequently, grain growth is avoided even after the material was exposed to a combination of very high temperatures and prolonged times, guaranteeing similar grain sizes before and after heat treatments. This indicates the thermal stability of the material.

In contrary, the AM counterpart seems to suffer significant grain growth at the temperature for solution treatment (1400 °C), showing ≈ 35% increase in grain sizes of the main BCC phase. Further heat treatments in lower temperatures for 30 h, however, induce a very slight grain growth.

Powder metallurgy prospects an interesting manufacturing alternative to the melting routes, e.g. arc-melting or induction melting, due to the potential enhancement of mechanical properties triggered by the homogeneous and fine-grained microstructures; with the possibility of producing dispersed ceramic particles within the matrices.

6.4.1.1 Use of Zr sponge vs. commercial powder as feedstock for mechanical alloying

The formation of metal matrix composites with induced formation of in-situ oxides dispersed within the matrix was comprehensively investigated in this work by mechanical alloying and sintering.

The intentional contamination induced in the feedstock materials prior to mechanical alloying was studied here by using elemental powders that contained the presence of contaminants. The O and C elements react with certain metallic powders, which they own highest affinity, and form oxides/ carbides.

In our work, this was the case of Zr. The previous section discussed the results of a metal matrix composite prepared by using Zr sponge as part of the feedstock material to produce the powder precursors for mechanical alloying, namely Precursors-A.

This section deals with the production of metal matrix composite prepared solely by mechanical alloying of powders with commercial purity as starting materials, namely

Precursors-B. The differences between both ways were thoroughly described in the Methods (4.2.1) and Results (5.4.2) sections.

The as-sintered $PM1_B$ is clearly very different than the one shown by $PM1_{A.}$ The $PM1_B$ bulk presents two BCC phases, ZrO and Al_3Zr. The main BCC phase is rich in Ti, Zr, Nb and Ta, the phase present in 93.6 wt.% and possesses grain size of 11.1 µm – a considerably coarser sizes than exhibited by $PM1_A$ in the as-sintered state. The latter showed a grain size average of the BCC phase of 1.8 µm. $PM1_A$ could not form a second BCC phase due to the formation of a high amount of ZrO crystal type, thus depleting its matrix of Zr. The formation of two BCC phases are seen in the arc-melted counterpart.

The ZrO particles possess grain sizes of 0.9 µm and are present in only 1.8 wt.% in $PM1_B$ - a significantly lower amount as compared to the one using Zr sponge as feedstock. The latter was present in 13.9 wt.% in its as-sintered state, yet with similar grain size. Additionally, Al_3Zr was found to be present in $PM1_B$ in 1.4 wt. %.

After heat treatment at 1400 °C for 1 h, due to the lack of ZrO in sufficient amounts pinning the grain boundaries, the grain sizes of the BCC phase importantly coarsen in $PM4_B$. Now, the BCC grains have an average of 33.5 µm, an increase in ≈ 30 % of its original size. The same phenomenon was seen for the arc-melted counterpart, which suffered an increase of ≈ 35 % of their BCC grains after exposed to the same heat treatment.

The chemical composition of the bcc phase resembles the one exhibited by the arc melted counterpart after heat treatments as well. This is probably due to the lack of ZrO in high amounts, as opposed to the $PM1_A$.

The second BCC phase is present in 12.5 wt.%. $PM4_A$, however, did not show presence of a second BCC, probably due to the formation of an important amount of ZrO, thus it could indicate that the Zr content was depleted from the BCC at the extent of hindering the formation of a B2 phase. It was shown by Soni et al. [92] that the B2 phase is rich in Zr. At this state, the ZrO exhibited an average grain size of 5.8 µm in 3.0 wt.%.

The grain sizes of the main BCC and oxides seem to stabilize after this stage for both PM alloys. Further heat treatments in lower temperatures (1050 °C and 600 °C) even after 30h do not cause significant growth of the phases. This is also seen by the arc-melted counterpart.

When the material is exposed to 1050 °C for 30 h, the formation of aluminides is visible in all materials. In $PM1_B$, the BCC grains have average grain size of 34.5 µm. They are present in 67.8 wt.%. BCC2 is present in 23.8 wt.%. Additionally, ZrO is present mostly in the grain boundaries in 3.5 wt.% and shows an average grain size of 5.3 µm.

Finally, when submitted to the last heat treatment at 600 °C for 30 h, the microstructure resembles the one exhibited by the arc-melted alloy. Surprisingly, the microstructures are very similar in some aspects, as evidenced by Fig. 85 and Fig. 71, both exhibiting BCC2 nano-sized precipitates, which hold similarities with the ones of B2 exhibited by [93]. SAED patterns would have been useful to determine the ordering by super lattice reflections.

The main BCC comprises 67.5 wt. % and possesses grain sizes of 30.0 µm. The BCC2 phase is present in 29.3 wt. %. The ZrO crystal structure comprises 3.2 wt. % with grain sizes of 2.1 µm.

In summary, once the RHEA is produced by powder metallurgy without sufficient in-situ formation of ODS particles, the induced changes in the materials behaviour seem to resemble those of the arc-melted counterpart. For instance, at some extent, the kinetics of grain growth, the phase transformations, chemical composition of phases are behaving more likely as a metallic alloy, rather than a composite.

By using a combination of a careful handling of elemental feedstock powders with commercial purity inside glovebox, it is possible to effectively reduce the contamination and formation of dispersed oxides within the matrix at some extent. The amount is significantly reduced when compared to the ones exhibited by PM_A, with corresponding maximum contents of 1.8 % and 13.9%, respectively, in the as-sintered states.

However, for applications in which ODS particles are envisaged, for instance in high temperature applications, one can use different feedstock products to produce refractory alloys, such as Zr sponge, as an alternative for effective production of homogeneously dispersed oxide particles within a metal matrix composite.

6.4.2 Basic mechanical properties

The hardness and elastic modulus of AM1 is the lowest among all samples. This is explained by the lack of oxides and secondary hard phases. The alloy is solely composed of two BCC phases in a dendritic/interdendritic morphology.

On the other hand, among the arc-melted samples, the highest hardness values are exhibited by both AM7 and AM10. Their values seem to be equivalent. This stems from the complex microstructure of these alloys, as they exhibit different kinds of very hard and brittle aluminides precipitates, such as Al_3Zr, Al_3Zr_2, $AlTi_2Zr$, Al_2Zr. The presence of these aluminides seems to increase the elastic modulus of these alloys. AM4 and AM13 show intermediate hardness values. AM13 shows slightly higher values of hardness and elastic modulus, probably due to the presence of HCP precipitates in very low amounts and additionally, this alloy exhibits a higher amount of ordered BCC phase within the BCC matrix solid solution as compared to AM4. The latter exhibits a BCC phase and, apparently ordered, BCC precipitates. This microstructure was similarly seen by Soni et al. [93].

The PM_A group shows the highest values of both average elastic modulus and hardness among all RHEAs. This is explained by the presence of ZrO in significant amount (13.9 wt. % in the as-sintered state) homogeneously dispersed within a BCC matrix. The highest values of hardness and elastic modulus were seen by the samples containing brittle aluminide precipitates, which are, in descending order of aluminides content: $PM7_A$, $PM10_A$ and $PM1_A$. $PM4_A$ and $PM13_A$, conversely, exhibit comparably lower values of hardness and elastic modulus. This is explained by the fact that their microstructures are composed solely of 1 BCC phase and ZrO. The second BCC phase was not detected on this material in any state.

The PM_B group does not exhibit a significant amount of oxides (from 1.8 wt.% in the as-sintered state up to 3.2 wt. % after exposing the material to 600 °C) as compared to PM_A group. The highest hardness and elastic modulus are exhibited by $PM7_B$ due to the presence of various brittle aluminides; followed by The $PM1_B$ (as-sintered), which also contains Al_3Zr in smaller amounts (1.4 wt. %). $PM4_B$ and $PM10_B$ own similar hardness and elastic modulus owning the lowest values, as seem on all other materials.

6.5 $Al_{0.3}NbTa_{0.8}Ti_{1.5}V_{0.2}Zr$

The $Al_{0.3}NbTa_{0.8}Ti_{1.5}V_{0.2}Zr$ was produced by powder metallurgy and arc-melting. The dissimilarities of the two manufacturing routes greatly affect the microstructures and mechanical properties of the final materials. The RHEA was exposed to severe conditions, such as temperatures $\geq 0.7T_m$ (melting temperature), e.g. heat treatments at 1400 °C as well as other conditions of aging. The relationship between the microstructures and the mechanical behaviour of these materials were investigated.

6.5.1 Microstructural characterization of arc-melted and PM alloys

The powder metallurgy material in the as-sintered state exhibits a nearly full-density bulk with a BCC matrix (in 74.7 wt.%) with grain sizes of 5.9 µm, rich in Ti, -Nb, -Ta and -Zr elements. An additional phase BCC2 was detected by XRD in 24.3 wt.%. This phase is too small in size, therefore was not possible to be assessed by EDS and EBSD. Other studies confirm the presence of two BCC crystal structures in similar compositions [36,92,93], possessing ordered and disordered lattices in a coherent interfacial relationship, these are the so-called refractory high-entropy superalloys. The ordering and coherency, however, was not assessed by this work yet, but will be subject to study by TEM in future studies.

Additionally, oxides were found in the as-sintered material preferentially in the grain boundaries in 1.0 wt.% and grain size of 0.9 µm. These were seen by SEM and its chemical composition was calculated by EDS. The small amount of oxides present in this material is due to a careful preparation before sintering. The powders handling was entirely done inside a glovebox with argon atmosphere. The calculation of oxygen content inside the chamber was lower than 0.1 ppm. The mechanical alloying is regarded as the main source of oxygen introduction since the powders were severely deformed by ball milling for 10 h. This is in accordance with other studies [117]. The sintering possibly slightly contributed as well, however the densification was performed in vacuum and for short time at the maximum temperature (15 min).

After exposing the PM material to 1400 °C, the BCC matrix has shown grain growth up to 18.0 µm and is present in 76.8 wt.%. Dissolution of the second bcc phase took place at certain extent, as visible by the reduction in content to values of 19.4 wt.% shown by XRD. It seems that 1 h at this temperature is not enough for obtaining a full dissolution of BCC2. CALPHAD calculations exhibited in Fig. 58 show that this belongs to a single BCC phase field.

The oxides content has risen to 3.8 wt.% according to XRD. The oxides seen to have suffered grain growth in the microstructure during heat treatments. There might be several reasons for

the increased presence of oxides, despite the heat treatments being performed in high vacuum and vented previously with argon, for guaranteeing no contamination during the time that the samples were inside the furnace.

High-entropy alloys were proven to exhibit high solubility of interstitial elements in their lattices [138,191–194]. This mechanism of introduction of elements in the interstitial vacancies to improve certain properties of metals is well documented in the literature [195]. The intense deformation caused by ball milling for 10 h might have introduced oxygen into the solid solution lattices, instead of forming oxides. However, heat treatment in such severe conditions at 1400 °C, a temperature ≥ $0.7T_m$, is possibly regarded as having induced further formation of oxides preferentially along the grain boundaries. The oxides already formed during sintering also suffered significant grain growth. Some of them might have own a nano-scale size and further grew in size.

The oxides were assessed by EDS maps and line spectrum, and they showed rich areas in especially in Ta and O elements. The SEM images indicate that these oxides grew preferentially on the grain boundaries.

One may notice the absence of pores in the as-sintered state, as compared to the images exhibited by the material after heat treatments, where it is possible to see pores and black regions pertaining to oxides. These seen to have been detached from the matrix due to prolonged mechano-chemical polishing by OPS, presenting weak interfacial bonds.

One may notice a very fine precipitates on the grain boundaries detected by SEM images (Fig. 79c,d) and Zr-rich, as shown by EDS mapping in Fig. 82. These might have appeared upon furnace cooling, since 1400 °C shows a single BCC phase field according to CALPHAD. This phase was not detected by XRD probably due to its very low content, under the resolution threshold of the technique.

This Zr rich phase suffered further growth when the material was subjected to 1050 °C for prolonged times (30h), shown by Fig. 84. This is most likely the HCP phase detected by XRD, in 4.8 wt.%. As this phase is too small in size, EBSD did not detect it.

Due to the formation of this Zr-rich phase along the grain boundaries, the BCC matrix is importantly depleted in Zr in AM8. The BCC matrix shows a grain size of 18.76 µm in 76.3 wt.%. The second BCC (BCC2) is present in 13.4 %, according to XRD, however still undetectable by EBSD due to its very fine size. The oxides are present in 5.5 wt. % and show and average particle size of 1.31 µm.

After exposed to 600 °C for 30 h, alternatively, the PM RHEA exhibits a rather interesting microstructure, comprised of BCC matrix (71.4 wt.%, grain size 17.4 µm) with nano-sized BCC precipitates of plate-like morphologies (in 20.0%), exhibited in Fig. 85. Oxides dispersed along the grain boundaries are present as well in 4.6% and grain sizes up to 1.1 µm. Another phase was detected by XRD, an HCP crystal structure in 4%. This phase was not detected by SEM, probably due to its very fine size.

The arc-melted material, in the as-melted state, exhibits much larger BCC grains as compared to the PM counterpart, showing average grain sizes of 147.2 µm in 100.0 wt.% content

according to XRD. This is in contradiction with the results obtained by SEM, where a two-phase field is visible by the dendritic/interdendritic regions, with dissimilar chemical compositions. This is explained by the fact that these two phases might possess very close lattice parameters and their patterns are overlapped on one another, in which the Rietveld refinement was not possible to resolve the slight differences. SAED patterns, however, may be able to identify both phases. Interdendrites are rich in Ti, Nb, Ta; dendrites are rich in Zr, Al and Ti. Similar results were obtained by Soni et al. [92] in similar composition for the BCC and B2 phases, respectively.

Heat treatment at 1400 °C for 1h seems to be sufficient for an efficient dissolution of the dendrites in AM5. A main BCC is exhibited in 88.3 wt.%, rich in Ti, Nb, Ta and Zr. The grains pertaining to this phase grew importantly after such homogenization, displaying values of 255.5 µm. The significant grain growth, in comparison with the PM counterpart, is regarded to the absence of oxides, therefore dislocation movement is not hindered at a comparable extent as in the PM RHEA.

A second BCC2 is present in 11.7 wt.%, showing that 1h is also not sufficient time to provide a single BCC phase field to the material. This phase is not detected by EBSD due to its very fine grain size.

Additional heat treatment at 1050 °C for 30h induces the precipitation of HCP phase in the material in 10.7 wt. %. This phase is Al and Zr rich. Al-Zr-rich intermetallics were observed elsewhere for refractory high entropy superalloys [196]. These were showed to be detrimental for the mechanical properties. Due to the HCP precipitation, the BCC matrix becomes depleted in Zr. The BCC phase comprises 74.2 wt.% of the alloy and shows an average grain size of 258.7 µm. Even after 30h at such high temperatures, there is no significant growth from the previous state, evidencing a certain stability of the phase. BCC2 appeared in 15.1 wt.% in a nano-sized scale.

Finally, at 600 °C for 30h, the arc-melted material shows a similar microstructure as displayed by PM, with a main BCC phase in 70.2%, with size of 246.5 µm, and BCC2 exhibits plate-like morphology in very fine nano-sized precipitates in the intragranular region with content of 25.5%. According to XRD, there is an HCP crystal structure on this alloy in 4.3 wt.% with crystal lattices different than the ones exhibited by the aging at 1050 °C. However, this phase was not detected by SEM.

One can notice that the phase formation in both manufacturing routes lead to similar results, with exception of oxides, similar phases appeared to be the present in both materials. This is possibly attributed to a not very high content of oxides in the PM material, at the extent of not compromising the formation of other phases.

The PM exhibits a much more refined microstructure as compared to its arc-melted bulks, induced by severe deformation caused by previous ball milling during mechanical alloying. The oxides are acting as importantly pinning the grain boundaries and avoiding further grain growth of the BCC matrix, even at very high temperatures of exposure and prolonged times, showing a contributing to a higher thermal stability of the material, at some extent.

6.5.2 Mechanical properties

The $Al_{0.3}NbTa_{0.8}Ti_{1.5}V_{0.2}Zr$ RHEAs produced by powder metallurgy and arc-melting were mechanically tested by microhardness, nanoindentation hardness, excitation for measurement of elastic modulus and flexural tests in room temperature. The last two techniques were performed on the heat-treated samples.

The PM material before and after heat treatments possess hardness and elastic modulus with values higher than their arc-melted counterparts. This stems from the fact that the PM RHEA acts as a composite, with in-situ formed oxides within a BCC metal matrix. Despite the production of both routes was solely made by feedstock materials with elements of commercial purity above 99.9 wt.%. Additionally, the powders were handled under protective atmosphere in a glovebox. Yet, oxide particles were in-situ formed and act as reinforcement to the material, increasing the hardness and elastic modulus of the material as compared to its arc-melted counterpart.

Among the PM samples, the as-sintered state exhibited the lowest hardness of them all. This is explained by the lowest content of oxides present in this state. The sample subjected to 1400 °C had an increased amount of oxides in comparison with the previous state, thus showing an increase in hardness, but still owing the second lowest hardness among the PM samples. This is because this material was exposed for the limited time of 1 h only in such high temperature.

On the other hand, the two remaining samples were exposed for a period of 30 h at 1050 (PM8) and 600 °C (PM14), therefore, they exhibit a significant increase in hardness values due to the increase in oxides content and their different microstructures. The PM8 RHEA exhibits a high amount of HCP phase along the grain boundaries, rich in Al and Zr. This most likely pertains to a certain aluminide's crystal structure, as the formation of aluminides was predicted by CALPHAD calculations. The previously studied composition $Al_{0.5}NbTa_{0.8}Ti_{1.5}V_{0.2}Zr$ evidenced the formation of many types of aluminides. None of them, though, corresponds to the same lattice parameters found by this HCP1 phase here in PM8 and AM8. This is probably because this $Al_{0.3}NbTa_{0.8}Ti_{1.5}V_{0.2}Zr$ composition is aluminum depleted; therefore the formation of phases varies, especially considering the aluminides formation. Aluminides possess very high hardness; therefore, the highest hardness is exhibited by PM8. Al-Zr-rich intermetallics were observed in refractory high entropy superalloys elsewhere [196] showing a deleterious mechanical behaviour.

PM14, conversely, do not exhibit formation of Al and Zr rich areas, even though shows the formation of a HCP2 phase with dissimilar lattice parameters. These phases, however, were not possible to be seen by SEM, probably due to their nano-sized character allied with low content. Nonetheless, very fine nanoprecipitates of a second BCC2 phase were evidenced to be formed in plate-like morphologies in significant amount within the intragranular regions of its BCC matrix. These nanoprecipitates allied with the increased oxides formation are regarded as the source of high values of hardness (the second highest) as well as the highest elastic modulus among them all.

The arc-melted RHEAs, on the other hand, show lower values of hardness compared to their powder metallurgy counterparts due to the absence of oxides. The as-melted material exhibits the lowest hardness of all alloys, due to its simple microstructure composed of BCC dendrites. AM5 (1400 °C for 1h) exhibits a similar hardness as the one of the previous states, due to being almost a single BCC phase with low amount of BCC2 precipitates. As expected, the highest hardness is exhibited by AM8. This sample was treated at 1050 °C for 30h – temperature range at which the aluminides formation is enhanced, thus improving the hardness of the material as a whole. AM14, however, do not show significant increase in hardness, maintaining the same levels of hardness exhibited by AM2 and AM8. This is probably due to the high amount of BCC1 and BCC2 phases' content allied with lack of aluminides and oxides.

The elastic modulus of the materials seems to increase with the increase in amount of secondary phases, similarly as it happens to composites, which follow the rule of mixtures. The highest elastic moduli were presented by PM14 and AM14. And the lowest in the states after homogenization (1400 °C for 1 h).

The elastic modulus of the materials calculated by nanoindentation hardness is higher than the ones shown by excitation method, however the same trend is seen in both methods. The higher values of elastic modulus with the former possibly stems from the size effect [197–199], in which the hardness tends to rise as the indent size decreases at nano/micro scales. This was described several times by the literature. One of the possible reasons is that geometrically necessary dislocations are created [200] in places where nanoindentation takes place, increasing the values of hardness and elastic modulus of the materials in the regions where the indents reached.

One may notice that the flexural strength of the PM materials is in any condition significantly higher, as compared to their arc-melted counterparts, attributed to the presence of ceramic particles as reinforcements.

The results of flexural tests show that PM14 and AM14 are the materials that achieved the highest flexural strengths. This is attributed to their unique microstructures possessing a BCC matrix and very fine nano-precipitates dispersed along the entire BCC grain regions. These nano-sized precipitates are visible in their respective SEM images and fractographic surfaces. It seems that these nano-sized BCC precipitates greatly strengthen the bulk materials when produced by both manufacturing routes. Conversely, the other samples did not have such high strengths, as they do not exhibit plate-like BCC nanoprecipitates.

Additionally, PM14 contains oxides imposing high strength to the material and acting as reinforcements in a metal BCC matrix. This greatly improves the flexural strength of the material to values up to 1202.6 MPa, in comparison to its arc-melted counterpart exhibiting a maximum value of strength up to 753.3 MPa. This renders approximately a 60% increase in strength at this condition due to use of powder metallurgy for the production of RHEAs.

All RHEAs exhibit a brittle character of the fracture behaviour. This is expected at room temperatures, since at such low temperatures, an intrinsic brittle behaviour is expect for

refractory metals. The ductility of refractory high entropy alloys at higher temperatures is expected to greatly improve, as shown by several other studies [84,85,92]. This is due to BCC metals characteristic brittle-to-ductile-transition (TBDT) phenomenon, therefore completely changing the behaviour of these alloys at higher temperatures. The assessment of the materials performance at high temperatures is planned as the next step of our future work.

In regard to the morphology of the fracture surfaces, the whole set of PM flexural samples exhibit mixture of inter and transgranular fractures, with multiple crack initiation sites.

PM14 shows prevalence of intergranular fracture along the grain boundaries, due to their weakening by presence of oxides, visibly detached during the flexural testing. This points to the weak interphase bonding between the matrix phase and the oxide particles, despite the high strength presented by the alloy at room temperature. PM5 and PM8 samples show similar behaviour. They show much higher fraction of transgranular fracture (cleavage), compared to PM14. The broken grains in PM5 and PM8 show either cleavage facets fracture features with protruding ridges or total cleavage fracture with flat surfaces.

The arc melted materials, on the other hand, displayed all fully transgranular fracture. Consequently, the grain boundaries are not weakened, in comparison to the grain interior area. Again, the material heat treated at 600 °C for 30 hours named AM14 endured the highest stresses. The transgranular fracture surfaces showed mostly cleavage facets. Additionally, the highly-magnified images (Fig. 94e-h) show that the fracture surfaces are not flat. Their excessive topology is caused by the presence of nano-precipitates of BCC phase. By this mechanism, the crack growth is hindered, leading to postponed total fracture compared to other sample lacking BCC nano-precipitates. AM5 and AM8 samples show similar behaviour, again similar to their corresponding PM materials. The samples displayed coarse-grained transgranular fracture, with relatively flat surfaces. At certain area on the fracture surface, cleavage facets and ridges are visible. However, at highly magnified images, the surfaces are much flatter compared to AM14. These facts imply that less energy was consumed for the crack propagation leading to earlier fracture (with respect to AM14).

7 Conclusions

In this work, the high entropy alloys $Al_{0.2}Co_{1.5}CrFeNi_{1.5}Ti$; $Al_{0.5}NbTa_{0.8}Ti_{1.5}V_{0.2}Zr$ and $Al_{0.3}NbTa_{0.8}Ti_{1.5}V_{0.2}Zr$ were prepared by powder metallurgy, by means of mechanical alloying and subsequent solid state sintering. The compositions were also prepared by melting routes for comparison, namely vacuum induction melting and casting for the first alloy; vacuum arc melting for the others. The microstructural characterization of the manufactured materials and their mechanical properties were evaluated, with special regard to their microstructural evolution before and after heat treatments.

The main general differences of the two processing routes are:

- When the powder metallurgy route is chosen, i.e. mechanical alloying by ball milling and subsequent sintering at solid state temperature, a successful production of metal matrix composites is feasible. This is due to in-situ reactions occurring during the process, producing a high entropy alloy's matrix reinforced with homogeneously dispersed ceramic particles (oxides/carbides).
- The amount of in-situ produced ceramic particles is dependent upon many factors. For instance: the purity of the feedstock materials before mechanical alloying; the powder handling either inside a glovebox under protective atmosphere or in air; the milling time; sintering temperature and time. These factors have a great influence on the contamination level of the bulk specimens; thus, one can adjust the amount of produced ceramic particles to the needs of the final material's application.
- The in-situ produced ceramic particles (oxides/carbides) have a great influence on the grain growth of powder metallurgy metal matrix composites. These particles suppress the grain growth of the microstructure during high temperature exposures even at prolonged times due to pinning of the grain boundaries. They retard dislocation movement, therefore greatly contributing to the strength of the material.
- In contrast, by using traditional vacuum induction melting or vacuum arc melting, pure metals possessing microstructures with significantly enlarged grain sizes are produced. An effective grain size refinement is possible, for instance, by cold deformation processes, however imposing important anisotropy.
- Melting routes in liquid state, e.g. casting, have problems to produce metals containing elements possessing high melting temperatures, e.g. refractories, since these often segregate and might not fully dissolve. At the same time, when low melting temperature elements are added to the alloying process, these may evaporate to a certain extent. Several melting cycles are necessary for a full homogenization of the piece, and adjustment in amount of low melting temperature elements are necessary in advance. Since powder metallurgy is a solid-state process, the mentioned segregation and evaporation phenomena do not occur.

The conclusions regarding $Al_{0.2}Co_{1.5}CrFeNi_{1.5}Ti$ composition are summarized below:

- The production routes, particularly the processing conditions (such as impact by mechanical alloying, temperatures and cooling rates) play a crucial role in dictating the final microstructural features, significantly influencing the mechanical and tribological properties of the two alloys.
- The PM course has an intrinsic propensity to form in-situ carbides during mechanical milling. As such, the PM alloy exhibited a uniform, fine-grained microstructure composed almost solely of a nano-sized FCC matrix (89%) with evenly dispersed nano-sized TiC particles (8%, formed in-situ during the mechanical milling), minor BCC phase and, additionally, intra-granular nano-sized coherent precipitates in an γ/γ′

relationship with the matrix. Such microstructure is analogous to that of some nickel-based superalloys.

- In contrast, the Cast HEA exhibited a coarse-grained microstructure containing 48% of the FCC matrix, 10% BCC phase and a 42% mixture of hard intermetallic phases (needle-shaped Laves and σ). Formation of the ordered phases is a consequence of the large negative enthalpy, triggering a segregation process during the cooling. Both microstructures are in good agreement with the predicted phases obtained by CALPHAD calculation.
- The PM alloy has exhibited a remarkable flexural strength Rmo = 2018 MPa, elastic modulus E = 258 GPa, and hardness 712 HV. These values were far superior to the cast counterpart (1101 MPa, 210 GPa, 682 HV), which was most likely deteriorated by the high content of unavoidable brittle phases. Surprisingly, in contrast to the strength values, the PM alloy displayed an unexpected ductile fracture behavior, potentially a consequence of the ductile nature of FCC phase and a strong TiC particle-matrix interface.
- At low loads, the PM alloy showed wear resistance surpassing that of the conventional wear-resistant tool steel AISI 52100 or Inconel 713. Unfortunately, the wear resistance significantly decreased under an increasing load. Despite the rather weaker mechanical properties, the cast alloy exhibited the best wear properties among all tested materials at both tested loads.
- Mild-oxidational wear is the predominant tribological regime for both PM and Cast HEAs. The adhesive wear's tendency of Cast HEA is hindered to some extent, since the volume fraction of the disordered FCC phase is about one half relative to its PM counterpart, as ductile FCC phase is more inclined to form adhesive bonds. Additionally, the hard TCP phases present in Cast HEA serve as barriers to delamination wear, thus the enhanced wear resistance may be explained.
- In overall comparison, PM process is better suited for the manufacturing of mechanically resistant, fine-grained HEAs with very homogenous microstructures and enhanced wear resistance. On the other hand, casting is better suited for manufacturing of wear resistant HEAs for applications where their intrinsic brittleness is not an issue.
- Upon heat treatments, even at temperatures close to the melting point of the alloy for up to 10h, PM HEA still exhibits a nanosized character, comprising a main FCC matrix and dispersed carbides, indicating thermal stability of the composite. The amount of the formed carbides slightly increases with the heat treatment performed in air.
- In contrast, the cast HEA, when submitted to the same heat treatments, shows significant grain growth compared to PM, due to the nature of the distinct fabrication

methods and lack of carbides on the cast. The heat treatment in air does not seem to lead to formation of oxides, thus indicating a certain resistance to oxidation.

- Heat treatment for 5h at 1000 °C is not enough to fully dissolve all secondary phases and reach a single-phase field. Upon 10 h of heat treatments, preferential orientation is still evident in cast HEA due to dendritic solidification during the casting.
- The elastic modulus of the PM HEA is relatively constant before and after heat treatments. This is attributed to the presence of carbides, stabilizing the grain sizes of the microstructure by pinning the grain boundaries, thus keeping them constant, even after 10 h at high temperatures.
- The cast counterpart shows a very brittle character due to the presence of laves and sigma phases. Upon heat treatments, the values of elastic modulus reach similar values of those of PM HEA due to partial dissolution of these phases.

The conclusions regarding the refractory high entropy alloys ($Al_{0.5}NbTa_{0.8}Ti_{1.5}V_{0.2}Zr$ and $Al_{0.3}NbTa_{0.8}Ti_{1.5}V_{0.2}Zr$) are summarized below:

- Concerning the effect of the milling time variation on the sintered bulks, it is possible to state that longer times of milling lead to more refined microstructures, containing higher amounts of oxides dispersed into the matrix.
- Regarding the influence of sintering temperatures on the properties of the refractory bulks, by using all tested sintered temperatures of 1200 °C, 1300 °C and 1600 °C combined with a uniaxial pressure of 50 MPa, it is possible to achieve full density samples. The bulks exhibited a homogeneous distribution of phases, with presence of in-situ formed homogeneously dispersed carbides, which are responsible for a grain-boundary pinning effect and stabilization of fine-grained microstructures even at very high temperatures of exposure.
- The $Al_{0.5}NbTa_{0.8}Ti_{1.5}V_{0.2}Zr$ RHEA produced by PM possesses very fine grain sizes even after heat treatments at very high temperatures for prolonged times. This is due to the ODS effect.
- The AM $Al_{0.5}NbTa_{0.8}Ti_{1.5}V_{0.2}Zr$ counterpart undergo substantial grain growth at the temperature of solution treatment (1400 °C), showing ≈ 35% increase in grain sizes of the main BCC phase. Further heat treatments in lower temperatures for 30 h, however, induce a very slight grain growth.
- By using a combination of a careful handling of elemental feedstock powders with commercial purity inside glovebox, it is possible to effectively reduce the contamination and formation of dispersed oxides within the matrix at some extent.
- When Zr sponge is used as feedstock material as intentional source of contamination prior to mechanical alloying of elemental powders (in $Al_{0.5}NbTa_{0.8}Ti_{1.5}V_{0.2}Zr$ stoichiometric ratio), the formation of in-situ ceramic particles in the as-sintered state

emerge up to about 14 % of the total weight of the material. In contrast, when one uses commercial powders with high purity as feedstock, the amount of ceramic particles is shown to be only about 2 wt.%. Yet, their grain sizes in the as-sintered states are comparable.

- Once the RHEA is produced by powder metallurgy without sufficient in-situ formation of ODS particles, the induced changes in the materials behaviour by applying heat treatments appear to resemble those of the arc-melted counterpart. The kinetics of grain growth, the phase transformations, chemical composition of phases are behaving more likely as a metallic alloy, rather than a composite.
- For applications in which ODS particles in a metal matrix are envisaged, for instance in high temperature applications, one can use different feedstock products to produce refractory alloys, such as Zr sponge, as an alternative for effective production of homogeneously dispersed oxide particles within a metal matrix composite. This is an alternative for adjusting the amount of ceramic particles formation is possible
- The studied $Al_{0.3}NbTa_{0.8}Ti_{1.5}V_{0.2}Zr$ produced by PM exhibits a much more refined microstructure as compared to its arc-melted bulks, induced by severe deformation caused by previous ball milling during mechanical alloying. The oxides are acting as importantly pinning the grain boundaries and avoiding further grain growth of the BCC matrix, even at very high temperatures of exposure and prolonged times, indicating a contribution, to some extent, to a higher thermal stability of the material.
- The PM material before and after heat treatments possess hardness, elastic modulus and flexural strengths with values higher than their arc-melted counterparts. This stems from the fact that the PM RHEA acts as a composite, with in-situ formed oxides within a BCC metal matrix. The elastic modulus of the materials seems to increase with the increase in amount of secondary phases upon heat treatments.
- A remarkable flexural strength of 1200 MPa was achieved for the refractory PM material upon the combination of heat treatments of 1400 ^{o}C for 1 h and subsequent 600^{o}C for 30 h. This value is approximately 60 % higher than that exhibited by the AM counterpart. This is attributed to the presence of ceramic particles acting as reinforcements in a metal matrix in PM bulk, and very fine nanoprecipitates of BCC in a plate-like morphology. The arc melted counterpart showed significantly lower strength at the same condition (753 MPa) yet exhibiting the best results among the tested arc-melted materials. The nano-sized BCC precipitates greatly strengthen the bulk materials when produced by both manufacturing routes. In opposition, the other samples did not have such high strengths, as they do not exhibit plate-like BCC nanoprecipitates.

- All $Al_{0.3}NbTa_{0.8}Ti_{1.5}V_{0.2}Zr$ RHEAs, before and after heat treatments, exhibit a brittle character of the fracture behaviour. This is anticipated at room temperature, since at such low temperatures, an intrinsic brittle behaviour is expected for refractory metals.

8 References

[1] P.C. Gasson, The Superalloys: Fundamentals and Applications R. C. Reed Cambridge University Press, The Edinburgh Building, Shaftesbury Road, Cambridge, CB2 2RU, UK, 2006. 372pp. Illustrated. £80. ISBN 0-521-85904-2., Aeronaut. J. 112 (2008) 291. https://doi.org/10.1017/S0001924000087509.

[2] Y. Bar-Cohen, High Temperature Materials and Mechanisms, 1st ed., CRC Press, Boca Raton, 2014. https://doi.org/https://doi.org/10.1201/b16545.

[3] W. Betteridge, S.W.K. Shaw, Development of superalloys, Mater. Sci. Technol. 3 (1987) 682–694. https://doi.org/10.1179/mst.1987.3.9.682.

[4] Gaoyuan Ouyang, High Temperature Structure Materials beyond Nickel Base Superalloy, J Mater Sci Nanomater. 1 (2017) e107. https://www.omicsonline.org/open-access/high-temperature-structure-materials-beyond-nickel-base-superalloy.pdf.

[5] C.L. Briant, Refractory Metals and Alloys, in: K.H.J. Buschow, R.W. Cahn, M.C. Flemings, B. Ilschner, E.J. Kramer, S. Mahajan, P.B.T.-E. of M.S. and T. Veyssière (Eds.), Elsevier, Oxford, 2001: pp. 8088–8095. https://doi.org/https://doi.org/10.1016/B0-08-043152-6/01453-4.

[6] J.-W. Yeh, S.-K. Chen, S.-J. Lin, J.-Y. Gan, T.-S. Chin, T.-T. Shun, C.-H. Tsau, S.-Y. Chang, Nanostructured High-Entropy Alloys with Multiple Principal Elements: Novel Alloy Design Concepts and Outcomes, Adv. Eng. Mater. 6 (2004) 299–303. https://doi.org/10.1002/adem.200300567.

[7] J.-W. Yeh, Physical Metallurgy of High-Entropy Alloys, JOM. 67 (2015) 2254–2261. https://doi.org/10.1007/s11837-015-1583-5.

[8] B.S. Murty, J.W. Yeh, S. Ranganathan, Chapter 2 - High-Entropy Alloys: Basic Concepts, in: B.S. Murty, J.W. Yeh, S.B.T.-H.E.A. Ranganathan (Eds.), Butterworth-Heinemann, Boston, 2014: pp. 13–35. https://doi.org/https://doi.org/10.1016/B978-0-12-800251-3.00002-X.

[9] S. Sheikh, S. Shafeie, Q. Hu, J. Ahlström, C. Persson, J. Veselý, J. Zýka, U. Klement, S. Guo, Alloy design for intrinsically ductile refractory high-entropy alloys, J. Appl. Phys. 120 (2016) 164902. https://doi.org/10.1063/1.4966659.

[10] J. Chen, X. Zhou, W. Wang, B. Liu, Y. Lv, W. Yang, D. Xu, Y. Liu, A review on fundamental of high entropy alloys with promising high–temperature properties, J. Alloys Compd. 760 (2018) 15–30. https://doi.org/https://doi.org/10.1016/j.jallcom.2018.05.067.

[11] Z. Li, K.G. Pradeep, Y. Deng, D. Raabe, C.C. Tasan, Metastable high-entropy dual-phase alloys overcome the strength–ductility trade-off, Nature. 534 (2016) 227. https://doi.org/10.1038/nature17981.

[12] B. Gludovatz, A. Hohenwarter, K.V.S. Thurston, H. Bei, Z. Wu, E.P. George, R.O. Ritchie, Exceptional damage-tolerance of a medium-entropy alloy CrCoNi at cryogenic temperatures, Nat. Commun. 7 (2016) 10602. https://doi.org/10.1038/ncomms10602.

[13] B. Gludovatz, A. Hohenwarter, D. Catoor, E.H. Chang, E.P. George, R.O. Ritchie, A fracture-resistant high-entropy alloy for cryogenic applications, Science (80-.). 345 (2014) 1153 LP – 1158. https://doi.org/10.1126/science.1254581.

[14] T. Yang, Y. Zhao, W. Liu, J. Kai, C. Liu, L12-strengthened high-entropy alloys for advanced structural applications, J. Mater. Res. 33 (2018) 2983–2997. https://doi.org/DOI: 10.1557/jmr.2018.186.

[15] Y.-J. Chang, A.-C. Yeh, The evolution of microstructures and high temperature properties of AlxCo1.5CrFeNi1.5Tiy high entropy alloys, J. Alloys Compd. 653 (2015) 379–385. https://doi.org/https://doi.org/10.1016/j.jallcom.2015.09.042.

[16] J.K. Jensen, B.A. Welk, R.E.A. Williams, J.M. Sosa, D.E. Huber, O.N. Senkov, G.B. Viswanathan, H.L. Fraser, Characterization of the microstructure of the compositionally complex alloy Al1Mo0.5Nb1Ta0.5Ti1Zr1, Scr. Mater. 121 (2016) 1–4. https://doi.org/https://doi.org/10.1016/j.scriptamat.2016.04.017.

[17] N.O. Senkov, D. Isheim, N.D. Seidman, L.A. Pilchak, Development of a Refractory High Entropy Superalloy, Entropy . 18 (2016). https://doi.org/10.3390/e18030102.

[18] X. Yang, Y. Zhang, P.K. Liaw, Microstructure and Compressive Properties of NbTiVTaAlx High Entropy Alloys, Procedia Eng. 36 (2012) 292–298. https://doi.org/https://doi.org/10.1016/j.proeng.2012.03.043.

[19] O.N. Senkov, S. V Senkova, C. Woodward, Effect of aluminum on the microstructure and properties of two refractory high-entropy alloys, Acta Mater. 68 (2014) 214–228. https://doi.org/https://doi.org/10.1016/j.actamat.2014.01.029.

[20] O.N. Senkov, G.B. Wilks, D.B. Miracle, C.P. Chuang, P.K. Liaw, Refractory high-entropy alloys, Intermetallics. 18 (2010) 1758–1765. https://doi.org/https://doi.org/10.1016/j.intermet.2010.05.014.

[21] I. Moravcik, L. Gouvea, J. Cupera, I. Dlouhy, Preparation and properties of medium entropy CoCrNi/boride metal matrix composite, J. Alloys Compd. 748 (2018). https://doi.org/10.1016/j.jallcom.2018.03.204.

[22] Z. Fu, W. Chen, H. Wen, D. Zhang, Z. Chen, B. Zheng, Y. Zhou, E.J. Lavernia, Microstructure and strengthening mechanisms in an FCC structured single-phase nanocrystalline Co25Ni25Fe25Al7.5Cu17.5 high-entropy alloy, Acta Mater. 107 (2016) 59–71. https://doi.org/https://doi.org/10.1016/j.actamat.2016.01.050.

[23] I. Moravcik, J. Cizek, L. Gouvea, J. Cupera, I. Guban, I. Dlouhy, Nitrogen Interstitial Alloying of CoCrFeMnNi High Entropy Alloy through Reactive Powder Milling, Entropy. 21 (2019) 363. https://doi.org/10.3390/e21040363.
[24] I. Moravcik, L. Gouvea, V. Hornik, Z. Kovacova, M. Kitzmantel, E. Neubauer, I. Dlouhy, Synergic strengthening by oxide and coherent precipitate dispersions in high-entropy alloy prepared by powder metallurgy, Scr. Mater. 157 (2018). https://doi.org/10.1016/j.scriptamat.2018.07.034.
[25] B.S. Murty, J.W. Yeh, S. Ranganathan, Chapter 1 - A Brief History of Alloys and the Birth of High-Entropy Alloys, in: B.S. Murty, J.W. Yeh, S.B.T.-H.E.A. Ranganathan (Eds.), Butterworth-Heinemann, Boston, 2014: pp. 1–12. https://doi.org/https://doi.org/10.1016/B978-0-12-800251-3.00001-8.
[26] H. Bhadeshia, R. Honeycombe, Chapter 2 - Strengthening of Iron and Its Alloys, in: H. Bhadeshia, R.B.T.-S.M. and P. (Fourth E. Honeycombe (Eds.), Butterworth-Heinemann, 2017: pp. 23–57. https://doi.org/https://doi.org/10.1016/B978-0-08-100270-4.00002-0.
[27] R.L. Brown, A review of: "STEELS: HEAT TREATMENT AND PROCESSING PRINCIPLES" by G. Krauss ASM International 497 pages, Second Edition, hard cover, $75, 1990., Mater. Manuf. Process. 6 (1991) 569–570. https://doi.org/10.1080/10426919108934789.
[28] B. Cantor, I.T.H. Chang, P. Knight, A.J.B. Vincent, Microstructural development in equiatomic multicomponent alloys, Mater. Sci. Eng. A. 375–377 (2004) 213–218. https://doi.org/https://doi.org/10.1016/j.msea.2003.10.257.
[29] E.P. George, D. Raabe, R.O. Ritchie, High-entropy alloys, Nat. Rev. Mater. 4 (2019) 515–534. https://doi.org/10.1038/s41578-019-0121-4.
[30] M.C. Gao, J.-W. Yeh, P.K. Liaw, Y. Zhang, eds., High-Entropy Alloys Fundamentals and Applications, 1st ed., Springer International Publishing, 2016. https://doi.org/10.1007/978-3-319-27013-5.
[31] S. Murty, B S; Yeh, J.W.; Ranganathan, High-Entropy Alloys, 1st ed., Butterworth-Heinemann, London, U.K., 2014.
[32] C.S. Smith, Four outstanding researches in metallurgical history., American Society for Testing and Materials, [Philadelphia?, 1963.
[33] Y. Zhang, T.T. Zuo, Z. Tang, M.C. Gao, K.A. Dahmen, P.K. Liaw, Z.P. Lu, Microstructures and properties of high-entropy alloys, Prog. Mater. Sci. 61 (2014) 1–93. https://doi.org/https://doi.org/10.1016/j.pmatsci.2013.10.001.
[34] Z. Li, D. Raabe, Strong and Ductile Non-equiatomic High-Entropy Alloys: Design, Processing, Microstructure, and Mechanical Properties, JOM. 69 (2017) 2099–2106. https://doi.org/10.1007/s11837-017-2540-2.
[35] D.B. Miracle, J.D. Miller, O.N. Senkov, C. Woodward, M.D. Uchic, J. Tiley, Exploration and Development of High Entropy Alloys for Structural Applications, Entropy. 16 (2014) 494–525. https://doi.org/10.3390/e16010494.
[36] D.B. Miracle, O.N. Senkov, A critical review of high entropy alloys and related concepts, Acta Mater. 122 (2017) 448–511. https://doi.org/https://doi.org/10.1016/j.actamat.2016.08.081.
[37] X. Yang, S.Y. Chen, J.D. Cotton, Y. Zhang, Phase Stability of Low-Density, Multiprincipal Component Alloys Containing Aluminum, Magnesium, and Lithium, JOM. 66 (2014) 2009–2020. https://doi.org/10.1007/s11837-014-1059-z.
[38] C.M. Rost, E. Sachet, T. Borman, A. Moballegh, E.C. Dickey, D. Hou, J.L. Jones, S. Curtarolo, J.-P. Maria, Entropy-stabilized oxides, Nat. Commun. 6 (2015) 8485. https://doi.org/10.1038/ncomms9485.
[39] J. Gild, Y. Zhang, T. Harrington, S. Jiang, T. Hu, M.C. Quinn, W.M. Mellor, N. Zhou, K. Vecchio, J. Luo, High-Entropy Metal Diborides: A New Class of High-Entropy Materials and a New Type of Ultrahigh Temperature Ceramics, Sci. Rep. 6 (2016) 37946. https://doi.org/10.1038/srep37946.
[40] S. Jiang, T. Hu, J. Gild, N. Zhou, J. Nie, M. Qin, T. Harrington, K. Vecchio, J. Luo, A new class of high-entropy perovskite oxides, Scr. Mater. 142 (2018) 116–120. https://doi.org/https://doi.org/10.1016/j.scriptamat.2017.08.040.
[41] J.W. Qiao, M.L. Bao, Y.J. Zhao, H.J. Yang, Y.C. Wu, Y. Zhang, J.A. Hawk, M.C. Gao, Rare-earth high entropy alloys with hexagonal close-packed structure, J. Appl. Phys. 124 (2018) 195101. https://doi.org/10.1063/1.5051514.
[42] A. Takeuchi, K. Amiya, T. Wada, K. Yubuta, W. Zhang, High-Entropy Alloys with a Hexagonal Close-Packed Structure Designed by Equi-Atomic Alloy Strategy and Binary Phase Diagrams, JOM. 66 (2014) 1984–1992. https://doi.org/10.1007/s11837-014-1085-x.
[43] K.J. Laws, C. Crosby, A. Sridhar, P. Conway, L.S. Koloadin, M. Zhao, S. Aron-Dine, L.C. Bassman, High entropy brasses and bronzes – Microstructure, phase evolution and properties, J. Alloys Compd. 650 (2015) 949–961. https://doi.org/https://doi.org/10.1016/j.jallcom.2015.07.285.
[44] J.O.A. Paschoal, H. Kleykamp, F. Thuemmler, Phase equilibria in the quaternary molybdenum-ruthenium-rhodium-palladium system, Zeitschrift Fuer Met. 74 (1983) 652–664. http://inis.iaea.org/search/search.aspx?orig_q=RN:15020686.
[45] Z.P. Lu, H. Wang, M.W. Chen, I. Baker, J.W. Yeh, C.T. Liu, T.G. Nieh, An assessment on the future development of high-entropy alloys: Summary from a recent workshop, Intermetallics. 66 (2015) 67–76. https://doi.org/https://doi.org/10.1016/j.intermet.2015.06.021.
[46] Y. Zhang, Y.J. Zhou, J.P. Lin, G.L. Chen, P.K. Liaw, Solid-Solution Phase Formation Rules for Multi-component Alloys, Adv. Eng. Mater. 10 (2008) 534–538. https://doi.org/10.1002/adem.200700240.
[47] J.W. Gibbs, On the Equilibrium of Heterogeneous Substances, Sci. Pap. J. Willard Gibbs. 1 (1906).
[48] B.S. Murty, J.W. Yeh, S. Ranganathan, Chapter 3 - Phase Selection in High-Entropy Alloys, in: B.S. Murty, J.W. Yeh, S.B.T.-H.E.A. Ranganathan (Eds.), Butterworth-Heinemann, Boston, 2014: pp. 37–56.

https://doi.org/https://doi.org/10.1016/B978-0-12-800251-3.00003-1.
[49] R.A. Swalin, Thermodynamics of Solids, 2nd ed., Wiley-VCH, 1972.
[50] A. Van de Walle, G. Ceder, The effect of lattice vibrations on substitutional alloy thermodynamics, Rev. Mod. Phys. 74 (2002) 11–45. https://doi.org/10.1103/RevModPhys.74.11.
[51] B. Fultz, Vibrational thermodynamics of materials, Prog. Mater. Sci. 55 (2010) 247–352. https://doi.org/https://doi.org/10.1016/j.pmatsci.2009.05.002.
[52] J. Wang, J. Li, Q. Wang, J. Wang, Z. Wang, C.T. Liu, The incredible excess entropy in high entropy alloys, Scr. Mater. 168 (2019) 19–22. https://doi.org/https://doi.org/10.1016/j.scriptamat.2019.04.013.
[53] Q. He, Y. Yang, On Lattice Distortion in High Entropy Alloys , Front. Mater. . 5 (2018) 42. https://www.frontiersin.org/article/10.3389/fmats.2018.00042.
[54] Z. Li, S. Zhao, R.O. Ritchie, M.A. Meyers, Mechanical properties of high-entropy alloys with emphasis on face-centered cubic alloys, Prog. Mater. Sci. 102 (2019) 296–345. https://doi.org/https://doi.org/10.1016/j.pmatsci.2018.12.003.
[55] J.-W. Yeh, S.-Y. Chang, Y.-D. Hong, S.-K. Chen, S.-J. Lin, Anomalous decrease in X-ray diffraction intensities of Cu–Ni–Al–Co–Cr–Fe–Si alloy systems with multi-principal elements, Mater. Chem. Phys. 103 (2007) 41–46. https://doi.org/https://doi.org/10.1016/j.matchemphys.2007.01.003.
[56] L.R. Owen, E.J. Pickering, H.Y. Playford, H.J. Stone, M.G. Tucker, N.G. Jones, An assessment of the lattice strain in the CrMnFeCoNi high-entropy alloy, Acta Mater. 122 (2017) 11–18. https://doi.org/https://doi.org/10.1016/j.actamat.2016.09.032.
[57] I. Moravcik, J. Cizek, Z. Kovacova, J. Nejezchlebova, M. Kitzmantel, E. Neubauer, I. Kubena, V. Hornik, I. Dlouhy, Mechanical and microstructural characterization of powder metallurgy CoCrNi medium entropy alloy, Mater. Sci. Eng. A. 701 (2017) 370–380. https://doi.org/https://doi.org/10.1016/j.msea.2017.06.086.
[58] Y.L. Zhao, T. Yang, Y. Tong, J. Wang, J.H. Luan, Z.B. Jiao, D. Chen, Y. Yang, A. Hu, C.T. Liu, J.-J. Kai, Heterogeneous precipitation behavior and stacking-fault-mediated deformation in a CoCrNi-based medium-entropy alloy, Acta Mater. 138 (2017) 72–82. https://doi.org/https://doi.org/10.1016/j.actamat.2017.07.029.
[59] F. Otto, A. Dlouhý, C. Somsen, H. Bei, G. Eggeler, E.P. George, The influences of temperature and microstructure on the tensile properties of a CoCrFeMnNi high-entropy alloy, Acta Mater. 61 (2013) 5743–5755. https://doi.org/https://doi.org/10.1016/j.actamat.2013.06.018.
[60] F.G. Coury, SOLID SOLUTION STRENGTHENING MECHANISMS IN HIGH ENTROPY ALLOYS, Colorado School of Mines, n.d. https://mountainscholar.org/bitstream/handle/11124/172516/GilCoury_mines_0052E_11599.pdf?sequence=1&isAllowed=y.
[61] S. GUO, C.T. LIU, Phase stability in high entropy alloys: Formation of solid-solution phase or amorphous phase, Prog. Nat. Sci. Mater. Int. 21 (2011) 433–446. https://doi.org/https://doi.org/10.1016/S1002-0071(12)60080-X.
[62] N.-X. Song, Hong-quan; Tian, Fuyang; Hu, Q.M.; Vitos, Levente; Wang, Y.; Shen, J.; Chen, Local lattice distortion in high-entropy alloys, Mater. Sci. 1 (2017) 8. https://doi.org/10.1103/PhysRevMaterials.1.023404.
[63] J.-W. Yeh, Alloy Design Strategies and Future Trends in High-Entropy Alloys, JOM. 65 (2013) 1759–1771. https://doi.org/10.1007/s11837-013-0761-6.
[64] K.-Y. Tsai, M.-H. Tsai, J.-W. Yeh, Sluggish diffusion in Co–Cr–Fe–Mn–Ni high-entropy alloys, Acta Mater. 61 (2013) 4887–4897. https://doi.org/https://doi.org/10.1016/j.actamat.2013.04.058.
[65] S. Guo, C. Ng, J. Lu, C.T. Liu, Effect of valence electron concentration on stability of fcc or bcc phase in high entropy alloys, J. Appl. Phys. 109 (2011) 103505. https://doi.org/10.1063/1.3587228.
[66] L. Qi, D.C. Chrzan, Tuning Ideal Tensile Strengths and Intrinsic Ductility of bcc Refractory Alloys, Phys. Rev. Lett. 112 (2014) 115503. https://doi.org/10.1103/PhysRevLett.112.115503.
[67] S. Ranganathan, Alloyed pleasures: Multimetallic cocktails, Curr. Sci. 85 (2003) 1404–1406.
[68] A. Gali, E.P. George, Tensile properties of high- and medium-entropy alloys, Intermetallics. 39 (2013) 74–78. https://doi.org/https://doi.org/10.1016/j.intermet.2013.03.018.
[69] Igor Moravcik, METAL MATRIX COMPOSITES PREPARED BY POWDER METALLURGY ROUTE, Brno University of Technology, 2017. https://www.vutbr.cz/www_base/zav_prace_soubor_verejne.php?file_id=160763.
[70] S.S. Sohn, A. Kwiatkowski da Silva, Y. Ikeda, F. Körmann, W. Lu, W.S. Choi, B. Gault, D. Ponge, J. Neugebauer, D. Raabe, Ultrastrong Medium-Entropy Single-Phase Alloys Designed via Severe Lattice Distortion, Adv. Mater. 31 (2019) 1807142. https://doi.org/10.1002/adma.201807142.
[71] G. Laplanche, A. Kostka, C. Reinhart, J. Hunfeld, G. Eggeler, E.P. George, Reasons for the superior mechanical properties of medium-entropy CrCoNi compared to high-entropy CrMnFeCoNi, Acta Mater. 128 (2017) 292–303. https://doi.org/https://doi.org/10.1016/j.actamat.2017.02.036.
[72] A.J. Zaddach, R.O. Scattergood, C.C. Koch, Tensile properties of low-stacking fault energy high-entropy alloys, Mater. Sci. Eng. A. 636 (2015) 373–378. https://doi.org/https://doi.org/10.1016/j.msea.2015.03.109.
[73] L. Patriarca, A. Ojha, H. Sehitoglu, Y.I. Chumlyakov, Slip nucleation in single crystal FeNiCoCrMn high entropy alloy, Scr. Mater. 112 (2016) 54–57. https://doi.org/https://doi.org/10.1016/j.scriptamat.2015.09.009.
[74] G. Meric de Bellefon, M.N. Gussev, A.D. Stoica, J.C. van Duysen, K. Sridharan, Examining the influence of stacking fault width on deformation twinning in an austenitic stainless steel, Scr. Mater. 157 (2018) 162–166. https://doi.org/https://doi.org/10.1016/j.scriptamat.2018.08.012.
[75] W. Guo, J. Su, W. Lu, C.H. Liebscher, C. Kirchlechner, Y. Ikeda, F. Körmann, X. Liu, Y. Xue, G. Dehm,

Dislocation-induced Breakthrough of Strength and Ductility Trade-off in a Non-equiatomic High-Entropy Alloy, Acta Mater. (2019). https://doi.org/https://doi.org/10.1016/j.actamat.2019.11.055.
[76] Z. Li, C.C. Tasan, H. Springer, B. Gault, D. Raabe, Interstitial atoms enable joint twinning and transformation induced plasticity in strong and ductile high-entropy alloys, Sci. Rep. 7 (2017) 40704. https://doi.org/10.1038/srep40704 http://www.nature.com/articles/srep40704#supplementary-information.
[77] J.Y. He, W.H. Liu, H. Wang, Y. Wu, X.J. Liu, T.G. Nieh, Z.P. Lu, Effects of Al addition on structural evolution and tensile properties of the FeCoNiCrMn high-entropy alloy system, Acta Mater. 62 (2014) 105–113. https://doi.org/https://doi.org/10.1016/j.actamat.2013.09.037.
[78] C. Ng, S. Guo, J. Luan, Q. Wang, J. Lu, S. Shi, C.T. Liu, Phase stability and tensile properties of Co-free Al0.5CrCuFeNi2 high-entropy alloys, J. Alloys Compd. 584 (2014) 530–537. https://doi.org/https://doi.org/10.1016/j.jallcom.2013.09.105.
[79] A. V Kuznetsov, D.G. Shaysultanov, N.D. Stepanov, G.A. Salishchev, O.N. Senkov, Tensile properties of an AlCrCuNiFeCo high-entropy alloy in as-cast and wrought conditions, Mater. Sci. Eng. A. 533 (2012) 107–118. https://doi.org/https://doi.org/10.1016/j.msea.2011.11.045.
[80] D.G. Shaysultanov, N.D. Stepanov, A. V Kuznetsov, G.A. Salishchev, O.N. Senkov, Phase Composition and Superplastic Behavior of a Wrought AlCoCrCuFeNi High-Entropy Alloy, JOM. 65 (2013) 1815–1828. https://doi.org/10.1007/s11837-013-0754-5.
[81] M.A. Hemphill, T. Yuan, G.Y. Wang, J.W. Yeh, C.W. Tsai, A. Chuang, P.K. Liaw, Fatigue behavior of Al0.5CoCrCuFeNi high entropy alloys, Acta Mater. 60 (2012) 5723–5734. https://doi.org/https://doi.org/10.1016/j.actamat.2012.06.046.
[82] O.N. Senkov, D.B. Miracle, K.J. Chaput, J.-P. Couzinie, Development and exploration of refractory high entropy alloys—A review, J. Mater. Res. 33 (2018) 3092–3128. https://doi.org/DOI: 10.1557/jmr.2018.153.
[83] O.N. Senkov, C. Woodward, D.B. Miracle, Microstructure and Properties of Aluminum-Containing Refractory High-Entropy Alloys, JOM. 66 (2014) 2030–2042. https://doi.org/10.1007/s11837-014-1066-0.
[84] O.N. Senkov, J.M. Scott, S. V Senkova, F. Meisenkothen, D.B. Miracle, C.F. Woodward, Microstructure and elevated temperature properties of a refractory TaNbHfZrTi alloy, J. Mater. Sci. 47 (2012) 4062–4074. https://doi.org/10.1007/s10853-012-6260-2.
[85] O.N. Senkov, G.B. Wilks, J.M. Scott, D.B. Miracle, Mechanical properties of Nb25Mo25Ta25W25 and V20Nb20Mo20Ta20W20 refractory high entropy alloys, Intermetallics. 19 (2011) 698–706. https://doi.org/https://doi.org/10.1016/j.intermet.2011.01.004.
[86] N.D. Stepanov, N.Y. Yurchenko, S. V Zherebtsov, M.A. Tikhonovsky, G.A. Salishchev, Aging behavior of the HfNbTaTiZr high entropy alloy, Mater. Lett. 211 (2018) 87–90. https://doi.org/https://doi.org/10.1016/j.matlet.2017.09.094.
[87] G. Dirras, L. Lilensten, P. Djemia, M. Laurent-Brocq, D. Tingaud, J.-P. Couzinié, L. Perrière, T. Chauveau, I. Guillot, Elastic and plastic properties of as-cast equimolar TiHfZrTaNb high-entropy alloy, Mater. Sci. Eng. A. 654 (2016) 30–38. https://doi.org/https://doi.org/10.1016/j.msea.2015.12.017.
[88] Y.D. Wu, Y.H. Cai, T. Wang, J.J. Si, J. Zhu, Y.D. Wang, X.D. Hui, A refractory Hf25Nb25Ti25Zr25 high-entropy alloy with excellent structural stability and tensile properties, Mater. Lett. 130 (2014) 277–280. https://doi.org/https://doi.org/10.1016/j.matlet.2014.05.134.
[89] Q. Zhou, S. Sheikh, P. Ou, D. Chen, Q. Hu, S. Guo, Corrosion behavior of Hf0.5Nb0.5Ta0.5Ti1.5Zr refractory high-entropy in aqueous chloride solutions, Electrochem. Commun. 98 (2018). https://doi.org/10.1016/j.elecom.2018.11.009.
[90] S. Sheikh, M. Bijaksana, A. Motallebzadeh, S. Shafeie, A. Lozinko, L. Gan, T.-K. Tsao, U. Klement, D. Canadinc, H. Murakami, S. Guo, Accelerated oxidation in ductile refractory high-entropy alloys, Intermetallics. 97 (2018). https://doi.org/10.1016/j.intermet.2018.04.001.
[91] S. Sheikh, S. Guo, S. Shafeie, H. Murakami, T.-K. Tsao, Aluminizing for enhanced oxidation resistance of ductile refractory highentropy alloys, Intermetallics. 103 (2018) 40–51. https://doi.org/10.1016/j.intermet.2018.10.004.
[92] V. Soni, O.N. Senkov, B. Gwalani, D.B. Miracle, R. Banerjee, Microstructural Design for Improving Ductility of An Initially Brittle Refractory High Entropy Alloy, Sci. Rep. 8 (2018) 8816. https://doi.org/10.1038/s41598-018-27144-3.
[93] V. Soni, B. Gwalani, T. Alam, S. Dasari, Y. Zheng, O.N. Senkov, D. Miracle, R. Banerjee, Phase Inversion in a Two-phase, BCC+B2, Refractory High Entropy Alloy, Acta Mater. (2019). https://doi.org/https://doi.org/10.1016/j.actamat.2019.12.004.
[94] O.N. Senkov, J.K. Jensen, A.L. Pilchak, D.B. Miracle, H.L. Fraser, Compositional variation effects on the microstructure and properties of a refractory high-entropy superalloy AlMo0.5NbTa0.5TiZr, Mater. Des. 139 (2018) 498–511. https://doi.org/https://doi.org/10.1016/j.matdes.2017.11.033.
[95] F. Wang, G.H. Balbus, S. Xu, Y. Su, J. Shin, P.F. Rottmann, K.E. Knipling, J.-C. Stinville, L.H. Mills, O.N. Senkov, I.J. Beyerlein, T.M. Pollock, D.S. Gianola, Multiplicity of dislocation pathways in a refractory multiprincipal element alloy, Science (80-.). 370 (2020) 95 LP – 101. https://doi.org/10.1126/science.aba3722.
[96] R.F. Gibson, PRINCIPLES OF COMPOSITE MATERIAL MECHANICS, 4th ed., CRC Press, Boca Raton, 2016. https://doi.org/https://doi.org/10.1201/b19626.
[97] C. Migliaresi, Chapter I.2.9 – Composites, in: Biomater. Sci., 2013: pp. 223–241. https://doi.org/10.1016/B978-0-08-087780-8.00024-3.
[98] Z.H. Stachurski, Mechanical behavior of materials, Mater. Today. 12 (2009) 44. https://doi.org/10.1016/S1369-7021(09)70086-0.
[99] R.M. Jones, Mechanics Of Composite Materials, 2nd ed., CRC Press, Boca Raton, 1999.

https://doi.org/https://doi.org/10.1201/9781498711067.
[100] R. Casati, M. Vedani, Metal Matrix Composites Reinforced by Nano-Particles—A Review, Metals (Basel). 4 (2014). https://doi.org/10.3390/met4010065.
[101] N. Srikanth, H.K.F. Calvin, M. Gupta, Effect of length scale of alumina particles of different sizes on the damping characteristics of an Al–Mg alloy, Mater. Sci. Eng. A. 423 (2006) 189–191. https://doi.org/https://doi.org/10.1016/j.msea.2005.10.070.
[102] X. Li, Y. Yang, X. Cheng, Ultrasonic-assisted fabrication of metal matrix nanocomposites, J. Mater. Sci. 39 (2004) 3211–3212. https://doi.org/10.1023/B:JMSC.0000025862.23609.6f.
[103] M. Li, A. Fang, E. Martinez-Franco, J.M. Alvarado-Orozco, Z. Pei, C. Ma, Selective laser melting of metal matrix composites: Feedstock powder preparation by electroless plating, Mater. Lett. 247 (2019) 115–118. https://doi.org/https://doi.org/10.1016/j.matlet.2019.03.092.
[104] L. Ivanchev, S.T. Camagu, G. Govender, Semi-Solid High Pressure Die Casting of Metal Matrix Composites Produced by Liquid State Processing, Solid State Phenom. 192–193 (2013) 61–65. https://doi.org/10.4028/www.scientific.net/SSP.192-193.61.
[105] J. Campbell, Chapter 14 - Melting, in: J.B.T.-C.C.H. (Second E. Campbell (Ed.), Butterworth-Heinemann, Boston, 2015: pp. 769–796. https://doi.org/https://doi.org/10.1016/B978-0-444-63509-9.00014-5.
[106] A. El-Kady, E.; Mahmoud, T.;Ali, On the Electrical and Thermal Conductivities of Cast A356/Al2O3 Metal Matrix Nanocomposites, Mater. Sci. Appl. 2 (2011) 1180–1187. https://doi.org/10.4236/msa.2011.29159.
[107] N. Llorca-Isern, C. Artieda-Guzmán, 9 - Metal-based composite powders, in: I. Chang, Y.B.T.-A. in P.M. Zhao (Eds.), Woodhead Publ. Ser. Met. Surf. Eng., Woodhead Publishing, 2013: pp. 241–272. https://doi.org/https://doi.org/10.1533/9780857098900.2.241.
[108] C. Suryanarayana, Mechanical alloying and milling, Prog. Mater. Sci. 46 (2001) 1–184. https://doi.org/https://doi.org/10.1016/S0079-6425(99)00010-9.
[109] O.A. Waseem, H.J. Ryu, Powder Metallurgy Processing of a W(x)TaTiVCr High-Entropy Alloy and Its Derivative Alloys for Fusion Material Applications, Sci. Rep. 7 (2017) 1926. https://doi.org/10.1038/s41598-017-02168-3.
[110] B. Kang, J. Lee, H.J. Ryu, S.H. Hong, Ultra-high strength WNbMoTaV high-entropy alloys with fine grain structure fabricated by powder metallurgical process, Mater. Sci. Eng. A. 712 (2018) 616–624. https://doi.org/https://doi.org/10.1016/j.msea.2017.12.021.
[111] I. Moravcik, J. Cizek, J. Zapletal, Z. Kovacova, J. Vesely, P. Minarik, M. Kitzmantel, E. Neubauer, I. Dlouhy, Microstructure and mechanical properties of Ni<inf>1,5</inf>Co<inf>1,5</inf>CrFeTi<inf>0,5</inf> high entropy alloy fabricated by mechanical alloying and spark plasma sintering, Mater. Des. 119 (2017). https://doi.org/10.1016/j.matdes.2017.01.036.
[112] C. Suryanarayana, E. Ivanov, V. V Boldyrev, The science and technology of mechanical alloying, Mater. Sci. Eng. A. 304–306 (2001) 151–158. https://doi.org/http://dx.doi.org/10.1016/S0921-5093(00)01465-9.
[113] M.S. El-Eskandarany, 4 - Ball milling as a powerful nanotechnological tool for fabrication of nanomaterials, in: M.S.B.T.-M.A. (Second E. El-Eskandarany (Ed.), William Andrew Publishing, Oxford, 2015: pp. 84–112. https://doi.org/https://doi.org/10.1016/B978-1-4557-7752-5.00004-8.
[114] M.S. El-Eskandarany, 2 - The history and necessity of mechanical alloying, in: M.S.B.T.-M.A. (Second E. El-Eskandarany (Ed.), William Andrew Publishing, Oxford, 2015: pp. 13–47. https://doi.org/https://doi.org/10.1016/B978-1-4557-7752-5.00002-4.
[115] Y. Lu, P.K. Liaw, The mechanical properties of nanostructured materials, JOM. 53 (2001) 31–35. https://doi.org/10.1007/s11837-001-0177-6.
[116] D.G. Morris, Mechanical Behaviour of Nanostructured Materials, Trans Tech, Zurich, 1998.
[117] I. Moravcik, A. Kubicek, L. Moravcikova-Gouvea, O. Adam, V. Kana, V. Pouchly, A. Zadera, I. Dlouhy, The Origins of High-Entropy Alloy Contamination Induced by Mechanical Alloying and Sintering, Met. . 10 (2020). https://doi.org/10.3390/met10091186.
[118] M.O.. Lu, L.; Lai, The Mechanical Alloying Process. In: Mechanical Alloying., in: Springer, Boston, 1998. https://doi.org/https://doi.org/10.1007/978-1-4615-5509-4_3.
[119] J. De, A.M. Umarji, K. Chattopadhyay, Origin of contamination and role of mechanochemistry during mechanical alloying: the case of Ag–Te alloys, Mater. Sci. Eng. A. 449–451 (2007) 1062–1066. https://doi.org/https://doi.org/10.1016/j.msea.2006.02.268.
[120] A. Kubicek, Vliv podmínek mechanického legování na kontaminaci práškových směsí a bulk materiálů, Vysoké učení technické v Brně, 2020.
[121] T.J. Rudzik, R.A. Gerhardt, Comparison of hot pressing and spark plasma sintering in the densification behavior of indium tin oxide-borosilicate glass composites, J. Am. Ceram. Soc. 101 (2018) 577–589. https://doi.org/10.1111/jace.15254.
[122] R. Yamanoglu, I. Daoud, E.A. Olevsky, Spark plasma sintering versus hot pressing – densification, bending strength, microstructure, and tribological properties of Ti5Al2.5Fe alloys, Powder Metall. 61 (2018) 178–186. https://doi.org/10.1080/00325899.2018.1441777.
[123] N. Saheb, Z. Iqbal, A. Khalil, A.S. Hakeem, N. Al Aqeeli, T. Laoui, A. Al-Qutub, R. Kirchner, Spark Plasma Sintering of Metals and Metal Matrix Nanocomposites: A Review, J. Nanomater. 2012 (2012) 983470. https://doi.org/10.1155/2012/983470.
[124] S.-J.L. Kang, 1 - SINTERING PROCESSES, in: S.-J.L.B.T.-S. Kang (Ed.), Butterworth-Heinemann, Oxford, 2005: pp. 3–8. https://doi.org/https://doi.org/10.1016/B978-075066385-4/50001-7.
[125] Y. Dong, H. Yang, L. Zhang, X. Li, D. Ding, X. Wang, J. Li, J. Li, I.-W. Chen, Ultra-Uniform Nanocrystalline Materials via Two-Step Sintering, Adv. Funct. Mater. n/a (2020) 2007750. https://doi.org/https://doi.org/10.1002/adfm.202007750.

[126] V.C. Nardone, K.M. Prewo, On the strength of discontinuous silicon carbide reinforced aluminum composites, Scr. Metall. 20 (1986) 43–48. https://doi.org/https://doi.org/10.1016/0036-9748(86)90210-3.
[127] F.A. Mirza, D.L. Chen, A Unified Model for the Prediction of Yield Strength in Particulate-Reinforced Metal Matrix Nanocomposites, Mater. . 8 (2015). https://doi.org/10.3390/ma8085138.
[128] T.W. Clyne, P.J. Withers, An Introduction to Metal Matrix Composites, Cambridge University Press, Cambridge, 1993. https://doi.org/DOI: 10.1017/CBO9780511623080.
[129] Z. Zhang, D.L. Chen, Contribution of Orowan strengthening effect in particulate-reinforced metal matrix nanocomposites, Mater. Sci. Eng. A. 483–484 (2008) 148–152. https://doi.org/https://doi.org/10.1016/j.msea.2006.10.184.
[130] M. Haghshenas, Metal–Matrix Composites, Ref. Modul. Mater. Sci. Mater. Eng. (2015). https://doi.org/10.1016/B978-0-12-803581-8.03950-3.
[131] Strengthening Mechanisms, Struct. Relations Nonferrous Met. (2005) 28–37. https://doi.org/https://doi.org/10.1002/0471708542.ch3.
[132] R.J. Arsenault, N. Shi, Dislocation generation due to differences between the coefficients of thermal expansion, Mater. Sci. Eng. 81 (1986) 175–187. https://doi.org/https://doi.org/10.1016/0025-5416(86)90261-2.
[133] Q.B. Nguyen, M. Gupta, Enhancing compressive response of AZ31B magnesium alloy using alumina nanoparticulates, Compos. Sci. Technol. 68 (2008) 2185–2192. https://doi.org/https://doi.org/10.1016/j.compscitech.2008.04.020.
[134] K.K. Meyers, Marc A; Chawla, Mechanical Behavior of Materials, 2nd ed., Cambridge University Press, 2008.
[135] M. Franklin, Scott V. and Mertens, F. and Marder, Portevin--Le Chatelier effect, Phys. Rev. E. 62 (2000) 8195--8206. https://doi.org/10.1103/PhysRevE.62.8195.
[136] G.P.M. Leyson, W.A. Curtin, Friedel vs. Labusch: the strong/weak pinning transition in solute strengthened metals, Philos. Mag. 93 (2013) 2428–2444. https://doi.org/10.1080/14786435.2013.776718.
[137] M. Wang, Z. Li, D. Raabe, In-situ SEM observation of phase transformation and twinning mechanisms in an interstitial high-entropy alloy, Acta Mater. 147 (2018) 236–246. https://doi.org/https://doi.org/10.1016/j.actamat.2018.01.036.
[138] J. Su, D. Raabe, Z. Li, Hierarchical microstructure design to tune the mechanical behavior of an interstitial TRIP-TWIP high-entropy alloy, Acta Mater. 163 (2019) 40–54. https://doi.org/https://doi.org/10.1016/j.actamat.2018.10.017.
[139] T.G. Nieh, J. Wadsworth, Hall-petch relation in nanocrystalline solids, Scr. Metall. Mater. 25 (1991) 955–958. https://doi.org/https://doi.org/10.1016/0956-716X(91)90256-Z.
[140] C.-C. Juan, M.-H. Tsai, C.-W. Tsai, W.-L. Hsu, C.-M. Lin, S.-K. Chen, S.-J. Lin, J.-W. Yeh, Simultaneously increasing the strength and ductility of a refractory high-entropy alloy via grain refining, Mater. Lett. 184 (2016) 200–203. https://doi.org/https://doi.org/10.1016/j.matlet.2016.08.060.
[141] R.C. Reed, The Superalloys: Fundamentals and Applications, 1st ed., Cambridge University Press, 2008.
[142] W.H. Liu, Z.P. Lu, J.Y. He, J.H. Luan, W. Zhijun, B. Liu, Y. Liu, M.W. Chen, C. Liu, Ductile CoCrFeNiMox high entropy alloys strengthened by hard intermetallic phases, Acta Mater. 116 (2016) 332–342. https://doi.org/10.1016/j.actamat.2016.06.063.
[143] M. Li, Y. Guo, H. Wang, J. Shan, Y. Chang, Microstructures and mechanical properties of oxide dispersion strengthened CoCrFeNi high-entropy alloy produced by mechanical alloying and spark plasma sintering, Intermetallics. 123 (2020) 106819. https://doi.org/https://doi.org/10.1016/j.intermet.2020.106819.
[144] T.L. Anderson, Fracture Mechanics: Fundamentals and Applications, Taylor & Francis CRC Press, Boca Raton, 2005.
[145] Y. Li, W; Liaw, P.K.; Gao, Fracture resistance of high entropy alloys: a review, United States, n.d. https://www.osti.gov/pages/servlets/purl/1543239.
[146] W. Li, P.K. Liaw, Y. Gao, Fracture resistance of high entropy alloys: A review, Intermetallics. 99 (2018) 69–83. https://doi.org/https://doi.org/10.1016/j.intermet.2018.05.013.
[147] T.L. Anderson, Fracture Mechanics, 4th ed., CRC Press, Boca Raton, 2017. https://doi.org/https://doi.org/10.1201/9781315370293.
[148] Z. Zhang, M.M. Mao, J. Wang, B. Gludovatz, Z. Zhang, S.X. Mao, E.P. George, Q. Yu, R.O. Ritchie, Nanoscale origins of the damage tolerance of the high-entropy alloy CrMnFeCoNi, Nat. Commun. 6 (2015) 10143. https://doi.org/10.1038/ncomms10143.
[149] L. Qi, D.C. Chrzan, Tuning Ideal Tensile Strengths and Intrinsic Ductility of bcc Refractory Alloys, Phys. Rev. Lett. 112 (2014) 115503. https://doi.org/10.1103/PhysRevLett.112.115503.
[150] L. Lilensten, J.-P. Couzinié, J. Bourgon, L. Perrière, G. Dirras, F. Prima, I. Guillot, Design and tensile properties of a bcc Ti-rich high-entropy alloy with transformation-induced plasticity, Mater. Res. Lett. 5 (2017) 110–116. https://doi.org/10.1080/21663831.2016.1221861.
[151] T. Yang, Y.L. Zhao, W.H. Liu, J.H. Zhu, J.J. Kai, C.T. Liu, Ductilizing brittle high-entropy alloys via tailoring valence electron concentrations of precipitates by controlled elemental partitioning, Mater. Res. Lett. 6 (2018) 600–606. https://doi.org/10.1080/21663831.2018.1518276.
[152] Y. Zou, S. Maiti, W. Steurer, R. Spolenak, Size-dependent plasticity in an Nb25Mo25Ta25W25 refractory high-entropy alloy, Acta Mater. 65 (2014) 85–97. https://doi.org/10.1016/j.actamat.2013.11.049.
[153] D.L. Zhang, Processing of advanced materials using high-energy mechanical milling, Prog. Mater. Sci. 49 (2004) 537–560. https://doi.org/https://doi.org/10.1016/S0079-6425(03)00034-3.
[154] I. Iron, S.I.C. on Technology, The Electric Arc Furnace, The Institute, 1981. https://books.google.cz/books?id=9vXkAAAAMAAJ.

[155] R. Schlatter, Vacuum Induction Melting Technology of High-temperature Alloys, Metallurgical Soc. of AIME, 1971. https://books.google.cz/books?id=8lt6mwEACAAJ.
[156] W.C. Oliver, G.M. Pharr, An improved technique for determining hardness and elastic modulus using load and displacement sensing indentation experiments, J. Mater. Res. 7 (1992) 1564–1583. https://doi.org/DOI: 10.1557/JMR.1992.1564.
[157] M.-H. Chuang, M.-H. Tsai, W.-R. Wang, S.-J. Lin, J.-W. Yeh, Microstructure and wear behavior of AlxCo1.5CrFeNi1.5Tiy high-entropy alloys, Acta Mater. 59 (2011) 6308–6317. https://doi.org/https://doi.org/10.1016/j.actamat.2011.06.041.
[158] J.F. Archard, Contact and Rubbing of Flat Surfaces, J. Appl. Phys. 24 (1953) 981–988. https://doi.org/10.1063/1.1721448.
[159] A. Renger, Johnson, K. L., Contact Mechanics. Cambridge etc., Cambridge University Press 1985. XII, 452 pp., £ 17.50 P/B. ISBN 0521347963, ZAMM - J. Appl. Math. Mech. / Zeitschrift Für Angew. Math. Und Mech. 69 (1989) 214. https://doi.org/10.1002/zamm.19890690713.
[160] L. Moravcikova-Gouvea, I. Moravcik, M. Omasta, J. Veselý, J. Cizek, P. Minárik, J. Cupera, A. Záděra, V. Jan, I. Dlouhy, High-strength Al0.2Co1.5CrFeNi1.5Ti high-entropy alloy produced by powder metallurgy and casting: A comparison of microstructures, mechanical and tribological properties, Mater. Charact. 159 (2020) 110046. https://doi.org/https://doi.org/10.1016/j.matchar.2019.110046.
[161] Y. Li, L. Wan, K. Chen, A look-up table based approach to characterize crystal twinning for synchrotron X-ray Laue microdiffraction scans, J. Appl. Crystallogr. 48 (2015) 747–757. https://doi.org/10.1107/S1600576715004896.
[162] P. Huang, G.Q. Dai, F. Wang, K.W. Xu, Y.H. Li, Fivefold annealing twin in nanocrystalline Cu, Appl. Phys. Lett. 95 (2009) 203101. https://doi.org/10.1063/1.3263948.
[163] R.O. Elliott, C.P. Kempter, Thermal Expansion of Some Transition Metal Carbides, J. Phys. Chem. 62 (1958) 630–631. https://doi.org/10.1021/j150563a030.
[164] S.C. Lim, M.F. Ashby, Overview no. 55 Wear-Mechanism maps, Acta Metall. 35 (1987) 1–24. https://doi.org/https://doi.org/10.1016/0001-6160(87)90209-4.
[165] Y. Wang, T. Lei, J. Liu, Tribo-metallographic behavior of high carbon steels in dry sliding: I. Wear mechanisms and their transition, Wear. 231 (1999) 1–11. https://doi.org/https://doi.org/10.1016/S0043-1648(99)00115-5.
[166] A.D. Anoop, A.S. Sekhar, M. Kamaraj, K. Gopinath, Modelling the mechanical behaviour of heat-treated AISI 52100 bearing steel with retained austenite, Proc. Inst. Mech. Eng. Part L J. Mater. Des. Appl. 232 (2015) 44–57. https://doi.org/10.1177/1464420715612235.
[167] L. Hitachi Metals, General Catalog of YSS Tool Steels, (2015). https://www.hitachi-metals.co.jp/e/products/auto/ml/pdf/yss_tool_steels_d.pdf (accessed August 5, 2019).
[168] G. Design, Tool steel, molybdenum alloy, AISI M2, regular carbon (high speed), CES EDUPACK. (2017) 1–5. https://riunet.upv.es/bitstream/handle/10251/113733/ANEXO_1532965393973614614919512854616 8.pdf?sequence=2&isAllowed=y (accessed August 3, 2019).
[169] Z. Fu, W. Chen, H. Xiao, L. Zhou, D. Zhu, S. Yang, Fabrication and properties of nanocrystalline Co0.5FeNiCrTi0.5 high entropy alloy by MA–SPS technique, Mater. Des. 44 (2013) 535–539. https://doi.org/http://dx.doi.org/10.1016/j.matdes.2012.08.048.
[170] V. Soni, O.N. Senkov, J.-P. Couzinie, Y. Zheng, B. Gwalani, R. Banerjee, Phase stability and microstructure evolution in a ductile refractory high entropy alloy Al10Nb15Ta5Ti30Zr40, Materialia. 9 (2020) 100569. https://doi.org/https://doi.org/10.1016/j.mtla.2019.100569.
[171] X.D. Xu, S. Guo, T.G. Nieh, C.T. Liu, A. Hirata, M.W. Chen, Effects of mixing enthalpy and cooling rate on phase formation of AlxCoCrCuFeNi high-entropy alloys, Materialia. 6 (2019) 100292. https://doi.org/https://doi.org/10.1016/j.mtla.2019.100292.
[172] K.A. Christofidou, T.P. McAuliffe, P.M. Mignanelli, H.J. Stone, N.G. Jones, On the prediction and the formation of the sigma phase in CrMnCoFeNix high entropy alloys, J. Alloys Compd. 770 (2019) 285–293. https://doi.org/https://doi.org/10.1016/j.jallcom.2018.08.032.
[173] B.S. Murty, J.W. Yeh, S. Ranganathan, Chapter 7 - Intermetallics, Interstitial Compounds and Metallic Glasses in High-Entropy Alloys, in: B.S. Murty, J.W. Yeh, S.B.T.-H.E.A. Ranganathan (Eds.), Butterworth-Heinemann, Boston, 2014: pp. 119–131. https://doi.org/https://doi.org/10.1016/B978-0-12-800251-3.00007-9.
[174] N. Saunders, A.P.B.T.-P.M.S. Miodownik, eds., Chapter 4 - Experimental Determination of Thermodynamic Quantities and Phase Diagrams, in: CALPHAD Calc. Phase Diagrams, Pergamon, 1998: pp. 61–87. https://doi.org/https://doi.org/10.1016/S1470-1804(98)80024-2.
[175] E.J. Pickering, R. Muñoz-Moreno, H.J. Stone, N.G. Jones, Precipitation in the equiatomic high-entropy alloy CrMnFeCoNi, Scr. Mater. 113 (2016) 106–109. https://doi.org/https://doi.org/10.1016/j.scriptamat.2015.10.025.
[176] I. Moravcik, J. Cizek, P. Gavendova, S. Sheikh, S. Guo, I. Dlouhy, Effect of heat treatment on microstructure and mechanical properties of spark plasma sintered AlCoCrFeNiTi<inf>0.5</inf> high entropy alloy, Mater. Lett. 174 (2016). https://doi.org/10.1016/j.matlet.2016.03.077.
[177] B.C. De Cooman, Y. Estrin, S.K. Kim, Twinning-induced plasticity (TWIP) steels, Acta Mater. 142 (2018) 283–362. https://doi.org/https://doi.org/10.1016/j.actamat.2017.06.046.
[178] T. Baudin, A.L. Etter, R. Penelle, Annealing twin formation and recrystallization study of cold-drawn copper wires from EBSD measurements, Mater. Charact. 58 (2007) 947–952. https://doi.org/https://doi.org/10.1016/j.matchar.2006.09.009.

[179] R. Chang, L.J. Graham, Low-Temperature Elastic Properties of ZrC and TiC, J. Appl. Phys. 37 (1966) 3778–3783. https://doi.org/10.1063/1.1707923.
[180] S. W. Freiman, J. Mecholsky, The Fracture of Brittle Materials: Testing and Analysis, 2012. https://doi.org/10.1002/9781118147757.
[181] D. Hull, D.J. Bacon, Chapter 3 - Movement of Dislocations, in: D. Hull, D.J.B.T.-I. to D. (Fifth E. Bacon (Eds.), Butterworth-Heinemann, Oxford, 2011: pp. 43–62. https://doi.org/https://doi.org/10.1016/B978-0-08-096672-4.00003-7.
[182] D. Hull, D.J. Bacon, Chapter 10 - Strength of Crystalline Solids, in: D. Hull, D.J.B.T.-I. to D. (Fifth E. Bacon (Eds.), Butterworth-Heinemann, Oxford, 2011: pp. 205–249. https://doi.org/https://doi.org/10.1016/B978-0-08-096672-4.00010-4.
[183] S. Mahdavi, F. Akhlaghi, Effect of the SiC particle size on the dry sliding wear behavior of SiC and SiC-Gr-reinforced Al6061 composites, J. Mater. Sci. 46 (2011) 7883–7894. https://doi.org/10.1007/s10853-011-5776-1.
[184] P. Ravindran, K. Manisekar, P. Rathika, P. Narayanasamy, Tribological properties of powder metallurgy – Processed aluminium self lubricating hybrid composites with SiC additions, Mater. Des. 45 (2013) 561–570. https://doi.org/https://doi.org/10.1016/j.matdes.2012.09.015.
[185] V. Matějka, Y. Lu, L. Jiao, L. Huang, G. Simha Martynková, V. Tomášek, Effects of silicon carbide particle sizes on friction-wear properties of friction composites designed for car brake lining applications, Tribol. Int. 43 (2010) 144–151. https://doi.org/https://doi.org/10.1016/j.triboint.2009.05.007.
[186] E.R.I. Mahmoud, M. Takahashi, T. Shibayanagi, K. Ikeuchi, Wear characteristics of surface-hybrid-MMCs layer fabricated on aluminum plate by friction stir processing, Wear. 268 (2010) 1111–1121. https://doi.org/https://doi.org/10.1016/j.wear.2010.01.005.
[187] Z. Sinha, A.; Farhat, Effect of Surface Porosity on Tribological Properties of Sintered Pure Al and Al 6061, Mater. Sci. Appl. 6 (2015) 549–566. https://doi.org/10.4236/msa.2015.66059.
[188] J.-M. Wu, S.-J. Lin, J.-W. Yeh, S.-K. Chen, Y.-S. Huang, H.-C. Chen, Adhesive wear behavior of AlxCoCrCuFeNi high-entropy alloys as a function of aluminum content, Wear. 261 (2006) 513–519. https://doi.org/https://doi.org/10.1016/j.wear.2005.12.008.
[189] M.J. Yao, K.G. Pradeep, C.C. Tasan, D. Raabe, A novel, single phase, non-equiatomic FeMnNiCoCr high-entropy alloy with exceptional phase stability and tensile ductility, Scr. Mater. 72–73 (2014) 5–8. https://doi.org/https://doi.org/10.1016/j.scriptamat.2013.09.030.
[190] I. Moravcik, L. Gouvea, V. Hornik, Z. Kovacova, M. Kitzmantel, E. Neubauer, I. Dlouhy, Synergic strengthening by oxide and coherent precipitate dispersions in high-entropy alloy prepared by powder metallurgy, Scr. Mater. 157 (2018) 24–29. https://doi.org/10.1016/J.SCRIPTAMAT.2018.07.034.
[191] I. Moravcik, V. Hornik, P. Minárik, L. Li, I. Dlouhy, M. Janovska, D. Raabe, Z. Li, Interstitial doping enhances the strength-ductility synergy in a CoCrNi medium entropy alloy, Mater. Sci. Eng. A. 781 (2020) 139242. https://doi.org/https://doi.org/10.1016/j.msea.2020.139242.
[192] Z. Wang, I. Baker, Z. Cai, S. Chen, J.D. Poplawsky, W. Guo, The effect of interstitial carbon on the mechanical properties and dislocation substructure evolution in Fe40.4Ni11.3Mn34.8Al7.5Cr6 high entropy alloys, Acta Mater. 120 (2016) 228–239. https://doi.org/https://doi.org/10.1016/j.actamat.2016.08.072.
[193] Z. Wang, I. Baker, Interstitial strengthening of a f.c.c. FeNiMnAlCr high entropy alloy, Mater. Lett. 180 (2016) 153–156. https://doi.org/http://dx.doi.org/10.1016/j.matlet.2016.05.122.
[194] Z. Lei, X. Liu, Y. Wu, H. Wang, S. Jiang, S. Wang, X. Hui, Y. Wu, B. Gault, P. Kontis, D. Raabe, L. Gu, Q. Zhang, H. Chen, H. Wang, J. Liu, K. An, Q. Zeng, T.-G. Nieh, Z. Lu, Enhanced strength and ductility in a high-entropy alloy via ordered oxygen complexes, Nature. (2018). https://doi.org/10.1038/s41586-018-0685-y.
[195] H.B. Huntington, Mobility of Interstitial Atoms in a Face-Centered Metal, Phys. Rev. 91 (1953) 1092–1098. https://doi.org/10.1103/PhysRev.91.1092.
[196] T.E. Whitfield, E.J. Pickering, L.R. Owen, C.N. Jones, H.J. Stone, N.G. Jones, The effect of Al on the formation and stability of a BCC – B2 microstructure in a refractory metal high entropy superalloy system, Materialia. 13 (2020) 100858. https://doi.org/https://doi.org/10.1016/j.mtla.2020.100858.
[197] G.M. Pharr, E.G. Herbert, Y. Gao, The Indentation Size Effect: A Critical Examination of Experimental Observations and Mechanistic Interpretations, Annu. Rev. Mater. Res. 40 (2010) 271–292. https://doi.org/10.1146/annurev-matsci-070909-104456.
[198] P.M. Sargent, Use of the Indentation Size Effect on Microhardness for Materials Characterization, in: P.J. Blau, B.R. Lawn (Eds.), Microindentation Tech. Mater. Sci. Eng., ASTM International, West Conshohocken, PA, 1985: pp. 160–174. https://doi.org/10.1520/STP32956S.
[199] G.Z. Voyiadjis, M. Yaghoobi, Review of Nanoindentation Size Effect: Experiments and Atomistic Simulation, Crystals. 7 (2017). https://doi.org/10.3390/cryst7100321.
[200] H. Gao, Y. Huang, Geometrically necessary dislocation and size-dependent plasticity, Scr. Mater. 48 (2003) 113–118. https://doi.org/https://doi.org/10.1016/S1359-6462(02)00329-9.

9 Abbreviations and symbols

AM	Arc Melting
b	Burger's Vector
BCC	Body Centered Cubic

BSE	Backscattered electrons
BTP	Ball to powder ratio
c_i	Atomic Fraction of i^{th} element
CALPHAD	Calculation of Phase Diagram
CCA	Complex Concentrated Alloys
d	Average grain size
E	Elastic Modulus
EBSD	Electron Backscattered Diffraction
ECCI	Electron Channeling Contrast Imaging
EDM	Electric Discharge Machining
EDS	Energy-Dispersive X-ray Spectroscopy
EDX	Energy-Dispersive X-ray Spectroscopy
f	Particle's Volume Fraction
F	Applied Normal Force
FIB	Focused Ion Beam
FCC	Face Centered Cubic
G	Shear Modulus
H	Enthalpy
HP	Hot Uniaxial Pressing
HCP	Hexagonal Closed Packed
HEA	High Entropy Alloy
IM	Intermetallic
k	Hall-Petch Coefficient
k_b	Boltzmann's constant
L_p	Interparticle spacing
M	Taylor's factor
MA	Mechanical Alloying
MEA	Medium Entropy Alloy
MMC	Metal Matrix Composite
n	Total number of constituent elements in a system
ODS	Oxide Dispersed Strengthened
PCA	Process Control Agent
PM	Powder Metallurgy
p_{max}	maximum contact pressure under a selected load
R	Gas constant (8.134 J/K/mol)
r_i	Atomic radius of the i^{th} element
RHEA	Refractory High Entropy Alloys
RMEA	Refractory Medium Entropy Alloys
S	Entropy
STEM	Scanning TEM imaging
S_{config}	Configurational Entropy
S_{ideal}	Ideal Entropy
S_{vib}	Vibrational contribution of Entropy
S_{elec}	Electronic Randomness contribution of Entropy
S_{mag}	Magnetic Dipole contribution of Entropy
SS	Solid Solution
SAED	Selected Area Electron Diffraction
SE	Secondary Electrons
SEM	Scanning Electron Microscopy
SFE	Stacking Fault Energy
SPS	Spark Plasma Sintering
T	Thermodynamic temperature
T_m	Temperature of melting
TEM	Transmission Electron Microscopy
TCC	Topologically Close Packed
TRIP	Transformation-Induced Plasticity
TWIP	Deformation-induced Twinning
VEC	Valence Electron Concentration
w	Number of States in the system
XRD	X-ray Diffraction
X_i	Mole fraction of the i^{th} component
γ	Interfacial Energy
δ	Atomic Size Difference
ΔG	Gibbs Free Energy variation

ΔG_{mix}	Gibbs Free Energy of Mixing variation
ΔH	Enthalpy variation
ΔH	Enthalpy of Mixing variation
ΔS	Entropy variation
ΔS_{mix}	Entropy of Mixing variation
σ	Stress
σ_{CS}	Coherency Strengthening
σ_{MMS}	Moduli Mismatch Strengthening
σ_0	Lattice Friction Stress
σ_{OS}	Order Strengthening
σ_{ORS}	Orowan Strengthening Contribution
σ_{PSS}	Particle shearing strengthening
σ_{SSS}	Solid Solution Strengthening
μ	Poisson's constant
σ_y	Yield Strength
σ_{uts}	Ultimate Tensile Strength
ε	Strain
ε_f	Strain to Failure

10 Publications

Impact journals

1- MORAVČÍK, I; PEIGHAMBARDOUST, N.S.; MOTALLEBZADEH, A.; **MORAVCIKOVA-GOUVEA, L.**; LIU, C.; PRABHAKAR, J.M.; DLOUHY, I.; LI, Z. Interstitial nitrogen enhances corrosion resistance of an equiatomic CoCrNi medium-entropy alloy in sulfuric acid solution. *Materials Characterization*, 2021, vol. 172, 110869. ISSN: 1044-5803.

2- **MORAVČÍKOVÁ-GOUVÊA, L.**; MORAVČÍK, I.; OMASTA, M.; VESELY, J.; CIZEK, J.; MINARIK, P.; CUPERA, J.; ZADERA, A.; JAN, V.; DLOUHY, I. High-strength Al0.2Co1.5CrFeNi1.5Ti high-entropy alloy produced by powder metallurgy and casting: a comparison of microstructures, mechanical and tribological properties. *Materials Characterization,* 2020, vol. 159, 110046. ISSN: 1044-5803.

3- MORAVČÍK, I.; KUBÍČEK, A.; **MORAVČÍKOVA-GOUVÊA, L**.; ADAM, O.; KAŇA, V.; POUCHLÝ, V.; ZÁDĚRA, A.; DLOUHÝ, I. The Origins of High-Entropy Alloy Contamination Induced by Mechanical Alloying and Sintering. *Metals*, 2020, vol. 10, no. 9, p. 1-15. ISSN: 2075-4701.

4- MORAVČÍK, I.; GAMANOV, S.; **MORAVČÍKOVÁ-GOUVÊA, L.**; KOVACOVA, Z.; KITZMANTEL, M.; NEUBAUER, E.; DLOUHY, I. Influence of Ti on the tensile properties of the high-strength powder metallurgy high-entropy alloys. *Materials*, 2020, vol. 13, no. 3, p. 0-18. ISSN: 1996-1944.

5- MORAVČÍK, I.; ČIŽEK, J.; **DE ALMEIDA GOUVÊA, L.**; ČUPERA, J.; GUBÁN, I.; DLOUHÝ, I. Nitrogen Interstitial Alloying of CoCrFeMnNi High Entropy Alloy through Reactive Powder Milling. *Entropy*, 2019, vol. 21, no. 4, p. 1-7. ISSN: 1099-4300.

6- MORAVČÍK, I.; **DE ALMEIDA GOUVÊA, L.**; HORNÍK, V.; KOVACOVA, Z.; KITZMANTEL, M.; NEUBAUER, E.; DLOUHÝ, I. Synergic strengthening by oxide and coherent precipitate dispersions in high-entropy alloy prepared by powder metallurgy. *Scripta Materialia,* 2018, vol. 157, no. 1, p. 24-29. ISSN: 1359-6462.

7- KRAJŇÁKOVÁ, P.; **DE ALMEIDA GOUVÊA, L.**; ČUPERA, J.; JAN, V.; DLOUHÝ, I.; SPOTZ, Z. Influence of multiple electron-beam remeltings on the characteristics of HVOF and CGDS sprayed conicraly coatings. *Materiali in tehnologije*, 2018, vol. 52, no. 3, p. 289-293. ISSN: 1580-2949.

8- MORAVČÍK, I.; **DE ALMEIDA GOUVÊA, L.**; ČUPERA, J.; DLOUHÝ, I. Preparation and properties of medium entropy CoCrNi/boride metal matrix composite. *Journal of Alloys and Compounds,* 2018, vol. 748, no. 748, p. 979-988. ISSN: 1873-4669.

Conference proceedings

1- **MORAVČÍKOVÁ-GOUVÊA, L.;** KOVACOVA, Z; KITZMANTEL, M.; NEUBAUER, E.; JAN, V.; DLOUHY, I. Influence of hot pressing sintering temperature on the properties of low-density Al0.5NbTa0.8Ti1.5V0.2Zr refractory high-entropy alloy. In *Materials Science Forum,* 2020*,* vol. 1016, p. 940-945. ISSN: 1662-9752.

2- **DE ALMEIDA GOUVÊA, L.**; KOVACOVA, Z.; JAN, V.; SPOTZ, Z.; KITZMANTEL, M.; NEUBAUER, E.; DLOUHY, I. Effect of sintering temperature on the microstructure and properties of Powder Metallurgy Hf0.5Nb0.5Ta0.5Ti1.5Zr Refractory High-Entropy Alloy. In *METAL 2019*. 1st edition, 2019. Brno: Tanger Ltd., 2019. s. 1486-1491. ISBN: 978-80-87294-92-5.

3- **DE ALMEIDA GOUVÊA, L.**; JAN, V.; DLOUHÝ, I. Preparation and Characterization of CoCrNi-Mo Metal Matrix Composite by Powder Metallurgy. In *METAL 2018.* 1st Edition, 2018. Brno: Tanger Ltd., 2018. p. 1545-1550. ISBN: 978-80-87294-84-0.

4- **DE ALMEIDA GOUVÊA, L.**; MORAVČÍK, I.; ČÍŽEK, J.; KRAJŇÁKOVÁ, P.; JAN, V.; DLOUHÝ, I. Characterization of Powder Metallurgy High-Entropy Alloys Prepared by Spark Plasma Sintering. *Materials Science Forum,* 2018, vol. 941, no. 1, p. 1053-1058. ISSN: 0255-5476.

5- **DE ALMEIDA GOUVÊA, L.**; ČÍŽEK, J.; ČUPERA, J.; JAN, V.; DLOUHÝ, I. MICROSTRUCTURE AND PROPERTIES OF MULTI-ELEMENTARY POWDERS OBTAINED BY COLD SPRAY DEPOSITION. In *METAL 2017.* 1st edition, 2018. Brno: Tanger Ltd., 2017. p. 1275-1280. ISBN: 978-80-87294-79-6.

11 Appendix A:

Use of zirconium sponge vs. commercial powder as feedstock for mechanical alloying

There are a number of ways studied in the literature for a successful production of metal matrix composites. When considering solid state processing, one alternative is the intentional addition of ceramic particles on the metallic powder mixtures for formation of a desired alloyed composition. For instance, boron carbide; yttrium carbide; iron nitride; etc. into metallic powders to form a sintered metal matrix composite with reinforced ceramic particles.

Other alternatives could be the production of in-situ ceramic particles through mechanical alloying and subsequent sintering of pure metallic powders. The presence of O, N and/or C elements could stem from the intrinsic contamination present during the process. The O, N and C elements react with certain metallic powders, which they own high affinity, and form oxides, carbides and/or nitrides.

The presence of contamination could be as well present in the feedstock powders prior to mechanical alloying. This is the case we studied here. Due to the difficulties on finding commercially available pure zirconium in powder form, the viability of producing metal matrix composites was studied by using Zr sponge instead of Zr powder with commercial purity as starting materials. The consequences of choosing either one or another greatly influence the final product.

The $Al_{0.5}NbTa_{0.8}Ti_{1.5}V_{0.2}Zr$ RHEA produced by powder metallurgy was manufactured using two different precursors before mechanical alloying in this study.

Zr sponge with commercial purity above 99 wt. % (Sigma Aldrich) was firstly milled into powder by ball milling (details in the Methods section). The milled powder possessed particle sizes under 45 μm. This milled zirconium powder added to a milling jar together with Al, Nb, Ta, Ti and V powders in $Al_{0.5}NbTa_{0.8}Ti_{1.5}V_{0.2}Zr$ stoichiometric ratio. These **alloyed** powders were named Precursors-A. After sintering, the bulk was named **$PM1_A$**. The results of microstructural characterization of this material were shown in the section 5.4.2.

Alternatively, Zr elemental powder with commercial purity of 99.5 wt. % (TLS, particles size from 45 to 150 μm) was alloyed together with powders of Al, Nb, Ti, Ta and V in $Al_{0.5}NbTa_{0.8}Ti_{1.5}V_{0.2}Zr$ stoichiometric ratio. The alloyed powders were named Precursors-B. After sintering, the bulk was named **$PM1_B$**. This bulk is subject to investigation in this section.

The influence of using different feedstock powders was studied when the materials are subjected to the exact same conditions of heat treatments and results are presented.

The XRD patterns for this group of materials are exhibited in Supplementary Fig. 1. The lattices are shown in the table below.

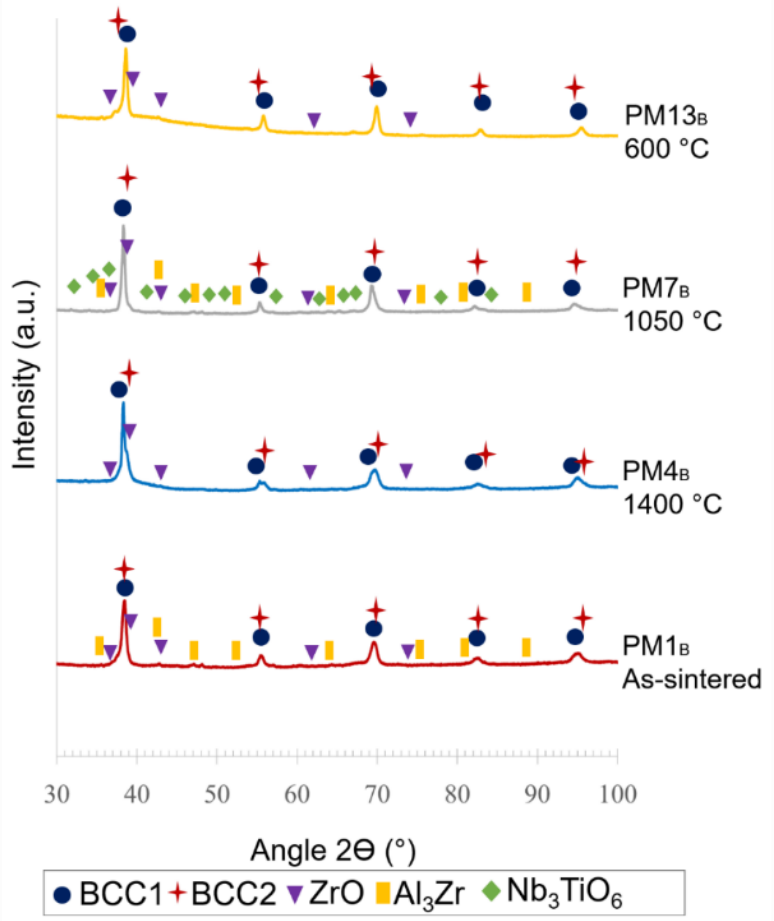

Supplementary Fig. 1. XRD patterns of PM$_B$ $Al_{0.5}NbTa_{0.8}Ti_{1.5}V_{0.2}Zr$ RHEA before and after heat treatments.

	PM1B - as sintered			PM4B - 1400 °C		
	a_{XRD}	c_{XRD}	wt.%	a_{XRD}	c_{XRD}	wt.%
BCC1	3.30	-	93.6	3.29	-	84.5
BCC2	3.29	-	3.2	3.30	-	12.5
ZrO	4.62	-	1.8	4.62	-	3
Al3Zr (I4/mmm)	4.09	17.32	1.4	-	-	-
	PM7A - 1050 °C			PM13A - 600 °C		
BCC1	3.29	-	67.8	3.30	-	67.5
BCC2	3.30	-	23.8	3.29	-	29.3
ZrO	4.63	-	3.5	4.63	-	3.2
Al3Zr (I4/mmm)	4.06	17.29	3.7	-	-	-
Nb_3TiO_6	7.92	14.56	1.2	-	-	-

Supplementary Table 1. Lattice parameters of the PM RHEAs produced with purely commercial powders.

The microstructures of the bulk sintered material before and after heat treatments are shown in Supplementary Fig. 2 and 3. One can notice that the microstructures consist of fine grains in all states, however the grain size distribution, morphology, chemical composition and phase composition are very dissimilar in the as-sintered state compared to the ones after heat treatments.

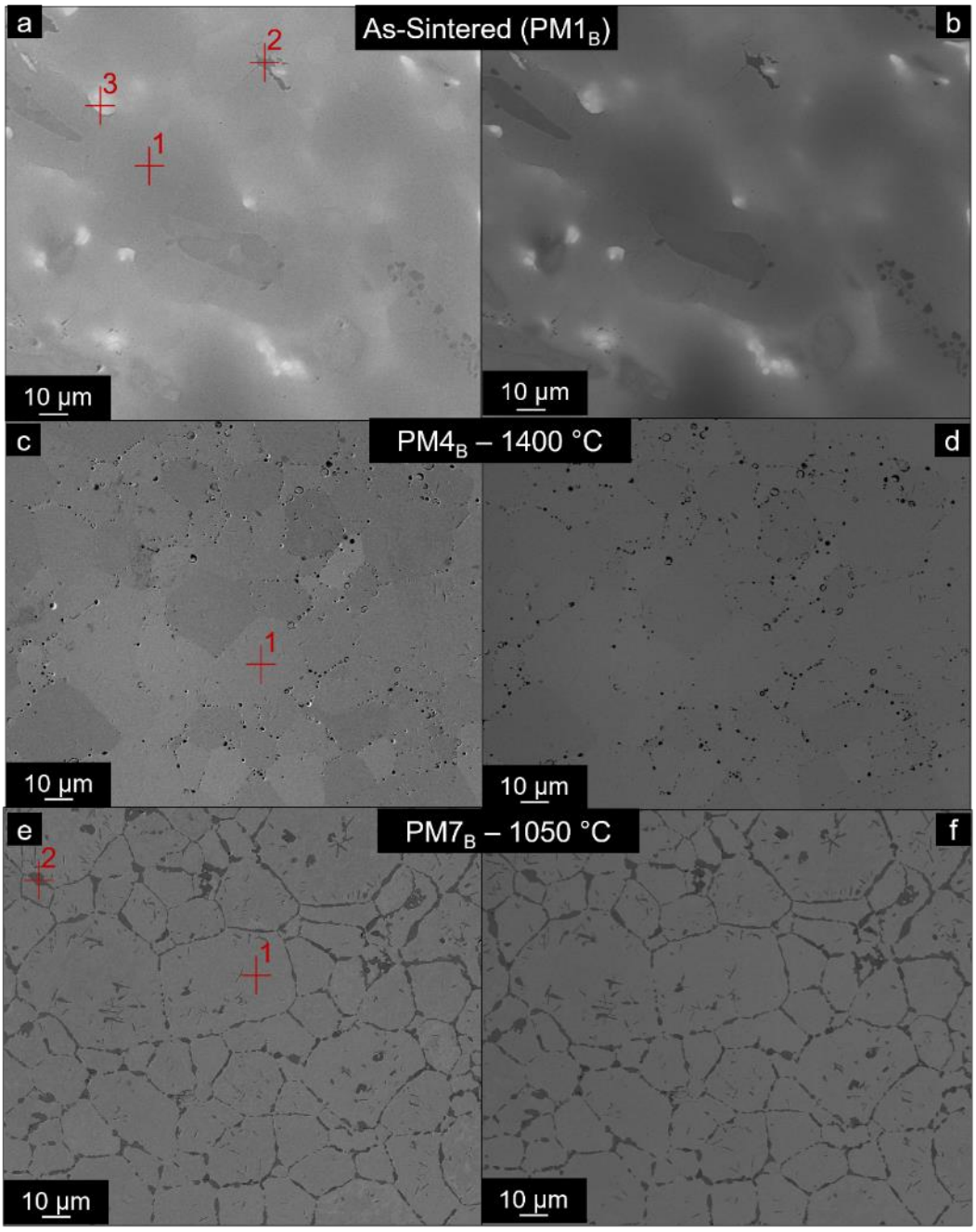

Supplementary Fig. 2. SEM images of microstructures of $Al_{0.5}NbTa_{0.8}Ti_{1.5}V_{0.2}Zr$ RHEA produced by powder metallurgy using precursor B: a) $PM1_B$ in the as-sintered state using SE mode. b) Corresponding image of $PM1_B$ utilizing BSE detector. c) RHEA after heat treatment at 1400 °C for 1 h ($PM4_B$) using SE mode d) Respective image of $PM4_A$ using BSE detector. e) RHEA after heat treatment at 1050 °C for 30 h ($PM7_B$) in SE mode. f) Respective image of $PM7_B$ using BSE detector. The red crosses represent EDS point analyses on each sample.

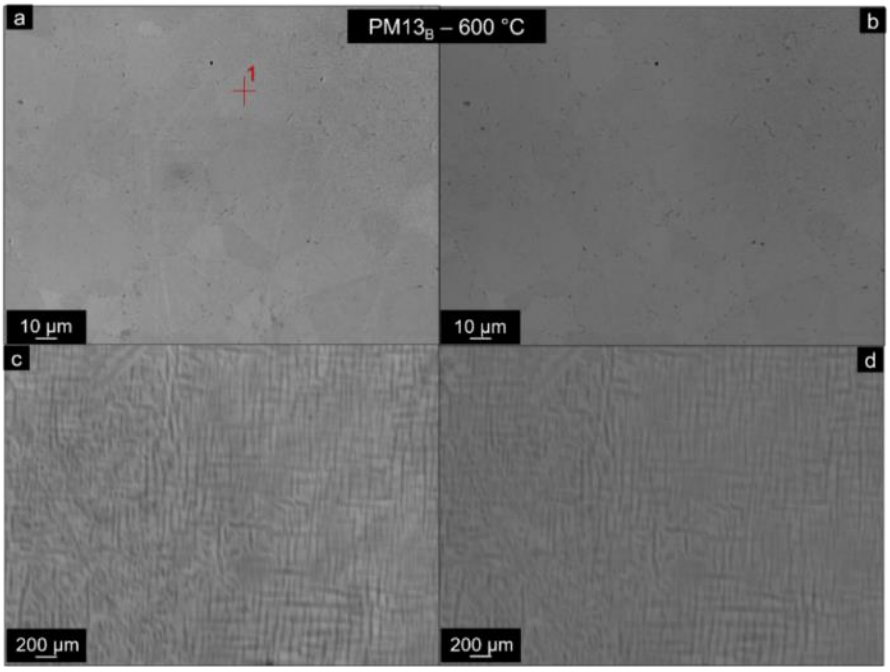

Supplementary Fig. 3. SEM images of microstructure of $PM13_B$ RHEA after subjected to 600 °C for 30 h. a) Overview using SE mode. b) Overview using BSE mode. c) Detail in higher magnification using SE mode. d) Detail in higher magnification using BSE mode.

The compositional aspects of each microstructure were assessed by a combination of SEM and EDS. The results are exhibited in Supplementary Fig. 2 ($PM1_B$ and $PM4_B$) and Supplementary Fig. 3 ($PM7_B$ and $PM10_B$).

	$PM1_B$ - As-sintered				$PM4_B$ - 1400 °C
[at.%]	Point 1 (BCC)	Point 2	Point 3	Map Sum Spectrum	Point 1 (BCC)
Al	10.9 +- 0.4	4.8 +- 3.2	-	9.2 +- 1.0	8.7 +- 0.8
Ti	34.4 +- 2.1	10.7 +- 1.4	-	31.0 +- 0.4	30.8 +- 1.1
V	3.8 +- 0.2	1.6 +- 0.5	-	4.1 +- 0.1	3.8 +- 0.3
Zr	18.2 +- 1.3	44.2 +- 1.5	-	21.8 +- 2.0	25.6 +- 0.4
Nb	16.1 +- 0.1	2.7 +- 0.7	-	18.6 +- 1.4	16.5 +- 0.7
Ta	16.6 +- 0.3	5.8 +- 1.1	100	15.3 +- 1.7	14.6 +- 1.0
O	-	30.0 +- 2.1	-	-	-

Supplementary Table 2. SEM/EDS point analysis of the studied RHEA in the as-sintered stated and after heat treatment at 1400 °C ($PM4_B$). The points correspond to the crosses displayed in Supplementary Fig. 2.

	$PM7_B$ - 1050 °C		$PM13_B$ - 600 °C
[at.%]	Point 1 (BCC)	Point 2	Point 1 (BCC)
Al	7.3 +- 0.1	3.5 +- 0.4	8.2 +- 0.2
Ti	32.0 +- 0.2	13.8 +- 0.2	30.5 +- 0.2
V	4.1 +- 0.7	2.3 +- 0.1	4.7 +- 0.4
Zr	16.7 +- 0.5	44.7 +- 0.6	18.3 +- 0.7
Nb	18.3 +- 0.5	3.3 +- 0.1	20.6 +- 0.4
Ta	18.6 +- 0.1	3.4 +- 0.2	17.4 +- 0.8
O	-	29 +- 1.4	-

Supplementary Table 3. SEM/EDS point analysis of the studied RHEA after heat treatments at 1050 °C and 600 °C. The points correspond to the crosses displayed in Supplementary Fig. 2 and 3.

The as-sintered state shows at least three distinct phases. Point 1 corresponds to the BCC phase, rich in Ti, Zr, Nb and Ta. Point 2 is rich mostly in O and Zr, therefore it probably corresponds to the ZrO. The presence of the other elements may be explained by the influence of the elements from the phase in the near vicinity. Point 3 points out to Ta particle, probably this particle is present due to insufficient mechanical milling and sintering time.

The map sum spectrum confirms the stoichiometric ratio desired for the alloy $Al_{0.5}NbTa_{0.8}Ti_{1.5}V_{0.2}Zr$.

After 1400 °C, the alloy exhibits a main BCC phase still rich in Ti, Zr, Nb and Ta. These are the same elements present in the BCC phase from the as-sintered state. Other phases were not possible to be assessed due to the resolution limit of the EDS.

After 1050 °C, the material exhibits the same BCC phase as the one of the previous states, and point 2 shows the ZrO mostly in the grain boundaries.

Subsequent heat treatment at 600 °C reveals a microstructure very similar as of the one exhibited by AM13, surprisingly. The BCC is rich in Ti, Zr, Nb and Ta with very fine nano-precipitates of a secondary BCC phase present.

EBSD analyses of the samples were performed to see the grains orientation, sizes, morphologies and distribution of grains. The results are visible in Supplementary Fig. 4. The green regions are areas which were not indexed by EBSD. The phases assessed by EBSD were BCC and ZrO.

The as-sintered material shows BCC phase with average grain size of (11.1 ± 2.0) μm. The oxides were found in very few areas and exhibit an average grain size of (0.9 ± 0.1) μm. No preferential orientation of the BCC grains was observed; however, the oxides seem to exhibit an unimportant orientation preference due to the very few grains detected by a single measurement. The maximum MUD values are not sufficiently high though to determine any important crystal preference.

The material heat treated at 1400 °C for 1 h shows a significant increase in BCC phase with grain sizes of (33.5 ± 2.4) μm. The oxides have grain sizes of (5.8 ± 0.7) μm. They seem to be segregated in certain areas. This is caused by insufficient milling time combined with short sintering times. This segregation is not present anymore after subjecting the material for prolonged heat treatment times.

After 30 h at 1050 °C, the oxides seem to disperse into the grain boundaries and possess average grain sizes of (5.3 ± 2.4) μm. The BCC exhibit similar grain sizes of (34.5 ± 1.1) μm as compared to the previous state. Both phases do no exhibit any important crystallographic preferential orientation under this condition. The green regions are areas which were not possible to be indeed by EBSD. These probably correspond to areas with high content of aluminides detected by XRD.

Finally, after 600 °C, the BCC phase shows grain size of (30.0 ± 1.5) μm and the oxides are dispersed in the grain boundaries, showing grain sizes of (2.1 ± 1.3) μm. No preferential crystallographic orientation was observed, considering the low maximum values of MUD.

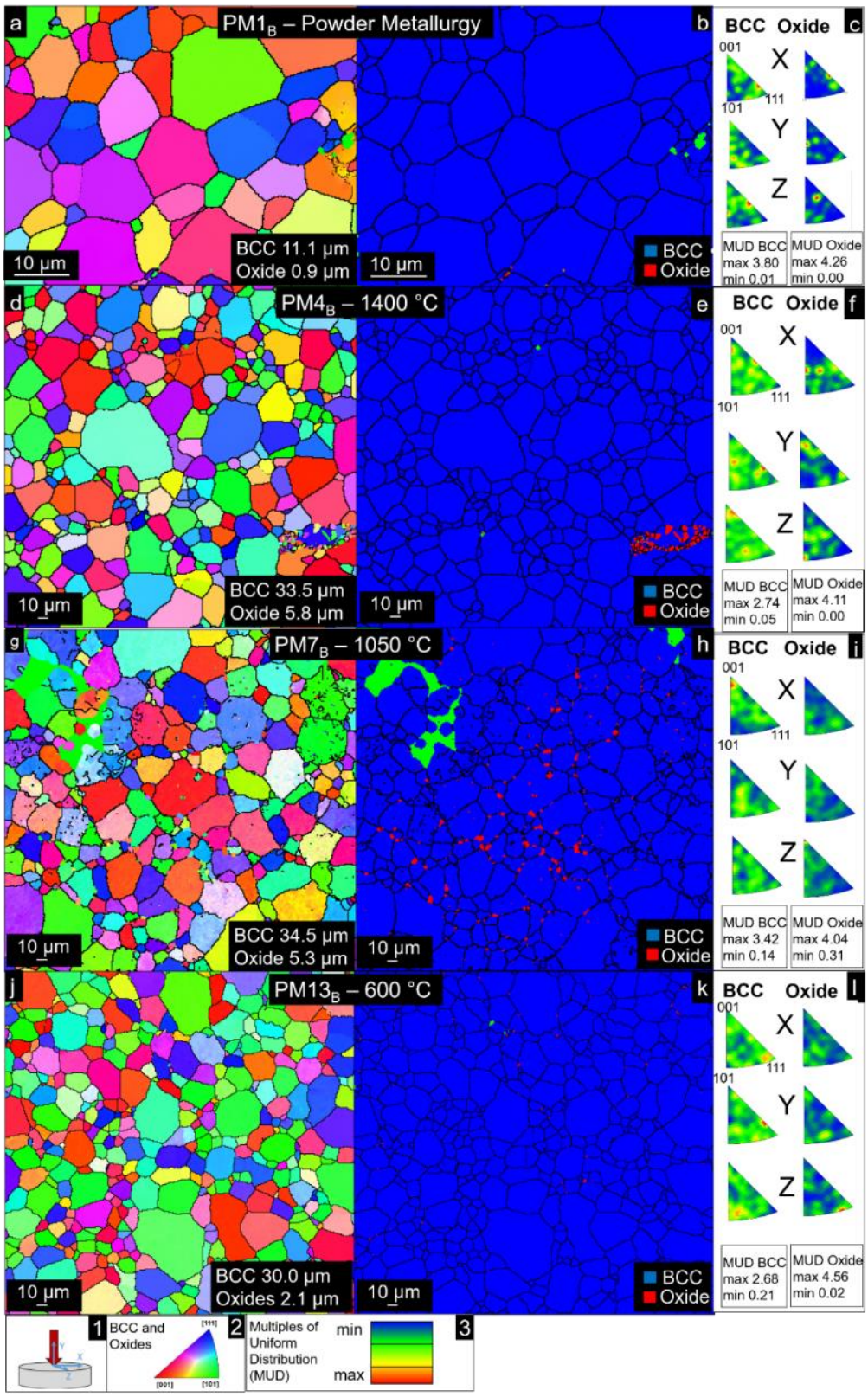

Supplementary Fig. 4. Representative SEM EBSD analysis of the PM_B RHEA. a,d,g,j) Grain orientation maps of $PM1_B$, $PM4_B$, $PM7_B$, and $PM13_B$ with reference direction Z denoted in 1, the grain orientation reference is shown in 2. b,e,h,k) Phase map showing distribution of BCC and Oxide phases in $PM1_B$, $PM4_B$, $PM7_B$, and $PM13_B$. c,f,i,l) Respective inverse pole figures denoting orientation in X, Y and Z direction with respective MUD reference in 3.